

January 2013

Long-Range, Passive Wireless Monitoring Using Energy-Efficient, Electrically-Small Sensor Nodes and Harmonic Radar Interrogator

Ibrahim Nassar

University of South Florida, inassar@mail.usf.edu

Follow this and additional works at: <http://scholarcommons.usf.edu/etd>

 Part of the [Other Earth Sciences Commons](#)

Scholar Commons Citation

Nassar, Ibrahim, "Long-Range, Passive Wireless Monitoring Using Energy-Efficient, Electrically-Small Sensor Nodes and Harmonic Radar Interrogator" (2013). *Graduate Theses and Dissertations*.
<http://scholarcommons.usf.edu/etd/4923>

This Dissertation is brought to you for free and open access by the Graduate School at Scholar Commons. It has been accepted for inclusion in Graduate Theses and Dissertations by an authorized administrator of Scholar Commons. For more information, please contact scholarcommons@usf.edu.

Long-Range, Passive Wireless Monitoring Using Energy-Efficient, Electrically-Small Sensor
Nodes and Harmonic Radar Interrogator

by

Ibrahim Turki Nassar

A dissertation submitted in partial fulfillment
of the requirements for the degree of
Doctor of Philosophy
Department of Electrical Engineering
College of Engineering
University of South Florida

Major Professor: Thomas M. Weller, Ph.D.
Lawrence Dunleavy, Ph.D.
Jing Wang, Ph.D.
Gokhan Mumcu, Ph.D.
Craig Lusk, Ph.D.
Jeffrey Frolik, Ph.D.

Date of Approval:
November 4, 2013

Keywords: Dual-band, Hoberman, re-configurable antenna, Vivaldi, 3-D antennas

Copyright © 2013, Ibrahim Turki Nassar

DEDICATION

This dissertation is dedicated to my father Dr. Turki Nassar for being the perfect father role model, for his inspiration, and for sacrificing all his life for our family and country, to my mother Rasmiah Nassar for her encouragement, continuous prayers, and belief in me, to my dear wife Hend for being a great Jordanian Arabic Muslim wife, being always optimistic, tolerating my seemingly excessive work and study times, and her sustainable and unconditional love, and to my beautiful princess daughter Rasmiah for always making me smile and lighthearted. They all are the secret behind my success.

ACKNOWLEDGMENTS

I sincerely thank my advisor, Prof. Thomas Weller, for his guidance, technical insight, and unlimited support throughout the past four years. I especially appreciate his great knowledge and experience, hard-working, successful management, patience, and great kindness and morality. His incredible hard-working, trust in my abilities, keen interest in my work, constructive comments, and deep work reviews had a serious influence on my motivation and professional growth. I would also like to thank my committee members for reviewing my dissertation and participating in the defense. Special thanks to Dr. Tapas Das for accepting to chair the dissertation defense.

I am very grateful to the administration, faculty, and staff of the University of South Florida, the college of engineering, the electrical engineering department, and the WAMI center for supporting the diversity, providing employment opportunities for the international student, and offering a great environment for working and studying. I greatly appreciate Dr. Lawrence Dunleavy's and Thomas Weller's efforts in offering various equipped research laboratory facilities. I am also very thankful to Sciperio and Modelithics incorporations for collaborating with us and always opening their facilities to us.

For financial support, I thank the National Science Foundation (NSF) for funding my research projects and the IEEE Microwave Theory and Technique Society (MTT-S) for awarding me a fellowship.

Finally, I would like to acknowledge all my lab mates and colleagues for their help, friendship, and interesting conversations including Scott Skidmore, Quenton Bonds, Bojana Zivanovic, Ebenezer Odu, Tony Price, Sergio Melais, Justin Boon, David Cure, James Cooper, James Mcknight, Michael Grady, Bryce Hotalen, Saurabh Gupta, Paul Deffenbaught, and Mohammed Abdin. Special thanks to Harvey Tsang for his unlimited help in the fabrication. Last but not least, my deepest thanks to Eduardo Rojas and Maria Cordoba and their families for their warm friendship.

TABLE OF CONTENTS

LIST OF TABLES	v
LIST OF FIGURES	vi
ABSTRACT	xvi
CHAPTER 1 : INTRODUCTION	1
1.1 Motivation	1
1.2 Major Technical Challenges	2
1.3 Technical Approach and Significance	4
1.4 Contributions	6
1.5 Dissertation Organization	9
CHAPTER 2 : LITERATURE REVIEW AND BACKGROUND	12
2.1 Structural Health Monitoring Systems	12
2.2 Harmonic Transponders	15
2.3 Electrically-Small Antennas Theories and Performance Limitations	19
2.4 Antenna Candidates for the Harmonic Radar Interrogator Unit	24
2.5 Reconfigurable Antennas	27
2.6 New Antenna and Microwave Circuit Manufacturing Technologies	30
2.7 Conclusion	32
CHAPTER 3 : PASSIVE HARMONIC TRANSCEIVER DESIGN	35
Note to Reader	35
3.1 Introduction	35
3.2 3-D Harmonic Transceiver Design	36
3.2.1 Passive Frequency Doubler Design	36
3.2.2 The Receive 2.4 GHz Antenna	39
3.2.3 The Transmit 4.8 GHz Antenna	41
3.3 Transceiver Performance Characterization	44
3.4 Sensor Emulation	47
3.5 Embedding in Sand	48
3.6 Conclusions	52
CHAPTER 4 : MINIATURIZED VIBRATION SENSOR NODE WITH 3-D MACHINED-SUBSTRATE ANTENNAS	53
4.1 Introduction	53
4.2 Transceiver Design	54

4.2.1	The Receive 2.4 GHz Antenna	55
4.2.2	The Transmit 4.8 GHz Antenna.....	56
4.2.3	The Impact of Substrate Machining.....	57
4.3	Experimental Results	58
4.4	Sensor Integration and Measurements	59
4.4.1	The Piezo Thin-Film Vibration Sensor.....	60
4.4.2	The Mechanical Sensors	62
4.5	Sensor Communication Range.....	66
4.6	Conclusion	67
CHAPTER 5 : DUAL-CHANNEL TRANSCEIVER DESIGN		68
5.1	Introduction.....	68
5.2	Transceiver Design	70
5.2.1	The 2.4/4.8 GHz Sensing Repeater.....	70
5.2.2	The 2.75/5.5 GHz Reference Repeater	73
5.3	Transceiver Performance	74
5.4	Transceivers Performance Comparison	76
5.5	Remote Channel Calibration.....	79
5.6	Node Identification	82
5.7	Embedding Impact.....	85
5.8	Conclusion	86
CHAPTER 6 : 3-D PRINTED ANTENNAS AND SENSOR NODE		88
Note to Reader		88
6.1	Introduction.....	88
6.2	3-D Small Antennas Fabricated with DAM.....	89
6.2.1	SLA Cube Antenna.....	89
6.2.2	FDM Cube Antenna.....	93
6.3	3-D Dual-Channel Sensor Node Fabricated with DAM.....	98
6.3.1	The 2.4/4.8 GHz Sensing Repeater.....	99
6.3.2	The 2.7/5.4 GHz Reference Repeater	102
6.4	Conclusions.....	104
CHAPTER 7 : DUAL-CHANNEL HARMONIC INTERROGATOR ANTENNA DESIGN.....		106
7.1	Introduction.....	106
7.2	Circular Patch Antenna (CPA) Array	108
7.2.1	CPA Array Design	108
7.2.2	CPA Array Performance	108
7.3	Miniaturization of the CPA Using Conformal 3-D Printing.....	110
7.4	Quasi-Yagi Dipole Antenna (QYDA) Array	112
7.4.1	Microstrip to Coplanar Strip Line Balun Design.....	112
7.4.2	QYDA Element Design	114
7.4.3	QYDA Array Design	115
7.5	Log-Periodic Dipole Antenna Array.....	117
7.6	Conclusion	121

CHAPTER 8 : RADIATING SHAPE-SHIFTING SURFACE BASED ON A PLANAR HOBERMAN MECHANISM	122
Note to Reader	122
8.1 Introduction.....	122
8.2 Antenna Structure	125
8.3 Antenna Design Using Electromagnetically-Coupled Parasitic Patches	126
8.4 Antenna Design Using Directly Connected Parasitic Patches.....	131
8.5 Antenna Design Using Directly Connected Parasitic Patches and Inserted Crossed-Slot.....	133
8.6 Broad-Band, Fixed-Beam Antenna Array	136
8.7 Conclusion	140
CHAPTER 9 : MECHANICALLY-RECONFIGURABLE, DUAL-BAND, CPW-FED SLOT ANTENNA	141
9.1 Introduction.....	141
9.2 Antenna Structure	144
9.3 Reconfigurable Antenna with Arbitrary Frequency Bands Ratio.....	146
9.4 Reconfigurable Antenna with a Frequency Ratio of Two	149
9.5 Dual-Band Slot Antenna Backed with a Cavity	151
9.6 Dual-Band Array Design	153
9.7 Conclusion	155
CHAPTER 10 : A NOVEL MULTI-OCTAVE VIVALDI ANTENNA DESIGN	156
10.1 Introduction.....	156
10.2 Vivaldi Antenna Radiation Mechanism and Bandwidth Limitations	159
10.3 Proposed Vivaldi Antenna Structure	162
10.4 The Performance of the Proposed Vivaldi Antenna	164
10.5 Conclusion	169
CHAPTER 11 : NON-DISPERSIVE PHASE SHIFTERS	170
Note to Reader	170
11.1 Introduction.....	170
11.2 Overview.....	171
11.3 CRLH TL Unit Cell Based Phase Shifter	172
11.4 Lumped Element 45° Phase Shifter Design	174
11.5 4-Bit Phase Shifter Design.....	175
11.6 Conclusion	176
CHAPTER 12 : SUMMARY AND RECOMMENDATIONS FOR FUTURE WORK.....	177
12.1 Summary	177
12.2 Recommendations for Future Work.....	178
REFERENCES	180
APPENDICES:.....	197

Appendix A: Copyright Permissions	198
A.1 Permissions for Chapter 3	198
A.2 Permission for Chapter 6.....	200
A.3 Permission for Chapter 8.....	201
A.4 Permission for Chapter 11.....	202
ABOUT THE AUTHOR	End Page

LIST OF TABLES

Table 2.1:	General interrogator antenna comparison.....	27
Table 3.1:	2.4 GHz receive antenna dimensions in mm	40
Table 3.2:	The 4.8 GHz transmit antenna dimensions in mm.....	43
Table 5.1:	Transceivers comparison and summary of the transceivers measured parameters.....	77
Table 5.2:	Comparison of the CG and electrical size with others from literature	78
Table 5.3:	Number of node IDs using a 2-3 GHz interrogator for different RF power levels (with polarization diversity)	84
Table 6.1:	The SLA antenna dimensions in mm.....	91
Table 6.2:	Measured and simulated antenna parameters for the SLA and PCB antennas.....	93
Table 6.3:	Measured and simulated FDM and PCB antenna parameters.	97
Table 8.1:	Comparison between the presented approach and results using an l-section matching network (mn).....	131
Table 9.1:	The dual-band slot antenna dimensions in mm.....	144

LIST OF FIGURES

Figure 1.1:	A conceptualization of the proposed wireless monitoring system.....	3
Figure 1.2:	Block diagram for passive wireless sensor being interrogated with an RF signal.....	5
Figure 2.1:	The radian sphere of radius a enclosing an antenna.	19
Figure 2.2:	The minimum radiation quality factor (Q) for a linearly polarized antenna.....	22
Figure 2.3:	The maximum antenna directivity.	24
Figure 3.1:	Block diagram of the schematic used to predict the frequency doubler performance.	38
Figure 3.2:	Simulated performance of the frequency doubler at 0V bias; conversion gain versus input power at f_1 of 2.4 GHz (left) and simulated conversion gain of the diode doubler versus frequency for different input powers.....	38
Figure 3.3:	The 2.4 GHz receive cube antenna.	39
Figure 3.4:	The approximate equivalent circuit model of the 2.4 GHz receive antenna.....	40
Figure 3.5:	The receive antenna input impedance (left), and the reflection coefficient between the receive antenna and the doubler input at -30 dBm input power and 0V bias (right).	41
Figure 3.6:	Simulated radiation patterns (in dB) of the 2.4 GHz receive antenna.	41
Figure 3.7:	The 4.8 GHz transmit antenna.	42
Figure 3.8:	The approximate equivalent circuit model of the 4.8 GHz transmit antenna.	43
Figure 3.9:	The 4.8 GHz antenna input impedance (left), and the reflection coefficient between the transmit antenna and the doubler output at -30 dBm input power and 0V bias (right).	43

Figure 3.10:	Simulated radiation patterns (in dB) of the 4.8 GHz transmit antenna.....	44
Figure 3.11:	A complete transceiver design (3D-view on top left; top-view on top right; fabricated 2.4/4.8 GHz harmonic repeater on bottom).....	45
Figure 3.12:	The experimental setup used to characterize the proposed harmonic transceiver.....	45
Figure 3.13:	The simulated and measured conversion gain versus frequency for different input powers at 0V bias.....	46
Figure 3.14:	The simulated and measured conversion gain versus input power at f_1 of 2.4 GHz and 0 V bias.....	46
Figure 3.15:	The measured conversion gain (dB) versus incidence angle (Y-Z plane, Figure 3.11) for different received power levels at f_1 of 2.4 GHz and 0V bias.....	47
Figure 3.16:	The measured conversion gain versus bias voltage at -30 dBm input power and f_1 of 2.4 GHz.....	48
Figure 3.17:	The measurement setup used to test the embedded harmonic transceiver.....	49
Figure 3.18:	Measured and averaged calibrated attenuation through a 20 cm sand layer versus frequency.....	50
Figure 3.19:	A comparison between the expected and measured CG versus frequency for received power of -30 dBm and 0V bias voltage in air and sand environments.....	50
Figure 3.20:	A comparison between the expected and measured CG versus input power at different f_1 and 0V bias voltage in air and sand environments.....	51
Figure 3.21:	The measured return signal level versus time for different modulation signals of frequency of 10 Hz and different amplitudes at f_1 of 2.38 GHz of the buried transceiver.....	52
Figure 4.1:	a) Photograph of the fabricated transceiver and the sensors used, b) the node with the piezo sensor, and c) the node with AG2401-1 switch sensor.....	54
Figure 4.2:	Transceiver design; 3-D view (top left), top-view (top right), photograph (bottom).....	55
Figure 4.3:	The reflection coefficient between the receive antenna and the doubler input at -30 dBm input power (left) and the simulated radiation patterns (in dB) of the 2.4 GHz antenna (right).....	56

Figure 4.4:	The reflection coefficient between the transmit antenna and the doubler input at -30 dBm input power (left) and the simulated radiation patterns (in dB) of the transmit antenna at 4.8 GHz (right).....	57
Figure 4.5:	Impact of the machining approach on the transceiver performance; a comparison table (left) and a CAD drawing of different transceiver iterations (right).	58
Figure 4.6:	The CG versus frequency for different received powers (left) and the CG versus input power for different f_1 (right).	59
Figure 4.7:	The measured CG (dB) versus incidence angle (YZ-plane, Figure 4.2).	59
Figure 4.8:	The experimental setup used to interrogate the proposed sensor node and detect vibration.....	60
Figure 4.9:	Measurement illustration (left) and the measured CG versus DC voltage for different RF input power (right).....	61
Figure 4.10:	The piezoelectric sensor output voltage versus time as measured using an oscilloscope (left) and the measured transceiver return signal level at $2 \cdot f_1$ with the piezoelectric sensor connected to the doubler input (right).	62
Figure 4.11:	Measurement illustration (left) and the measured return power difference at f_1 of 2.341 GHz when the DC return path is switched between open and closed states (right).	63
Figure 4.12:	The measured return power versus time for different received power levels for f_1 of 2.341 GHz using the AG2401-1 ball switch.....	64
Figure 4.13:	The measured return power versus time for different received power levels for f_1 of 2.341 GHz using the ASLS-2 shock/acceleration switch..	65
Figure 4.14:	The received return signal strength versus distance using a 43 dBm EIRP transmitter and 10 dB gain receiver.	67
Figure 5.1:	A CAD view of the proposed node (left) with a hypothetical sphere of 15.5 mm radius and a photograph of the fabricated design (right).	71
Figure 5.2:	Illustration of the sensing repeater, side view (left) and top view (right).....	72
Figure 5.3:	The simulated reflection coefficient between the receive antenna and the doubler input (left) and between the transmit antenna and the doubler output (right) of the sensing repeater at -30 dBm input power and 0V bias.....	72

Figure 5.4:	The simulated E-and H-plane radiation patterns of the sensing repeater receive antenna at 2.4 GHz (left) and transmit antenna at 4.8 GHz (right).	75
Figure 5.5:	Illustration of the reference repeater, side view (left) and top view (right).	75
Figure 5.6:	The measured CG of the dual-channel transceiver versus frequency for different received powers (left) and the simulated and measured CG versus received power at f_1 of 2.4 GHz and 2.75 GHz (right).	75
Figure 5.7:	The dual-channel transceiver shown with an inserted sensor.	76
Figure 5.8:	The expected communication range for different antenna radiation efficiency.	78
Figure 5.9:	The measurement setup used to perform the remote channel calibration.	80
Figure 5.10:	The measured received power level from the transceivers versus bias voltage at -30 dBm input power and f_1 of 2.4 GHz.	81
Figure 5.11:	Illustration of the calibration measurement setup (left) and the measured return power for different f_1 versus bias voltage applied to the sensing repeater at -30 dBm input power (right).	82
Figure 5.12:	The variation in extracted sensor voltage versus ΔP_r for different received power due to angle of incidence uncertainty (left) and δP_r for different azimuth angle and received power at 0 V bias (right).	83
Figure 5.13:	Illustration of the embedding experimental setup.	85
Figure 6.1:	The fabricated cube antennas using PCB (left) and stereolithography (right) fabrication methods.	90
Figure 6.2:	The SLA antenna design.	90
Figure 6.3:	The measured and simulated S_{11} for the PCB design (left) and the SLA design (right).	92
Figure 6.4:	Comparison between measured E-plane (left) and H-plane (right) radiation patterns for the SLA and the PCB designs.	93
Figure 6.5:	A photograph of the 3-D machined substrate cube antenna fabricated with the FDM process (left) and fabricated with the PCB technology (right).	94
Figure 6.6:	A CAD illustration of the proposed FDM cube antenna.	95

Figure 6.7:	The measured dielectric constant (ϵ_r) and loss tangent of the ABS material for different frequencies.....	96
Figure 6.8:	The simulated and measured S_{11} of the presented FDM antenna design (left) and the measured E-plane and H-plane radiation patterns (right).	97
Figure 6.9:	Comparison of G/Q ratio of the presented antenna designs and other miniaturized antennas.	98
Figure 6.10:	A CAD view of the printed 3-D dual channel node with a hypothetical sphere of 15 mm radius (left) and a photograph of the fabricated node (right).	99
Figure 6.11:	Illustration of the 3-D printed node sensing repeater, side view (left) and top view (right).	100
Figure 6.12:	The simulated reflection coefficient between the receive antenna and the doubler input (left) and between the transmit antenna and the doubler output (right) of the 3-D printed node sensing repeater at -30 dBm input power and 0V bias.	100
Figure 6.13:	The simulated E-and H-plane radiation patterns of the 3-D printed node sensing repeater receive antenna at 2.4 GHz (left) and transmit antenna at 4.8 GHz (right).....	101
Figure 6.14:	Simulated CG of the 3-D printed node sensing repeater and multiplier for different input power levels at f_1 of 2.4 GHz.....	101
Figure 6.15:	Illustration of the 3-D printed node reference repeater, side view (left) and top view (right).	102
Figure 6.16:	The simulated reflection coefficient between the receive antenna and the doubler input (left) and between the transmit antenna and the doubler output (right) of the 3-D printed node repeater at -30 dBm input power and 0V bias.	103
Figure 6.17:	The simulated E-and H-plane radiation patterns of the 3-D printed node reference repeater receive antenna at 2.7 GHz (left) and transmit antenna at 5.4 GHz (right).....	103
Figure 6.18:	Simulated CG of the 3-D printed node reference repeater and multiplier for different input power levels at f_1 of 2.7 GHz.	103
Figure 7.1:	Illustration of the fabricated dual-channel circular patch antenna array.....	109

Figure 7.2:	The simulated S_{11} of the transmit (left) and receive (right) CPA arrays.	109
Figure 7.3:	The measured E-and H-plane radiation patterns of the transmit CPA array at 2.4 GHz (left) and the receive CPA array at 4.8 GHz (right).	110
Figure 7.4:	Illustration of the miniaturized (top-left) and regular (top-right) circular patch antennas and a side view of the miniaturized patch (bottom).	111
Figure 7.5:	A comparison of the measured S_{11} of the miniaturized conformal patch antenna and the regular patch antenna.	111
Figure 7.6:	A comparison of the measured radiation patterns of the miniaturized and regular patch antenna; H-plane (left) and E-plane (right).	112
Figure 7.7:	Illustration of the dual-channel quasi-Yagi bow-tie dipole antenna array; side view (left) and top view (right).	113
Figure 7.8:	Illustration of the balun dimensions in mm.	113
Figure 7.9:	Simulated S-parameters of the baluns used to feed the quasi-Yagi dipole antenna arrays.	114
Figure 7.10:	Illustration of the receive and transmit quasi-Yagi dipole antenna dimensions in mm.	115
Figure 7.11:	Simulated S_{11} of the dual-channel quasi-Yagi dipole antenna array; transmitting array (left), and receiving array (right).	116
Figure 7.12:	Simulated gain of the dual-channel quasi-Yagi dipole antenna array; transmitting array (left), and receiving array (right).	116
Figure 7.13:	The simulated radiation patterns of the transmit antenna array at different frequencies; E-plane (left) and H-plane (right).	117
Figure 7.14:	The simulated radiation patterns of the receive antenna array at different frequencies; E-plane (left) and H-plane (right).	117
Figure 7.15:	Illustration of the 3-D printed LPDA array; side view (left) and top view (right).	119
Figure 7.16:	Simulated and measured S_{11} of the 3-D printed log-periodic dipole antenna array (left) and simulated realized gain in the endfire direction (right).	120
Figure 7.17:	Measured radiation patterns of the 3-D printed log-periodic dipole antenna array; E-plane (left) and H-plane (right).	120

Figure 8.1:	Illustration of the planar Hoberman linkage with the actuation rings and a motor: a) in the uncompressed position, b) the compressed position, and c) a side view.....	123
Figure 8.2:	Prototype antenna with Hoberman linkage and the two rings (left); table showing the layer stack-up (right).	124
Figure 8.3:	a) The circular microstrip antenna geometry and b) measured and simulated S_{11} of the antenna without the parasitic patches.....	126
Figure 8.4:	View of the RSSS mechanism without the actuation rings: a) unperturbed and b) compressed ($X1=7\text{mm}$) (right).	127
Figure 8.5:	Equivalent circuit model for the geometry with EM-coupled parasitic patches.....	128
Figure 8.6:	The simulated and modeled S_{11} of the geometry with EM-coupled parasitic patches for different $X1$ values in mm.	129
Figure 8.7:	The measured and simulated S_{11} of the geometry with EM-coupled parasitic patches for different $X1$ values in mm.	130
Figure 8.8:	The measured co-and cross-pol radiation patterns for the geometry with EM-coupled parasitic patches for $X1=17$ mm at 3.02 GHz, and for $X1=8$ mm at 2.77 GHz; E-plane (left) and H-plane (right).	130
Figure 8.9:	a) The RSSS with shorting vias (second geometry) and b) the simulated S_{11} for different $X1$ values in mm.	132
Figure 8.10:	The measured and simulated S_{11} for the second geometry for different $X1$ values.	133
Figure 8.11:	The measured co- and cross-pol radiation patterns for the second geometry for $X1 = 14$ mm at 2.23 GHz and $X1 = 11$ mm at 2.62 GHz; E-plane (left) and H-plane (right).	133
Figure 8.12:	a) The RSSS with shorting vias and crossed-slots (third geometry) and b) the simulated S_{11} for $X1= 17$ mm.	134
Figure 8.13:	a) The simulated S_{11} of the third geometry for different $X1$ values, and b) illustration of the structure for $X1= 5$ mm.	135
Figure 8.14:	The simulated E-plane radiation patterns of the third geometry for different $X1$ values.....	135

Figure 8.15:	A 2×2 array illustration: (left) uncompressed array ($X_1 = 17\text{mm}$, $X_r = 50\text{ mm}$), (right) compressed array ($X_1 = 8.5\text{ mm}$, $X_r = 70\text{ mm}$).	137
Figure 8.16:	The simulated S_{11} (left) and simulated E-plane radiation pattern (right) of the array for two states.....	138
Figure 8.17:	The simulated E-plane radiation pattern of the array if the element spacing is not changed.	138
Figure 8.18:	The simulated E-plane radiation pattern (left) and the simulated axial ratio (right) of the CP array for two states.	139
Figure 8.19:	The simulated E-plane radiation pattern of the CP array if the element spacing is not changed.	139
Figure 9.1:	Illustration of the reconfigurable dual-band antenna with arbitrary frequency ratio; top view (top) and side view (bottom).	143
Figure 9.2:	Configuration of the dual-band antenna structure.	145
Figure 9.3:	The measured and simulated S_{11} of the dual-band slot antenna.	145
Figure 9.4:	Dual-band slot antenna measured radiation patterns; H-plane (left) and E-plane (right).....	146
Figure 9.5:	The configuration of the dual-band slot antenna with arbitrary frequency ratio.	147
Figure 9.6:	The simulated S_{11} of the dual-band antenna with arbitrary frequency ratio for different X_1 and $X_u = 0\text{ mm}$ (left) and different X_u and $X_1 = 0\text{ mm}$ (right).	147
Figure 9.7:	The measured (dashed) and simulated (solid) S_{11} for $X_u=0\text{ mm}$ and different X_1 values.....	148
Figure 9.8:	The measured (dashed) and simulated (solid) S_{11} for $X_1=0\text{ mm}$ and different X_u values.....	148
Figure 9.9:	Measured E-and H-plane for $X_1 = 12\text{ mm}$ and $X_u = 0\text{ mm}$ at 3 GHz (left) and for $X_1 = 0\text{ mm}$ and $X_u = 5\text{ mm}$ at 5 GHz.	149
Figure 9.10:	The configuration of the dual-band slot antenna with frequency ratio of 2 and one motor..	150
Figure 9.11:	The simulated S_{11} of the dual-band antenna with a frequency ratio of 2	

	for different X1 values.....	150
Figure 9.12:	Simulated E- and H-plane radiation patterns of the dual-band slot antenna with a frequency ratio of 2 for X1 = 10 mm at 3 GHz (left) and 6 GHz (right).	151
Figure 9.13:	A photograph of the cavity-backed dual-band slot antenna.....	152
Figure 9.14:	Simulated and measured S ₁₁ of the dual-band cavity-backed slot antenna.	152
Figure 9.15:	Measured E- and H-plane radiation patterns of the dual-band cavity-backed slot antenna at 2 GHz (left) and 4 GHz (right).	153
Figure 9.16:	Illustration of the dual-band cavity-backed slot antenna array configuration.	154
Figure 9.17:	Simulated E- and H-plane radiation patterns of the dual-band cavity-backed slot antenna array at 2 GHz (left) and 4 GHz (right).	154
Figure 10.1:	Photograph of the proposed Vivaldi antenna with/without the parasitic ellipse (top view).....	159
Figure 10.2:	Illustration of the radiation mechanism of Vivaldi antennas.	160
Figure 10.3:	Illustration of the E-field distribution at high frequencies.....	162
Figure 10.4:	Illustration of the geometry of the proposed antipodal Vivaldi antenna.	163
Figure 10.5:	The electric field distribution of the proposed Vivaldi antenna with and without the parasitic ellipse at 17 GHz.	163
Figure 10.6:	Comparison of the measured and simulated S ₁₁ of the proposed Vivaldi antenna with and without the director.....	165
Figure 10.7:	Comparison of the simulated realized gain in the endfire direction of the proposed Vivaldi antenna with and without the director (left) and comparison of the measured and simulated gain difference between the two antennas (right).	165
Figure 10.8:	Comparison of the simulated E-plane radiation patterns with and without the parasitic ellipse at a) 2 GHz, b) 5 GHz, c) 7 GHz, d) 10 GHz, e) 12 GHz, f) 15 GHz, g) 20 GHz, and h) 25 GHz.	166
Figure 10.9:	Comparison of the measured E-plane radiation patterns with and without the parasitic ellipse at a) 5 GHz, b) 7 GHz, c) 10 GHz, d) 12 GHz, e) 15 GHz, and f) 20 GHz.	167

Figure 10.10: Gain comparison of the proposed antenna and typical antipodal Vivaldi without the director and with different sizes.....	168
Figure 10.11: The simulated gain of the proposed antenna with/without the director for different substrate thicknesses.	169
Figure 11.1: Lumped element circuit model of a CRLH unit cell (Left) and representative $K-\omega$ diagrams of a balanced CRLH unit cell being switched from state #1 to state #2 (right).....	174
Figure 11.2: Equivalent circuit representations of the 45 degree two-state phase shifter (left) and the fabricated circuits for each state (right).	175
Figure 11.3: The simulated and measured S_{11} (top-left), S_{22} (top-right), S_{21} bottom-left), and phase difference between the two-circuit states (bottom-right).	175
Figure 11.4: Illustration of a 4-bit CRLH transmission line phase shifter.	176

ABSTRACT

This dissertation investigates the use of the harmonic radar technique for passive wireless sensing applications. Issues of DC power consumption, high RF activation power, large node size, and short communication range associated with the existing passive wireless sensing technologies are addressed by the development of novel, completely passive, high efficiency, compact 3-D harmonic sensor nodes. The node transceiver employs a passive frequency doubler to return the second harmonic of the interrogation signal, and electrically-small 3-D antennas to achieve the compactness and high efficiency. The developed nodes fit inside a sphere with a diameter < 3 cm and achieve communication range > 60 m using a 43 dBm EIRP interrogator. Effective modulation is demonstrated experimentally using low cost commercial vibration sensors. To address major challenges associated with long-range, embedded, passive wireless sensing including sensor node identification and remote channel calibration, a 3-D dual-channel transceiver is developed. To the best of the author's knowledge, the presented dual-channel transceiver is the first completely passive design with built-in passive remote channel calibration and identification capabilities, and the presented nodes have the best overall performance among previously published designs, in terms of conversion efficiency, communication range, and occupied volume. To reduce the cost and weight and improve the manufacturing process of the proposed nodes, the 3-D digital additive manufacturing and conformal direct printing technologies are employed.

The harmonic interrogator antenna design is also an underlying focus of this work. Different interrogator antenna candidates are developed based on different design approaches. The first approach is based on the use of dual-channel antenna array, where one channel is used for transmission and the second channel is used for reception. Two dual-channel harmonic interrogator antennas that consist of 4-element circular patch antenna arrays and 2-element quasi-Yagi dipole antenna arrays are implemented. The second approach employs mechanically reconfigurable antennas to reduce the size and maintain persistent radiation properties over wide frequency bandwidth. Two mechanical reconfiguration methods are developed; the first method is based on the use of Hoberman's planar foldable linkage to vary the operating frequency of planar circular patch antennas and the second mechanical reconfiguration method is based on the use of a rack and pinion mechanism to reconfigure dual-band slot antennas. The third approach employs a single channel multi-octave Vivaldi antenna to provide the capability to interrogate a large number of harmonic tags that are widely spaced in frequency. To improve the antenna radiation performance over a broad frequency range, a new method based on the introduction of a parasitic elliptical patch in the flare aperture is proposed. This method enables gain and bandwidth improvement compared to what has been reported for Vivaldi antennas with a compact size. To provide the interrogator the capability to steer the radiation beam for locating and tracking sensor nodes, a topology to develop a miniature, non-dispersive switchable 4-bit phase shifter is proposed on the basis of composite right/left handed transmission line unit cells.

CHAPTER 1 : INTRODUCTION

1.1 Motivation

The global society is increasingly dependent upon larger and more complex networks of civil infrastructure that are costly to maintain. In the United States alone, the government spending on highway infrastructure amounted to \$41 billion in 2009 as reported by the U.S. congressional budget office. These infrastructures, especially those for transportation, are often subjected to long-term deterioration due to factors such as corrosion of the steel reinforcement, high continuous vibration, high pH concentration, overloading, and natural catastrophic events [1, 2, 3]. This degradation can lead to severe consequences on the public safety and economy which necessitates continuous assessment of the infrastructure health. The early stage detection of fatigue and damage can be very beneficial in providing an early warning and allowing the recovery of the structure before the fatigue expands and human safety is threatened.

The necessity for reliable infrastructure health assessment has motivated research activity on distributed wireless sensors which are seen as a technology that can potentially provide near continuous and near real-time non-destructive monitoring [4, 5, 6]. In order to efficiently provide such monitoring capabilities, the sensor device may be preferred to be deeply embedded within the structure for an extended period of time in direct proximity of the physical or chemical activity of interest. However, embedding the sensing devices into a natural environment introduces different challenges and limitations. One of the major issues is the DC power consumption as the operating lifetime should be maximized due to the difficulty of in-field

servicing of the sensors. This constraint necessitates either that the node has sufficient on-board energy resources to sustain an active device for the deployment lifetime, or that the node be passive. For use in civil infrastructure the former approach is not tenable thus motivating much recent work on passive wireless sensing systems [7, 8, 9, 10]. Various energy harvesting methods [11, 12, 13, 14, 15] have also been developed to mitigate the power consumption issue. However, they are not suitable for many embedding environments due to the limited availability of ambient power.

The objective of this research is to advance the state of the art of low-power, passive wireless sensing. Major challenges associated with passive wireless sensing such as sensor node size, power consumption, communication range, sensor node identification, and remote channel calibration are addressed in this dissertation. This research primarily concentrates on 1) producing electrically-small, inexpensive, light-weight, energy-efficient sensor nodes that are targeted for deeply-embedded and through-life structural health monitoring of civil infrastructures and 2) developing novel harmonic radar interrogator antennas to enhance the interrogation process.

1.2 Major Technical Challenges

Figure 1.1 illustrates a conceptualization of the proposed wireless monitoring system. An interrogator will be used to communicate with sensor nodes embedded in a structure. The sensor nodes are completely passive, with no on-board power source or external power harvesting. In order to provide long-term, continuous, and near real-time monitoring capabilities, there are different challenges and issues will be introduced. The challenges that will be addressed in this dissertation are discussed below.

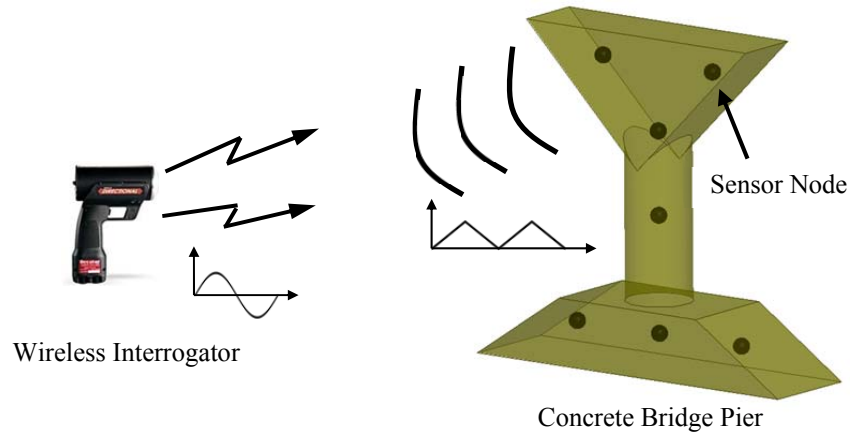


Figure 1.1: A conceptualization of the proposed wireless monitoring system.

- a) **Sensor Node Size:** the issue of node geometry is an important consideration in this work. The compact node geometry is desirable for deployment ease and to ensure that the integrity of the structure being monitored is not compromised. However, as the sensor node volume shrinks, antenna efficiency can be the limiting factor of the overall transceiver performance. Therefore, a compromise between the node size and efficiency is required.
- b) **Wireless Transmission Range:** the major drawback of the current passive wireless sensors is the short communication range. For example, the radio frequency identification (RFID) sensors communication range is typically few meters in a free space environment. The short range limits the ability to periodically assess the health of infrastructure. While the embedded sensing device will have an enhanced sensing capability, at the same time embedding will limit further the communication range due to the higher propagation loss of the non-air propagation channel (e.g., concrete or soil). The transmission range and channel loss limit the amount of RF power that can be received by the sensor and require the sensing device to operate at very low RF power levels.
- c) **Embedding Impact:** the surrounding medium directly affects the antenna impedance and the operating frequency. As it is desirable to have the sensing device be with a compact

geometry, the antenna impedance bandwidth can be very narrow (~1%) thus the dielectric loading of the surrounding medium may cause significant loss in the overall node efficiency.

- d) Propagation Channel Calibration: the conditions of the wireless environment may change, affecting the characteristics of the communication channel (e.g., media attenuation) between the interrogator and the sensor node. This requires the interrogator-node link (i.e., propagation channel) to be remotely calibrated in a periodic manner after the node is already deployed.
- e) Passive Node Identification: when different sensors are deployed within the same structure, some means of knowing which node is being activated is needed. As the sensor nodes need to be passive, the signal processing at the node will be limited requiring the development of passive identification techniques. Increasing the communication range will also introduce limitations on the maximum number of nodes, distance between the nodes, and the interrogator antenna design.

1.3 Technical Approach and Significance

An effective passive sensor node transceiver design for deeply embedded, long life, long range monitoring should be optimized for low RF power operation. A well-known approach for providing such power is through radio frequency (RF) interrogation [16, 17] (Figure 1.2). Both passive RFID and SAW-based devices operate on this premise but are constrained to short-range implementations due to their requisite high activation power [18, 19, 20]. An approach that has been shown to use lower RF activation power than RFID or SAW-based methods is harmonic radar. This approach uses the RF interrogation technique to communicate with a sensor tag that employs a passive frequency doubler to return the second harmonic of the interrogation signal [21, 22, 23, 24]. Relying on the reception of the second harmonic, instead of the fundamental

signal, avoids signal clutter and transmitter-receiver bleed-through issues [25] that are considered the major range limitations.

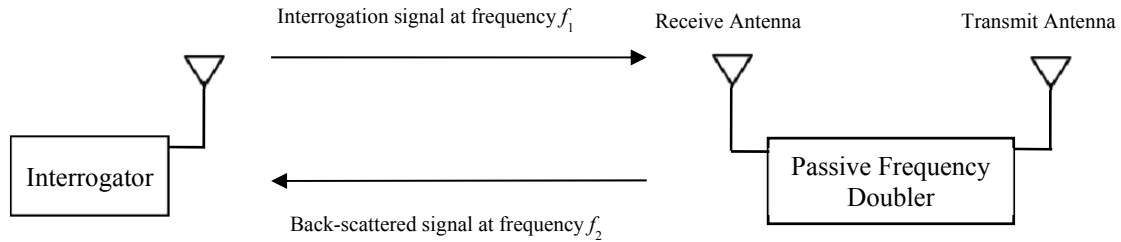


Figure 1.2: Block diagram for passive wireless sensor being interrogated with an RF signal.

Although harmonic radar technique requires a larger tag footprint compared to an RFID design due to the use of two antennas, 3-D antennas can be employed to miniaturize the occupied volume and maintain acceptable performance. As the transmitted power is low, efficient antennas are required for achieving successful transmission and reception of data between the sensor nodes and the interrogator. 3-D antennas are often preferred for applications that require high efficiency concurrently with small size, since these antennas make more efficient use of the available volume for radiation by realizing relatively long antenna lengths. For the wireless sensor application space, 3-D antenna designs have the additional benefit of making available the structure interior for sensor and/or electronics placement. In addition, the 3-D sensor node design approach facilitates the wireless interrogation and the node deployment. While the fabrication process required for a 3-D antenna will be more complex than that for a typical 2-D antenna, 3-D digital additive manufacturing and printing methods will be utilized to address this drawback.

The interrogation process will be enhanced by developing novel harmonic radar interrogator antennas. The interrogator antenna is desired to have high gain, narrow beamwidth, wide bandwidth with persistent radiation characteristics, light weight, small size, and low cost. Instead of using a high power source, the high gain antenna will allow distant nodes to be

interrogated without reducing the isolation between the transmitted signal and the sensor response. The light weight and small size antenna is desired to allow the realization of a hand held interrogator and the narrow beamwidth and wide bandwidth with persistent radiation characteristics are desired to maximize the number of the uniquely identified nodes, as will be discussed in Section 5.6, and facilitate the interrogation and identification processes. The high gain, narrow beamwidth and wide bandwidth characteristics, however, cannot be realized with a light weight small antenna size. Therefore, different antenna design options will be investigated in this work including narrow band and broad band dual-channel antenna arrays, mechanically reconfigurable antennas, and a single-channel multi-octave Vivaldi antenna. To provide the capability to steer the interrogator radiation beam, a switchable 4-bit phase shifter will also be investigated.

1.4 Contributions

The main contributions from this work fall within the following categories:

- a) Adding valuable studies and techniques on designing small antennas.

The simulation, experimental results, and radiation characteristics of the proposed antennas have yielded an understanding of the limitations for each design and their potential to provide solutions for small sensor node design. A new approach to the design of dipole antennas on a cube configuration that has the ability to house sensor electronics inside the cube structure without significantly degrading its performance is presented. The antenna designs developed based on this approach compare well with high efficiency, electrically small antennas that have been described in the open literature. In addition, a new machined-substrate approach that enables significant improvements in the size and performance of the node is proposed.

b) Development of harmonic transceivers for the purpose of passive wireless sensing.

Different harmonic transceiver designs are developed in this research that offer a combination of zero DC power consumption, low RF power operation, high conversion efficiency, modulation capability, and omni-directional radiation patterns. To the best of the author's knowledge, the developed harmonic transceivers have the best overall performance among previously published designs, in terms of conversion gain, communication range, and occupied electrical volume. In addition, unlike previously reported designs, the transceivers have a 3-D miniature form factor that is readily adapted to different packaging requirements.

c) Addressing the remote channel calibration challenge and investigating the passive node identification issue.

Two new approaches for remote channel calibration of passive sensors are proposed in this dissertation. To the best of the author's knowledge these approaches will be the first to harness a passive remote sensor calibration concept. Passive node identification is also studied and investigated in this work. The identification approach gives the ability to distinguish between multiple nodes located within the interrogator beam angle, and will allow the interrogation range to increase without introducing limitations on the maximum number of nodes, distance between the nodes, and the interrogator antenna design.

d) Development of a compact dual-channel transceiver.

A compact, 3-D dual-channel transceiver for passive wireless sensor node design is developed. The transceiver contains two harmonic transceivers, one to be connected to a sensor and one to provide a reference signal for remote channel calibration and node identification. To the best of the authors' knowledge, the presented transceiver is the first completely passive design with built-in passive remote channel calibration and identification capability.

e) Demonstration of different modulation capabilities of the proposed harmonic transceiver designs.

Two methods for sensor integration to modulate the transceiver return signal were investigated. Effective modulation was demonstrated using low cost commercial vibration sensors.

f) Development of new methods to the design of mechanically reconfigurable antennas.

Two new methods for the design of mechanically reconfigurable planar antennas were developed. The first method is based on the use of Hoberman's planar foldable linkage to vary the electromagnetic properties of the antenna. This method is applied in the design of frequency-tunable planar microstrip patch antennas demonstrating good frequency tunability range with essentially constant gain and radiation patterns. The use of this method for the design of reconfigurable microwave phased antenna array system with non-dispersive radiation characteristics is also investigated. The second mechanical reconfiguration method is based on the use of a rack and pinion mechanism. This method is employed in the design of frequency-tunable dual-band slot dipole antennas. Two prototypes are designed based on this approach demonstrating $> 40\%$ tunability range for each frequency band.

g) Proposing a new method for improving the radiation characteristics and bandwidth of the antipodal Vivaldi antenna.

To improve the Vivaldi antenna radiation performance over a wide frequency range, a new method based on the introduction of a parasitic elliptical patch in the flare aperture is proposed. The method allows the gain to be improved at high frequencies without compromising the low frequency performance, enabling gain and bandwidth improvement compared to what has been reported for Vivaldi antennas with a compact size.

h) Proposing a new topology to the design a switchable non-dispersive 4-bit phase shifter.

A new topology to develop a miniature, non-dispersive switchable 4-bit phase shifter on the basis of composite right/left handed transmission line unit cells is proposed. The proposed design can be used to steer the interrogator radiation beam.

i) Showing the advantages of the use of the digital additive manufacturing and 3-D printing technologies in the design of efficient RF components.

The digital additive manufacturing and 3-D printing technologies have been used in the design of electrically-small 3-D antennas, compact 3-D sensor nodes, and planar antennas enabling the realization of low-cost, light-weight, efficient, miniaturized RF devices with improved manufacturing reliability and repeatability.

1.5 Dissertation Organization

The dissertation is divided into twelve chapters. Chapter one and twelve correspond to the introduction and summary, respectively, and the rest of the chapters present the main content of this dissertation research.

Chapter two provides a literature review of the existing passive wireless sensing technologies, existing harmonic transceivers, small antennas theory and performance limitations, antenna candidates for the harmonic radar interrogator, reconfigurable antennas, and new antennas and microwave circuit manufacturing technologies.

The design, testing, and analysis of passive 3-D harmonic transceiver design are presented in Chapter three. The sensing capability and the integration with practical sensors are discussed in this chapter. Experimental results to demonstrate the suitability of the design for embedded environment are also given.

Chapter four describes the design of a miniaturized sensor node with 3-D machined-substrate antennas. Effective modulation is demonstrated using commercial vibration sensors. Outdoor measurements to determine the node-interrogator communication range are also illustrated in this chapter.

Chapter five illustrates a dual-channel transceiver design. The transceiver contains separate harmonic transceivers for sensing and to provide a reference signal (no sensor) for remote channel calibration and identification. This chapter also analyzes remote channel calibration and discusses the node identification. In addition, comparisons between the transceivers presented in this dissertation and with other designs from the literature are given.

Chapter six shows the advantages of the use of digital additive manufacturing and 3-D printing technologies in the design of electrically-small 3-D antennas and compact 3-D sensor nodes. Two 3-D small antennas fabricated with the stereolithography and fused deposition modeling processes are presented. A 3-D compact sensor fabricated with the fused deposition modeling method and 3-D conformal printing is also presented.

Chapter seven presents the first approach for the design of the harmonic interrogator antenna. The approach is based on the use of dual-channel arrays. Two designs are developed based on this approach. The first one consists of 4-element circular microstrip patch antenna arrays and the second one consists of 2-element quasi-Yagi dipole antenna arrays. To miniaturize the circular patch array, an approach using the 3-D printing technology is illustrated and to expand the interrogator bandwidth a 3-D printed log-periodic dipole antenna array is presented.

In Chapter eight a new method for designing reconfigurable antennas using a foldable mechanism to change the radiating surface area is presented. Using a planar Hoberman linkage different resonant frequency-tunable circular patch antennas are developed. The proposed

mechanism is also employed in the design of a reconfigurable microwave phased antenna array system.

Chapter nine proposes a new method for the design of tunable dual-band slot antennas. Using a rack and pinion mechanism, two mechanically reconfigurable dual-band slot antennas are designed. Testing of the impact of backing the antenna with a cavity and preliminary analysis of integrating the antenna into a three-element array arrangement are also given.

Chapter ten illustrates the design of a multi-octave interrogator antenna. The antenna is a novel Vivaldi designed using a new method based on the introduction of a parasitic elliptical patch in the flare aperture. This method enables gain and bandwidth improvement compared to what has been reported for Vivaldi antennas with a compact size.

Chapter eleven proposes a topology for the design of a switchable 4-bit non-dispersive phase shifter. This design can be used for steering the interrogator antenna radiation beam. To demonstrate this topology a 45° lumped element design is implemented.

CHAPTER 2 : LITERATURE REVIEW AND BACKGROUND

2.1 Structural Health Monitoring Systems

Different research communities are aggressively exploring novel sensing technologies capable of providing an automated, non-destructive structural health monitoring. Over the past decades different monitoring techniques have been developed including strain measurements, acoustic emissions [26], guided-wave scattering [27], and optical techniques [28]. These techniques primarily employ piezoelectric, strain gauges, and optical fiber sensors [7]. While damage detection is enabled, these methods require cable connections for the power and data transmission which introduces implementation difficulties and increase significantly the cost. Recently, the wireless sensing technology emerged to advance the conventional monitoring systems for reduced cost. Many wireless sensors have been developed for the use in structural monitoring [29, 30, 31, 32, 33] and a number of them are currently commercially available. A number of the commercial sensors have also been implemented in practice, including the Mote wireless sensor platform and platforms from the Ember and Microstrain companies [34]. While these sensors are well suited for structural monitoring and reduced the implementation complexity, they all have high cost, finite lifetime and require battery replacement. More recently, research activities investigating techniques to enable the realization of completely passive wireless sensors have been activated. The advantages of the passive wireless sensors are the infinite lifetime and the low cost. The existing passive wireless sensors can be categorized as

oscillating and resonance circuit sensors, RFID sensors, and harmonic and intermodulation sensors.

The resonant circuit sensors have been used for strain and moisture measurements. They basically consist of an antenna coupled to LC or RC circuits. The LC or RC circuit function is to transform the strain into a shift in the resonant frequency of the antenna. Different sensors have been developed based on this principle using solenoidal inductors [35], coaxial resonant cavities [36], incompressible liquids [37], and carbon fiber polymers [38]. These sensor devices use the wireless interrogation and the near-field coupling to the reader for data transmission. The read range of this passive sensing method is very limited.

The RFID devices can be classified into two categories; silicon based tags and surface acoustic wave (SAW) tags. The silicon tag consists of an integrated circuit (IC) chip connected to an antenna and uses the microwave signal from a specialized reader for power and communication. When illuminated with an electromagnetic wave, the tag responds by reflecting a modulated signal with a unique identification code. These tags require DC power to function that can either be obtained directly from a battery or wirelessly from the reader. The battery-less RFID tag rectifies the received interrogation signal, to generate the required threshold voltage to power the IC chip. Due to signal propagation loss and regulatory limits on the broadcasting power, the interrogation range is limited to ~50 cm and ~10 m for the inductively coupled devices and UHF tags, respectively [39]. The power constraint also limits the highest frequency of operation and thereby the tag size. In the other hand, a SAW RFID device consists of an antenna and a transducer [40, 41]. The transducer converts the signal received by the antenna into acoustic surface wave that propagates through a piezoelectric crystal. Part of this wave reflects back and then is reconverted by the transducer into an electromagnetic wave that

propagates back to the reader [42]. The SAW propagation velocity is less than the velocity of an electromagnetic wave. By designing the SAW RFID chip to be of a suitable length, a time delay can be readily introduced between the reader's transmit and receive signals, which helps in separating the environmental echoes and spurious received signals. Separating the echoes allows the reading range to expand (~20m [20]) and the reader transmitted power to be reduced. The longer range and lower transmitted power makes the SAW tags more suitable for the implementation in harsh environments. The highest frequency of operation of a SAW tag is also limited to few GHz due to the inability to realize transducers with very small traces on the SAW substrate. In addition, the SAW tag costs more than the silicon based tag.

While the RFID technology is mainly used for identification, the RFID tag functionality can be enhanced by integrating sensors. Recently, the interest in incorporating a sensor with an RFID tag to obtain different information about the physical world has risen [17, 39, 43]. Sensor enhanced RFID tags have numerous applications and suitable for embedded monitoring, however, the required proximity to the reader remains the major drawback.

In the previously discussed systems the interrogation and response signal are both with the same frequency. The return signal serves both to transmit data and to distinguish from clutter. In order to enhance the interrogation and allow the communication range to expand, the interrogation signal should be separated from any interference. This has led to the development of the harmonic and intermodulation transponders. The intermodulation principle was first demonstrated for telemetry applications in 1973 [44]. The advantage of the intermodulation scheme over the harmonic approach is the smaller frequency separation which facilitates the transceiver design. The intermodulation transponder consists of an antenna connected to a mixing element and a sensing element. When illuminated with two signals at different

frequencies, the transponder transmits the sensor data at one of the intermodulation frequencies. A passive sensor based on the intermodulation principle has been demonstrated in [45] for the use in wireless monitoring with maximum interrogation range of 9 m and conversion efficiency of -35 dB at -15 dBm received power. The intermodulation transponders can be implemented using the MEMS technology which offers lower cost and higher operating frequency limits [46]. In contrast, harmonic transponders provide larger frequency separation between the transmit and the receive signals which allow the interrogation range to expand and reduces the problem of false detection. In addition, the operation frequency can be much higher depending on the frequency multiplier elements used. A literature review of the harmonic transponders is provided in the next section.

2.2 Harmonic Transponders

A harmonic transponder consists of a frequency multiplier and two antennas. It operates by receiving the interrogation signal through the receive antenna, multiplying the frequency, and transmitting back the harmonic signal through the transmit antenna. The frequency multiplication can be implemented by introducing non-linearity using active or passive components. Active frequency multipliers generally employ transistors and CMOS circuits (due to their low cost) and have high conversion efficiency, however, the RF and DC power consumption is high [47, 48]. In contrast, passive multipliers have lower conversion efficiency and can operate at lower RF power levels.

There are different approaches for harmonic generation. One approach to generate harmonics is by integrating a non-linear transmission line (NLTL). A transponder design that integrates a NLTL is demonstrated in [49]. The NLTL is basically a conventional microstrip transmission line that is periodically loaded with variable shunt capacitance, the capacitance can

be varied by integrating varactor diodes and varying their bias voltage. The periodic loading makes the transmission line act as a low pass filter which enhances the harmonic generation within the desired band by blocking the power spread to the higher order harmonics. This approach also provides wide impedance bandwidth and facilitates the impedance matching with the antennas. The transponder presented in [49] achieves conversion gain of -10 dB at 0 dBm input power and a communication range < 0.8 m. The second harmonic generation efficiency and bandwidth of this technique can be further enhanced by employing composite right/left-handed (CRLH) transmission lines instead of right-handed transmission lines as presented in [50].

Another approach to generate harmonics is by employing a frequency mixer. The mixer can be implemented using an antiparallel Schottky diode pair [51]. This configuration produces only odd term harmonics and the third order harmonic is the dominant radiated product. The advantages of this design are the broadband frequency response and the resulting large frequency separation between the interrogation signal and the return signal. The reliance on the third order harmonics, however, results in low conversion efficiency.

Harmonic generation with good conversion efficiency at very low received RF power and without consuming DC power can be achieved by the introduction of Schottky diodes. In general, these diodes have low signal loss at high frequencies, due to their low junction capacitance. The primary design challenge is in obtaining a sufficient match to their large complex impedances using low-loss, compact matching networks. The diode-based harmonic transponder design approach has found use in different tracking systems for over 30 years [22, 24, 52]. In 1980 a transponder design was used for detecting victims under the snow [22]. The transponder design consists of two rectangular microstrip patch antennas. With this design victims buried at a depth of 2.5 m were successfully detected. In [24] a transponder tag was

designed using two half-wave dipole antennas for tracking bees. The tag was designed to operate at the fundamental frequency of 9.41 GHz and was simply formed with copper coated steel wires. The frequency multiplication stage consists of a Schottky diode in parallel with an inductive loop and the maximum measured conversion efficiency was -33 dB. Recently, the harmonic transponder has been used for tracking amphibians during the cryptic period of their life history [52], the migration of the emerald Ash Borer [23], and small endangered species [53].

For the tracking applications, the harmonic radar approach can provide an accurate positioning system. Interrogating a mobile object or organism that has an attached harmonic transponder allows the distance and direction of a target to be determined. The position can be obtained simply from the power ratio of the transmitting and receiving signals [23, 53]. However, the accuracy and range with this approach is very limited because of the sensitivity to the environmental and system losses. The time delay between transmitted and received pulse signals can be measured to avoid the reliance on the signal amplitude and improve the accuracy [54], but the range remains limited by the pulse width. The frequency modulated continuous wave (FMCW) radar technique can also be used for this purpose, if a high power continuous source is available [55]. The accuracy can be further enhanced by employing different coded positioning techniques such as the pseudorandom code [21]. By applying these codes it is possible to achieve a range accuracy to within 0.1 m in ideal conditions.

Some harmonic radar tracking systems are also currently commercially available. A radar tracking system for locating a golf ball has been developed by the RadarGolf Inc. in California (<http://www.radargolf.com/>). This system has a tracking range of 30 m and the transponder size is the same as the golf ball. Another tracking system has been developed by Recco in Sweden (<http://www.recco.com/>). The system was developed for locating buried victims under the snow.

The Recco's transponder measures 3×5 cm and can achieve a communication range of 90 m. While these harmonic transponders were successfully implemented and achieve good communication range, they have large sizes and are not suitable for embedded monitoring.

In recent literature, some researchers have attempted to miniaturize the transponder size and improve the conversion efficiency by employing different antenna design techniques [56, 23, 57, 58]. In [23] the transponder was designed using modified Minkowski loop antennas with fractal geometry. The tag measures $(0.2 \lambda \times 0.2 \lambda)$ mm and has a maximum conversion efficiency of -11 dB. In [57] the tag was designed using shorted quarter-wave patch antennas and the measured maximum conversion efficiency and size are -13.7 dB and $(0.21 \lambda \times 0.1 \lambda \times 0.006 \lambda)$ mm³, respectively. Planar meandered line antennas have also been employed in the harmonic transponder design [58] to achieve a maximum conversion efficiency of -16.7 dB and size of $(0.1 \lambda \times 0.038 \lambda \times 0.035 \lambda)$ mm³. Nevertheless, all these studies have been limited to modifying the transceiver geometry in a planar form and the sensing capability and integration were not addressed.

Some researchers have also investigated the abandonment of the use of two antennas in the harmonic transponder design for the purpose of realizing small footprint. In [59] the use of a dual-band antenna has been investigated. This approach can significantly reduce the overall occupied area, however, difficulties in the integration with the frequency doubler circuit and in achieving a sufficient impedance match at both of the operating bands are introduced. In [60] a study of the RFID sensor self-generated harmonics has been performed for the purpose of investigating the possible exploitation of the backscattered harmonics. It was found that the reradiated harmonics can be used to carry information, however, these harmonics are detectable at a much shorter range than the fundamental backscattered signal.

2.3 Electrically-Small Antennas Theories and Performance Limitations

In recent decades the interest in electrically small antennas has been steadily increasing. The continuous advancements in wireless sensing, tracking, and communication applications drive demands for smaller antennas and multifunction wireless devices with enhanced performance. Small antennas are found in cell phones, handheld wireless equipment, sensor nodes, RFIDs, laptops, USBs, GPS devices, etc. Despite the increasing demand for small antennas, these antennas are subjected to limitations and their performance is governed by physical laws [61].

An electrically small antenna can be defined as antenna with a volume smaller than the radian sphere defined by Wheeler [62]. The radian sphere is a hypothetical sphere with a radius (a) of $\lambda/2\pi$ and represents the boundary between the near field and the far field. The configuration described by Wheeler is illustrated in Figure 1.1. This relationship can be expressed as below:

$$ka < 1, \quad (2.1)$$

where $k=2\pi/\lambda$ (radians/meter), λ = free space wavelength (meters), and a = radius of sphere enclosing the maximum dimension of the antenna (meters).

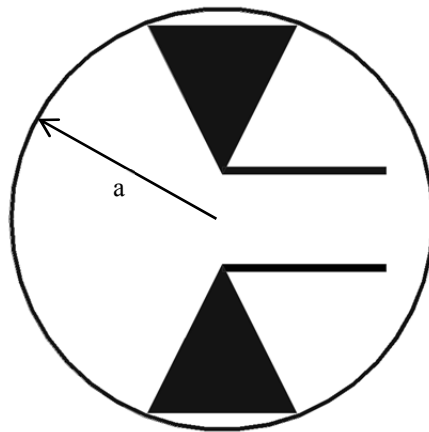


Figure 2.1: The radian sphere of radius a enclosing an antenna.

Small antennas fundamental performance limits were first explored by Wheeler in 1947 [62]. Wheeler proposed that a small antenna behaves essentially as a capacitor or inductor which needs to be driven with a feeding element of opposite kind to be tuned to resonance [63]. The amount of available power received or transmitted by a small antenna is independent of the size. This fact is only true at one frequency and if the small antenna is resonant at that frequency without adding loss. As the antenna size decreases, the radiation pattern and gain slightly change, however, the radiation resistance decreases which makes the impedance matching to a load over a reasonable bandwidth difficult without introducing losses. In order to find a practical relationship between the size and bandwidth limitation, Wheeler defined the radiation power factor. The conclusion of his studies is that the radiation power factor is proportional to the physical volume of the radian sphere and a reasonable approach to increase the radiation power factor is by exploiting the sphere volume effectively [64]. Larger antennas have larger radiation resistance, and thereby the impedance bandwidth is generally wider and the matching efficiency is higher. A weakness of his study is the assumption that there is only one radiated spherical mode with small antennas, which is only true for extremely small antennas.

Chu subsequently derived the minimum radiation quality factor (Q) of an omnidirectional antenna [65]. Unlike Wheeler's work, the fields outside the smallest possible sphere circumscribing the antenna were considered in his derivation. The external fields to the sphere surrounding an antenna, due to an arbitrary current inside the sphere, are represented by spherical wave functions, called modes. These modes deliver power independently from each other. By expanding the spherical wave function outside the sphere and representing each radiated mode with an equivalent lumped circuit model, the radiation Q was calculated for each mode.

Harrington [66] has also attempted to find the relation between the size and the bandwidth of the antenna. He treated the fields of each spherical wave as it is excited in a spherical waveguide and found the energy and power using the transmission line theory. In his analysis he assumed that the antenna has equal excitation of the TE and TM waves, and the resulted calculated Q factor was approximately half of that calculated by Chu.

Hansen used the same concept of the smallest sphere that encloses the small antenna, and mentioned that higher order modes become evanescent for $ka < 1$. Through his work and based on Chu analysis, he derived the following approximate formula for Q [67]:

$$Q = \frac{1+3(ka)^2}{(ka)^3[1+(ka)^2]}, \quad (2.2)$$

which shows that Q varies inversely with the cube of the radius of the sphere. This expression gives the Q for the lowest TM modes. If both of the lowest TE and TM modes were excited, the Q value should be divided by a factor of two.

Mclean reexamined the Chu derivation and Hansen's approximate expression for Q [68]. Based on Harrington's definition for the radiation Q, he derived the following near exact expression for the minimum radiation Q (Q_L) for a linearly polarized antenna:

$$Q_L = \frac{1}{(ka)^3} + \frac{1}{ka^2}, \quad (2.3)$$

he also derived the minimum Q for circularly polarized antennas, which is expressed as:

$$Q_1 = \frac{1}{2} \left(\frac{1}{(ka)^3} + \frac{2}{ka} \right), \quad (2.4)$$

For very small antennas, it can be noticed that the above two expressions for the quality factor become similar, and agree with the other expressions from the other authors. Figure 2.2 shows a graphical representation of eq. 2.3. As seen, as the volume shrinks, the quality factor increases rapidly, therefore the bandwidth decreases. This is attributed to the increase in the

reactive part of the antenna impedance and the decrease of the radiation resistance. High Q factor is a problem in most of the communication systems, since impedance matching becomes difficult and the bandwidth is very narrow.

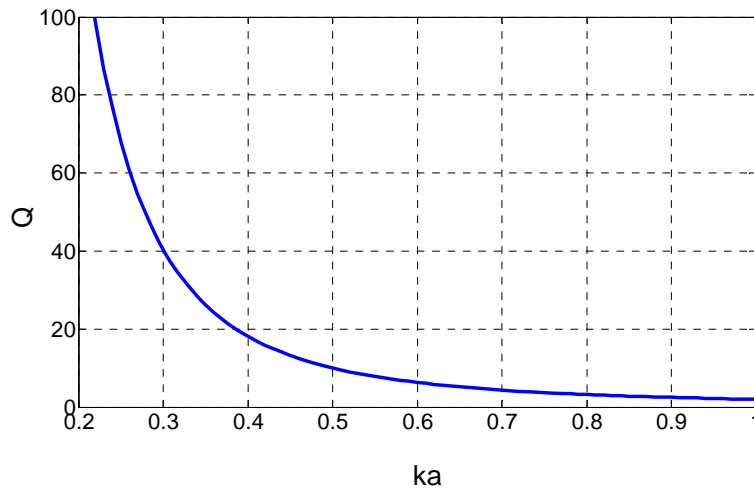


Figure 2.2: The minimum radiation quality factor (Q) for a linearly polarized antenna.

Recently Sten et al. evaluated the limits on the fundamental Q of a small antenna near a conducting plane [69]. He found that the Q factor depends on the radius of the smallest sphere that encloses the antenna and its image and the antenna orientation. Horizontal and vertical electrically small antennas over a large ground plane have different Q values. Horizontal antennas have higher Q values and as the separation distance to the conductor surface decreases, the radiation efficiency decreases due to the increase in the stored near field energy.

The small antenna theory development is still active up to now. Researchers are still attempting to provide various expression of the minimum Q with more accurate approximations [70]. Some of these studies that worth mentioning here include; Theile [71], Geyi [72], Yaghjian and Best [73], Kwon [74, 75], Pozar [76], Hansen and Collin [77], Thal [78], and Vandenbosch [79]. In general, the expressions given in (eq. 2.3) and (eq. 2.4) are widely accepted and deviate slightly from the newly derived formulas.

While the concentration of most of the studies is on Q , the bandwidth quantity is of more interest and universally applicable. The relation between the radiation Q and the maximum achievable bandwidth has long been controversial. In general, as the radiation Q increases the maximum achievable bandwidth decreases, therefore, it was commonly accepted to assume that the fractional bandwidth equals $\sim 1/Q$. However, the bandwidth and reflection coefficient of an antenna are also related, and this introduces ambiguity to the Q and bandwidth relationship. In order to remove this ambiguity, the relation between the Q , bandwidth, and reflection coefficient was studied by different authors [80, 81]. A simple approximate expression that relates these parameters for an RLC circuit type is given below [82]:

$$BW = \frac{S-1}{Q\sqrt{S}}, \quad (2.5)$$

where S is the voltage standing wave ratio and BW is the fractional bandwidth. The BW is defined here as the difference between the two frequencies on either side of the center frequency at which S is the same.

Small antennas usually have omni-directional patterns with a doughnut shape and a maximum directivity of 1.5. However, by applying different electric and magnetic dipole arrangements other patterns are possible with a directivity ranging approximately from 1.5 to 3 [83]. Theoretically, a small antenna can be constructed from a short electric and magnetic dipole to have a directivity of 3, which is called Huygen's source [84]. In addition, small antennas that require ground plane backing can have directivity that approaches 3. The following reasonable formula can be used to find the maximum directivity of small and large antennas [84]:

$$D_{\max} = (ka)^2 + 3, \quad (2.6)$$

this formula is plotted in Figure 2.3. As seen, the directivity decreases slowly with decreasing the antenna size and remains constant for very small sizes. This behavior led to the classification of

small antenna as super directive antennas [83]. In general, it is acceptable to assume the maximum gain to be 3 for small directive antennas, and 1.5 for small omni-directional antennas.

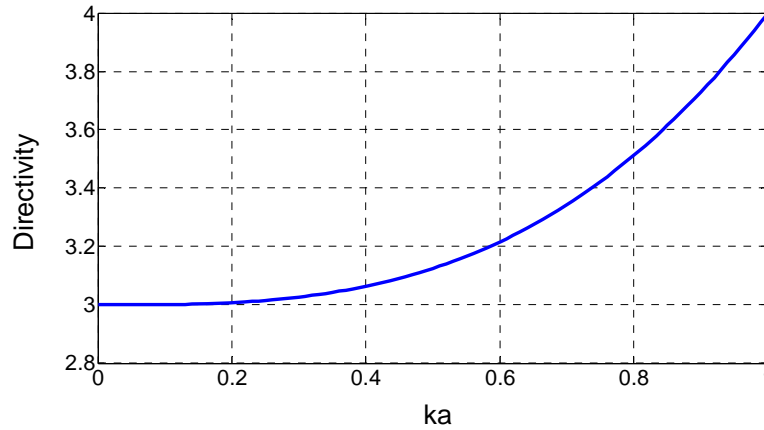


Figure 2.3: The maximum antenna directivity.

In order to find the best antenna design performance that makes optimum use of the available volume, the gain and bandwidth need to be considered simultaneously. The bandwidth limit derivation does not account for the losses and the gain limit does not consider the realized impedance bandwidth. Therefore, the product of the gain and bandwidth index is commonly used to describe the antenna performance. This performance index equals approximately to the ratio of gain/Q for most of the antennas. This ratio physically stands for the ratio of radiation intensity to the stored energy around the antenna and allows antenna designers to tradeoff gain and Q for a specified antenna size in a quantitative manner [85, 86]. However, the tradeoff is very limited as the Q itself has a lower bound.

2.4 Antenna Candidates for the Harmonic Radar Interrogator Unit

For harmonic radar applications, compact, light-weight antennas with sufficient directional performance are desired. For certain radar applications the operating bandwidth is also preferred to be broad. In general, the antennas that can be used for the harmonic interrogator

design can be classified into planar and non-planar antennas. The planar antennas including spiral, microstrip, aperture, and wire antennas offer the advantage of simplicity, ease of fabrication and integration with the radar unit, light weight, and low cost. While the non-planar antennas such as horn, dish, and helical antennas generally have better directional performance. To enhance the directional performance of the planar structures, they are usually designed in array arrangements.

Table 2.1 lists different interrogator antenna candidates and their parameters. The parameters listed in the table are dependent on the size and geometry of the antenna structure, therefore, the provided values are generic. The directional performance is quantified by the gain, efficiency, front-to-back ratio (FBR), and half power beam width (HPBW). Each structure offers a set of advantages and disadvantages. For example, patch antennas offer high FBR, very low profile, ease of integration and fabrication, and good gain, however, the bandwidth is very narrow. Different techniques to enhance the bandwidth exist, but this comes at the expense of the other antenna parameters. Slot antennas are low profile, have wide band performance, and are compatible with different feeding structures, but they have bi-directional radiation pattern. The radiation pattern of a slot antenna can be made unidirectional by placing a cavity in the back side of the antenna, however, the bandwidth will be narrowed and the cavity needs to be deep to maintain good radiation efficiency. Traveling-wave planar structures such as the Vivaldi antenna offer unidirectional high gain radiation patterns and improved bandwidth over the resonant type antennas, however, the performance is frequency dispersive and the size is large. In addition, these structures have mutual coupling issues which make their use in array arrangements less attractive. The quasi-Yagi dipole antenna is very attractive radiator for the harmonic radar interrogator design. It is a uni-planar, unidirectional, resonant type antenna with a compact size

and broadband characteristics. It has an endfire radiation pattern and is a suitable element for linear arrays. The drawback of this antenna structure is the required balanced feed and transition to coplanar strips (CPS) which introduce bandwidth limitations. The log-periodic dipole antenna array has similar radiation characteristics to the quasi-Yagi dipole antenna and can have a bandwidth of $\sim 2:1$ if the number of element used is large. The realized gain of this antenna, however, is small compared to the size and the peak gain is moderate only in a small portion of the bandwidth. The horn and dish antennas can have high gain and directive pattern over broad bandwidth, but the size would be very large. In addition, their non-planar structures introduce difficulties in the integration with the radar unit and thus they are generally used in stationary radars.

For the harmonic radar application there are two interrogator design methodologies to cover the interrogation bandwidth. The first methodology is the use of two separate antennas for the reception and transmission. This methodology provides the advantage of higher isolation between the receive and transmit paths and simplifies the interrogator design. The second methodology is the use of one broadband antenna to cover both of the reception and transmission bands. In order to cover this frequency range, the bandwidth is required to be larger than 66% (or 2:1). This bandwidth requirement limits the antenna choice to the Vivaldi and log-periodic dipole antennas from the planar antennas list and the horn antenna from the non-planar list and all require large sizes. To allow the use of one antenna with reduced size and profile, dual-band planar antennas can be incorporated. While the dual-band antennas generally have low gain, they can be designed in an array configuration. The challenge with the dual band arrays is in realizing frequency bands ratio of 2 with frequency invariant radiation patterns and polarization purity due

to the necessity to adjust the array element spacing. These arrays usually find use in the modern cellular communication and radar systems [87, 88].

Table 2.1: General interrogator antenna comparison

Antenna	Pattern	Directivity	Gain (dB)	HPBW	BW	FBR
Patch	Broadside	Uni-directional	5-7	$\sim 120^\circ$	3%	~ 20 dB
Slot	Broadside	Bi-directional	~ 5	$\sim 90^\circ$	25%	0 dB
Bow Tie Slot	Broadside	Bi-directional	~ 6	$\sim 90^\circ$	30%	0 dB
Cavity Backed Slot	Broadside	Uni-directional	~ 7	$\sim 60^\circ$	8%	~ 15 dB
Quasi Yagi Dipole	End fire	Uni-directional	~ 6	$\sim 100^\circ$	40%	~ 15 dB
Vivaldi	End fire	Uni-directional	3-10	$\sim 120^\circ$ - 50°	UWB	> 12 dB
Log-periodic dipole array	End fire	Uni-directional	Dependent on the size	$\sim 70^\circ$	$\sim 2:1$	~ 15 dB
Spiral	Broadside	Bi-directional	> 7	70 - 90°	30:1	0 dB
Leaky Wave	Scannable	Directive	~ 10	$> 20^\circ$	$> 40\%$	~ 20 dB
Helix	End fire	Uni-directional	High	small	56%	High
Horn	Broadside	Directive	10-20	$> 15^\circ$	20:1	High
Dish	Broadside	Directive	High	\gg small	$> 5\%$	High

Frequency tunable antennas can also be employed in the interrogator design to provide the ability to interrogate different nodes that operate at different frequencies. The challenge of this design approach is in realizing a wide tunable range without introducing losses. This antenna design topology is discussed more in depth in Section 2.5.

2.5 Reconfigurable Antennas

Reconfigurable microwave antennas are of interest in many applications, providing multi-band, secure, and/or anti-jam communications capability. The primary benefit of such antennas is that multiple functions are included in a single design, therefore providing the potential for reduced system size, weight, and cost. Fundamentally, the reconfiguration can be achieved by physical and/or electrical modifications made to the antenna, or an impedance

matching network that is connected to the antenna. The parameters that may be altered include the operating frequency, radiation pattern, polarization and beam direction. The reconfiguration may be achieved using switches, diodes, micro-electro-mechanical (MEM) devices, and tunable materials [89, 90]. However, these conventional methods provide limited tunability range, add complexity, and degrade the overall communication performance due to the added loss and potential non-linearity induced upon the RF signal.

Recently, research activities have attempted to realize mechanically reconfigurable antennas based on different mechanisms to mitigate the above issues [91, 92, 93]. Basically, the primary benefits of these methods are reducing the cost and complexity and improving the tunability range. The mechanical reconfiguration can be accomplished by a variety of actuators including piezo-vibration motors, electric motors, and hydraulic cylinders. The drawbacks of these mechanical actuators are generally the slow speed and the high power consumption. Moving parts can also introduce reliability issues.

Some mechanically reconfigurable antennas have been developed by incorporating movable parasitic elements. In [91] a mechanically actuated two-layer electromagnetically-coupled microstrip antenna with variable frequency, bandwidth, and gain has been demonstrated. The antenna performance was reconfigured by placing a parasitic director above the patch antenna and varying its vertical spacing. In [92] movable V-shaped parasitic elements incorporated to realize a pattern reconfigurable antenna. Another mechanically pattern reconfigurable square ring patch antenna has been demonstrated in [93]. The reconfiguration with this antenna is achieved by moving a parasitic plate within the ring patch. In [94] a reconfigurable ultra-wideband log-periodic dipole array antenna was introduced. The reconfiguration was achieved through the discrete adjustment of the array elements and spacing.

While this design approach provides wide tunability range, the mechanism to achieve the adjustment of the antenna configuration has not been proposed. In general, all these developed mechanically reconfigurable antennas have limited tuning range and few frequency tunable antennas have been demonstrated. This review shows that there is clearly room for improvement in current mechanically reconfigurable antenna topologies.

Recently, new reconfigurable antennas using liquid metals have emerged. The reconfiguration is basically achieved by injecting liquid metal alloys into a microfluidic channels to modify the shape of the conductive part of the antenna. For example, the conductive elements of the antenna can be induced to flow in response to external stimuli changing the length of the antenna and thus the operating frequency [95]. This approach can also be used to vary the pattern and polarization and for steering the beam [96]. The liquid nature of the reconfigurable elements is advantageous in avoiding the failure of the moving parasitic solid elements. The challenge with this design topology is in controlling the way liquid metal changes its shape in a fast manner. Viscosity, elasticity, conductivity, safety, and cost of the available liquid metals are also issues that still need to be addressed. In addition, realizing reversible reconfiguration with this design approach is very difficult which makes it more suitable for the design of flexible antennas [97, 98] and sensor antennas [99].

Reconfigurable structures based on smart materials have also been developed [100, 101, 102, 103]. With the smart material technology, electromechanical actuators based on electro-active polymers can be designed. An example of a mechanically reconfigurable antennas using smart material is illustrated in [103] where a shape memory alloy actuator was used to adjust the height of a helix antenna. Adjusting the helix height resulted in altering the antenna pattern and gain. The major issues with the smart materials include the sensitivity to temperature and their

hysteresis behavior. In addition, this reconfiguration method is not easily applicable to many antenna structures.

For the sake of the harmonic radar interrogator design, the mechanical reconfiguration can be very beneficial. It allows the use of the low profile, narrowband antennas to reduce the overall interrogator size realizing a portable hand held interrogator. Having an interrogator with a wide tuning range allows different nodes that operate at different frequencies to be interrogated. In addition to the frequency tuning, mechanical actuators can be incorporated to realize non-dispersive array pattern and steering the radiation beam which simplify the localization and identification of different nodes that operate at different frequencies. The non-dispersive array pattern, which is a drawback of the broadband antennas, can be realized by tuning the array element spacing and distance to the ground of the broadband antennas that require ground plane backing. Steering the beam can be achieved by rotating the antenna or a reflector. A reconfigurable impedance surface that performs as a reconfigurable beam steering reflector has been demonstrated in [104] showing that this approach is very effective.

2.6 New Antenna and Microwave Circuit Manufacturing Technologies

Recently, different manufacturing technologies have emerged to improve the standard fabrication techniques capabilities and offer greater design flexibility. One of these technologies is the 3-D direct digital additive manufacturing (DDAM) [105]. Additive manufacturing (AM) was first introduced before more than 20 years, and since then it has been expanding rapidly in a global scale [106]. It is advantageous in terms of functionality, material usage, time, cost, and dimensions. This technology consists of a broad family of other technologies such as silk screening, micro-dispensing, 3-D printing [107], electron beam melting, laser sintering [108], fused deposition modeling (FDM), and stereolithography (SL) [109]. AM is a layer-by-layer

based fabrication method of polymers and conductors that allows for fast, low cost manufacturing of arbitrary 3-D structures with reduced weight and very small spatial resolution and dimensionality from 3-D CAD models. The 3-D DDAM technology has been widely used in a variety of applications including commercial production and prototyping and lately it has found use in the RF and microwave circuits manufacturing domain.

One of the microwave components that can significantly benefit from the 3-D DDAM is the antenna. Based on the discussion provided in Section 2.3, 3-D antennas are found to offer the best compromise between size, bandwidth, and radiation efficiency. However, the use of 3-D antennas is limited in part due to the cumbersome traditional fabrication techniques that suffer from the difficulty and poor repeatability and reliability. With the emergence of 3-D DDAM technology, these challenges will be addressed and efficient light weight 3-D antennas can be manufactured. 3-D DDAM increases the performance of miniaturization and provides additional design freedom. Unlike conventional fabrication methods (i.e., printed circuit board technology (PCB)), DDAM allows the antenna substrate shape and thickness to be optimized and avoid the reliance on the standard commercial microwave substrates. It enables significant performance improvement of some antennas, by providing the freedom to place the dielectric material only in strategic locations reducing the dielectric material use and thereby reducing the dielectric loss and substrate diffraction impact on the radiation pattern. This is also beneficial in antenna array design by inserting defects in the substrate for antenna mutual coupling reduction. In addition, DDAM gives the antenna designers the ability to optimize the antenna structure to better fit the package and the final wireless product. Instead of having the antennas as separate components which increases the cost, antennas can be printed on conformal surfaces and directly connected to the feeding traces. The ability to print on non-planar surfaces increases antenna placement

options and reduces the overall size. Furthermore, this technology eliminates the need for hazardous chemical materials use and has safety consequences. The disadvantage of this technology is the narrow material choice. Drawbacks of the available materials compared to other technologies include impact resistance, toughness, surface smoothness, temperature, and losses. In addition, the available dielectric materials have low dielectric constant (< 3.6) which limits the miniaturization ability. However, different techniques and materials to overcome these limitation are currently under development and becoming mature [110, 111].

Another manufacturing technology that has been recently developed and used for the design of microwave antennas is the laser direct structuring (LDS). With this technology circuit layouts on 3-D structures can be produced using a laser beam (www.LPKF.com). While this technology has the potential for reduced weight, fabrication time, and occupied space of highly sophisticated products, it is not capable of producing arbitrary 3-D structures. It relies on injection moulding of the carrier structure. The choice of the carrier material is limited to thermoplastic. The LDS technology is capable of efficiently producing thin tracks and gaps on non-planar surface, however, the surface height is limited to 24 mm and the angle of inclination has to be $< 77^\circ$. These restrictions make this technology more reliable for the production of conformal antennas and interconnects, such as those found in smart phones and portable electronics.

2.7 Conclusion

Passive structural health monitoring has been an active area of research in the last decades. The implementation difficulties and cumbersome use of the wired monitoring sensor platforms has prompted research on wireless techniques. Different wireless monitoring methods have been developed, however, sensor node size and communication range are the major

limitations of these methods. The short read range limitation has stimulated the development of the harmonic transponder. These transponders separate the interrogation signal from interference and allow the interrogation range to expand, therefore they have found use in different tracking applications. A review of the existing harmonic transponders revealed that these transponders could be used to develop passive sensors that will advance the existing wireless structural health monitoring systems. While these transponders may have larger footprints, 3-D antennas can be incorporated to miniaturize the size.

The studied small antenna limitations studied verified that larger antennas are generally more efficient, especially for wide bandwidth applications. However, it was found that if an antenna is restricted by a maximum dimension but not by an occupied volume, the performance can be improved by exploiting the available volume. Consequently, 3D antennas are preferred for applications that require efficiency concurrently with small size, since these antennas make more efficient use of the available volume by realizing relatively long antenna lengths. 3D antennas are also beneficial in providing additional space within the inner structure for other uses, such as storage room for batteries or other circuit elements.

Reviewing the performance of different antenna structures shows that different antenna candidates can be used in the design of the harmonic interrogator. In order to realize a handheld interrogator, the antenna is preferred to be with a compact geometry and light weight. To avoid the use of two separate antennas, the antenna frequency bandwidth has to be greater than 66%. Dual-band antennas can also be considered to reduce the interrogator size and weight. In order to provide additional interrogation capabilities such as interrogating different nodes that operate at different frequencies and automated node localization, mechanical reconfiguration can be incorporated for tuning the frequency and steering the radiation beam. While mechanical

reconfiguration has speed, power consumption, and reliability issues, it is found to be highly effective from the reconfiguration perspective.

Different manufacturing technologies have recently emerged. These technologies have the potential to advance the antenna and sensor node designs. The 3-D DDAM can be utilized to improve the manufacturing reliability of 3-D microwave structures. In addition, it gives additional design freedom and improves the miniaturization process efficiency. The design of small, efficient antennas with reduced weight and cost can be enabled with this manufacturing technology.

CHAPTER 3 : PASSIVE HARMONIC TRANSCEIVER DESIGN

Note to Reader

Portions of this chapter have been previously published in [112] and [113], and have been reproduced with permission from IEEE. Permissions are included in Appendix A.

3.1 Introduction

In this chapter, we leverage developments in passive GaAs Schottky diode-based multipliers and conjugate-matched 3-D antenna design to develop a novel, compact, high conversion gain harmonic transceiver. The design builds upon the transceiver approach presented in [57] and incorporates 3-D antennas similar to those presented in [114]. In order to emulate the effect of the sensor, a DC network is added to enable modulation of the re-transmitted signal. The eventual goal is to demonstrate the harmonic transceiver for embedded wireless sensing applications that employ remote interrogation (>50 m) and to fit the sensor node, including the sensor electronics, within a 3 cm diameter sphere. To achieve this interrogation range and meet the sensor node size constraint, f_1 was chosen to be 2.4 GHz. At this frequency the proposed device diagonal measures $0.24 \lambda_1$. At RF input power level ranges between -30 and -10 dBm, the transceiver has an overall conversion gain of > -13 dB. In comparison to [57], the presented design has shown more than 11 dB conversion gain improvement at RF input power of -30 dBm and similar electrical size. In addition, the design presented herein has omni- (versus uni-)

directional interrogation capability. The variation in conversion gain of the presented design at -20 dBm input power over all azimuth incidence angles is ~ 4 dB, such that the relative orientation between the interrogator and sensor node is not a critical factor in overall link performance.

The impact of burying the harmonic transceiver in sand to demonstrate its suitability for embedded, remote monitoring is investigated in this chapter. The transceiver was embedded in a sand box at a depth of 15 cm and characterized. To minimize the effects of the dielectric loading and degradation of the impedance match due to the sand, the transceiver was placed in a cubical box of foam (with electrical properties similar to air) with a side dimension of 5 cm. The foam box could be replaced by a lightweight, air-core shell in a more refined implementation.

The following sections present the design, testing and analysis of the harmonic transceiver. Section 3.2 describes the transceiver design and the results of multiple experimental validations are given in Section 3.3. Section 3.4 discusses the sensing capability and the integration with practical sensors and Section 3.5 presents a preliminary study of the imbedding impact.

3.2 3-D Harmonic Transceiver Design

In this section the 3-D harmonic transceiver design is presented. The device operates by receiving a 2.4 GHz signal, doubling the frequency, and re-radiating a 4.8 GHz signal. Section 3.2.1 describes the frequency doubler design and Sections 3.2.2 and 3.2.3 illustrate the receive and transmit 3-D antenna designs, respectively.

3.2.1 Passive Frequency Doubler Design

In passive frequency multipliers, Schottky barrier diodes are often utilized [115] due to their strong non-linear current-voltage characteristics. In this work, a GaAs Schottky diode

(HSC9161) was selected. This diode has low signal loss at the frequency of interest and it turns on at a very low induced voltage due to its low barrier junction. The main parameter of interest in characterizing a multiplier design is the conversion gain (CG). The CG of a diode doubler is expressed as follows:

$$CG = P_{out} (dBm) - P_{in} (dBm), \quad (3.1)$$

where in this case P_{out} is the output power of the multiplier at the second harmonic (4.8 GHz) and P_{in} is the input power at the fundamental frequency (2.4 GHz).

Agilent's *Advanced Design System* software (ADS 2009u1) was used to predict the multiplier response (Figure 3.1). Details about the diode model used in the simulations are given in [57]. The source shown in the schematic represents the receive antenna and the load is the transmit antenna. To deliver and collect maximum power to/from the diode, the antennas were designed to be conjugate-matched with the doubler input/output impedances. Because of the diode non-linearity, the power transfer conditions are dependent on the loads presented to the doubler at the fundamental and the harmonic frequencies. Thus to accurately predict the multiplier response, harmonic impedances up to the fourth order were accounted for in the simulation. The number of harmonics was limited due to the minimal performance difference at the 4th harmonic. To ensure that the appropriate impedance is represented at the source for each reflected harmonic, band-pass filters were utilized. The values of the antenna impedances at harmonic frequencies were extracted using Ansoft's *High Frequency Structure Simulator* (HFSS) version 11.

A DC bias connection was included in the frequency doubler design. The bias is supplied to the diode input through an 18 nH series inductor (Coilcraft 0402) and 8.2 pF shunt capacitor (Johanson 0201). The purpose of including the DC bias connection is only to impart amplitude

modulation on the retransmitted signal (as detailed in Section 3.4). In addition, this connection provides a DC return path on the input side of the diode. For the output side, the DC path is provided by a shunt shorted stub which was added to the 4.8 GHz antenna feeding network (discussed in Section 3.2.3).

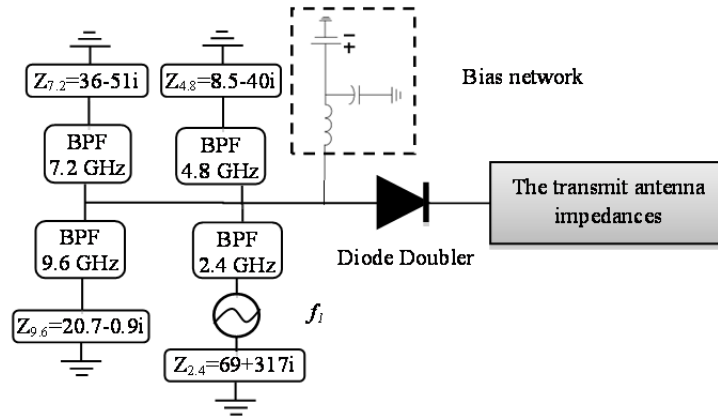


Figure 3.1: Block diagram of the schematic used to predict the frequency doubler performance.

Figure 3.2 (left) shows the simulated CG of the doubler versus input power at the center frequency of 2.4 GHz. As seen, the CG is approximately -17 dB at -30 dBm input power and maximum CG (-13.4 dB) occurs at -19 dBm input power. The conversion gain versus frequency for input powers of -20 and -30 dBm is presented in Figure 3.2 (right). The simulated 3 dB CG bandwidth is 1.7% and 2.5% at input powers of -30 dBm and -20 dBm, respectively. This CG bandwidth dependence on the power is due to the power-dependence of the diode impedance.

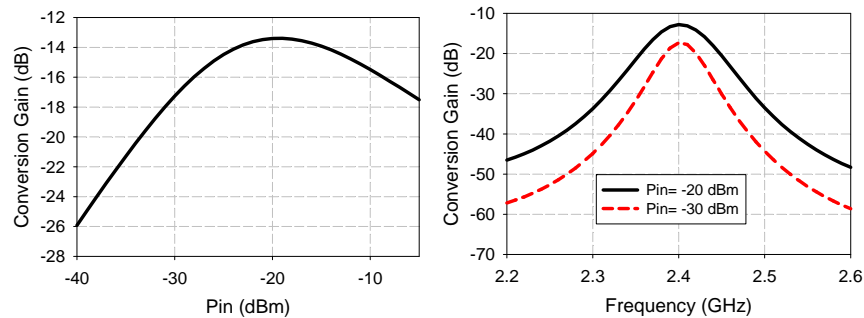


Figure 3.2: Simulated performance of the frequency doubler at 0V bias; conversion gain versus input power at f_i of 2.4 GHz (left) and simulated conversion gain of the diode doubler versus frequency for different input powers.

3.2.2 The Receive 2.4 GHz Antenna

The 2.4 GHz (receive) antenna is illustrated in Figure 3.3. This antenna is similar to the design presented in [114] which was developed for 50Ω systems. The substrate is Rogers/RT Duroid 6010 with a nominal relative dielectric constant (ϵ_r) of 10.2, and a thickness of 50 mils (1.27 mm). The antenna consists of a half-wave dipole conformed onto a cubical surface. The dipole arms are wrapped around the cube sides, and are terminated with meandered sections. The meandered sections are oriented as shown to preserve the balanced current distribution on the dipole arms. The dipole is center-fed by a parallel plate balun, rising vertically along the center face. The antenna feeding network also includes a meandered microstrip matching line and a 50Ω microstrip line.

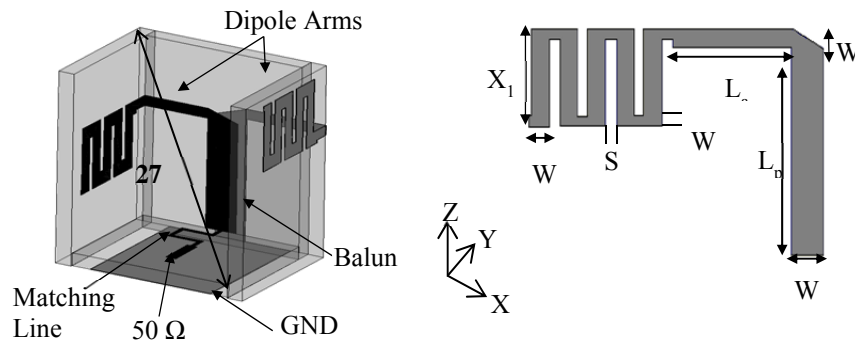


Figure 3.3: The 2.4 GHz receive cube antenna.

Based on the diode doubler ADS simulation, the 2.4 GHz antenna should present an impedance of $69+317i \Omega$ at 2.4 GHz for maximum CG at -30 dBm input power. To match the antenna input impedance to this desired impedance, *Ansoft HFSS 11* was used to optimize parameters such as: the meander line dimensions, the width and length of the non-meandered sections, the width of the parallel plate transformer, the length of the 50Ω line, and the width and length of the matching line. The eventual addition of the transmit antenna caused a

downward frequency shift in the receive antenna response of ~ 0.1 GHz, which was corrected for in the final designs. Table 3.1 shows the 2.4 GHz antenna dimensions.

Table 3.1: 2.4 GHz receive antenna dimensions in mm

L_a	5.2	L_{50}	3.0
W_a	1.0	W_{50}	0.8
L_p	11.0	X_1	4.0
W_p	2.5	W	1.0
S	0.5	W_2	1.3
Ground Length	8.27	Ground Width	10.0

An approximate equivalent circuit model of the antenna is given in Figure 3.4; here Z_o is the characteristic impedance and Z_a is the approximate antenna input impedance at 2.4 GHz. The characteristic impedances of the parallel plate transformer and the meandered matching line are 37Ω and 96Ω , respectively. The simulated 2.4 GHz antenna input impedance and the reflection coefficient between the 2.4 GHz antenna and the doubler input at -30 dBm input power are illustrated in Figure 3.5. The input impedance at 2.4 GHz is $59+315i \Omega$ and the 10 dB return loss bandwidth is 1%. Figure 3.5 (right) shows that the reflected power at the fundamental frequency is very low. The reflection coefficient for RF input power ≤ -20 dBm is approximately the same.

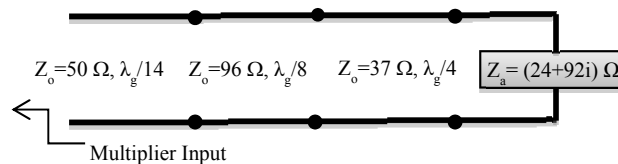


Figure 3.4: The approximate equivalent circuit model of the 2.4 GHz receive antenna.

Figure 3.6 shows the simulated E- and H-plane radiation patterns at 2.4 GHz. Relative to the coordinate system in Figure 3.3, the H-plane is the Y-Z plane and the E-plane is the X-Y plane. The antenna demonstrates an omni-directional pattern in the H-plane with only 0.8 dB

variation. The maximum radiation occurs broadside to the non-meandered portions of the dipole arms with a peak gain of 0.5 dBi. The E-plane null is not as deep as a regular dipole antenna (only 6.8 dB) due to the incomplete cancellation of the radiated far-fields from the non-meandered sections of the dipole arms. The tilt in the E-plane pattern is due to ground plane interference.

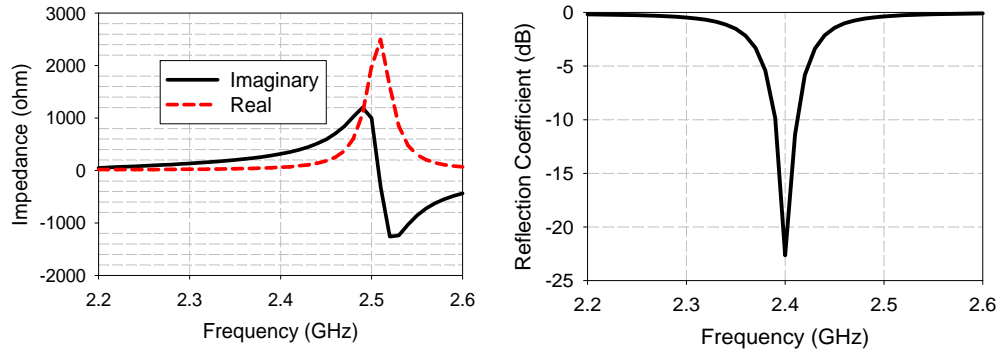


Figure 3.5: The receive antenna input impedance (left), and the reflection coefficient between the receive antenna and the doubler input at -30 dBm input power and 0V bias (right).

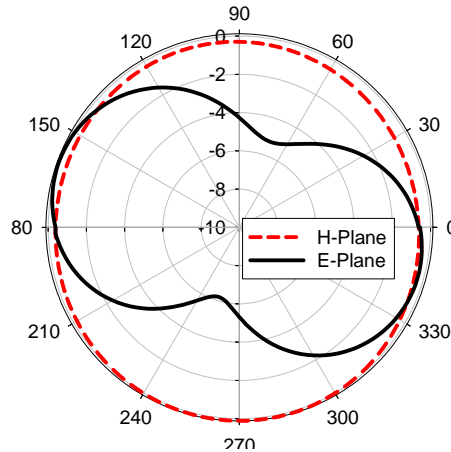


Figure 3.6: Simulated radiation patterns (in dB) of the 2.4 GHz receive antenna.

3.2.3 The Transmit 4.8 GHz Antenna

The 4.8 GHz (transmit) antenna is located on the side of the cube opposite to the receive antenna (Figure 3.7). Here, the dipole arms and the balun are designed on a common cube side.

The dipole arms are rotated in a clock-wise/counter clock-wise manner to preserve a balanced

current distribution on the dipole arms. The antenna feeding network consists of a meandered microstrip matching line and a $50\ \Omega$ line. Between the meandered line and the $50\ \Omega$ line, a shunt shorted-stub is added.

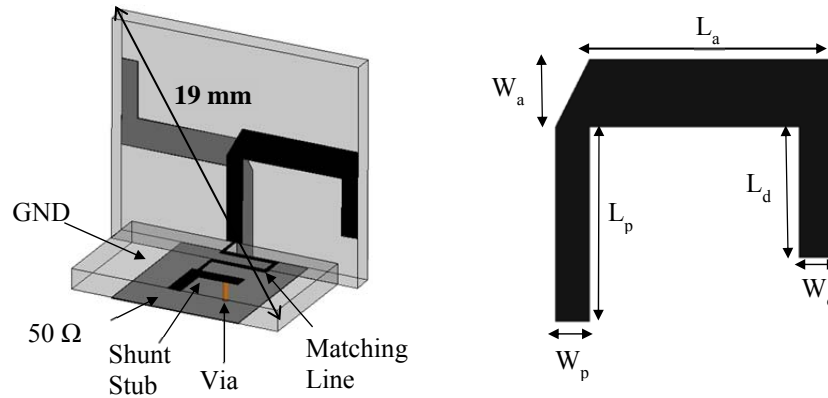


Figure 3.7: The 4.8 GHz transmit antenna.

For optimal frequency conversion gain at $-30\ \text{dBm}$ input power, the ADS doubler simulation shows that the 4.8 GHz transmit antenna should present an impedance of $15+152i\ \Omega$ at 4.8 GHz; this result was obtained from simulations of the transmit antenna in the presence of the receive antenna. In order to match the 4.8 GHz antenna input impedance to the desired impedance, the width and length of the dipole arms, the quarter wave transformer width, and the meandered matching line width and length were all optimized. Also, the length and width of the shunt stub were subsequently tuned. The shunt stub was added to increase the reactive part of the input impedance and to give a DC return path to the diode doubler. The final approximate equivalent circuit model of this antenna is shown in Figure 3.8. Table 3.2 shows the 4.8 GHz antenna dimensions.

The simulated transmit antenna input impedance and the reflection coefficient between the transmit antenna input and the doubler output at $-30\ \text{dBm}$ are shown in Figure 3.9. The 10 dB return loss bandwidth is 1.4%, and the antenna input impedance at 4.8 GHz is $17.6+156i\ \Omega$. Figure 3.10 shows the simulated radiation patterns at 4.8 GHz. The antenna exhibits an omni-

directional pattern in the H-plane with a variation of 4.5 dB and a peak gain of 3.4 dBi. The variation over the H-plane is due to the diffraction and reflection from the 2.4 GHz antenna substrate and ground plane. For the same reason, the peak gain is higher than a regular half-wave dipole due to the increase in the directivity.

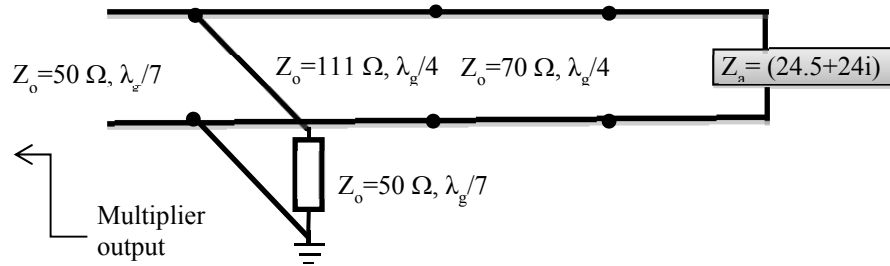


Figure 3.8: The approximate equivalent circuit model of the 4.8 GHz transmit antenna.

Table 3.2: The 4.8 GHz transmit antenna dimensions in mm

L_{a1}	5.2	L_{50}	3.0	W_d	1.0
W_{a1}	1.8	W_{50}	0.8	W_{p1}	1.0
L_{p1}	5.25	L_d	3.5	Via radius	0.35
Stub Length	3.0		Stub Width	0.8	
Ground Length	8.77		Ground Width	8.0	

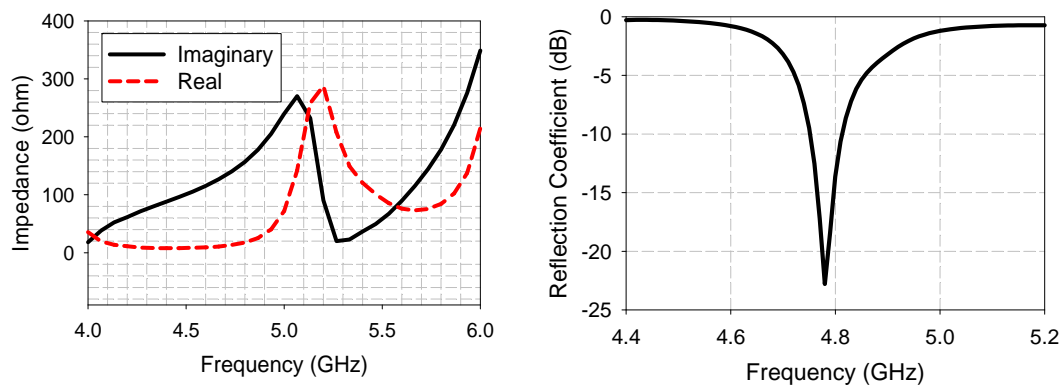


Figure 3.9: The 4.8 GHz antenna input impedance (left), and the reflection coefficient between the transmit antenna and the doubler output at -30 dBm input power and 0V bias (right).

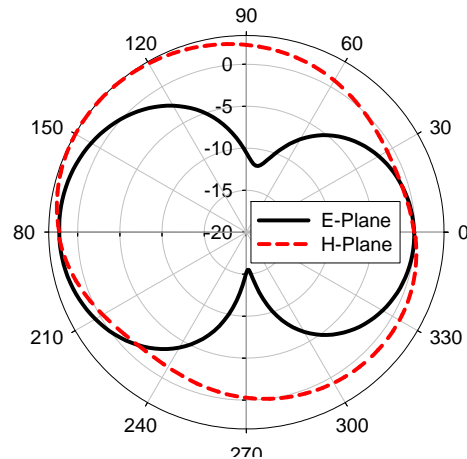


Figure 3.10: Simulated radiation patterns (in dB) of the 4.8 GHz transmit antenna.

3.3 Transceiver Performance Characterization

The integrated transceiver design is illustrated in Figure 3.11. The transceiver was fabricated using a printed circuit board milling machine and assembled manually. Silver epoxy was used to attach the diode and lumped components, and copper wire was used to create the via connections to the ground plane. Measurements were performed inside an anechoic chamber (Figure 3.12) where the harmonic transceiver receives the transmitted f_1 signal, doubles the frequency, and re-radiates a $2f_1$ signal. A vector network analyzer (VNA) was used to send the transmitted signal and a spectrum analyzer (SA) was used for measuring the received signal power level. Low pass filters were added in the transmit path to filter out the VNA-generated harmonics. Path spreading loss was calculated using Friis transmission equation [116]. The measurements were executed over a 1 m distance and the transceiver was oriented in the direction where the maximum CG was recorded. The two interrogator antennas (transmit and receive) were placed 1.3 m apart to reduce mutual coupling.

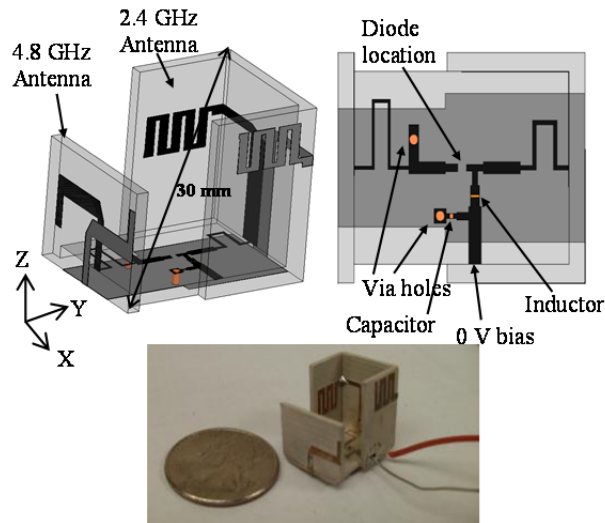


Figure 3.11: A complete transceiver design (3D-view on top left; top-view on top right; fabricated 2.4/4.8 GHz harmonic repeater on bottom).

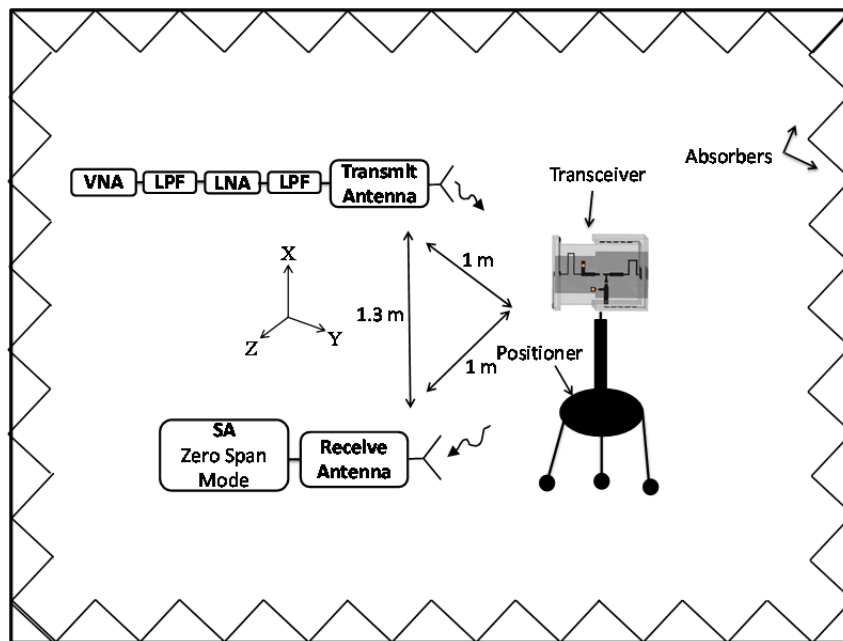


Figure 3.12: The experimental setup used to characterize the proposed harmonic transceiver.

Figure 3.13 shows the simulated and measured conversion gain of the transceiver over frequency for different input powers and zero volt bias. The simulated 3 dB CG bandwidth is 2.5% and 1.7% at input powers of -20 dBm and -30 dBm, respectively. The measured maximum CG is recorded at 2.4 GHz. The measured CG peak value is -9.25 dB and -13.3 dB at RF input

power levels of -20 dBm and -30 dBm, respectively. The measured 3 dB CG bandwidth at -20 dBm is ~3%, while it is ~2.5% at -30 dBm.

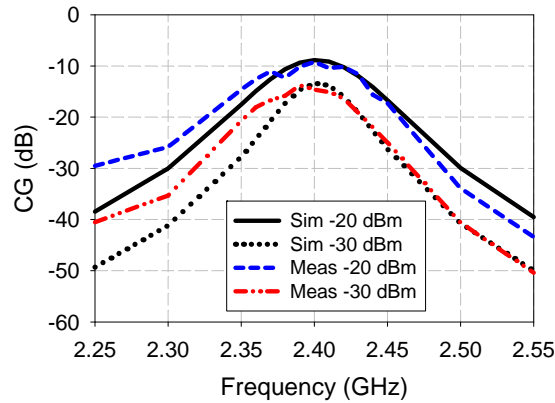


Figure 3.13: The simulated and measured conversion gain versus frequency for different input powers at 0V bias.

The CG versus input power at 2.4 GHz was also measured and is compared with the simulated data in Figure 3.14. The simulated CG of the entire transceiver was calculated by adding 4 dB (the sum of antenna gains) to the simulated CG curve of the multiplier alone. As seen, the measured curves are well matched with the simulated curve and the two transceivers show similar performance.

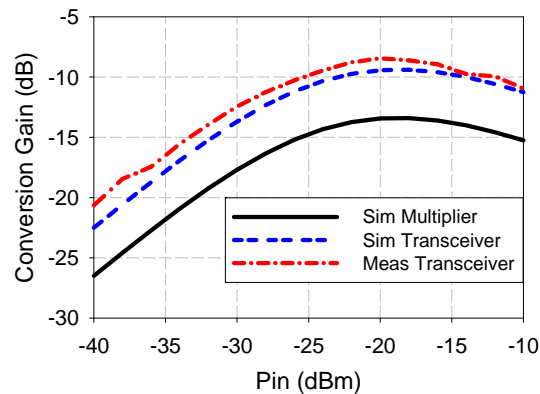


Figure 3.14: The simulated and measured conversion gain versus input power at f_i of 2.4 GHz and 0 V bias.

Figure 3.15 demonstrates the measured CG performance versus angle of incidence over the E-and H-plane radiation patterns of the receive and transmit antennas. Relative to the

coordinate system in Figure 3.11, the H-plane is the Y-Z plane and the E-plane is the X-Z plane. The measurements were performed at f_1 of 2.4 GHz and zero volt bias. The measured variation in CG over the H-plane for received powers of -20 and -30 dBm is 4 and 5 dB, respectively. The CG variation dependence on the received power is expected, since the variation over the transceiver receive antenna H-plane (0.8 dB) changes the received power level at the diode input, and the doubler has a non-linear CG relation with input power (Figure 3.14). The measured cross-polarization isolation level, defined here as the ratio between the return signal levels from the transceiver for co- and cross-polarized interrogation signals, is ~ 30 dB.

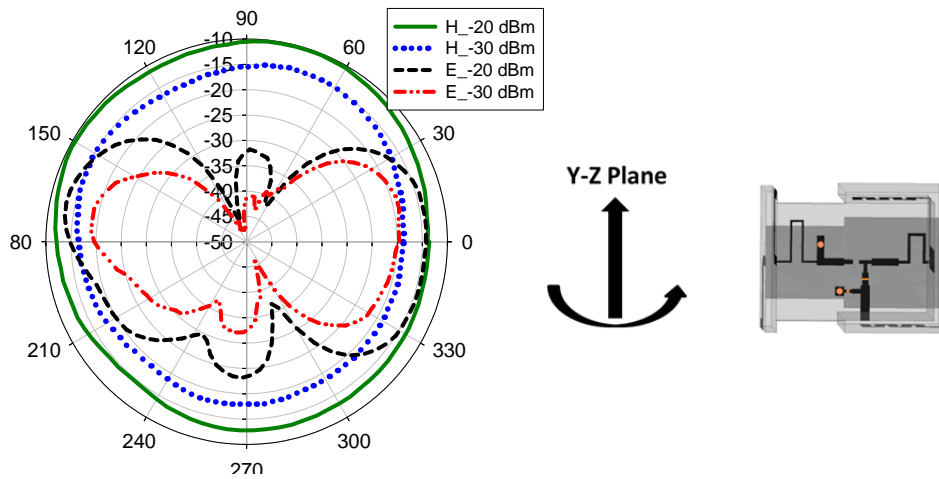


Figure 3.15: The measured conversion gain (dB) versus incidence angle (Y-Z plane, Figure 3.11) for different received power levels at f_1 of 2.4 GHz and 0V bias.

3.4 Sensor Emulation

In order to facilitate the use of the harmonic transceiver in a sensing application, the ability to modulate the return signal has been included. Using the DC network that connects to the diode input, a bias voltage can be applied to change the impedance match with the receive antenna causing a change in the CG and allowing for amplitude modulation of the re-transmitted signal from the transceiver. Figure 3.16 demonstrates the CG behavior versus bias voltage at -30 dBm input power and 2.4 GHz incident frequency. As seen, the performance is very sensitive to

the applied bias voltage; a 0.1 V bias decreases the transmitted power by 17 dB. This sensitivity for small applied voltage would allow for amplitude modulation of the back-scatter signal.

As mentioned before, the 3-D approach provides the capability of housing the sensor electronics inside the structure. This requires that the transceiver performance is insensitive to the insertion of objects (e.g. sensors) inside the cube. To demonstrate, the tag was tested with metallic and lossy dielectric (ϵ_r of 10 and loss tangent of 0.1) blocks measuring $2.5 \times 2 \text{ mm}^3$ placed inside on the bottom side of the cube. Experimental results show that the transceiver performance is not degraded with these blocks, which occupy a larger volume than many practical sensors. The sensor integration is discussed more in depth in Chapter 4.

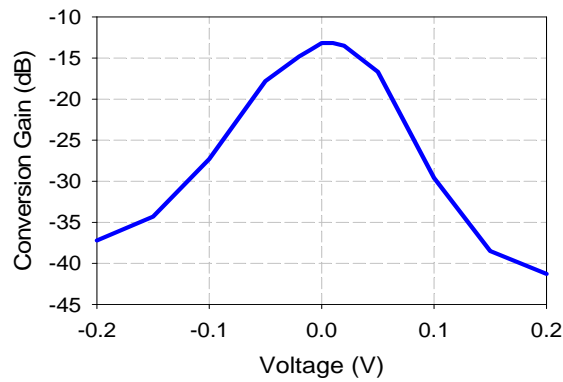


Figure 3.16: The measured conversion gain versus bias voltage at -30 dBm input power and f_i of 2.4 GHz.

3.5 Embedding in Sand

In this section the impact of burying the harmonic transceiver in sand to determine its suitability for embedded, remote monitoring is investigated. Figure 3.17 illustrates the measurement setup used to characterize the transceiver buried in a box of sand and metal bars. The cubical sand box side dimension is 30 cm and the metal bars have a diameter of 1 cm and height of 20 cm. The bars were inserted in the sand box to more effectively represent a structure with the steel rebar reinforcements. In this experiment the transceiver was placed inside a 5 cm

cubical box of foam to reduce the dielectric loading of the sand. Simulations have shown that placing the repeater inside a 3 cm diameter sphere will mitigate this issue, however, the 5 cm cubical box was used for durability during the measurements.

In order to estimate the RF signal attenuation through the sand, laboratory measurements inside an anechoic chamber were first performed. Two antennas (a receiver and transmitter) were used in this experiment to measure S_{21} through the box filled with sand. To calibrate the signal attenuation, S_{21} through an empty box was then measured and subtracted from the previous S_{21} measurement. The attenuation of the sand versus frequency is shown in Figure 3.18. The high ripple shown in the measurement is attributed to signal diffraction at the air/sand interfaces and multi-path reflections of the experimental setup. To reduce these effects the data was averaged using a linear function, Figure 3.18. Thus the imaginary part of the sand dielectric constant is not assumed to vary with frequency, which is typical for low moisture sand [117]. Based on the averaged data, the sand box causes an attenuation of ~ 4.5 dB at f_1 of 2.4 GHz and f_2 of 4.8 GHz.

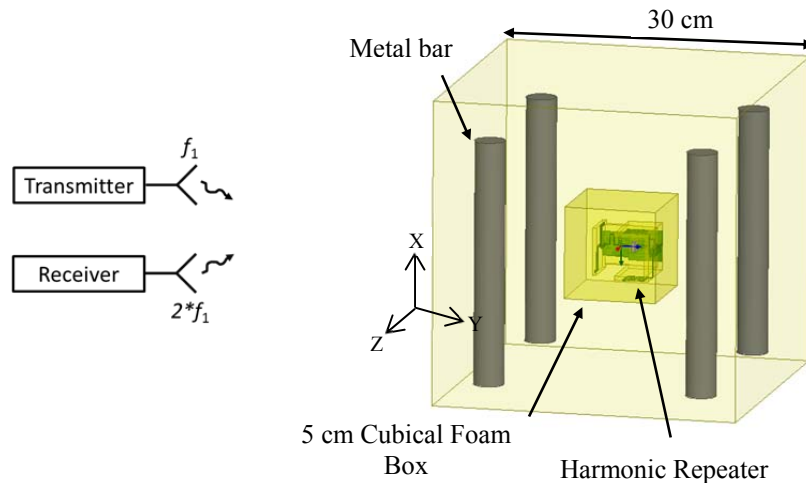


Figure 3.17: The measurement setup used to test the embedded harmonic transceiver. Note: the figure is not drawn to scale.

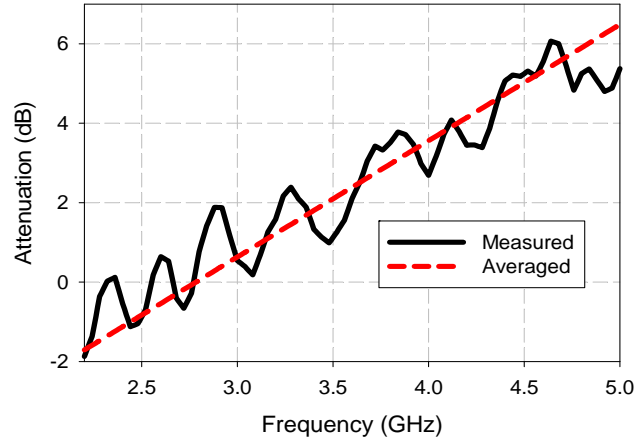


Figure 3.18: Measured and averaged calibrated attenuation through a 20 cm sand layer versus frequency.

Figure 3.19 shows a comparison between the expected and measured CG versus frequency of the harmonic transceiver with and without the sand box. The transceiver receive and transmit antennas were oriented where the maximum CG was recorded. The maximum CG is recorded at f_1 of 2.38 GHz when the repeater is buried in the sand box. This shift from the 2.4 GHz design frequency is due to the dielectric loading of sand which can be corrected for by re-optimizing the design to operate in a sand environment or by enlarging the air box enclosing the transceiver. The decrease in the CG of the buried repeater is due to the signal attenuation through the sand layer.

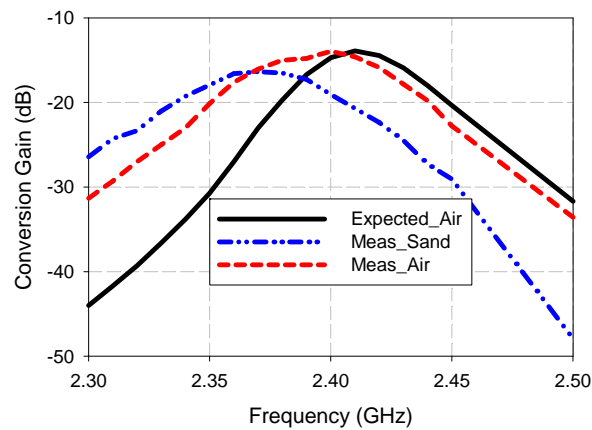


Figure 3.19: A comparison between the expected and measured CG versus frequency for received power of -30 dBm and 0V bias voltage in air and sand environments.

Figure 3.20 compares the expected and measured CG versus received power at different f_1 and 0 V bias voltage. The expected CG of the buried repeater was calculated by subtracting the estimated signal attenuation through the sand box (4.5 dB, Figure 3.18) from the expected CG in the air environment. As seen, the measured CG of the buried repeater at 2.38 GHz and the measured CG in the air environment match the expected data well.

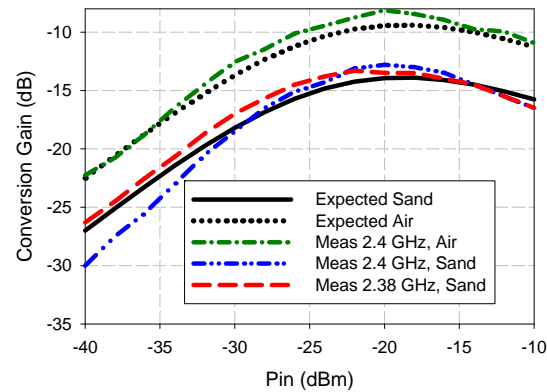


Figure 3.20: A comparison between the expected and measured CG versus input power at different f_1 and 0V bias voltage in air and sand environments.

In order to study the harmonic transceiver ability to modulate the return signal while it is buried in sand, a function generator was used to apply a sinusoidal AC signal of a frequency of 10 Hz at the diode doubler input and the power level of the return signal was measured versus time, Figure 3.21. This modulation signal represents the signal that will eventually be provided by a sensor. As seen, when the amplitude of the AC signal is set to 0V, the return signal level is constant. By applying a low amplitude signal (10 mV), an amplitude modulated return signal can be detected. This measurement shows that harmonic transceiver is capable of effectively modulating the return signal while it is buried in sand.

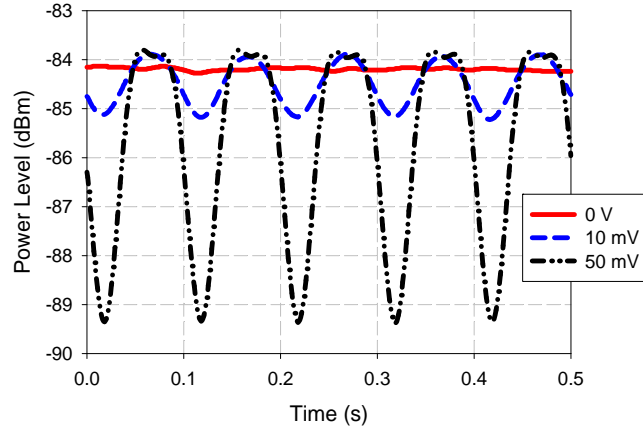


Figure 3.21: The measured return signal level versus time for different modulation signals of frequency of 10 Hz and different amplitudes at f_1 of 2.38 GHz of the buried transceiver.

3.6 Conclusions

A 3-D integrated harmonic transceiver has been developed for the purpose of passive wireless sensing. The proposed design offers a combination of zero DC power consumption, low RF power operation, high conversion gain, modulation capability, and omni-directional radiation patterns. Furthermore, unlike previously reported designs, the repeater has a miniature form factor that is readily adapted to different packaging requirements. The significant conversion gain improvement of the proposed transceiver will result in an extended communication range for free space sensing applications.

The impact of embedding the harmonic transceiver in a sand environment has been investigated. Experimental results revealed that this embedding has minimal impact on the transceiver efficiency and thus its interrogation range. The presented design has shown the capability for housing practical sensors and effectively modulating the return signal while it is buried in sand, suggesting that this design is suitable for embedded remote structural health monitoring.

CHAPTER 4 : MINIATURIZED VIBRATION SENSOR NODE WITH 3-D MACHINED-SUBSTRATE ANTENNAS

4.1 Introduction

In this chapter, compact 3-D passive sensor nodes are demonstrated for civil infrastructure vibration monitoring (Figure 4.1) [118]. The transceiver part of the sensors is designed following the design approach presented in Chapter 3. The sensor node operates by receiving an interrogation signal at 2.4 GHz (f_i), doubling the frequency, and transmitting back an amplitude modulated signal at 4.8 GHz ($2f_i$). To minimize the volume of the node without degrading the efficiency, a new machined-substrate approach is proposed. By using this approach for the antennas it is possible to fit the device within a sphere with a diameter of 21 mm, which is equal to $\lambda_1/6$ and constitutes a 32% size reduction relative to the design presented in Chapter 3. Despite the size reduction, the transceiver operates with an overall conversion efficiency of > -15 dB for an RF input power level range between -20 to -30 dBm, and exhibits omni-directional interrogation capability.

Different sensor types can be integrated with the proposed sensor node to modulate the return signal and provide information about the embedding environment. In this work, effective modulation is demonstrated using a commercial piezoelectric thin-film sensor and with mechanical vibration- and shock-sensitive switches. The piezoelectric sensor generates an AC voltage that is applied to the doubler input to change the impedance match conditions with the antennas and thus change the return signal power level. The mechanical switches impart

amplitude modulation to the return signal by opening and closing the doubler DC return current path.

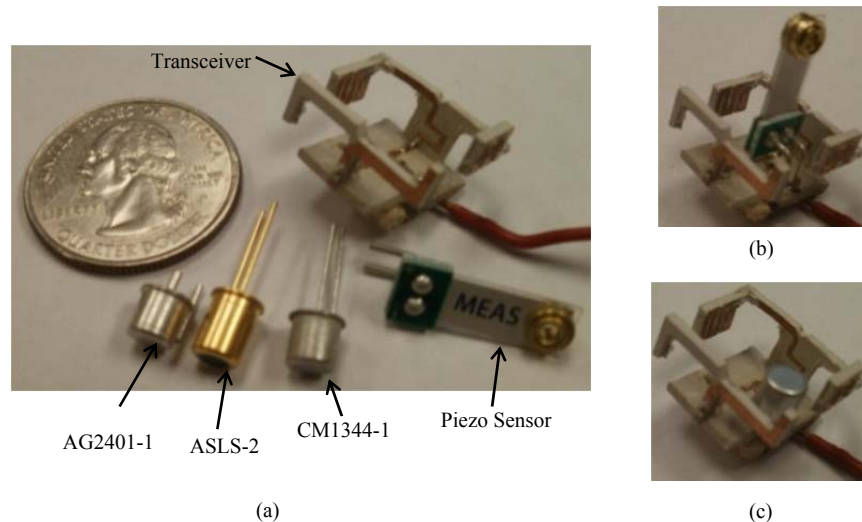


Figure 4.1: a) Photograph of the fabricated transceiver and the sensors used, b) the node with the piezo sensor, and c) the node with AG2401-1 switch sensor.

The design and simulation of the substrate-machined transceiver are presented in Section 4.2 and different experimental results to characterize the transceiver performance are illustrated in Section 4.3. Section 4.4 demonstrates the modulation capability of the sensor node and describes the vibration tests, and Section 4.5 illustrates the outdoor communication range test.

4.2 Transceiver Design

Similar to the transceiver presented in Section 3.2, the transceiver design consists of a diode-based frequency doubler and 3-D receive and transmit antennas (Figure 4.2). The transceiver was milled on the same substrate material and assembled manually. The primary contribution of this work in terms of antenna design is to show the advantage of removing (machining) unnecessary substrate around the antenna metallization. This approach allows for size miniaturization without degrading the radiation performance. The design of the receive and

transmit 3-D antennas, and a comparative analysis of the machining approach are described in the following sections.

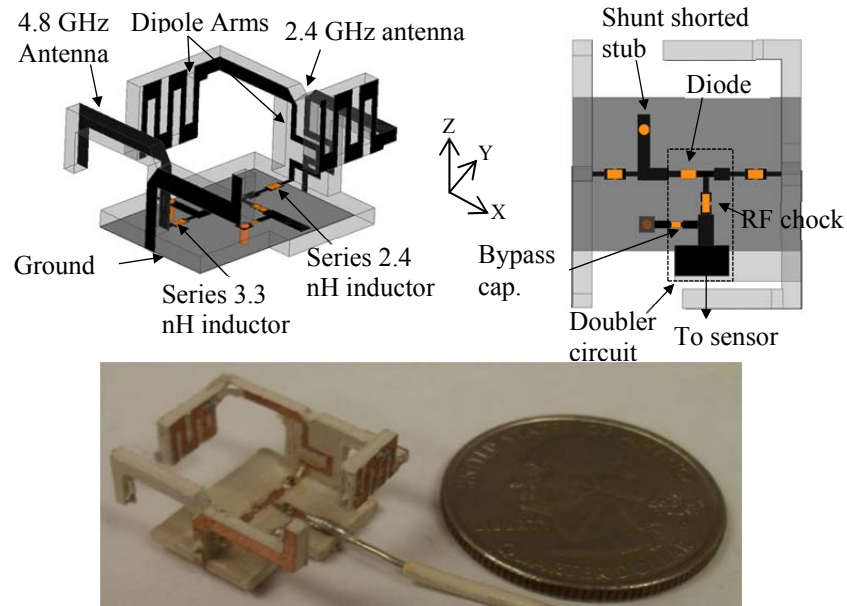


Figure 4.2: Transceiver design; 3-D view (top left), top-view (top right), photograph (bottom).

4.2.1 The Receive 2.4 GHz Antenna

Figure 4.2 (top left) illustrates the receive antenna design. The antenna is a half-wave dipole wrapped around a cube surface. The dipole arms were meandered to minimize their size and center-fed by a meandered parallel-plate, quarter-wave transformer with Z_o of 100Ω on the vertical side. On the upper surface of the bottom of the cube, a microstrip transmission line that is $\lambda/25$ in length with a Z_o of 96Ω , a series 2.4 nH inductor (Coilcraft 0402), and a $\lambda/40$ 50Ω line are used as matching elements. To reduce the mismatch loss and the reflected power at the fundamental frequency, the antenna input impedance is conjugate-matched to the doubler input impedance, Figure 4.3 (left). The simulated antenna impedance at 2.4 GHz is $53+j301 \Omega$. Figure 4.3 (right) shows the simulated E- and H-plane radiation patterns at 2.4 GHz . Relative to the coordinate system in Figure 4.2, the H-plane is the Y-Z plane and the E-plane is the X-Y plane.

The antenna demonstrates an omni-directional pattern in the H-plane with only 0.3 dB variation. The maximum radiation occurs broadside to the non-meandered portions of the dipole arms with a peak gain of 0.95 dBi (simulated efficiency of 84%). The tilt in the E-plane pattern is due to ground plane interference and operating the antenna off-resonance.

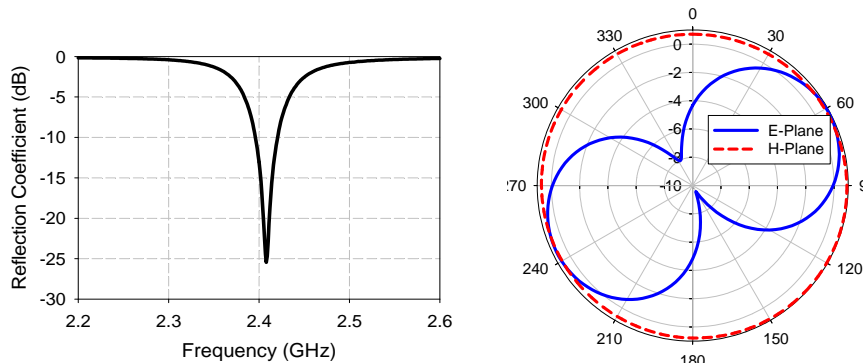


Figure 4.3: The reflection coefficient between the receive antenna and the doubler input at -30 dBm input power (left) and the simulated radiation patterns (in dB) of the 2.4 GHz antenna (right).

4.2.2 The Transmit 4.8 GHz Antenna

The transmit antenna is illustrated on the far left-hand side of Figure 4.2. The feeding network consists of a series 3.3 nH inductor (Coilcraft 0402), shunt shorted stub of $\lambda/8$ length with Z_0 of 50 Ω , and a $\lambda/15$ 50 Ω line; the shunt stub also provides a DC return path to the diode doubler. Figure 4.4 (left) shows the simulated reflection coefficient between the doubler output and the antenna input, which presents an impedance of $20+j147 \Omega$ at 4.8 GHz. Figure 4.4 (right) shows the simulated transmit antenna radiation patterns at 4.8 GHz. The variation over the H-plane is 3.2 dB and the peak gain is 2.6 dB (efficiency of 93%). As noted above, ground plane reflection and interference from the other antenna cause some pattern distortion and tilting.

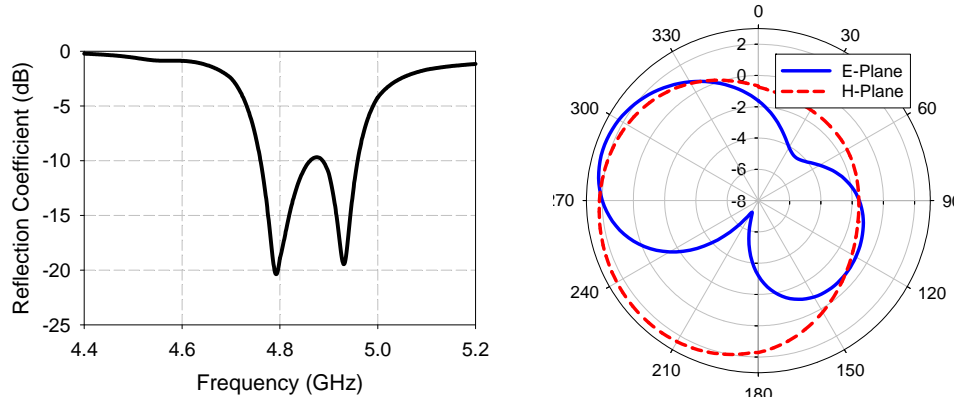


Figure 4.4: The reflection coefficient between the transmit antenna and the doubler input at -30 dBm input power (left) and the simulated radiation patterns (in dB) of the transmit antenna at 4.8 GHz (right).

4.2.3 The Impact of Substrate Machining

Figure 4.5 demonstrates the significant benefit of applying the machined substrate approach on the transceiver performance. This technique allows the use of high dielectric constant materials in strategic locations to minimize the antenna size without degrading the overall node performance. In particular, proximity effects between the closely spaced antennas and diffraction that occurs at the substrate edges are both mitigated, which helps to minimize pattern tilt and gain variation over the antenna H-plane. The removal of material also reduces dielectric loss which improves radiation efficiency. Comparing the performance of the transceiver without applying the machining (1st iteration) to the proposed transceiver design shows that the pattern distortion is reduced by 6 dB and the radiation efficiency of the transmit antenna is increased by ~20%. The second iteration shows the impact of reducing the size of the design presented in Section 3.2 to be similar to the size of the design presented in this section without machining the substrate. As seen, reducing the size without machining the substrate structure increases the gain variation over the transmit antenna by 2.5 dB and reduces the efficiency by 9%. Pattern distortion is of great importance for embedded sensing applications as

it is equivalent to misalignment between the interrogator and sensor node antennas, and will therefore limit the communications range.

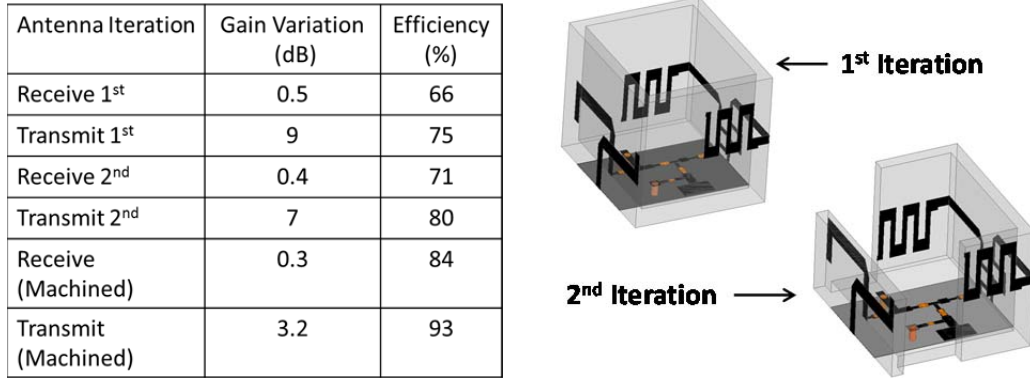


Figure 4.5: Impact of the machining approach on the transceiver performance; a comparison table (left) and a CAD drawing of different transceiver iterations (right).

4.3 Experimental Results

The machined-substrate transceiver was characterized inside an anechoic chamber using the same measurement setup shown in Figure 3.12. Figure 4.6 illustrates the measured and simulated CG performance for different interrogation signal frequencies (left) and different input power levels (right). The simulated CG of the transceiver was calculated by adding 3.5 dB (the sum of antenna peak gains) to the simulated CG curve of the multiplier alone. As seen in the figure, the maximum CG value occurs at 2.341 GHz and closely matches the predicted results. This shift from the 2.4 GHz design frequency is attributed to fabrication and assembly errors. The measured CG 3 dB bandwidth is 2.5% and 1.8% at input powers of -20 dBm and -30 dBm, respectively. Figure 4.7 shows the measured CG over different angles of incidence and for different received power levels. In this measurement the transceiver was rotated around the H-plane of the antennas (Y-Z plane relative to Figure 4.2). The measured variation in CG for received powers of -20 and -30 dBm is 3.6 and 4 dB, respectively.

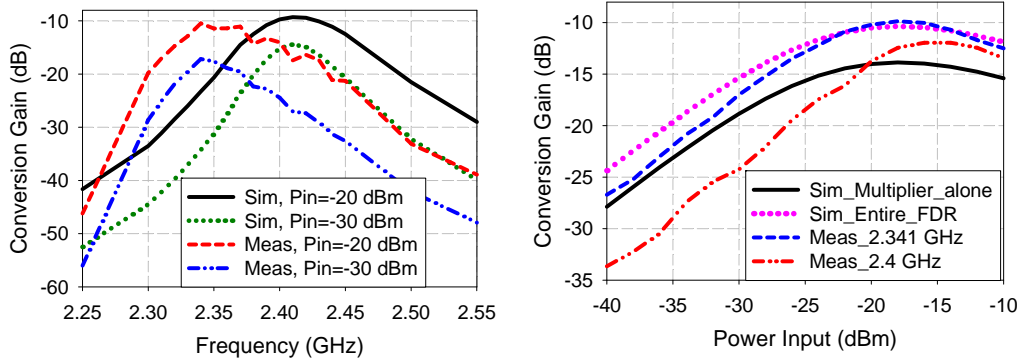


Figure 4.6: The CG versus frequency for different received powers (left) and the CG versus input power for different f_i (right).

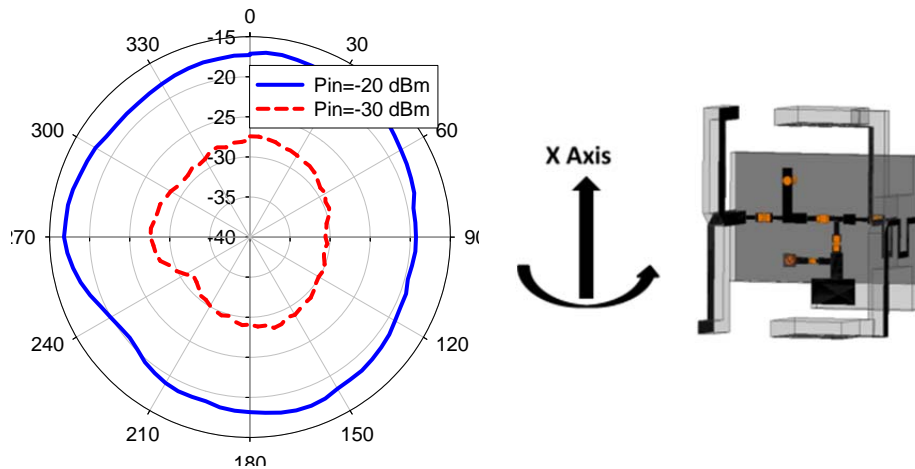


Figure 4.7: The measured CG (dB) versus incidence angle (YZ-plane, Figure 4.2).

4.4 Sensor Integration and Measurements

The measurement setup used to detect vibration using the proposed sensor node is depicted in Figure 4.8. The measurements were performed inside an anechoic chamber where the node is interrogated by a signal generated using a VNA and the return signal is measured using a SA in the zero span mode. While the sensor node is being interrogated, a Labworks shaker was excited with a function generator to drive the sensor into vibration. Due to mechanical configuration constraints (primarily the size of the shaker) the sensor was soldered onto a circuit board and connected to the transceiver through copper wires, rather than being directly

connected within the transceiver during the vibration testing. As mentioned in Section 4.1, two sensor types are used in this work and demonstrated below.

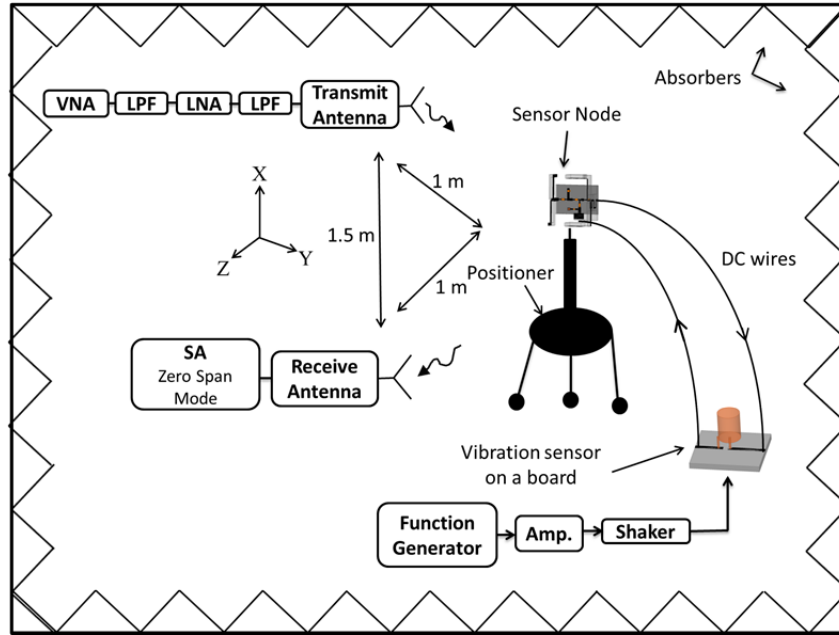


Figure 4.8: The experimental setup used to interrogate the proposed sensor node and detect vibration.

4.4.1 The Piezo Thin-Film Vibration Sensor

It was found in Chapter 3 that by applying DC voltage to the diode doubler input, amplitude modulation can be imparted to the return signal. The voltage changes the diode impedance match with the antennas thus changing the CG of the transceiver. To test the capability to modulate the return signal of the machined-substrate transceiver the CG was measured for different applied DC voltages and different power levels, Figure 4.9. As seen, the CG is very sensitive to the applied voltage, as a 0.1 V bias decreases the CG by > 14 dB. Thus using a passive sensor that can generate voltage, such as the piezoelectric sensors, will provide amplitude modulation.

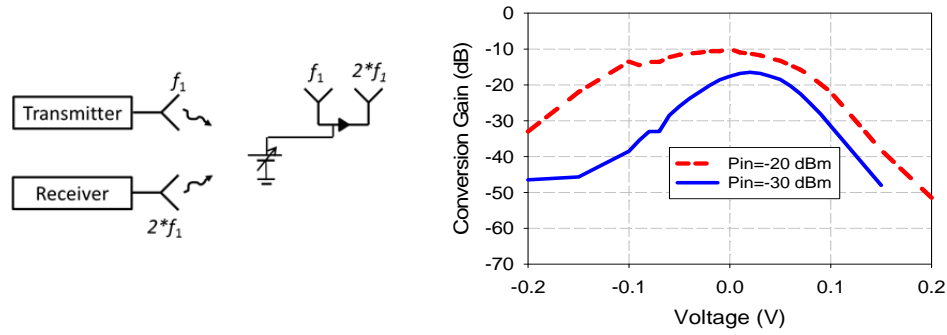


Figure 4.9: Measurement illustration (left) and the measured CG versus DC voltage for different RF input power (right).

The piezo thin-film vibration sensor used is the MiniSense 100 from Measurement Specialties. During testing the sensor was excited at a vibration frequency of 40 Hz and amplitude of 9 g (deflection of 2.5 mm). The output voltage waveform from the sensor was measured using an oscilloscope with a load impedance of 1 M Ω . The voltage waveform is illustrated in Figure 4.10 (left); as seen, the peak voltage is ~3 V and the measured frequency is ~40 Hz. Figure 4.10 (right) illustrates the node return signal power level versus time for a received RF power level of -30 dBm. The return power is approximately the same when the DC network is open-circuited and when the sensor is attached but is not driven into vibration. However, when the sensor vibrates the return power has a peak to peak variation of ~1 dB and a frequency of ~40 Hz. Based on Figure 4.9, the voltage across the doubler that causes this power level reduction is ~10 mV. The difference in the oscilloscope impedance and the doubler impedance (~2.2 k Ω) is the reason for the drop from 3 V to 10 mV, since the capacitive input (~500 pF) of the sensor combines with the load resistance to create a high pass filter. Additional testing was performed to ensure that the integration of the piezoelectric sensor with the transceiver would not produce adverse proximity effects. The sensor was attached inside the transceiver structure as seen in Figure 4.1 b and no degradation in the CG was observed. However, placing this sensor inside the node restricts the fluctuation of the sensor cantilever film

that would reduce the generated voltage. In order to increase the voltage delivered to the doubler at a given vibration level, enabling lower vibration frequencies and amplitudes to be detected more easily, the sensor needs to be designed to have a larger capacitive input. Another approach is to add an additional circuit to the doubler to increase its impedance, such as a transformer. These approaches, however, may result in increasing the volume of the node.

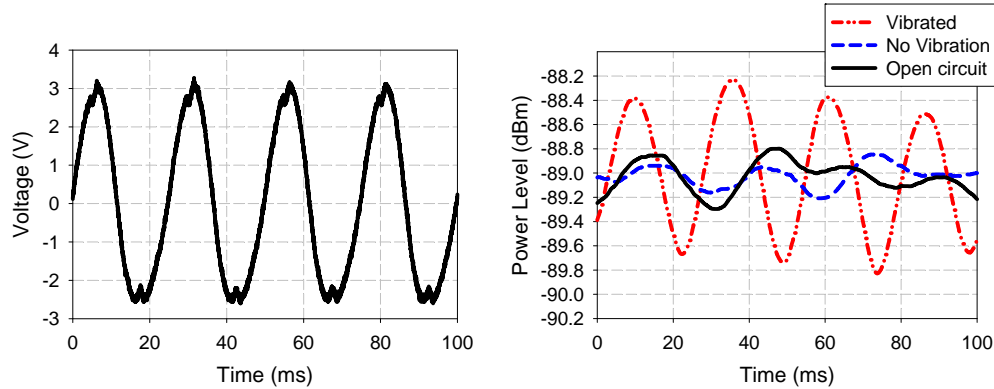


Figure 4.10: The piezoelectric sensor output voltage versus time as measured using an oscilloscope (left) and the measured transceiver return signal level at $2f_1$ with the piezoelectric sensor connected to the doubler input (right).

4.4.2 The Mechanical Sensors

For the structural health monitoring application the vibration frequency and amplitude are both usually very low [119, 120]. Although the piezo thin-film sensor is more suitable for detecting high frequency stimuli, it was found through analysis and experimental results that mechanical switches can be effectively used to provide low vibration frequency and low amplitude detection capability. The sensors used for this demonstration are the CM1344-1, AG2401-1, and ASLS-2 from Comus International. These sensors offer the additional benefit of being hermetically sealed for long lifetime operation. They usually are found in analog and digital circuitry for various applications such as anti-theft devices, smart appliances and security systems.

The aforementioned mechanical switches can be integrated into the sensor node in different manners to impart modulation to the return signal. In this work the switch is used to open and close the diode DC current return path at the doubler input. This approach decouples the mechanical switch from the RF path, thereby alleviating the need to accurately model switch behavior at microwave frequencies and providing a more controlled transceiver response. As seen in Figure 4.11, opening and closing the DC current path causes the return signal to vary between 3.1-8.5 dB for an RF input power of -30 to -20 dBm. This behavior avoids extreme “on/off” characteristics regardless of the normal or resting state of the mechanical switch and could be advantageous when communications with the node are needed even if it is not vibrating. For example the node can provide a reference signal to calibrate the propagation channel for other nearby sensors, determine the sensor location, or be used for identification.

The AG2401-1 sensor is a low cost ball switch that has the ability to detect very low vibration frequencies and amplitudes. Depending on its position and orientation, this sensor may rest in the open or closed state and once it is driven into vibration it continually changes its state as long as the motion continues. When it is in the closed state, the contact resistance is less than 1 Ω . Its cylindrical case has a diameter of 4 mm and height of 4.5 mm.

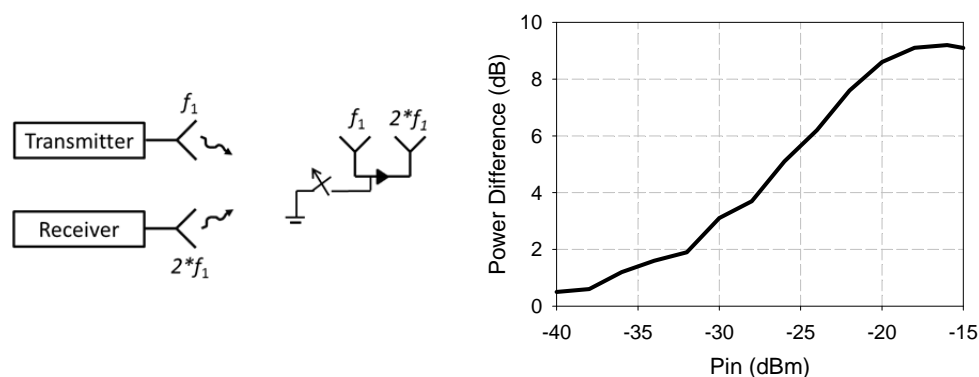


Figure 4.11: Measurement illustration (left) and the measured return power difference at f_1 of 2.341 GHz when the DC return path is switched between open and closed states (right).

As seen in Figure 4.12, driving the AG2401-1 into vibration with a frequency of 0.1 Hz and amplitude of 0.01 g induces the sensor to change its state and thereby vary the power level received back from the node during interrogation. The excursions of the data for the vibrated state from the closed state data occur near the peaks in the mechanical excitation waveform. It was shown experimentally that this sensor is able to measure the vibration frequency accurately, as in this example where the detected frequency is 0.098 Hz, and the sensor responds to vibration amplitude ranges between 0-1 g. The sensor is also directional in that it is sensitive to vibration only in the direction shown in Figure 4.12.

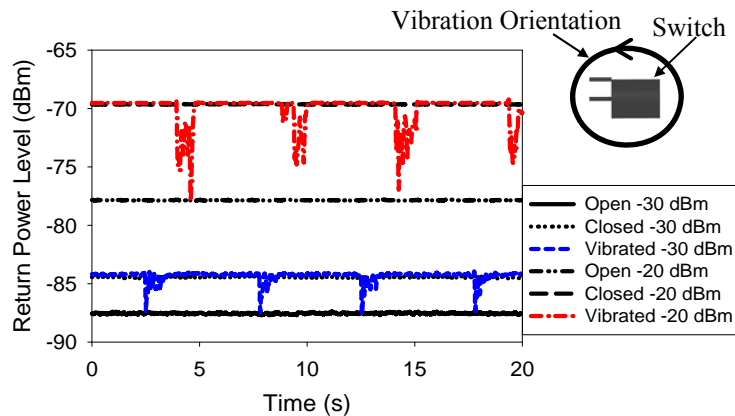


Figure 4.12: The measured return power versus time for different received power levels for f_1 of 2.341 GHz using the AG2401-1 ball switch. The vibration frequency is 0.1 Hz and the amplitude is 0.01 g.

In order to detect stronger shocks, as might be excited by an earthquake, the ASLS-2 spring-damped ball switch proved to be effective. This switch needs to be driven by vibration amplitudes between 2-4.9 g in order to change its state. Figure 4.13 shows the response when the sensor was excited using a 30 Hz, 2.3 g amplitude vibration waveform. Unlike the AG2401-1, the ASLS-2 responds only when the vibration waveform is above or below the zero state and not to both positive and negative excursions. As seen, the resting state is open and the return power level peak-to-peak variation is approximately 4.6 dB and 2 dB for RF received power of -20

dBm and -30 dBm, respectively. The power variation is lower with this sensor due to the higher contact resistance in the closed state.

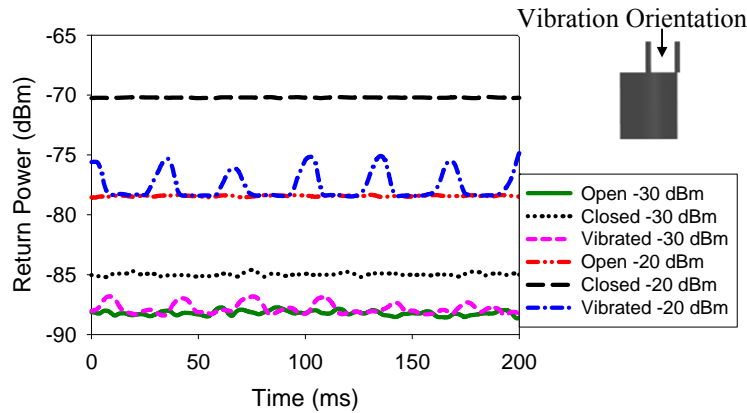


Figure 4.13: The measured return power versus time for different received power levels for f_1 of 2.341 GHz using the ASLS-2 shock/acceleration switch. The vibration frequency is 30 Hz and the amplitude is 2.3 g.

A similarly-sized mercury switch, model CM1344-1, was also tested with the sensor node. This class of switches has a longer operating lifetime than ball switches, and a higher cost. It offers also the additional benefit of being responsive to vibration along any axis and may therefore be advantageous for embedded sensing applications where the orientation of the deployed sensor nodes is difficult to control. This switch is normally in the open state and when it is subjected to vibration it intermittently changes its state near the peaks of the excitation wave. Experimental testing with this switch showed that vibration frequencies from 3-40 Hz were detectable, although when the frequency is >10 Hz the vibration frequency is difficult to correlate with the excitation signal frequency.

The proposed sensor node has also the capability of simultaneously housing multiple sensors without considerable performance degradation. In many situations it is desirable to use a single sensor node for different concurrent applications reducing the size, cost, and identification complexity. As the AG2401-1 and the ASLS-2 switch sensors change state only when the vibration is within specific non-overlapping amplitude and frequency ranges, they can be

integrated in parallel giving the capability of detecting low and high amplitude acceleration. The sensor node was simulated and tested with those mechanical switches in place and no performance sensitivity was observed. In order to have the sensors oriented to be normally in the open state, a specific node orientation might be required. This limitation can be overcome by integrating the sensors in a different topology or using other sensor candidates.

4.5 Sensor Communication Range

Outdoor measurements were performed to validate the transceiver performance in a long-range free space environment. Figure 4.14 shows the return signal level versus interrogation distance using a 43 dBm EIRP (effective isotropic radiated power) transmitter and 10 dB gain receiver. The expected power level was calculated based on the CG measurement performed inside the anechoic chamber (Figure 4.6, right) and assuming a free space line-of-sight communication link. Assuming that the lowest received signal level that can be detected is -125 dBm, the transceiver range is found to be ~60 m. This range is calculated based on a received signal level of -125 dBm at the interrogator detection stage; when using a spectrum analyzer for signal detection, this power level provides ~10 dB headroom given a 10 kHz resolution bandwidth. In order to verify the expected range, outdoor measurements were performed using a setup similar to that shown in Figure 3.12. During measurement the interrogator antennas and transceiver were placed at a height of ~1.5 m above the ground and oriented where the maximum CG value was recorded (interrogated from the top, +Z-axis). The range was measured by varying the interrogator-transceiver distance and tracking the return signal level for a fixed transmitted power. The measurement was performed over distances range between 10-45 m. The power received does not decay exponentially with increasing interrogation distance due to the non-linear CG behavior of the transceiver versus received power. As seen in the figure the measured

and expected data are well matched. The accuracy in these measurements was +/- 1 dB. This experiment reveals that when using the harmonic radar approach under these conditions the communication range is mainly limited by the level of the transmitted power.

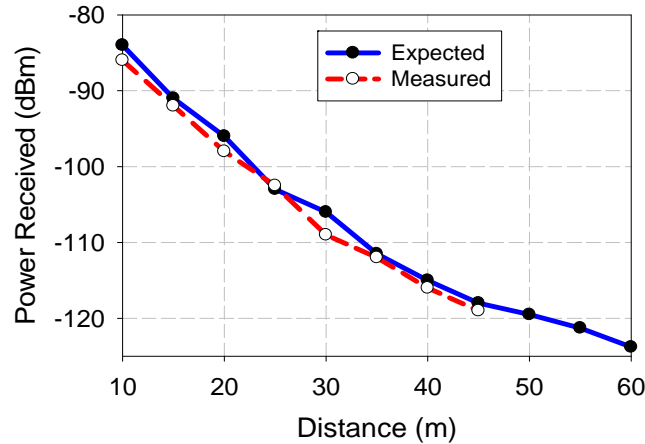


Figure 4.14: The received return signal strength versus distance using a 43 dBm EIRP transmitter and 10 dB gain receiver.

4.6 Conclusion

Compact, energy-efficient, low-cost, passive vibration sensor nodes have been developed. Significant improvements in the size and performance of the node have been enabled by the introduction of machined substrates for the antennas. Two types of low-cost commercial vibration sensors were used to demonstrate the modulation capability of the proposed node. Using the mechanical switch sensors, very low vibration frequency can be detected which makes the design more suitable for structural health monitoring. The outdoor field test revealed that the proposed vibration sensor nodes are good candidates for long range embedded passive sensing.

CHAPTER 5 : DUAL-CHANNEL TRANSCEIVER DESIGN

5.1 Introduction

In this chapter, a novel, compact, 3-D passive dual-channel transceiver is developed [121]. The transceiver contains separate harmonic repeaters for sensing and to provide a reference signal (no sensor) for remote channel calibration and identification. Each repeater consists of receive and transmit monopole antennas and a frequency doubler. The size constraint has motivated the use of meandered monopole antennas rising vertically relative to the ground plane to make available the interior of the structure for sensor electronics placement. The sensing repeater operates by receiving a signal at 2.4 GHz and transmitting a signal back at 4.8 GHz, while the reference repeater operates at 2.75/5.5 GHz for this demonstration. The measured conversion gain of the sensing repeater for an RF input power of -20 dBm is -12.4 dB while it is -8 dB for the reference repeater. The diagonal of the transceiver measures 0.25λ at the fundamental frequency of 2.4 GHz. To the best of the author's knowledge, the presented transceiver is the first completely passive design with built-in passive remote channel calibration and identification capability.

Remote channel calibration is an important challenge associated with passive embedded wireless monitoring. When the sensor node is deployed in a structure, it is of concern to periodically calibrate the propagation channel (between the interrogator and the node) to obtain a proper reading from the sensor, and confirm that the node is functioning properly. This calibration challenge can be addressed by placing a reference node in close proximity to the node

of concern and using frequency or polarization diversity to distinguish between the nodes. The drawback of this approach is the requirement for an additional reference node to be placed close to each sensing node. With the dual-channel transceiver the propagation channel can be calibrated by varying the interrogation signal frequency to interrogate the sensing repeater then the reference repeater. This calibration method does not require varying the interrogation signal polarization and does not require a separate reference node to be placed close to the sensing node, thus reducing the occupied volume by $> 50\%$.

Node identification is also a major challenge with long-range passive wireless monitoring. When different sensors are deployed within the same structure, some means of knowing which node is being interrogated is needed. Different passive identification techniques have been proposed to be used with chip-less RFID tags, such as introducing time delays (time coding) [122] and multi-resonator bits (frequency coding) [123]. These techniques can possibly be combined with the proposed node design to address the identification problem. With the dual-channel transceiver, however, the problem can also be addressed using frequency diversity, i.e., operating the reference and sensing channels at different frequencies. This approach gives the ability to distinguish between multiple nodes located within the interrogator beam angle, and will allow the interrogation range to increase without introducing limitations on the maximum number of nodes, distance between the nodes, and the interrogator antenna design. Although the number of unique node identifications is limited, even given the moderately narrow bandwidth of the transceivers, reasonable numbers can be obtained if used in combination with other techniques (e.g., polarization diversity). This identification method can also be used for tracking and identifying adjacent mobile objects.

In the following sections, the design, testing and analysis of the sensor node are presented. Section 5.2 illustrates the transceiver design and Section 5.3 gives different experimental results to demonstrate the performance of the design. Comparisons between the transceivers presented in this dissertation and with other designs from the literature are given in Section 5.4. Section 5.5 analyzes remote channel calibration and Section 5.6 discusses the identification capability. A preliminary study of the impacts of embedding the proposed transceiver in a dry sand environment is presented in Section 5.7.

5.2 Transceiver Design

The proposed transceiver design consists of two harmonic repeaters, one used for sensing and one used to provide a reference signal, Figure 5.1. Each harmonic repeater consists of a frequency doubler and meandered monopole receive and transmit antennas. The frequency doubler used is similar to the doubler presented in Chapter 3. The antennas were designed using HFSS 14. The node was fabricated using a milling machine and assembled manually. The substrate is Rogers/RT Duroid 6006 with a relative permittivity (ϵ_r) of 6.15 and a thickness of 50 mils.

5.2.1 The 2.4/4.8 GHz Sensing Repeater

Figure 5.2 illustrates the sensing repeater design. The repeater operates by receiving a signal at f_1 of 2.4 GHz and transmitting a return signal at $2 \cdot f_1$ of 4.8 GHz. The receive antenna is fed by a microstrip line (ML) on the top surface of the round base with a characteristic impedance (Z_0) of 76Ω and electrical length of $\lambda_g/16$. While the transmit antenna is fed by a ML with a length of $\lambda_g/13$ and Z_0 of 74Ω and a $\lambda_g/20$ shunt shorted stub with a Z_0 of 63Ω . Fig. 2 (right) shows the doubler circuit. The bias network is added to provide an interface to the sensor.

The bias network consists of a 27 nH series inductor (Coilcraft 0402) and 8.2 pF shunt capacitor (Johanson 0201). ADS 2009u1 was used to simulate the doubler and find the optimum impedances that the antennas need to present to the doubler input/output to provide the best CG at -30 dBm input power. Based on this simulation, it was found that the receive antenna needs to present an impedance of $93+j358 \Omega$ at 2.4 GHz and the transmit antenna needs to present an impedance of $25+j200 \Omega$ at 4.8 GHz. To provide these impedances, HFSS 14 was used to optimize parameters such as the number of the monopole meandered sections, width of the sections, spacing of the sections, and the feeding network parameters. The complete transceiver configuration (see Figure 5.1) was used for these simulations. To fine tune the impedance match, a $\lambda_g/10$ 64 Ω shunt shorted tuning stub was added to the doubler circuit. This shorted stub also provides a DC path for the diode return current (Figure 5.2, right). Figure 5.3 shows the reflection coefficient between the receive antenna and the doubler input, and the transmit antenna and the doubler output at -30 dBm input power. As seen, the reflected power at the fundamental frequency is very low.

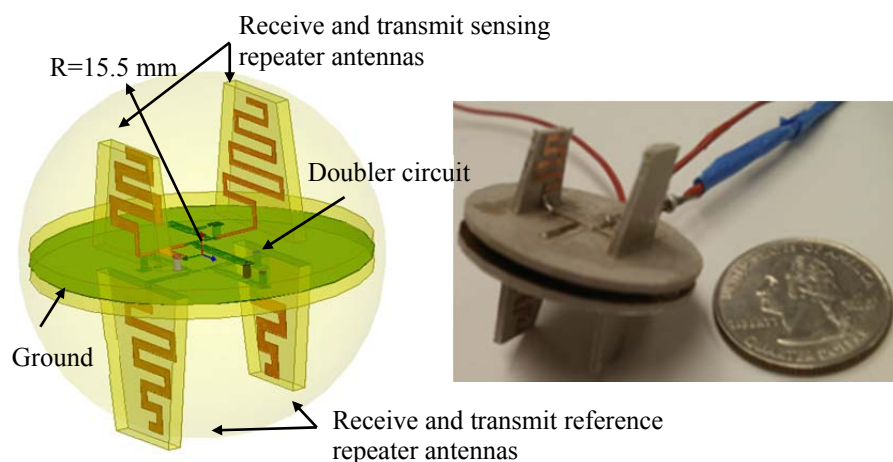


Figure 5.1 A CAD view of the proposed node (left) with a hypothetical sphere of 15.5 mm radius and a photograph of the fabricated design (right).

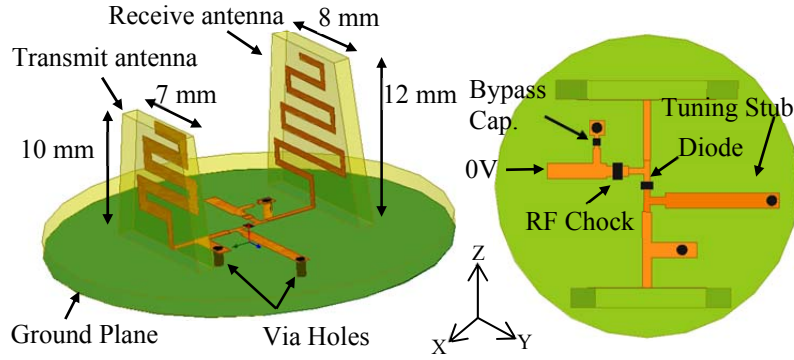


Figure 5.2: Illustration of the sensing repeater, side view (left) and top view (right).

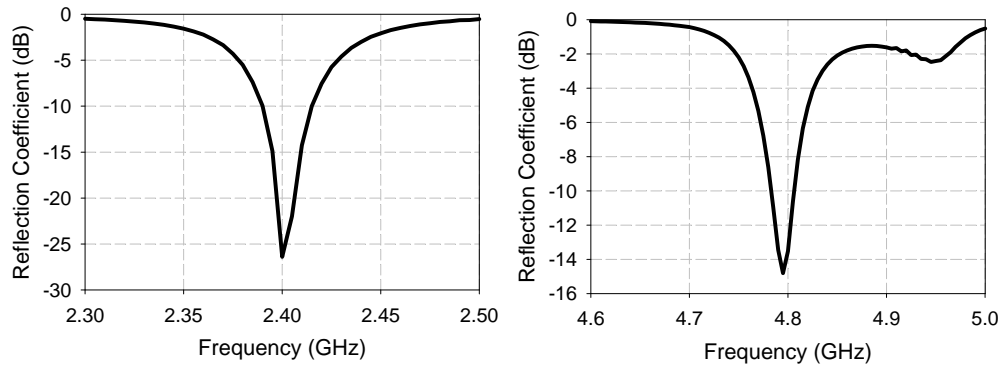


Figure 5.3: The simulated reflection coefficient between the receive antenna and the doubler input (left) and between the transmit antenna and the doubler output (right) of the sensing repeater at -30 dBm input power and 0V bias.

One of the main antenna design goals in this work was to minimize the size without significantly degrading the H-plane gain variation (the omni-directional pattern) to facilitate interrogation. This was achieved by minimizing the size of the substrate supporting the antenna to reduce edge diffraction, and by reducing the coupling between the antennas. The coupling was reduced by optimizing 1) the size of the ground plane, 2) the distance between the antennas, and 3) the height of the antennas. In addition, the meander pattern of the antenna trace and the location of each antenna have significant contribution to the coupling. As seen in Figure 5.1, the receive and transmit antennas were placed on opposite sides of the node and the meandering direction is chosen so that the induced near-field currents on each parasitic antenna oppose the current direction on each driven antenna, thus self-canceling the unwanted radiated far-fields.

Reducing the coupling has additional benefit of having the reference signal independent of the modulated return signal.

Figure 5.4 shows the simulated radiation patterns of the receive and transmit antennas at 2.4 GHz and 4.8 GHz, respectively. The antennas are linearly polarized along the Z-axis, relative to the coordinate system shown in Figure 5.2. As seen the antennas demonstrate omni-directional patterns in the XY-plane. The gain variation over the receive antenna H-plane is 1.6 dB while it is 2 dB for the transmit antenna. The receive antenna peak gain is 0.9 dB with a simulated radiation efficiency of 78.5%. The peak gain and radiation efficiency of the transmit antenna are 1.1 dB and 67%, respectively. The distortion shown in the pattern, especially the E-plane, is due to 1) the relatively small ground plane size, 2) coupling from the other antennas, and 3) operating the antenna off resonance. For the same reasons the radiation efficiency and gain were degraded.

5.2.2 The 2.75/5.5 GHz Reference Repeater

Figure 5.5 illustrates the reference repeater. For this demonstration the repeater was designed to receive a signal at f_1 of 2.75 GHz and transmit a signal back at $2 \cdot f_1$ of 5.5 GHz. Based on simulated data, the frequency separation between the sensing and reference repeater can be reduced to 200 MHz at the fundamental frequency without a significant increase in the coupling between the antennas. If smaller frequency spacing is required, the distance between the antennas and the ground plane size need to be increased. The receive antenna is fed by a $\lambda_g/14$ 69 Ω ML and a 3.9 nH series inductor (Coilcraft 0402). The transmit 5.5 GHz antenna is fed by a $\lambda_g/11$ 69 Ω ML and a $\lambda_g/18$ shunt shorted stub with a Z_o of 64 Ω . Similar to the doubler circuit of the sensing repeater, an additional shunt shorted stub of an electrical length of $\lambda_g/9$ and Z_o of 64 Ω was added to fine tune the impedance match. The bias network is included in this design for measurement purposes only. Based on the ADS simulation, it was found that the

receive and transmit antennas should present an impedance of $67+j250 \Omega$ at 2.75 GHz and an impedance of $30+j160 \Omega$ at 5.5 GHz, respectively. The reference repeater reflection coefficients between the antennas and doubler circuit, as well as the radiation patterns, are similar to those of the sensing repeater. The variation over the receive antenna H-plane is 1 dB while it is 0.8 dB for the transmit antenna. The receive antenna peak gain is 1.8 dB with a simulated radiation efficiency of 94.5%. The peak gain and radiation efficiency of the transmit antenna are 2 dB and 98%, respectively. The reference repeater antennas have better gain and efficiency performance than those of the sensing repeater because of the relative increase in the occupied electrical size.

5.3 Transceiver Performance

The transceiver performance was characterized inside an anechoic chamber using the same measurement setup shown in Figure 3.12. Figure 5.6 shows the measured and simulated CG performance for different input power levels and f_1 . The simulated CG of the entire repeater was calculated by adding the sum of antenna gains to the simulated CG curve of the multiplier alone. For an input power of -30 dBm, the CG maxima are -15.5 dB at f_1 of 2.4 GHz, and -15.7 dB at f_1 of 2.75 GHz. The 3 dB CG bandwidth is 2% and 1.25% at f_1 of 2.4 GHz and input powers of -20 dBm and -30 dBm, respectively. At f_1 of 2.75 GHz, the 3 dB CG bandwidth is ~2.5% for input powers of -20 dBm and -30 dBm. As seen in Figure 5.6 (right), the measured CG versus received power at f_1 of 2.4 GHz is well matched with the simulated curve while there is a difference between the measured and simulated curves at f_1 of 2.75 GHz at low power. This difference can be attributed to fabrication and assembly errors.

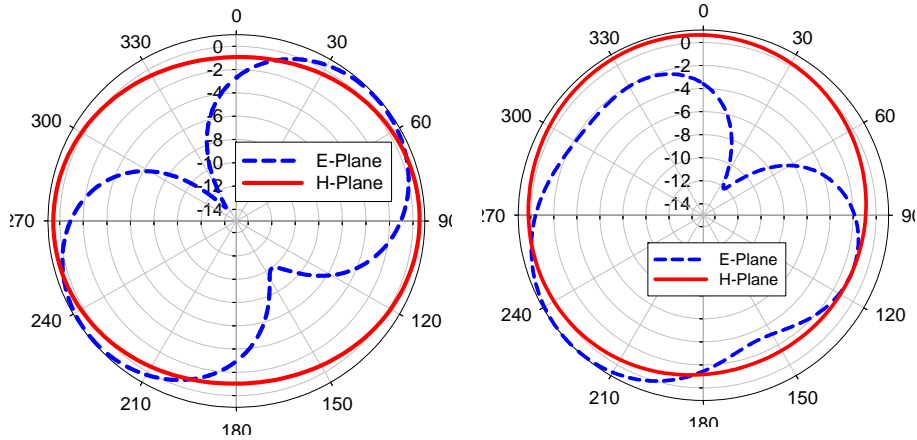


Figure 5.4: The simulated E- and H-plane radiation patterns of the sensing repeater receive antenna at 2.4 GHz (left) and transmit antenna at 4.8 GHz (right).

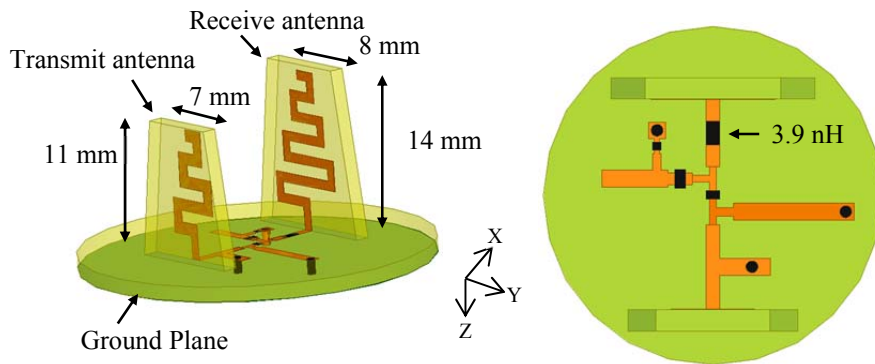


Figure 5.5: Illustration of the reference repeater, side view (left) and top view (right).

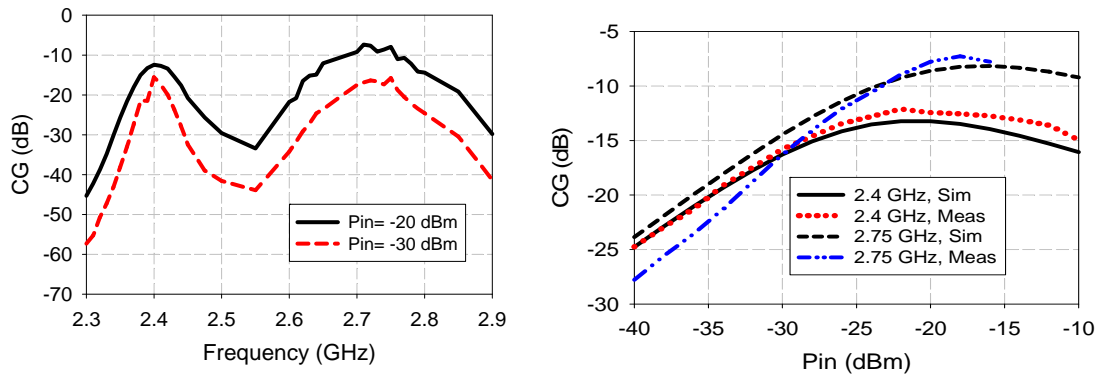


Figure 5.6: The measured CG of the dual-channel transceiver versus frequency for different received powers (left) and the simulated and measured CG versus received power at f_1 of 2.4 GHz and 2.75 GHz (right).

In order to determine the sensitivity of the transceiver to housing a sensor within the structure, full-wave simulations were performed that included a physical model for a commercial

piezo thin film vibration sensor (MiniSense 100NM from Measurement Specialties) as shown in Figure 5.7. The presence of the sensor causes a frequency shift of 10 MHz and 1% reduction in the radiation efficiency of the receive antenna and 1 dB increase in the gain variation over the transmit antenna H-plane. This degradation can be mitigated by re-optimizing the design while the sensor is included.

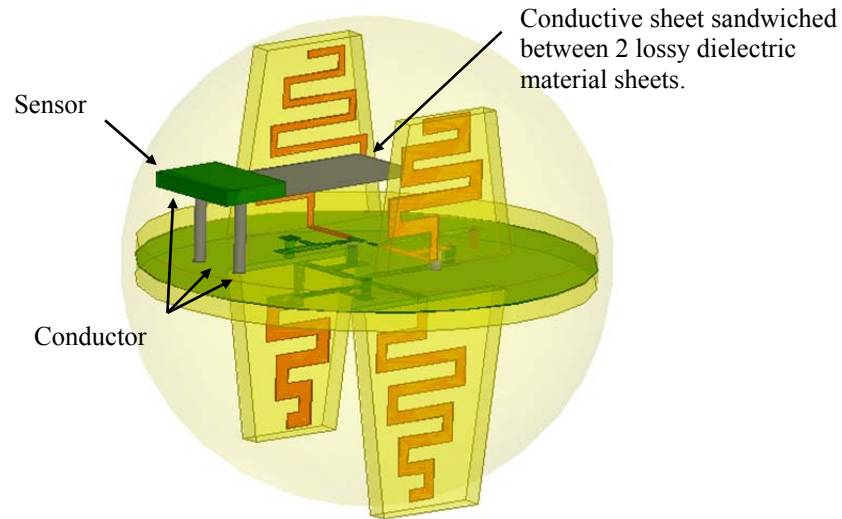


Figure 5.7: The dual-channel transceiver shown with an inserted sensor.

5.4 Transceivers Performance Comparison

Table 2.1 compares the transceivers presented in this dissertation and lists their measured parameters. Depending on the application and the sensor that will be used, each transceiver has some advantages and disadvantages compared to the other ones. The non-machined transceiver (presented in Chapter 3) provides the highest CG at lower RF input power which is beneficial in extending the communication range. It also has the widest CG bandwidth and is the simplest design. The machined transceiver is the smallest design with the lowest weight and has CG that is worse than the CG of the non-machined transceiver by 2 dB at RF power level of -30 dBm, however, the fabrication complexity is higher and the design reliability in real-world operating

conditions is lower compared to the non-machined transceiver. If the integrated sensor used requires channel calibration, the dual-channel transceiver provides the smallest size by having a built-in reference channel. In addition, if frequency coding is desired for the identification, the dual-channel transceiver has the potential to address the identification challenge and maximize the number of unique IDs. However, this transceiver is the most complex, the most costly, and requires the most fabrication time.

Table 5.1: Transceivers comparison and summary of the transceivers measured parameters

Parameter	Dual-Channel	Machined	Non-Machined
CG (dB), $P_{in} = -20$ dBm	-12.45	-10.2	-9.25
CG (dB), $P_{in} = -30$ dBm	-15.5	-15.3	-13.3
3 dB CG BW%, $P_{in} = -20$ dBm	2	2.5	3.2
3 dB CG BW%, $P_{in} = -30$ dBm	1.25	1.8	2.6
Size (λ)	0.25	0.16	0.24
Fabrication complexity, cost, fabrication time	Highest	Medium	Lowest
Weight	Highest	Lowest	Medium

Table 5.2 shows a comparison of the maximum CG, operating power, and electrical size of the presented transceiver designs and other harmonic repeater tags from the literature. As seen, the proposed designs show better CG with similar overall electrical occupied volume. As discussed before, the ability to integrate a sensing capability has also been a focus of this work that is distinct from some of the previously presented harmonic tags. In addition, unlike the previously reported designs, the proposed designs have a 3D miniature form factor that is readily adapted to different packaging requirements. Furthermore, the presented designs have omni- (versus uni-) directional interrogation capability.

Table 5.2: Comparison of the CG and electrical size with others from literature

	Max CG (dB)	RF Power (dBm)	Size (λ)	f_i (GHz)
Dual-channel Transceiver	-7.2	-18	0.28	2.75
Dual-channel Transceiver	-12	-22	0.25	2.4
Non-machined Transceiver	-8.4	-20	0.24	2.4
Machined Transceiver	-9.8	-18	0.16	2.4
[23]	-11	-41	0.265	5.9
[57]	-13.7	-15.53	0.25	1.3
[58]	-35.4	-19.5	0.24	1.3

The transceiver efficiency enhancement is significant because it increases the detection range, which is needed for embedded remote monitoring applications. Figure 5.8 illustrates the relationship between the receive and transmit antennas radiation efficiency and the expected communication range using a 43 dBm EIRP transmitter and 10 dB gain receiver. In these calculations, it was assumed that the minimum detectable signal is -120 dBm and both of the transceiver receive and transmit antennas have similar radiation efficiency. As seen, the use of antennas with radiation efficiency of 50% compared to 90% results in a decrease in the interrogation range by 27%.

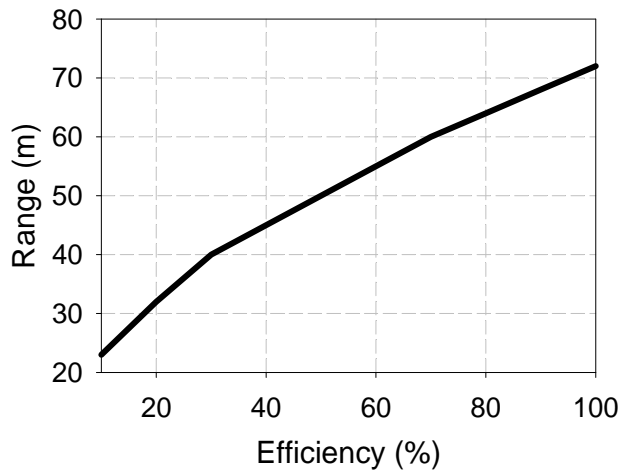


Figure 5.8: The expected communication range for different antenna radiation efficiency.

5.5 Remote Channel Calibration

Calibration of the propagation channel becomes a practical challenge for the implementation of a long-range passive embedded monitoring system. Such calibration is required when the exact characteristics of the interrogator-node link are unknown or vary with time. When the signal that is returned from the sensing repeater changes slowly over time, as would occur for a temperature sensor, the reference repeater can be used to provide a constant signal level to compare with the sensor activity. For the sensors that provide a relatively high frequency modulated return signal, the reference signal can be used to ensure that the node is operable and to determine the location of the node. For both of these scenarios, the reference signal can also be used to identify the node as will be discussed in Section 5.5.

Two new approaches for remote calibration are proposed in this work. The first approach [112] includes the use of two, single-channel, orthogonally-polarized nodes that are in close proximity and operate as a single unit; one of the nodes has no local stimulus and is referred to as the reference node, while the second node operates as the sensing node and has the local stimulus (DC bias in this demonstration) connected to the diode multiplier. For this demonstration the transceiver design presented in Chapter 3 is used. To minimize the coupling between the transceivers and distortion in their radiation patterns, one of the transceivers is placed in the radiation pattern null of the other. Through simulation and experimental testing it was found that a separation distance of 8 mm between the nodes resulted in minimal change in the performance of either transceiver relative to the single, isolated node performance.

The measurement setup used to perform the remote calibration is shown in Figure 5.9. This test was conducted in an anechoic environment to illustrate the ability of the approach to provide a channel calibration. The transmit and receive interrogator antennas are linearly

polarized, and were rotated to interrogate either transceiver #1 (sensor node) or transceiver #2 (reference node).

Figure 5.10 shows the measured return signal power level from the two transceivers for different bias voltages applied to transceiver #1. As expected, transceiver #2 provides a stable reference signal level that changes by less than 1 dB whereas transceiver #1's return varies > 20 dB as the bias on transceiver #1 changes. In practice (i.e., when sensors are deployed in the field), the transceiver #2 response would be subtracted from the measured transceiver #1 response to provide a calibrated sensor reading.

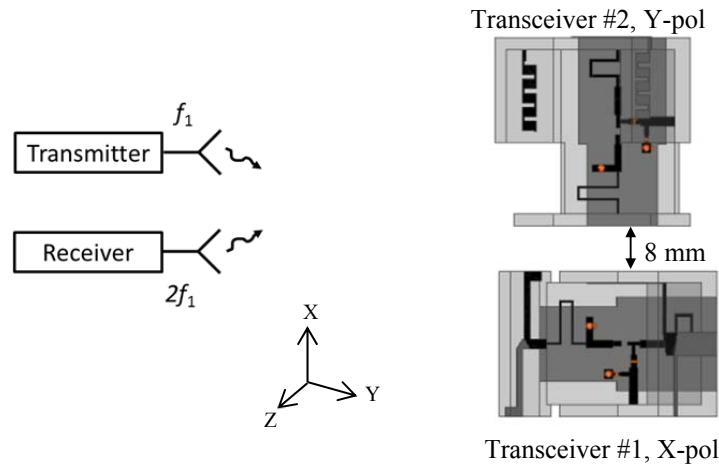


Figure 5.9: The measurement setup used to perform the remote channel calibration.

The dynamic range of this calibration approach is limited by the cross-polarization isolation between the reference and sensing nodes, and magnitude of the sensor-generated DC voltage. As provided in Section 3.3, the measured cross-polarization isolation is ~30 dB, and Figure 3.16 shows that the CG of the sensor transceiver will drop by 30 dB with 0.2V applied DC bias. Consequently, a sensed stimulus that created more than 0.2V DC bias would result in a return signal that could not be distinguished from the unintended signal returned from the reference transceiver.

In order to avoid varying the interrogation signal polarization and the use of two separate nodes, the second remote calibration approach is proposed. This approach is based on varying the interrogation signal frequency to interrogate the sensing repeater then the reference repeater of the dual-channel transceiver. Figure 5.11 (right) illustrates the measured return power level at f_1 of 2.4 GHz and f_1 of 2.75 GHz for different applied bias voltage to the sensing repeater and different received power. This measurement was performed as illustrated in Figure 5.11 (left). As seen, when interrogating the transceiver with a signal frequency of 2.75 GHz, the reference repeater provides a nearly constant return signal at $2 \cdot f_1$ of 5.5 GHz that is unaffected by the bias on the sensing repeater; the variation of the 5.5 GHz signal amplitude is only +/- 0.5 dB and +/- 0.3 dB for RF input power of -20 and -30 dBm, respectively. Conversely, interrogating the transceiver with a signal frequency f_1 of 2.4 GHz provides a return signal at $2 \cdot f_1$ of 4.8 GHz that is highly sensitive to the applied DC voltage; 0.1 V bias decreases the return signal by > 16 dB. By subtracting the amplitude of the 5.5 GHz return signal from the 4.8 GHz return signal, the modulated return signal can be corrected for channel effects. This difference between the return signal from the reference and sensing repeaters is referred to as ΔP_r .

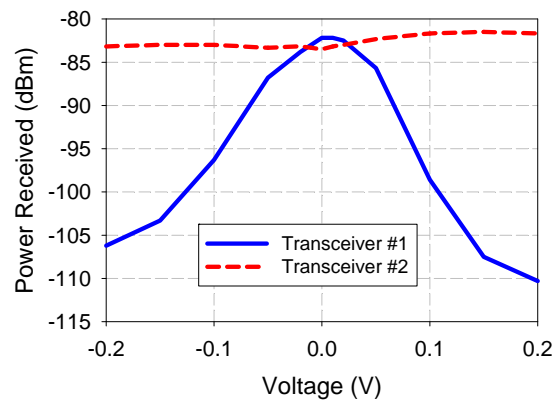


Figure 5.10: The measured received power level from the transceivers versus bias voltage at -30 dBm input power and f_1 of 2.4 GHz.

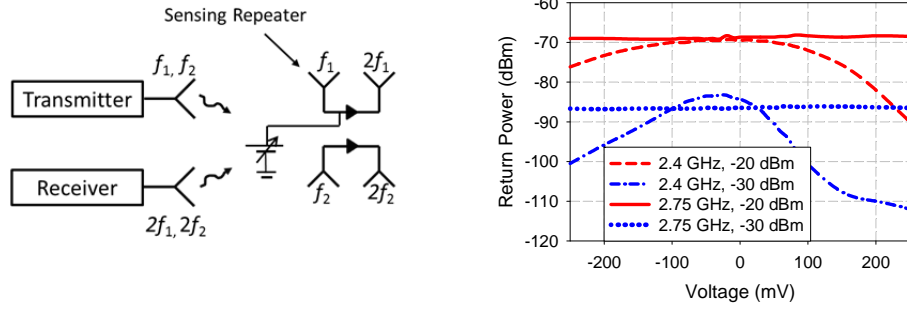


Figure 5.11: Illustration of the calibration measurement setup (left) and the measured return power for different f_1 versus bias voltage applied to the sensing repeater at -30 dBm input power (right).

Since the H-plane radiation patterns at the sensing and reference repeater frequencies have a gain difference that changes versus angle, the calibrated sensor reading can have uncertainty. That is, in addition to the sensor activity, ΔP_r will vary depending on the angle of incidence (ϕ) of the interrogation signal which may not be known to high accuracy. Based on the simulated radiation patterns, the maximum ΔP_r variation (δP_r) at 0 V bias versus angle is found to be ~ 2.2 dB for RF input power of -20 dBm and -30 dBm (Figure 5.12 right). Using the data in Figure 5.11 (right), δP_r can be superimposed on ΔP_r to determine the corresponding variation that would be found in the extracted value of the sensor-provided voltage (Figure 5.12 (left)). For sensors that generate voltage between 60-200 mV, the maximum voltage variation is 5 mV and 6.5 mV for RF input power of -30 dBm and -20 dBm, respectively. This variation assumes that the angle of incidence may vary between 0° and 360° , however, in an actual application the angular uncertainty may be much less than 45° . For simplification, it was assumed in this assessment that the sensor provides only positive voltages.

5.6 Node Identification

A method for identifying individual nodes, when no or very limited signal processing is possible at the node, is investigated in this section. Different approaches can be used to address

this challenge, such as introducing time or phase delay between the nodes or through frequency diversity. Due to potentially severe multi-path propagation environments, however, the frequency diversity method is more viable for embedded sensing. In the proposed dual-channel transceiver, identification can be performed if a unique design frequency is chosen for the reference repeater of each node; in operation, the interrogation frequency can be swept until the return signal peaks and the node is identified. Given the narrowband characteristics of the nodes, the identification signal from the interrogator is easily isolated from the sensor activity. Furthermore, both the reference and sensing repeater frequencies can be selectable which squares the number of unique node identifications (IDs). The use of high Q filters to further reduce the CG bandwidth of the repeater would noticeably degrade the CG efficiency.

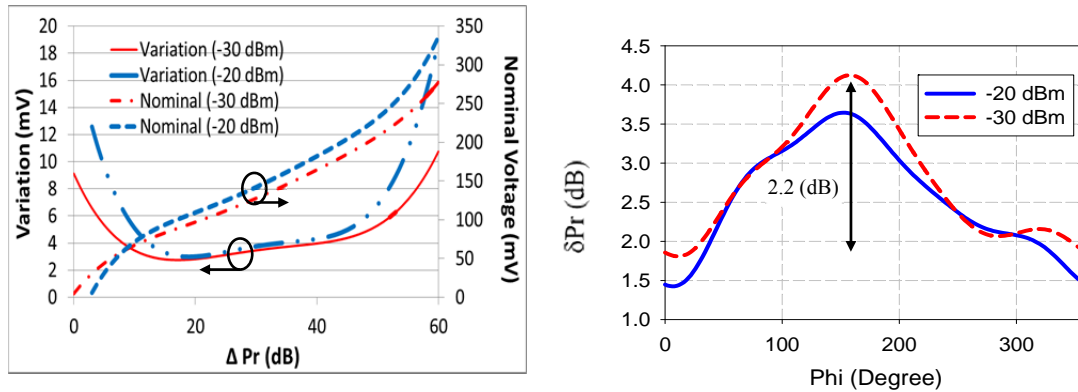


Figure 5.12: The variation in extracted sensor voltage versus ΔP_r for different received power due to angle of incidence uncertainty (left) and δP_r for different azimuth angle and received power at 0 V bias (right).

One approach that can further increase the ID count without affecting performance is to combine polarization and frequency diversity. The antennas used in the proposed transceiver design are linearly polarized, and when deployed adjacent nodes can be oriented to have a given amount of polarization mismatch. A conservative estimate is that 5 dB of mismatch would be sufficient to distinguish between adjacent nodes. Due to the non-linear CG versus power slope,

the measured co-pol to cross-pol ratio was found to be at least 40 dB; therefore, polarization diversity can increase the number of IDs by a factor of 8.

Table 5.3 provides the expected number of IDs assuming the interrogator operating bandwidth is 2-3 GHz and the amplitude isolation between the nodes is required to be 5 dB. As shown, by changing the node polarization and the reference repeater frequency, the number of nodes is 48 and 56 for RF power levels of -20 dBm and -30 dBm received at the node, respectively. These numbers are calculated using the interrogator bandwidth divided by the repeater bandwidth (both in MHz) multiplied by 8 for the polarization diversity factor; cases with < 200 MHz separation between the sensing and reference frequencies were excluded. Changing both the reference and sensing repeater operating frequencies and the polarization will increase the number of IDs to 768 and 2112 for RF power levels of -20 dBm and -30 dBm, respectively. Employing frequency diversity to both channels has the additional significant benefit of allowing different nodes located within the interrogator beam angle to be identified, thus overcoming the limitations on the distance between the deployed nodes, interrogation distance, and interrogator antenna design (directivity, beam width and size).

Table 5.3: Number of node IDs using a 2-3 GHz interrogator for different RF power levels (with polarization diversity)

	-20 dBm	-30 dBm
5 dB CG BW (sensing repeater)	5%	3.2%
5 dB CG BW (reference repeater)	3%	1.6%
Min no. of nodes, changing reference repeater frequency	48	56
Min no. of nodes, changing sensing and reference repeater frequency	768	2112

5.7 Embedding Impact

In this section a preliminary study of the impact of embedding the proposed dual-channel transceiver in a sand environment is presented. Figure 5.13 illustrates the experimental setup that was used which is identical to the setup shown in Figure 3.17. During the measurement, the transceiver was oriented to achieve the maximum CG. The CG maxima occurred at shifted f_1 frequencies of 2.39 GHz and 2.72 GHz with similar bandwidths to what was measured in air; the frequency shifts can be corrected for by optimizing the design to operate in a sand environment. The embedding also caused degradation in the CG by 1 dB (at 2.39 GHz) and 6 dB (at 2.72 GHz) for -20 dBm input power; the degradation was approximately 2 dB higher at each frequency for -30 dBm input power. This degradation is due to attenuation through the sand layer and the frequency shift that causes differences in the impedance match conditions, and for these reasons the degradation at 2.72 GHz is much higher. In addition, the embedding experiment illustrated a decrease in the co-pol to cross-pol isolation by 8 dB. This decrease is due to signal diffraction at the air/sand interfaces and multi-path reflections of the experiment setup.

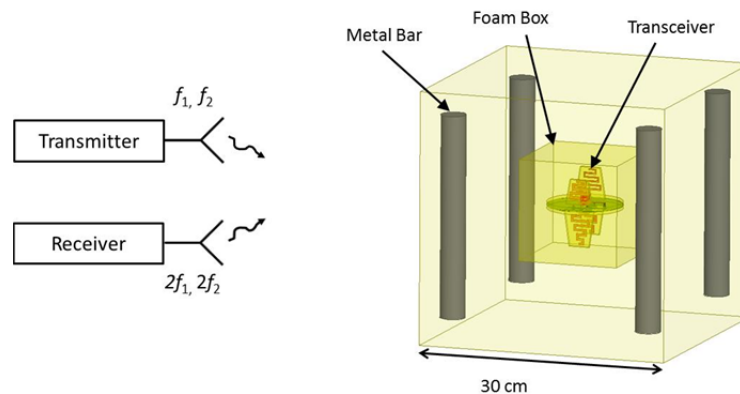


Figure 5.13: Illustration of the embedding experimental setup. Note: the figure is not drawn to scale.

The effect of the surrounding medium on the frequency of the CG maxima and the polarization of the return signal will cause uncertainty in the node ID, and will require the

frequency spacing and polarization mismatch level between the IDs to be larger. For certain sensing environments where the multi-path and interference levels are high, difficulties in the proposed remote channel calibration approach will also be introduced. In such environments, if the frequency difference between the transceiver channels is large, the difference in the channel loss at each frequency can be difficult to estimate and more extensive analysis will be needed to calibrate the propagation channel.

5.8 Conclusion

This chapter presented the development of a completely passive, compact, 3-D integrated dual-channel transceiver for the purpose of narrow-band, long-range, wireless sensing. The presented design has built-in remote channel calibration and node identification capabilities, which makes it distinct from previously presented transceiver. It has shown the ability to effectively modulate the return signal and is insensitive to sensor electronics placement within its structure.

Two new approaches for remote calibration have been also proposed to enable the determination of path loss between the interrogator and the remote node. In addition, the passive node identification issue has been investigated. The identification can be addressed by employing frequency diversity and polarization diversity. Employing these approaches in combination resulted in reasonable IDs number. The impact of embedding the proposed transceiver in a sand environment was studied. The experimental results revealed that the embedding has minimal impact on the CG efficiency and the operating frequency, however, limitations to the proposed identification method and the remote channel calibration approach were introduced.

A comparison between the presented transceivers and with other designs from the literature was presented in this chapter. Each transceiver shows advantages and disadvantages over the other designs. The comparison with others from literature shows that the presented designs outperform previously published designs on the combined basis of conversion efficiency, communication range, and total node volume. In addition, the presented transceivers are advantageous in terms of having a 3D miniature form factor that is readily adapted to different packaging requirements and having omni-directional interrogation capability.

CHAPTER 6 : 3-D PRINTED ANTENNAS AND SENSOR NODE

Note to Reader

Portions of this section have been previously published in [124], and have been reproduced with permission from IEEE. Permission is included in Appendix A.

6.1 Introduction

In this chapter, we show the advantages of the use of digital additive manufacturing (DAM) and 3-D printing technologies in the design of electrically-small 3-D antennas and compact 3-D sensor nodes. The use of these advanced manufacturing technologies enables the realization of low-cost, light-weight, efficient 3-D RF devices with improved manufacturing reliability and repeatability.

Two 3-D small antennas and a 3-D compact sensor node fabricated with additive manufacturing and 3-D printing are presented herein. The first antenna is fabricated with the stereolithography (SLA) process for an operational frequency of 2.45 GHz. Its measured 10 dB RL BW and gain are 3.75% and -0.5 dBi, respectively. The antenna fits in a sphere of radius $\lambda/8.6$ and weighs 1.4 g. The second antenna is fabricated with fused deposition modeling (FDM) for an operational frequency of 2.4 GHz. The measured 10 dB return loss bandwidth and gain are 3.6% and 1.72 dBi, respectively. This antenna fits inside a $\lambda/10.5$ radius sphere and weighs 0.5 g. Both of these designs are compared to prototypes fabricated with the PCB technology.

The 3-D compact sensor is fabricated with the fused deposition method and 3-D conformal printing. The design of the node is similar to the dual-channel transceiver presented in Chapter 5, which consists of two harmonic repeaters. The first (sensing) repeater operates by receiving a 2.4 GHz signal and re-radiating a 4.8 GHz modulated return signal, while the second (reference) repeater is designed to receive a 2.7 GHz signal and re-radiates a 5.4 GHz return signal. The 3-D printed sensor node fits inside a sphere of radius of 15 mm ($\lambda/8.3$ at 2.4 GHz) and weighs 2.5 g. The simulated maximum conversion efficiency of the reference and sensing repeater is 5.9% and 3.2%, respectively.

In the following sections, the design, testing, and analysis of the 3-D antennas and sensor node are presented. Section 6.2 illustrates the 3-D antennas design and Section 6.3 describes the design and analysis of the sensor node.

6.2 3-D Small Antennas Fabricated with DAM

6.2.1 SLA Cube Antenna

In this section, a half-wave dipole antenna designed on a cube configuration and fabricated using the stereolithography method is presented. The antenna design approach has been originally demonstrated using the PCB fabrication method at 2.4 GHz [114]. The design is based on the meandered line dipole antenna [125], fabricated on two sides of the cube and connected to a balun on a third side, Figure 6.1. A comparison of the experimental results of the two prototypes is given in this section.

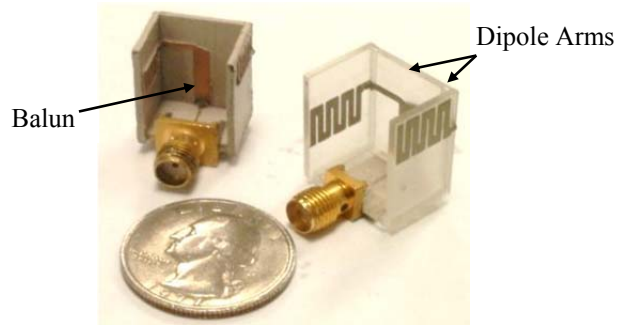


Figure 6.1: The fabricated cube antennas using PCB (left) and stereolithography (right) fabrication methods.

a) Antenna Design and Fabrication

The cube antenna design is illustrated in Figure 6.2. The antenna consists of a half-wave dipole conformed onto three sides of the cube and connected to a balanced-to-unbalanced line transition on the central side. The end of the dipole arms are meandered for miniaturizing the size and wrapped around the cube sides in a symmetric manner to preserve the balanced current distribution on the dipole arms. The antenna is fed from the inner bottom cube surface by a 50Ω microstrip line and a $\lambda_g/6$ 130Ω matching line. The parallel plate balun characteristic impedance is 53Ω . The antenna was designed using *Ansoft HFSS 11* to operate at 2.45 GHz. The SLA substrate material has a nominal relative dielectric constant (ϵ_r) of 3.5, loss tangent ($\tan\delta$) of 0.0446, and a thickness of 50 mils. The antenna dimensions are listed in Table 6.1.

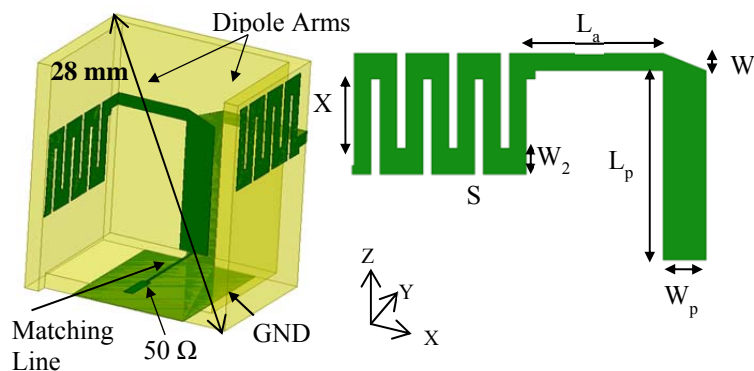


Figure 6.2: The SLA antenna design.

Table 6.1: The SLA antenna dimensions in mm

L_a	6.25	50 Ω line length	3
W_a	1	50 Ω line width	0.8
L_p	11	X_1	4
W_p	2.5	W	1
S	0.5	W_2	1.5
Ground Length	12.3	Ground Width	10
Matching line width	0.2	Matching line length	8

The antenna was fabricated at the W.M. Keck Center at the University of Texas at El Paso using the stereolithography process. Stereolithography is an additive manufacturing process that uses dispensing coupled with an ultraviolet (UV) light to build and cure parts in a layer-by-layer manner. It has the capability of creating arbitrary 3-D microwave structures with improved reliability and fabrication repeatability [6]. However, the material choice is limited and the currently available materials are lossy, relative to the other commercial microwave substrates (e.g. those from Rogers Corporation). The silver paste conductive traces were patterned using micro-dispensing. For the comparison with the PCB design, the substrate material used is Rogers/RT Duroid 6010 which has ϵ_r of 10.2 and $\tan\delta$ of 0.0023 with a thickness of 50 mils.

b) Experimental Results

The simulated and measured S_{11} for the PCB and SLA antenna designs are compared in Figure 6.3. The data are matched for the PCB design while there is a deviation of 40 MHz between predicted and measured results with the SLA design. This deviation could be attributed to soldering errors in attaching the coaxial connector and deviation in the dielectric constant of the SLA material. It is also shown that the SLA 10 dB RL BW has increased by a factor of 1.8, relative to the PCB design. The bandwidth enhancement is related to the increase in the antenna

size, the lower dielectric constant of the SLA material, and the increased dielectric and conductor loss.

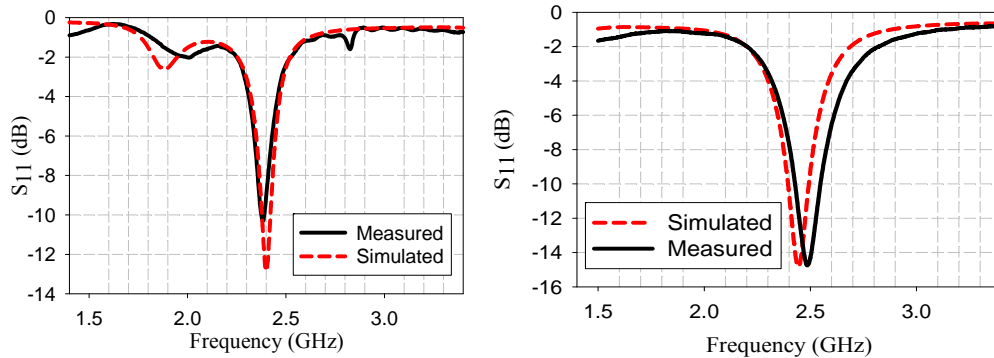


Figure 6.3: The measured and simulated S_{11} for the PCB design (left) and the SLA design (right).

Figure 6.4 shows the measured E- and H-plane radiation patterns for the two designs. The antennas are linearly polarized in the horizontal direction (x-axis), relative to the coordinate system in Figure 6.2. The E-plane tests were performed by rotating the antennas in the azimuth plane from 0° to 360° at an elevation angle of 0° in the XZ-plane. For the H-plane pattern the antennas were rotated along the YZ-plane. The SLA design radiation patterns are normalized to the PCB design patterns. As seen, there is approximately a 2.5 dB decrease in the gain with the SLA design. It was verified through simulation that this decrease is due to the dielectric loss of the SLA material. The variation over the H-plane is due to diffraction from the substrate material and reflection from the ground plane. The two designs demonstrate similar omni-directional patterns with the maximum radiation occurring broadside to the non-meandered portions of the dipole arms.

The measured and simulated antenna parameters for the PCB and the SLA designs at the resonant frequency are listed in Table 6.2. As seen, there is a good match between the measured and simulated data for the PCB and the first SLA design. The data shows that using the SLA

material results in a decrease in the peak gain by 2.5 dB, increase in the return loss bandwidth by a factor of 1.8, and increase in the electrical size by a factor of 1.3.

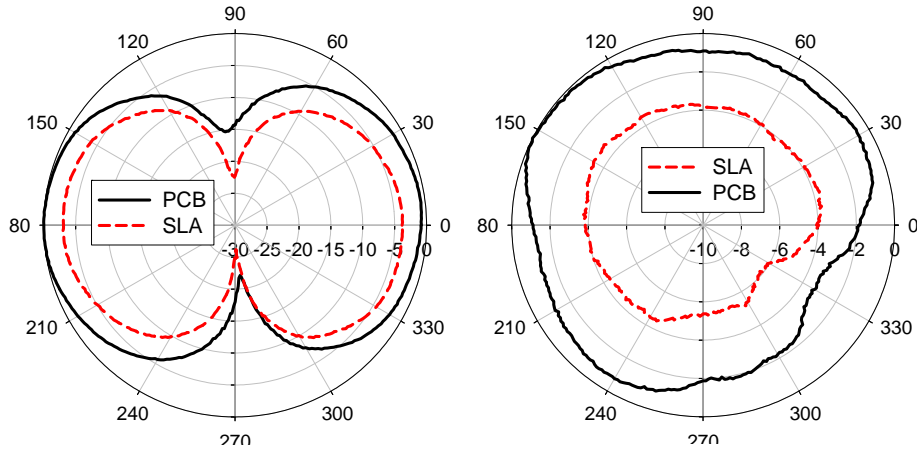


Figure 6.4: Comparison between measured E-plane (left) and H-plane (right) radiation patterns for the SLA and the PCB designs.

Table 6.2: Measured and simulated antenna parameters for the SLA and PCB antennas

Parameter	SLA	PCB [114]
Simulated Directivity	1.5	1.6
Measured 10 dB RL BW (%)	3.75	2
Simulated 10 dB RL BW (%)	3.5	1.9
Measured Peak Gain (dBi)	-0.5	2
Simulated Peak Gain (dBi)	-1	1.37
Weight (g)	1.4	2.4
ka	0.73	0.55

6.2.2 FDM Cube Antenna

In this section, a high efficiency, electrically-small, light-weight, 3-D machined-substrate antenna is presented [126]. The antenna is a half-wave dipole antenna conformed into a cubical shape and fabricated with a hybrid between the FDM and 3-D printing methods, Figure 6.5. This approach has been originally demonstrated using the PCB fabrication method in [127]. A

comparison of the experimental results of the FDM and PCB prototypes and other 3-D antenna designs from the literature is given here.



Figure 6.5: A photograph of the 3-D machined substrate cube antenna fabricated with the FDM process (left) and fabricated with the PCB technology (right).

a) Antenna Design and Fabrication

Figure 6.6 illustrates the FDM antenna design. The antenna is a half-wave dipole conformed into a cubical shape. The dipole arms are loaded with sinusoidal meandered sections to miniaturize the size and oriented in a clock wise/counter clock wise manner to preserve the balanced current distribution on the feed. The feeding network consists of a $\lambda_g/25$ 96Ω microstrip line and a $\lambda_g/5$ meandered microstrip line on the upper surface of the bottom of the cube, and a parallel plate transformer rising vertically along one side. The characteristic impedance of the meandered microstrip line and the parallel plate transformer is 148Ω and 83Ω , respectively. The antenna was designed using *Ansoft HFSS 14* to operate at 2.4 GHz.

One of the advantages of the FDM and 3-D printing methods is the reduction in material use, since they are additive approaches. Unlike the design presented in Section 6.2.1, the substrate material surrounding the antenna and between the meandered sections is unnecessary; only the material that supports the conductive traces is required, Figure 6.6. This approach enables gain and efficiency improvement and size decrease as has been demonstrated in Chapter 4 and will be shown in the experimental results.

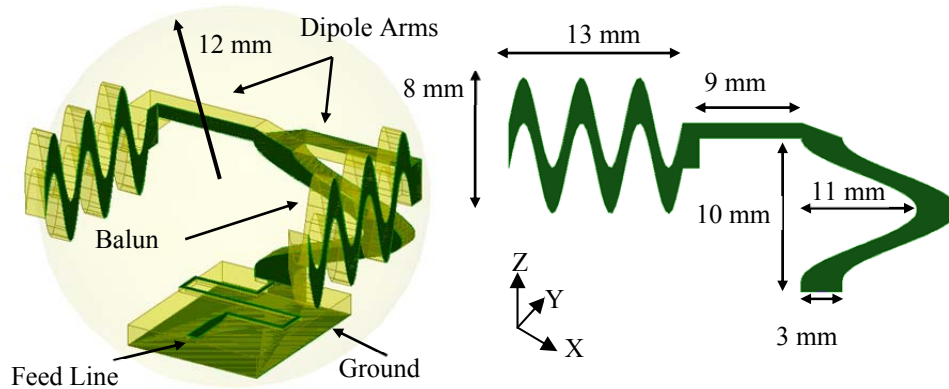


Figure 6.6: A CAD illustration of the proposed FDM cube antenna.

The substrate material was built using a Dimension SST 768 3D Printer at the College of Engineering of the University of South Florida. The printer uses FDM, which is a common 3D printing method that extrudes liquefied thermoplastic material through a heated nozzle to deposit layers as fine as 0.178 mm. The range of material is limited by the need to extrude the material into a coil prior to printing. In this work the substrate material used is Acrylonitrile Butadiene Styrene plus (ABSplus) with a thickness of 60 mils. The ABS material has good impact resistance, toughness, and electrical properties that are comparable to the commercial microwave laminates, however, printing the ABS material using the FDM process usually results in a poor surface smoothness that can limit the minimum realized trace width. This issue is mitigated in this work by depositing a channel for the thin conductive traces to guide the silver ink flow. The electrical properties were measured using a thin sheet tester from Damaskos Inc. and the material is found to have a nominal relative dielectric constant (ϵ_r) of ~ 2.4 and loss tangent ($\tan\delta$) of ~ 0.0038 at 2.4 GHz, Figure 6.7. The antenna was then metalized, with thick film silver ink (Dupont CB-028), using the nScript 3D-450 which uses micro-dispensing and is a form of direct print additive manufacturing (DPAM) [128]. Unlike conventional dispensing, it is capable of printing 20 μm wide traces at a speed of 500 mm per second over a conformal surface with a wide range of materials, from 1 centipoise (cps) to 1,000,000 cps.

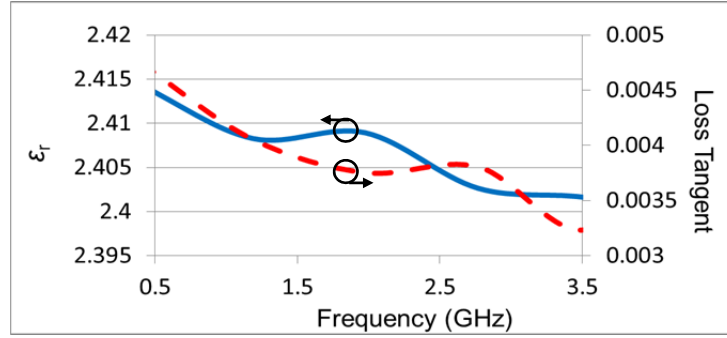


Figure 6.7: The measured dielectric constant (ϵ_r) and loss tangent of the ABS material for different frequencies.

b) Experimental Results

Figure 6.8 (left) compares the simulated and measured S_{11} of the presented design. As seen, the data are well matched. The simulated and measured 10 dB return loss (RL) bandwidth (BW) is 3.4% and 3.6%, respectively. Figure 6.8 (right) shows the measured E- and H-plane radiation patterns. The antenna is linearly polarized in the horizontal direction (x-axis), relative to the coordinate system in Figure 6.6, with a measured co-pol to cross-pol ratio of 23 dB. As seen in Figure 6.8 (right), the antenna exhibits omni-directionality in the H-plane with a measured variation of 2.4 dB. The maximum radiation occurs broadside to the non-meandered sections of the dipole arms with a measured peak gain of 1.72 dBi.

Table 6.3 summarizes the presented antenna parameters at 2.4 GHz. For comparison sake, the parameters of a similar PCB prototype are also listed. The PCB design is a similar 3-D antenna that uses Rogers/RT Duroid 6010 which has ϵ_r of 10.2 and $\tan\delta$ of 0.0023 with a thickness of 50 mils and was fabricated using a milling machine and assembled manually. Comparing the presented design to the PCB design shows efficiency decrease of ~21%, size increase by 20%, bandwidth improvement of 33%, and weight reduction of 60%. The major reason for the efficiency degradation is the very low conductivity of the used silver ink material

compared to the copper material used with the PCB design (less by a factor of ~29). Using silver ink material with conductivity similar to copper improves the efficiency by 14%.

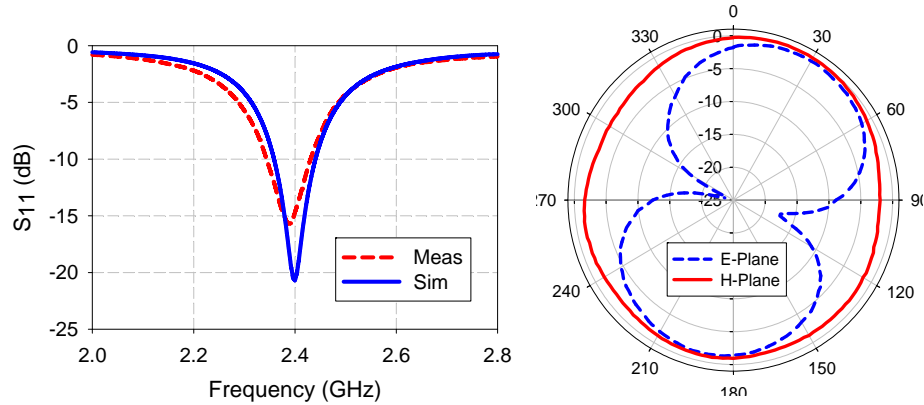


Figure 6.8: The simulated and measured S_{11} of the presented FDM antenna design (left) and the measured E-plane and H-plane radiation patterns (right).

Table 6.3: Measured and simulated FDM and PCB antenna parameters.

Parameter	FDM	Machined PCB [127]
Simulated Directivity	1.6	1.62
Measured 10 dB RL BW (%)	3.6	2.7
Simulated 10 dB RL BW (%)	3.3	2.85
Measured G (dBi)	1.5	2.5
Simulated G (dBi)	1	2
Simulated Efficiency (%)	76.5	98
Weight (g)	0.5	1.3
ka	0.6	0.5

Figure 6.9 compares the gain over quality factor ratio (G/Q) for the designs presented in this work, different 3-D designs fabricated with different process from the literature, and the G/Q ratio limit. The G/Q limit was calculated using $G=1.5$ and the expression for the minimum radiation Q for a linearly polarized antenna given in Eqn. 2.3. The G/Q ratio was calculated for each of the presented designs based on the maximum gain and the Q at the frequency of operation. This comparison shows that the FDM cube antenna presented in this section has

performance that is similar to the PCB machined substrate antenna [127] and the 4-arm spherical helix antenna presented in [129], and better performance than the printed spherical antenna presented in [130], the SLA cube antenna, the PCB cube [114], and the cube antenna with foldable liquid crystal polymer substrate (LCP) [131].

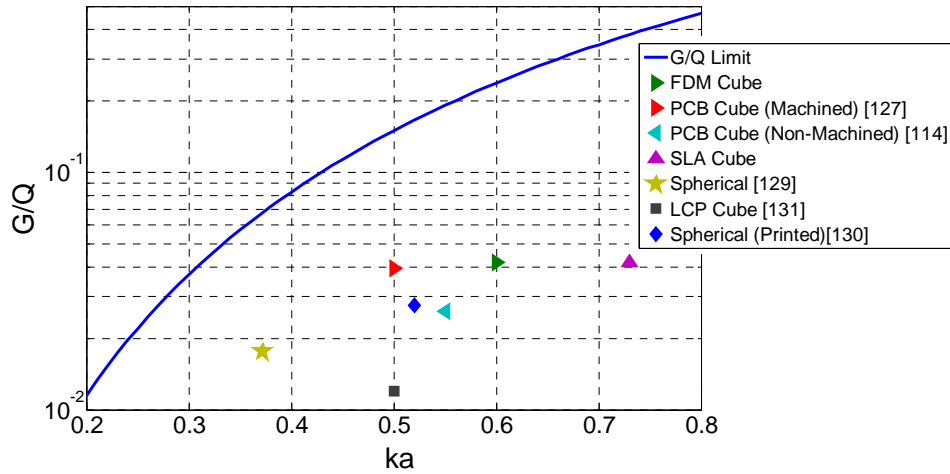


Figure 6.9: Comparison of G/Q ratio of the presented antenna designs and other miniaturized antennas.

6.3 3-D Dual-Channel Sensor Node Fabricated with DAM

As mentioned in Section 6.1, the proposed 3-D printed transceiver design is similar to the design presented in Chapter 5. It consists of two harmonic repeaters, one used for sensing and one used to provide a reference signal. Each harmonic repeater consists of a frequency doubler and meandered monopole receive and transmit antennas printed on curved substrate surfaces. The doubler uses a GaAs Schottky diode (Agilent HSCH-9161). The antennas were designed using HFSS 15 and the frequency doubler was designed using ADS 2009u1. The substrate material was built using the Dimension SST 768 3D Printer at the College of Engineering of the University of South Florida and then metalized, with Dupont CB028, using the nScript 3D-450 machine.

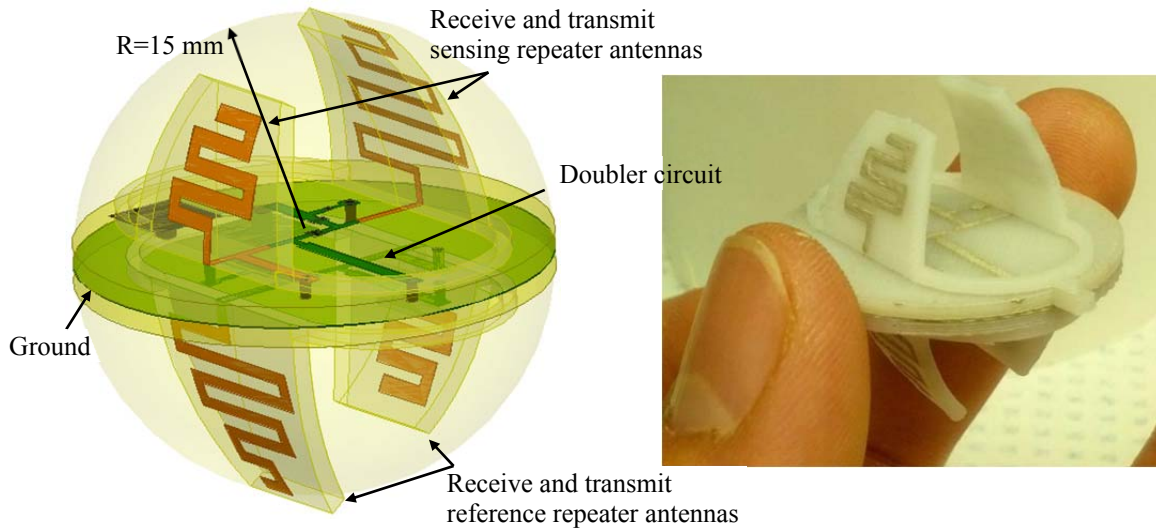


Figure 6.10: A CAD view of the printed 3-D dual channel node with a hypothetical sphere of 15 mm radius (left) and a photograph of the fabricated node (right).

6.3.1 The 2.4/4.8 GHz Sensing Repeater

Figure 6.11 illustrates the sensing repeater design. The receive antenna is fed by a microstrip line (ML) on the top surface of the round base with a characteristic impedance (Z_0) of 110Ω and electrical length of $\lambda_g/19$. While the transmit antenna is fed by a ML with a length of $\lambda_g/9.6$ and Z_0 of 108Ω and a $\lambda_g/6.6$ shunt shorted stub with a Z_0 of 93.5Ω . Figure 6.11 (right) shows the doubler circuit. The bias network consists of a 36 nH series inductor (Coilcraft 0402) and 8.2 pF shunt capacitor (Johanson 0201). Based on the ADS simulation, the receive and transmit antennas should present an impedance of $80+j364 \Omega$ at 2.4 GHz and an impedance of $34+j230 \Omega$ at 4.8 GHz , respectively, to provide the best CG at -30 dBm input power. To fine tune the impedance match, a $\lambda_g/4.8$ 93.5Ω shunt shorted tuning stub was added to the doubler circuit. Although the permittivity of the ABS material used for this design is lower than the permittivity of the design presented in Chapter 5 by a factor of 2.6, the occupied volume of the entire node is the same. The node size is maintained by meandering and patterning the antenna traces on curved substrate surfaces. Figure 6.12 shows the reflection coefficient between the

receive antenna and the doubler input, and the transmit antenna and the doubler output at -30 dBm input power. As seen, the antennas are well-matched to the doubler circuit.

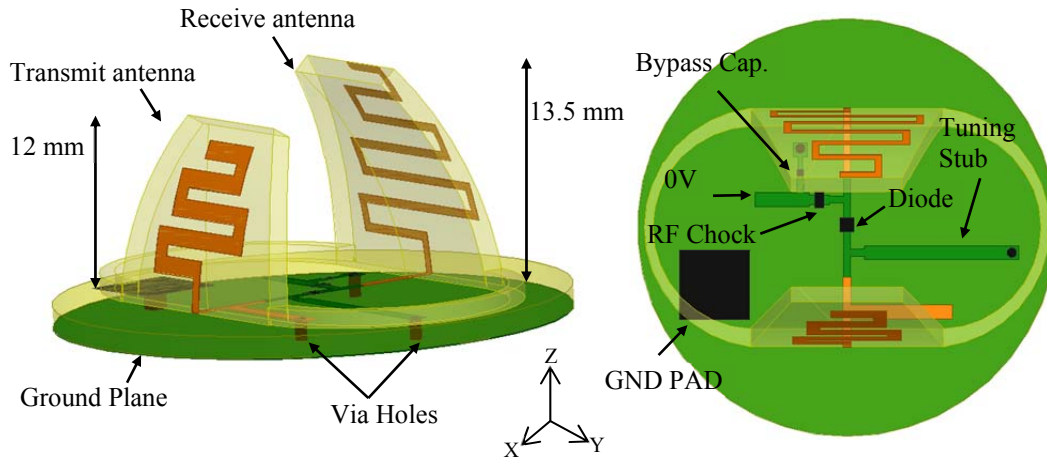


Figure 6.11: Illustration of the 3-D printed node sensing repeater, side view (left) and top view (right).

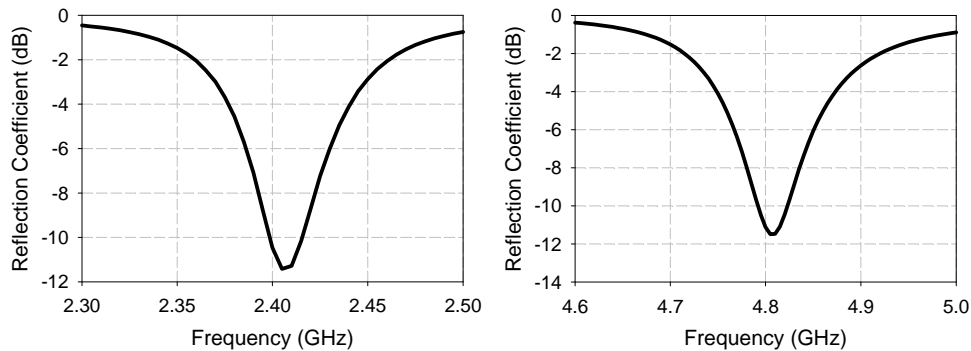


Figure 6.12: The simulated reflection coefficient between the receive antenna and the doubler input (left) and between the transmit antenna and the doubler output (right) of the 3-D printed node sensing repeater at -30 dBm input power and 0V bias.

Figure 6.13 shows the simulated radiation patterns of the receive and transmit antennas at 2.4 GHz and 4.8 GHz, respectively. The antennas are linearly polarized along the Z-axis, relative to the coordinate system shown in Figure 6.11. As seen the antennas demonstrate omnidirectional patterns in the XY-plane. The gain variation over the receive antenna H-plane is 1.3 dB while it is 2 dB for the transmit antenna. The receive antenna peak gain is -1.8 dBi with a simulated radiation efficiency of 44.5%. The peak gain and radiation efficiency of the transmit

antenna are 1.3 dB and 84%, respectively. Simulations have shown that using silver ink material with conductivity similar to copper improves the receive antenna efficiency by 30% and the transmit antenna efficiency by 14%.

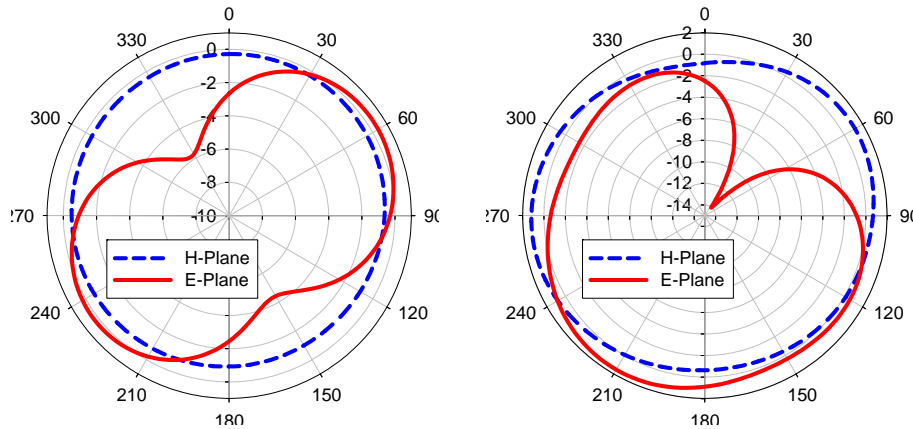


Figure 6.13: The simulated E-and H-plane radiation patterns of the 3-D printed node sensing repeater receive antenna at 2.4 GHz (left) and transmit antenna at 4.8 GHz (right).

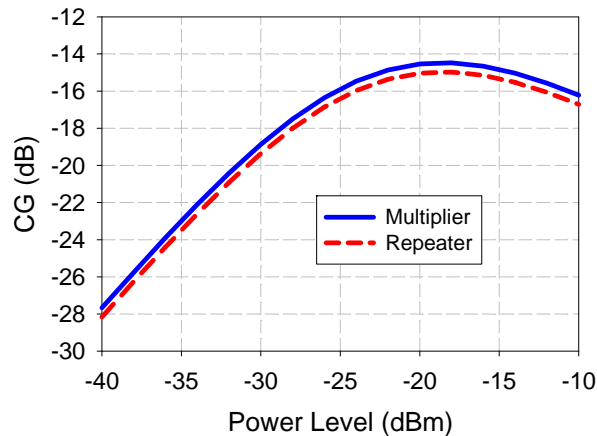


Figure 6.14: Simulated CG of the 3-D printed node sensing repeater and multiplier for different input power levels at f_i of 2.4 GHz.

Figure 6.14 shows the simulated CG of the doubler and the entire repeater at f_i of 2.4 GHz and different input power levels. The simulated CG of the entire repeater was calculated by adding the sum of antenna gains to the simulated CG curve of the multiplier alone. For an RF input power of -30 dBm, the CG is -19.4 dB. The CG peak value is -15 dB, occurs at RF power

level of -20 dBm. Compared to the sensing repeater presented in Chapter 5 the peak CG is degraded by 3 dB.

6.3.2 The 2.7/5.4 GHz Reference Repeater

Figure 6.15 illustrates the reference repeater. The receive 2.7 GHz antenna is fed by a $\lambda_g/21$ 101 Ω ML and the transmit 5.4 GHz antenna is fed by a $\lambda_g/8.4$ 100 Ω ML and a $\lambda_g/7.8$ shunt shorted stub with a Z_o of 93 Ω . Similar to the doubler circuit of the sensing repeater, an additional shunt shorted stub of an electrical length of $\lambda_g/5.25$ and Z_o of 93 Ω was added to fine tune the impedance match. To maximize the CG at RF input power of -30 dBm, the ADS simulation shows that the receive and transmit antennas should present an impedance of $70+j285 \Omega$ at 2.7 GHz and an impedance of $40+j230 \Omega$ at 5.4 GHz, respectively. The reference repeater reflection coefficients between the antennas and doubler circuit, as well as the radiation patterns, are similar to those of the sensing repeater (see Figure 6.16 and Figure 6.17). The variation over the receive antenna H-plane is 1 dB while it is 1.35 dB for the transmit antenna. The receive antenna peak gain is 0 dBi with a simulated radiation efficiency of 63%. The peak gain and radiation efficiency of the transmit antenna are 1.95 dBi and 81.4%, respectively.

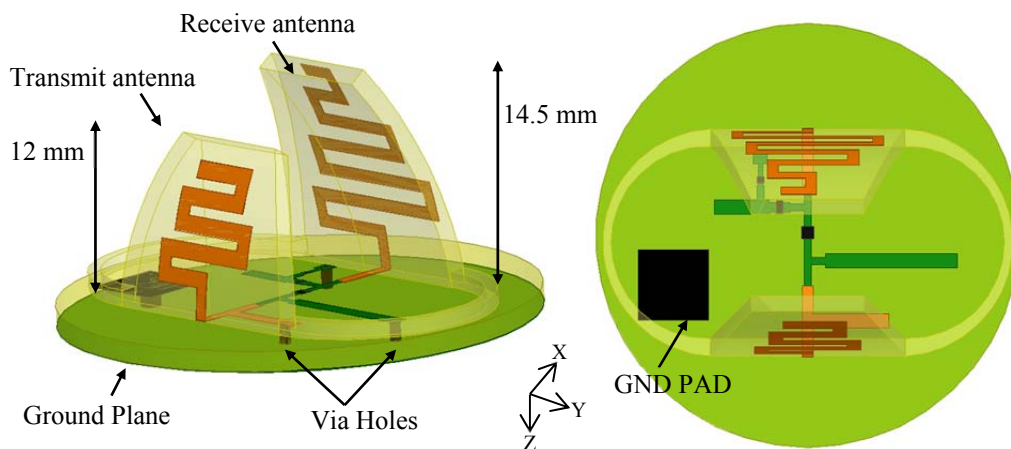


Figure 6.15: Illustration of the 3-D printed node reference repeater, side view (left) and top view (right).

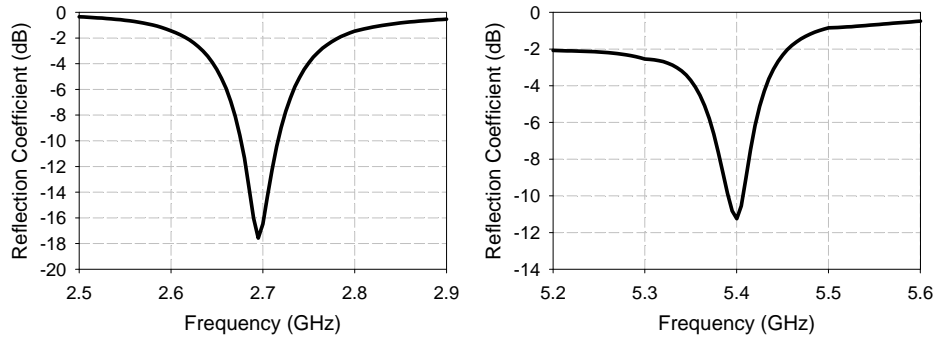


Figure 6.16: The simulated reflection coefficient between the receive antenna and the doubler input (left) and between the transmit antenna and the doubler output (right) of the 3-D printed node repeater at -30 dBm input power and 0V bias.

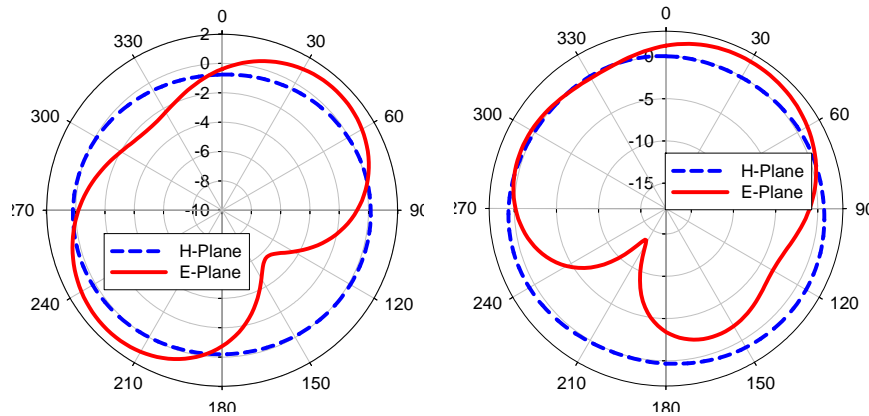


Figure 6.17: The simulated E- and H-plane radiation patterns of the 3-D printed node reference repeater receive antenna at 2.7 GHz (left) and transmit antenna at 5.4 GHz (right).

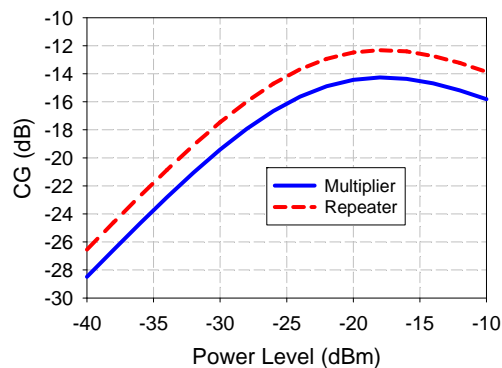


Figure 6.18: Simulated CG of the 3-D printed node reference repeater and multiplier for different input power levels at f_1 of 2.7 GHz.

The simulated CG of the doubler and the entire reference repeater at f_1 of 2.7 GHz and different input power levels are given in Figure 6.18. For an RF input power of -30 dBm, the CG

is -17.5 dB. The peak CG value is -12.3 dB, occurs at RF power level of -18 dBm. Compared to the reference repeater presented in Chapter 5, the CG is degraded by 4 dB.

6.4 Conclusions

Two 3-D cube antennas have been designed and fabricated using the additive manufacturing and micro-dispensing method. Good agreement is found between the expected and measured results for both of the designs. The first cube antenna substrate was fabricated using the stereolithography process. The SLA material has good surface smoothness that allows patterning small feature size traces, however, it has high dielectric loss. Due to the lossy material used, the antenna gain was decreased by 2.5 dB relative to the PCB version of the antenna that was made using low loss microwave laminate. Approaches to improve the SLA antenna performance include using grooved structures for feed lines and reducing the amount of the substrate material in the vicinity of the antenna. The second cube antenna was fabricated with the fused deposition modeling using the ABS material. The ABS material has good impact resistance, toughness, and electrical properties that are comparable to the commercial microwave laminates, however, printing the ABS material using the FDM process results in a poor surface smoothness that can limit the minimum realized trace width. This issue is mitigated in this work by depositing a channel for the thin conductive traces to guide the silver ink flow. A comparison with other designs from the literature fabricated with different processes shows that the presented FDM design compares well with the high efficiency electrically small antennas. This comparison also reveals that using FDM and 3-D printing is promising and high performance antennas can be realized with the currently available materials. The use of the advanced 3-D manufacturing methods addressed issues of design reliability and fabrication repeatability and significantly reduces the antenna weight.

A 3-D dual-channel passive transceiver has also been designed to be fabricated with the fused deposition modeling and conformal 3-D printing. The design of the node is similar to the dual-channel transceiver presented in Chapter 5. The simulated maximum conversion efficiency of the reference and sensing repeater is 5.9% and 3.2%, respectively. Compared to the design presented in Chapter 5, the weight is reduced by 67%, the occupied volume is similar, the peak CG of the reference repeater is reduced by 4 dB and the peak CG of the sensing repeater is degraded by 3 dB, and the mass production difficulty and the manual assembly of the design is improved. Using silver ink material with conductivity similar to copper improves the efficiency of the reference repeater by 2 dB and the sensing repeater by 3 dB.

CHAPTER 7 : DUAL-CHANNEL HARMONIC INTERROGATOR ANTENNA DESIGN

7.1 Introduction

An approach for the harmonic interrogator antenna design is to use a dual-channel antenna array, where one channel is used for transmission and the second channel is used for reception. The advantages of this approach are; 1) the high isolation between the receiving and transmitting channels, 2) the reduced number of components and complexity of the interrogator unit, and 3) the potential for smaller size compared to a single-channel broadband antenna.

In this chapter, two dual-channel harmonic interrogator antenna designs are presented. The first design contains two four-element circular patch antenna (CPA) arrays, one for reception and one for transmission. The transmitting channel array operates at 2.4 GHz with a measured 10 dB RL BW of 2% and the receiving channel array operates at 4.8 GHz with a measured 10 dB RL BW of 4.2%. The measured gain and HPBW of the transmitting and receiving arrays are 12.1 dBi and 40°, and 13 dBi and 35°, respectively. The FBR ratio of both of the arrays is greater than 33 dB. The integrated planar array is very low profile and has a size of $1.28 \lambda \times 1.28 \lambda \times \lambda/50$ at f_0 of 2.4 GHz and weight of 49.5 g. To miniaturize the CPA array, the 3-D printing technology can be used to print the patches on conformal curved substrate surface. Using this approach, the array occupied area and weight can be reduced by 14% at the expense of 2 dB gain degradation.

In order to provide the capability to interrogate various sensor nodes that operate at different frequencies, the second dual-channel interrogator antenna is designed based on an integrated two two-element quasi-Yagi dipole antenna (QYDA) arrays. The transmitting array is

designed to cover the 2-3 GHz frequency range (or 40% BW) and the receiving array covers the 4-6 GHz frequency range. To minimize the size, the antennas were designed to be rising vertically above the ground. The integrated QYDA array measures $0.7 \lambda \times 0.71 \lambda \times 0.42 \lambda$ at f_0 of 2 GHz and weights 16.3 g. The gains of the receiving and transmitting arrays vary over the frequency range between 8-9.5 dBi and 8-10.2 dBi, respectively. This gain variation is considered low compared to other broadband antennas. The FBR over the entire frequency range of both of the QYDA arrays is greater than 11 dB. The HPBW of the transmit array changes from 72° to 52° as the frequency changes from 2 to 3 GHz. For the receive array, it changes from 52° to 32° as the frequency changes from 4 to 6 GHz.

In order to expand the capability of the dual-channel interrogator array to have wider bandwidth, a broadband log-periodic dipole antenna (LPDA) array has been investigated. Only the transmitting channel LPDA array design is considered in this work. To reduce the size and weight of the LPDA array, the 3-D printing technology is used to shape the dipoles with a smooth sinusoidal curve and to deposit the dielectric material only to support the conductive parts. The printed antenna weighs 1.8 g and has gain > 4 dBi over the 2.25-3.75 GHz frequency range. It exhibits 17% size reduction with minimal gain degradation, compared to a standard LPDA array with similar bandwidth and number of elements.

In what follows, the design, testing, and analysis of the dual-channel arrays are presented. Section 7.2 discusses the CPA array design and Section 7.3 presents an approach for miniaturizing the CPA array using the 3-D printing. Section 7.4 illustrates the QYDA array design and Section 7.5 describes the design of the 3-D printed LPDA array.

7.2 Circular Patch Antenna (CPA) Array

7.2.1 CPA Array Design

The dual-channel microstrip patch antenna array is illustrated in Figure 7.1. Each array consists of four circular patch antennas (2×2 arrangement). A circular patch antenna can be treated as a circular cavity and it supports modes which are perpendicular to the patch [132], as with a rectangular microstrip antenna. The transmitting circular patch radius (R_1) is 22.5 mm and the receiving patch radius (R_2) is 11 mm, which are approximately $\lambda_g/4$. The substrate and ground plane radius (R_g) is 80 mm. The distance from the center of the 2.4 GHz patches to the center of the array (X_1) is 50 mm and the distance from the center of the 4.8 GHz patches to the center of the array (X_2) is 30 mm. X_1 and X_2 were optimized for the highest gain in the broadside direction. All of the array elements are fed in phase from the bottom using coaxial probes. The receive 4.8 GHz antennas and their feeds are rotated in the manner shown in Figure 7.1 to minimize the occupied area and ensure the alignment of the current polarization with the transmit antennas; all the antennas are horizontally polarized. The feed location is also optimized to match the input impedance to 50Ω . The substrate is an FDM printed ABS material with a thickness of 100 mils and the patches are printed with silver ink.

7.2.2 CPA Array Performance

Figure 7.2 illustrates the measured and simulated S_{11} of the receive and transmit array antennas. The deviation between the measured and simulated data is attributed to fabrication errors. As seen, the transmit antenna 10 dB RL BW is 2% and the receive antenna BW is 4.2%. The transmit antenna has wider BW due to the larger electrical thickness. Wider BW performance can be achieved by employing the multilayer and stacked-patch design approach

[133], aperture coupled design approach [134], and the L-probe feeding approach [135, 136]. Figure 7.3 shows the measured E-and H-plane radiation patterns of the receive and transmit antenna arrays. The measured transmit antenna gain is 12.1 dBi with a HPBW of 40° and FBR of 37 dB and the receive antenna gain is 13 dBi with a HPBW of 35° and FBR of 33 dB.

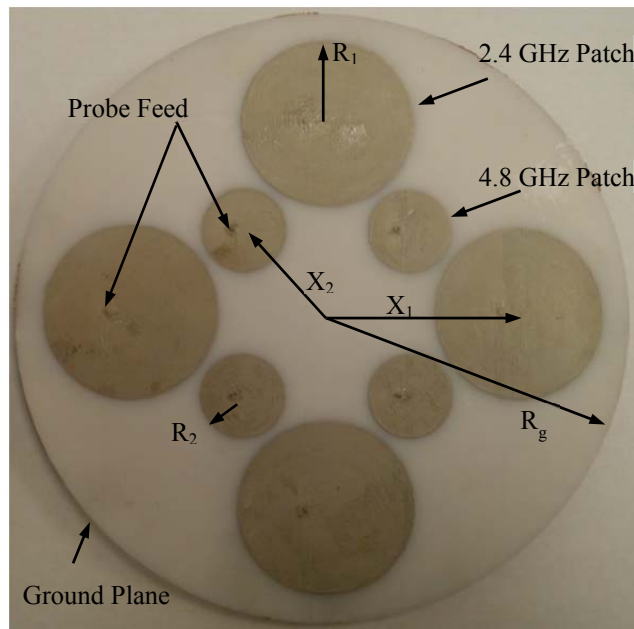


Figure 7.1: Illustration of the fabricated dual-channel circular patch antenna array.

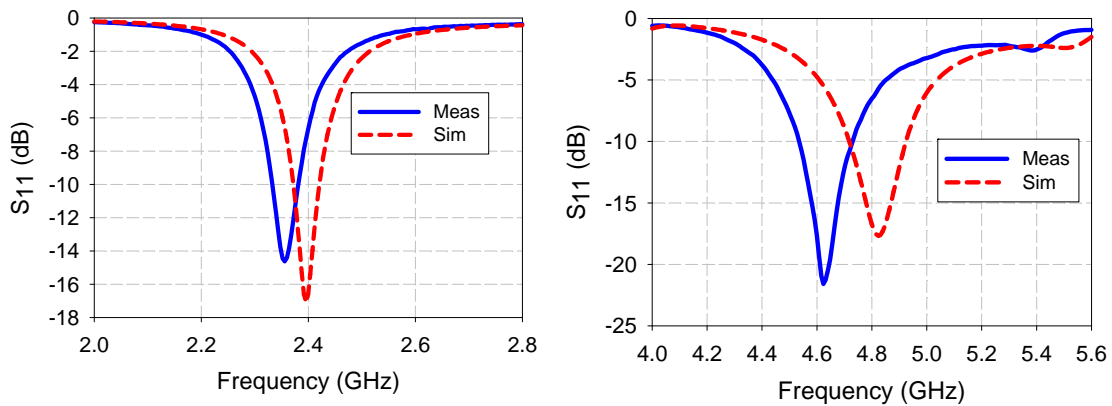


Figure 7.2: The simulated S_{11} of the transmit (left) and receive (right) CPA arrays.

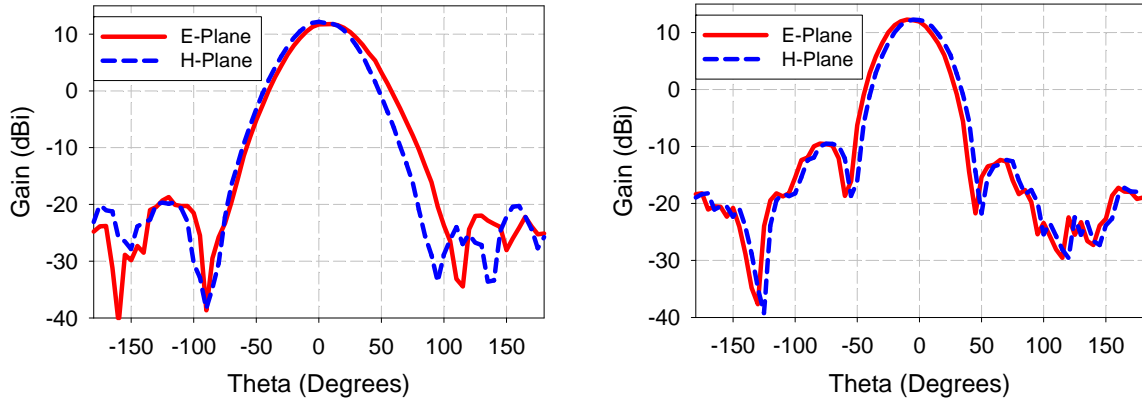


Figure 7.3: The measured E-and H-plane radiation patterns of the transmit CPA array at 2.4 GHz (left) and the receive CPA array at 4.8 GHz (right).

7.3 Miniaturization of the CPA Using Conformal 3-D Printing

Miniaturizing the size of the microstrip patch antenna is highly desirable for different applications. Methods for minimizing the patch antenna size include employing high-permittivity substrates and thick multilayer substrates [137], inserting slots into the patch [138], and loading the patch with shorting pins [139]. In this work, we miniaturized the patch by exploiting the capability of the 3-D printing technology in creating arbitrary 3-D structures with conformal surfaces. Instead of printing the antenna on a substrate with planar surfaces, the patch is printed on a conformal surface meandered in the vertical direction (Figure 7.4 left). The top surface of the substrate was meandered using a sine function ($\text{Height}(Z) = 1.5 \times \sin(0.5 \times \pi \times Z) \times \sin(0.5 \times \pi \times Z)$) to vary the substrate height between 50 and 100 mils. The substrate material and thickness are similar to the design presented in Section 7.2.1. To illustrate the effect of this approach, a regular patch antenna was also fabricated (Figure 7.4 right). Both of the antennas were designed to operate at 2.3 GHz. The circular patch radius is 19.5 mm, which is reduced by 14% compared to the regular patch.

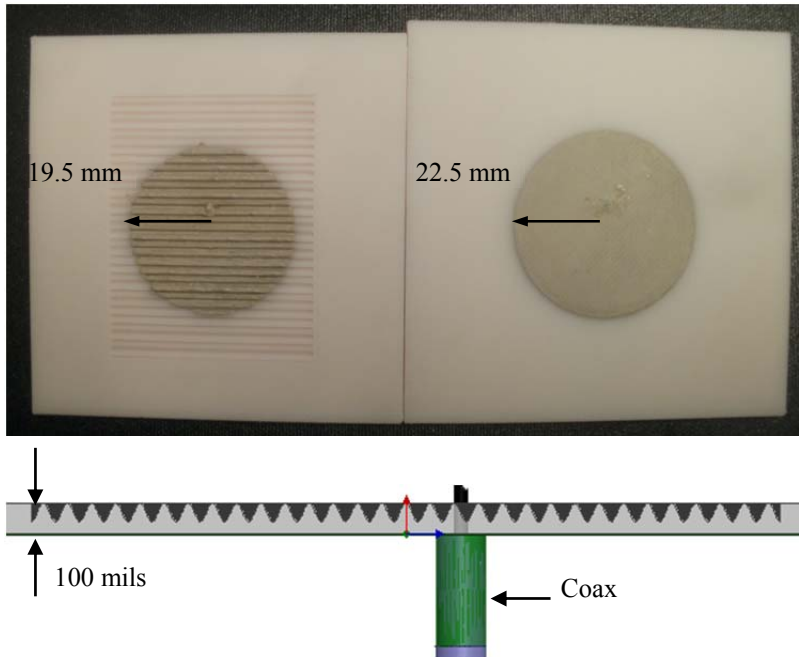


Figure 7.4: Illustration of the miniaturized (top-left) and regular (top-right) circular patch antennas and a side view of the miniaturized patch (bottom).

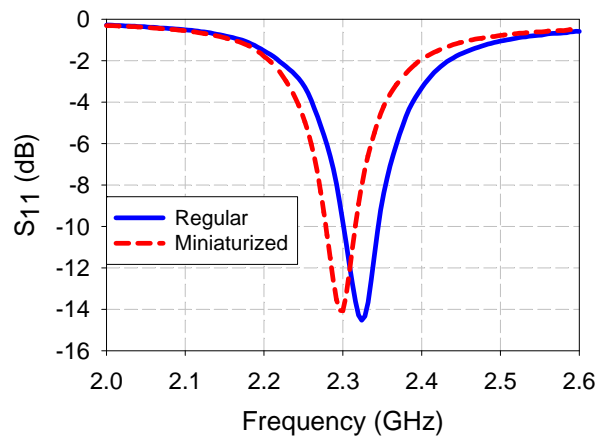


Figure 7.5: A comparison of the measured S_{11} of the miniaturized conformal patch antenna and the regular patch antenna.

A comparison between the measured S_{11} of the miniaturized conformal patch antenna and the regular patch is given in Figure 7.5. The 10 dB RL BW of the miniaturized antenna is 1.6%, which is reduced by 0.3% compared to the non-meandered patch. Figure 7.6 compares the measured E-and H-plane radiation patterns between the two antennas. The measured peak gain of the miniaturized conformal patch is 5 dBi, while it is 7.1 dBi for the antenna without

miniaturization (2.1 dB degradation). The measured HPBW of the regular and miniaturized patch is 70° and 80° , respectively.

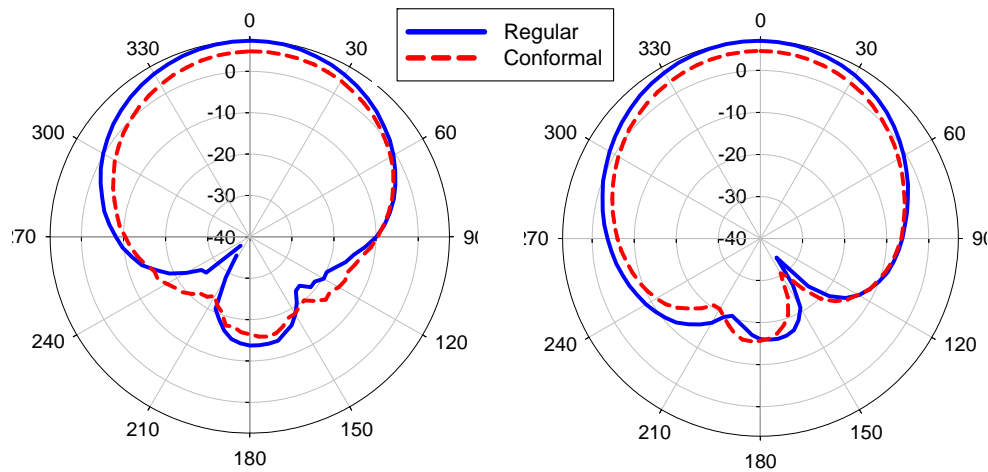


Figure 7.6: A comparison of the measured radiation patterns of the miniaturized and regular patch antenna; H-plane (left) and E-plane (right).

7.4 Quasi-Yagi Dipole Antenna (QYDA) Array

Figure 7.7 illustrates the two-element (2×1) quasi-Yagi dipole antenna array. Compared to the circular patch antenna array, this array has a 3-D structure and provides broadband characteristics and endfire radiation. The antenna element consists of a driver, a director, and a broadband microstrip to coplanar strip line (CPS) balun backed with a truncated ground plane. The array is fabricated on a 50 mils ABS substrate with metallization printed of silver ink. The following sections describe the balun design, antenna element design, and array performance.

7.4.1 Microstrip to Coplanar Strip Line Balun Design

The balun used to feed the dipole antenna with a balanced current is a microstrip to coplanar strip line (CPS) transition [140]. The balun operates by dividing the signal using a symmetric T-junction into two paths and delays the signal traveling on one path by 180 degrees. This balun serves also as an impedance transformer. The simulation of the balun was performed

using HFSS 14 by exciting two modes (even and odd mode) at the CPS side and one (even) mode at the microstrip line side. The odd mode represents the electric fields coupling between the adjacent strip lines and the even mode represents the coupling to the ground. The purpose of the balun simulation is to 1) minimize the insertion loss, 2) ensure the 180 degree phase delay between the adjacent strip lines, and 3) improve the impedance match over the desired frequency range. Figure 7.8 illustrates the balun dimensions of the receive and transmit antennas.

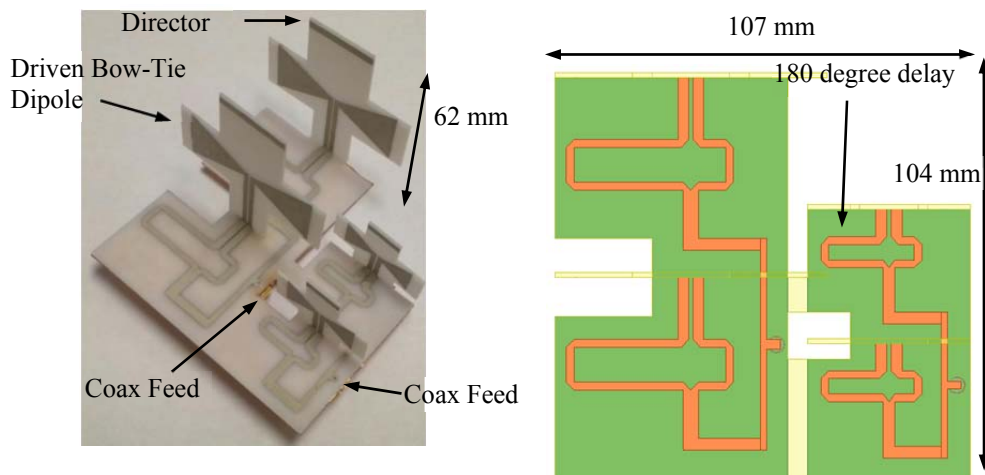


Figure 7.7: Illustration of the dual-channel quasi-Yagi bow-tie dipole antenna array; side view (left) and top view (right).

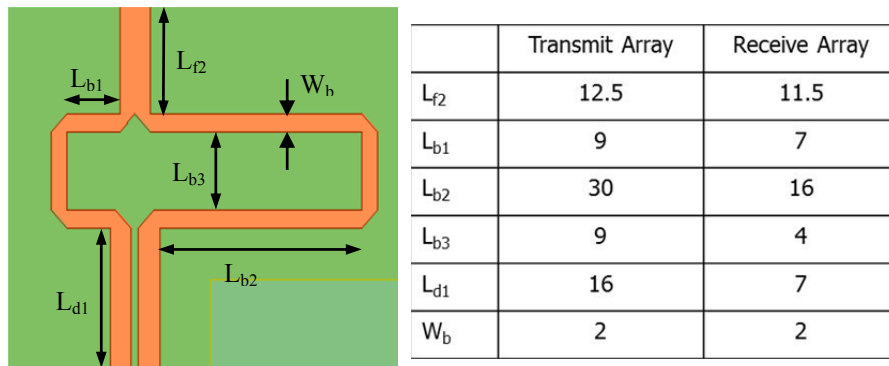


Figure 7.8: Illustration of the balun dimensions in mm.

Figure 7.9 shows the simulated S-parameters of the balun used for the transmit and receive antenna. S_{21} represents the forward transmission coefficient from the input terminal to

the CPS output terminal for the odd mode operation. As seen, the two baluns demonstrate good impedance match over the 2-3 GHz and 4-6 GHz frequency ranges, in reference to 50 Ω sources.

The loss over both of the balun sections is less than 1 dB over the entire frequency ranges.

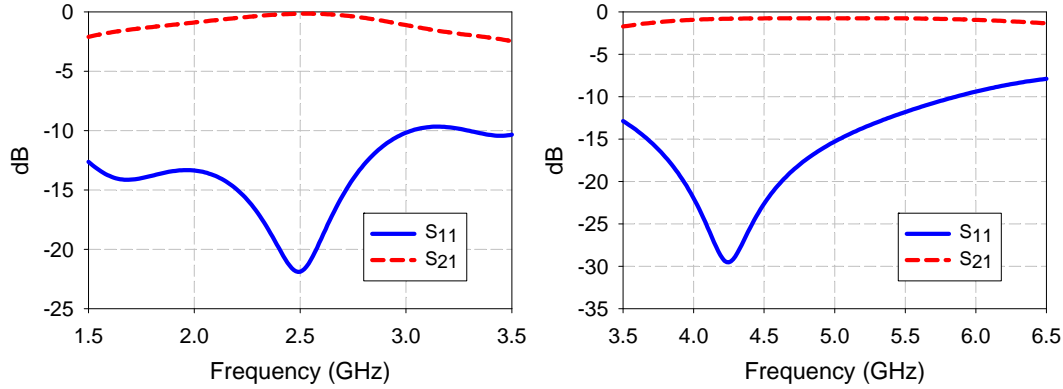


Figure 7.9: Simulated S-parameters of the baluns used to feed the quasi-Yagi dipole antenna arrays.

7.4.2 QYDA Element Design

The antenna element used in the array design is a quasi-Yagi bow-tie dipole (Figure 7.7). This antenna structure is used due to its endfire directional radiation pattern and broadband characteristics. The antenna consists of three parts; a reflector (truncated ground plane here), a driver element, and a director [141]. The driver element is a half wavelength resonator. The planar biconical shape purpose is to widen the impedance bandwidth [142] and the director enables the radiation to be focused in the endfire direction. The width of the director and its distance to the driver element also impacts the gain and impedance. For optimum gain, the length of the director and the distance to the driver should be $\sim\lambda/4$. Figure 7.10 illustrates the receive and transmit antenna dimensions.

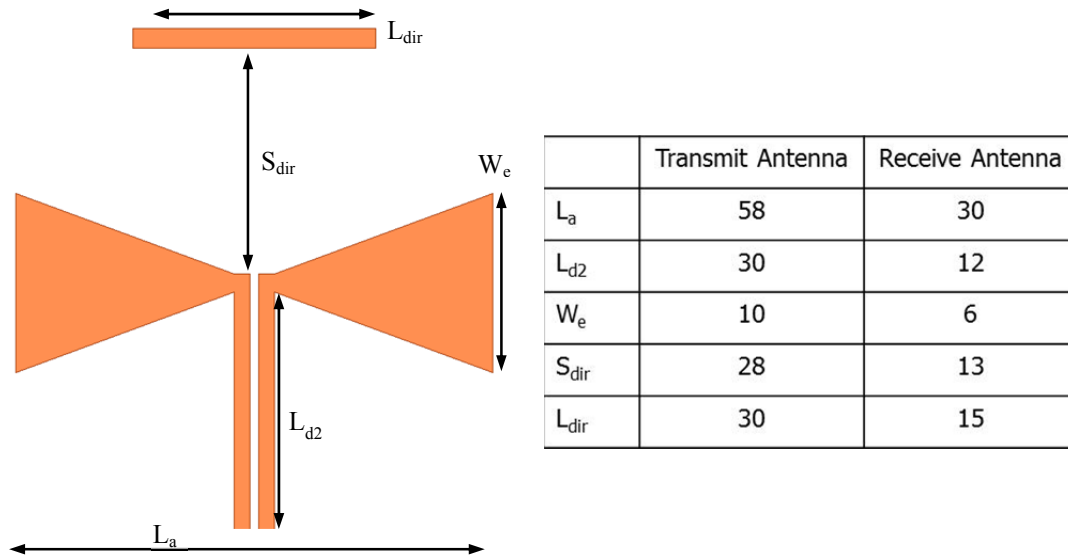


Figure 7.10: Illustration of the receive and transmit quasi-Yagi dipole antenna dimensions in mm.

7.4.3 QYDA Array Design

After designing the antenna elements, a two-element array is composed, see Figure 7.7. The antennas were designed to be rising vertically above the ground. This configuration is used to minimize the array occupied area and to have the main beam of both of the arrays directed in the same direction. The distance between the antennas of the transmit and receive arrays is $\sim \lambda/3$ at the lower frequency band.

Figure 7.11 shows the simulated S_{11} of the transmit and receive arrays. As seen, the antennas maintain good impedance match over the 2-3 GHz and 4-6 GHz frequency ranges. The simulated gain of both of the arrays over frequency is illustrated in Figure 7.12. The transmitting array maintains a gain greater than 8 dBi over the 2-3 GHz frequency range and the receiving array maintains a gain greater than 9 dBi over the 4.2-6 GHz range. The gain and impedance bandwidth of this antenna can be enhanced by using a wider bandwidth balun as those proposed in [143, 144, 145].

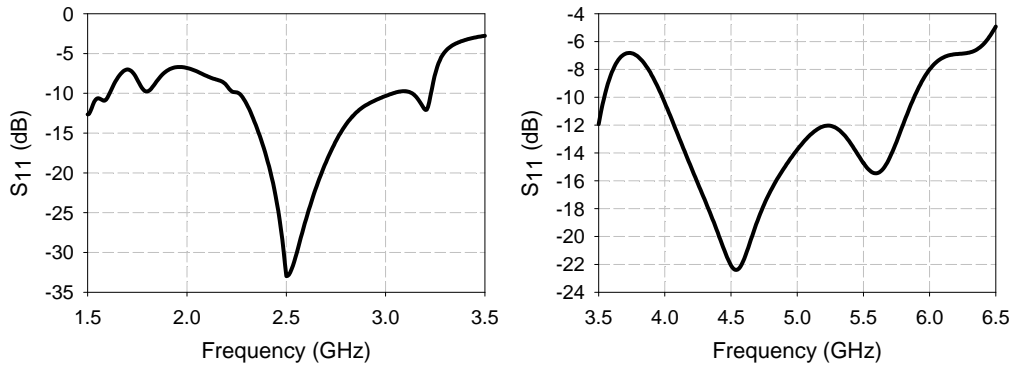


Figure 7.11: Simulated S_{11} of the dual-channel quasi-Yagi dipole antenna array; transmitting array (left), and receiving array (right).

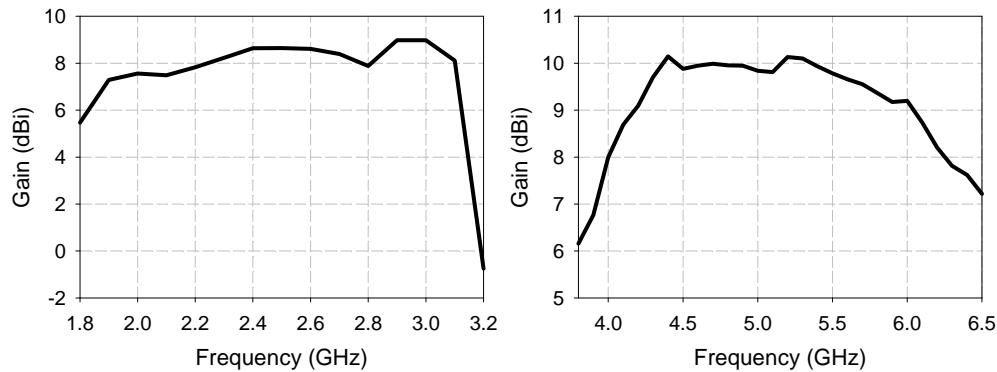


Figure 7.12: Simulated gain of the dual-channel quasi-Yagi dipole antenna array; transmitting array (left), and receiving array (right).

The E-and H-plane radiation patterns of the transmit array at different frequencies are illustrated in Figure 7.13. As seen, the radiation pattern is persistent over the entire frequency range. As the frequency changes from 2 to 3 GHz, the HPBW changes from 72° to 52° over the H-plane and the FBR changes from 9-15 dB. Figure 7.14 shows the simulated radiation patterns of the receive array. The HPBW changes from 52° to 32° as the frequency changes from 4 to 6 GHz. The FBR of the receive array is approximately 13 dB over the entire frequency range. It is worth mentioning here that simulations have shown that increasing the number of elements of the array from two to four using this configuration resulted in reducing the HPBW, however,

without a remarkable increase in the peak gain. This is attributed to the relatively wide beamwidth of the antenna element.

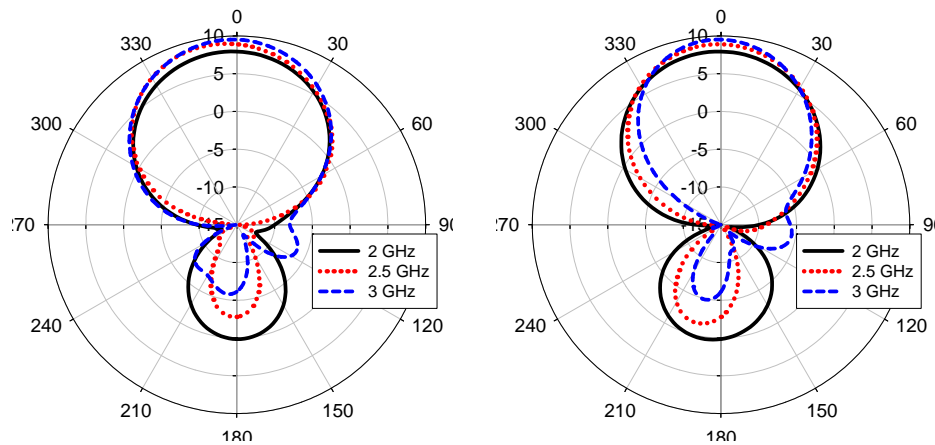


Figure 7.13: The simulated radiation patterns of the transmit antenna array at different frequencies; E-plane (left) and H-plane (right).

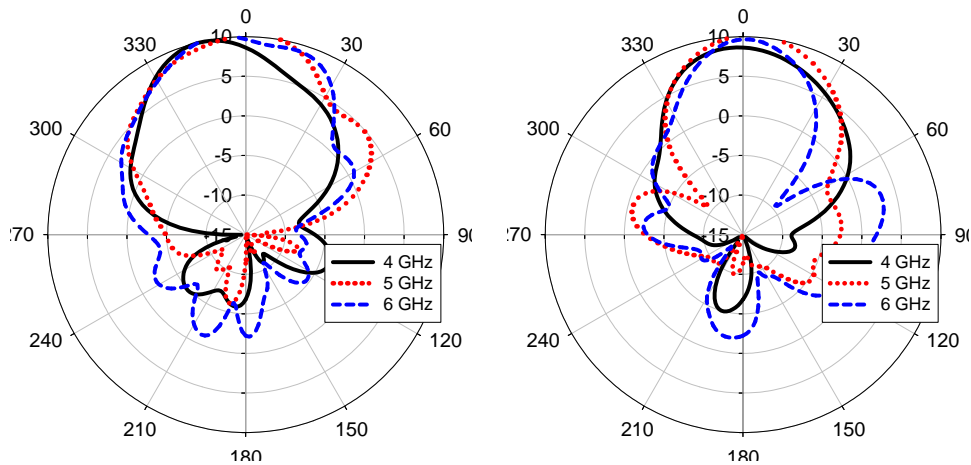


Figure 7.14: The simulated radiation patterns of the receive antenna array at different frequencies; E-plane (left) and H-plane (right).

7.5 Log-Periodic Dipole Antenna Array

Another candidate that can be used in the design of the dual-channel harmonic interrogator to improve the bandwidth is the log-periodic dipole antenna (LPDA) array [146]. This antenna is capable of providing a bandwidth of 2:1 with persistent radiation pattern. The LPDA also has high directivity with low cross-polarization ratio over wide frequency range. Due

to these radiation characteristics, this antenna is widely used for radio broadcasting and radar applications.

The LPDA array radiation mechanism is similar to the Yagi-Uda antenna, where some dipoles function as the driver, reflector, and director elements depending on the operating frequency and the elements electrical length [147]. The antenna can also be viewed as a series fed array of parallel dipoles. The length of the longest element determines the lowest frequency and the length of the shortest element determines the upper frequency limit. The gain and bandwidth of the array is mainly determined by the number of the dipoles used.

Reducing the LPDA array size and weight has been always of interest and various techniques to minimize the element length have been employed. The antenna size can be reduced by the use of high permittivity material, if the antenna is printed on a dielectric substrate, and by loading the dipoles with lumped reactive elements [148]. Another miniaturization technique has been proposed in [149] based on loading the dipoles with cylindrical hat covers. The most commonly used approach, however, is meandering the dipole length by the introduction of different shapes, such as the Koch-shaped lines [150], rectangular meandered lines [151], and algorithm-generated shapes [152].

In this work, we present a light-weight LPDA array fabricated with the 3-D printing technology. Using 3-D printing the dipole length is reduced by shaping the arms with a smooth sinusoidal curve and the weight is reduced by machining the substrate. The dielectric substrate is only used to support the conductive part. Figure 7.15 illustrates the 3-D printed LPDA array. The antenna is designed to cover the 2-4 GHz frequency range. The number of the elements (N) used in this work is 7 and the ratio between the elements length, width, and spacing (K) is designed to be 0.8. The spacing factor (σ) is selected to be 0.15. The width and length of the longest dipole is

selected to be 4 mm and 70 mm ($\sim\lambda/2$ at 2 GHz), respectively. The arms are meandered in the vertical direction using a sinusoidal curve ($2.5 \times \sin(0.1 \times \pi \times Z) \times \sin(0.1 \times \pi \times Z)$, where Z is the height) to vary the height of the arms between 0 and 2.5 mm. The dipoles are series fed with a parallel plate transmission line with a width optimized to be 2 mm for better impedance match. To improve the impedance matching, a shunt shorted stub is added at the end of the feed line. For measurement purpose, a coaxial feed line is added, Figure 7.15. The coaxial line is running over the lower plate of the feed line conductor, and the coaxial center pin conductor is attached to the upper plate of the feed line printed on top. This feeding technique ensures balanced currents on the dipole arms [146].

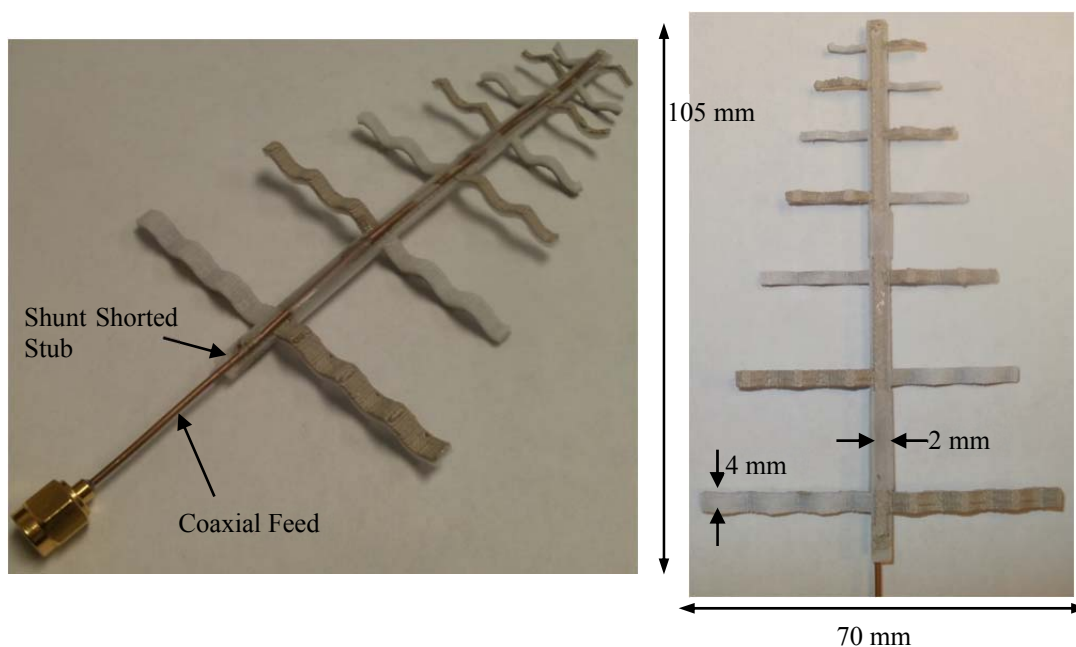


Figure 7.15: Illustration of the 3-D printed LPDA array; side view (left) and top view (right).

Figure 7.16 (left) shows the measured and simulated S_{11} of the 3-D printed LPDA array. As seen, the antenna has a good impedance match over the 2-7 GHz frequency range. Figure 7.16 (right) illustrates the measured and simulated gain of the antenna. The antenna measured gain is > 4 dBi over the 2.25-3.75 GHz frequency range and > 2 dBi over the 2.25-5.5 GHz

range. The measured maximum gain is 6.75 dBi and occurs at 2.5 GHz. This gain is similar to the expected gain using a standard LPDA array according to [153], however, the bandwidth is improved by 17%.

The measured E-and H-plane radiation patterns of the antenna at different frequencies are shown in Figure 7.17. The HPBW over the E-plane is 60° , 60° , 50° , and 40° for frequencies of 3, 4, 5, and 6 GHz, respectively. The FBR is > 20 dB over the 3-6 GHz frequency range.

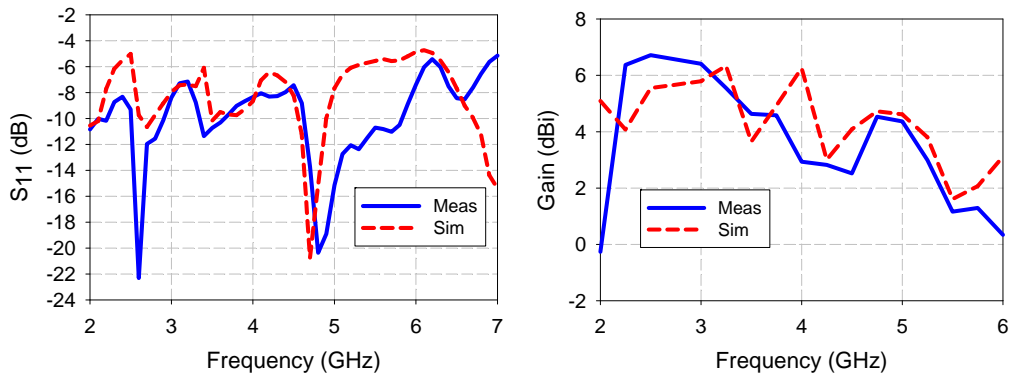


Figure 7.16: Simulated and measured S_{11} of the 3-D printed log-periodic dipole antenna array (left) and simulated realized gain in the endfire direction (right).

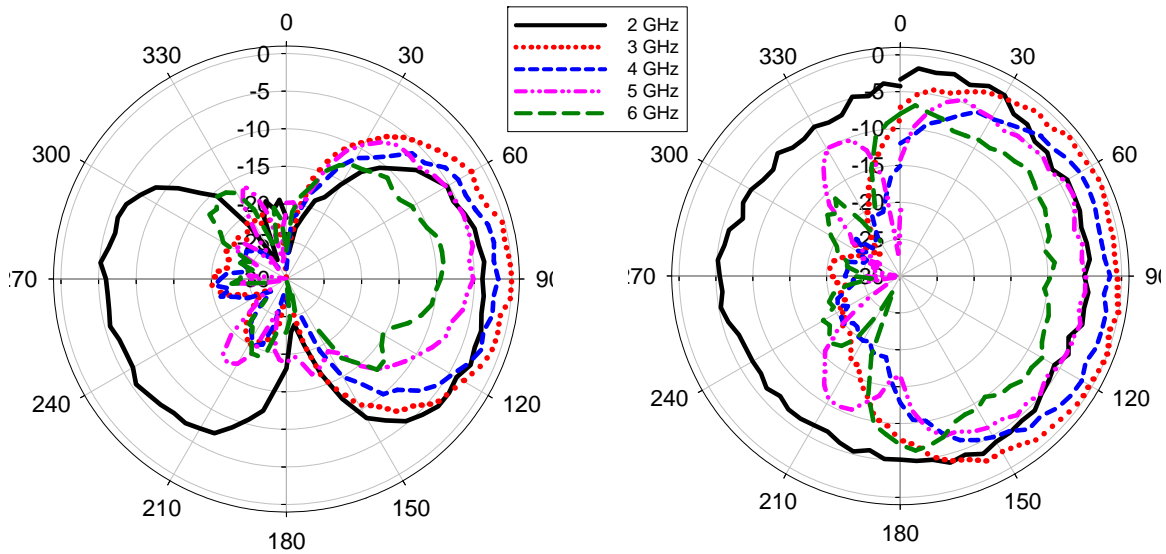


Figure 7.17: Measured radiation patterns of the 3-D printed log-periodic dipole antenna array; E-plane (left) and H-plane (right).

7.6 Conclusion

In this chapter, two dual-channel arrays have been designed on the basis of circular patch and quasi-Yagi dipole antennas. Each array offers some advantages and disadvantages for the harmonic interrogator design. The circular patch array offers the advantages of being low-profile, light weight, planar, easy to fabricate and integrate, and having high FBR, high gain, and narrow beamwidth compared to the occupied area. However, the array is inherently narrowband. The quasi-Yagi dipole antenna array is advantageous in terms of the broadband characteristics which allow the interrogation of different harmonic sensor nodes that operates at different frequencies, however, it suffers from the poor FBR, low gain, and wider beamwidth compared to the size, and the increased design complexity. To minimize the CPA array the 3-D printing technology can be used to print the array elements on a curved-substrate surface. By using a sine function to vary the height of the substrate by 50%, the antenna size and weight were reduced by 14% and the gain was reduced by 2 dB.

If it is of interest to expand the bandwidth of the interrogator array, the LPDA array can be used to provide a 2:1 bandwidth with constant directional radiation characteristics. While the standard LPDA array is usually large, the 3-D printing can be employed to reduce the weight and length of the dipoles and provide bandwidth improvement with minimal gain degradation.

CHAPTER 8 : RADIATING SHAPE-SHIFTING SURFACE BASED ON A PLANAR HOBERMAN MECHANISM

Note to Reader

Portions of this chapter have been previously published in [154], and have been reproduced with permission from IEEE. Permission is included in Appendix A.

8.1 Introduction

As illustrated in Chapter 7, planar microstrip patch antennas offer several advantages for the harmonic interrogator design. The major drawback of these antennas is the narrowband performance. An effective approach to improve the bandwidth of these antennas is by making them reconfigurable. In this chapter, a new method is presented for designing reconfigurable antennas using a foldable mechanism to change the radiating surface area [154]. Specifically, a planar Hoberman linkage is employed to develop resonant frequency-tunable antennas (Figure 8.1). These structures are built based on radially-foldable linkage kinematic theory [155]. The linkage consists of two symmetrical, semi-rigid blocks sandwiched between two mirror actuation rings, and all are connected using pin joints. The actuation rings are added to uniformly compress the linkage; when the rings rotate with respect to each other, the linkage pin joints are pushed inward resulting in a change in the effective surface area of the antenna. Similar linkages have been proposed for reconfigurable antenna dishes and in CubeSat designs to increase the

surface area of solar cell arrays [156]. The radiating shape-shifting surfaces (RSSS) in this work effectively utilize the like symmetries of the linkage structure and the radiating surface to vary the electromagnetic properties of the antennas. This design concept can be employed in the design of the harmonic radar interrogator antenna for the purpose of improving the performance and reducing the total size.

The presented mechanism can be actuated by a variety of means including piezo-vibration motors, electric motors, hydraulic cylinders, and shape memory alloys. The calculated required power to fully compress the presented linkage (1 cm radial distance) in one second is ~ 0.2 W, which is relatively high. However, the proposed structure was not optimized for low power consumption, and improvements in this respect could be achieved by reducing the linkage thickness and size.

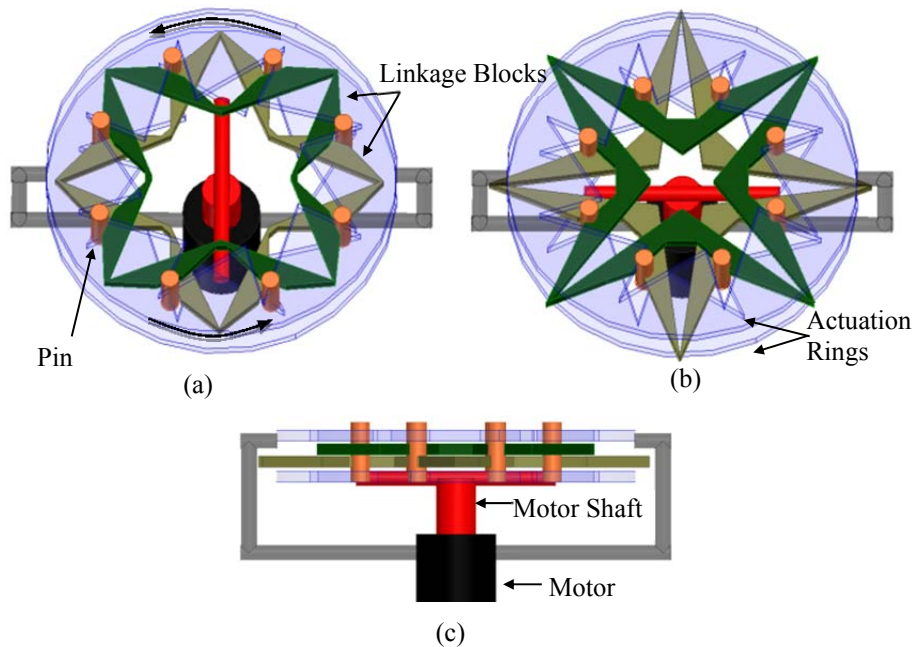


Figure 8.1: Illustration of the planar Hoberman linkage with the actuation rings and a motor: a) in the uncompressed position, b) the compressed position, and c) a side view.

The presented foldable mechanism can be employed to develop various reconfigurable antenna structures. In this work, the Hoberman linkage is used to develop three resonant

frequency-tunable antennas. In all of the designs, the antenna structure consists of a circular microstrip patch antenna surrounded by four quarter-circle parasitic patches. By attaching the parasitic patches to the upper block of the Hoberman linkage, they can be moved over the circular antenna to vary its operating frequency. The first presented structure uses electromagnetically-coupled parasitic patches (Figure 8.2) and provides >10% frequency tunability. For the second design, in which the parasitic patches make electrical contact with the circular patch, greater than 26% tuning bandwidth is achieved. Minimal impact on the gain, radiation patterns, and the 10 dB return loss bandwidth can be achieved for both of the presented designs. Over the tuning range the polarization in both antennas remains linear. By inserting crossed-slot apertures opening in the circular patch of the second design, the tuning bandwidth is improved to be greater than 36.5% (third design). With this prototype, however, the gain varies from 1 dBi to 5 dBi over the tuning range.

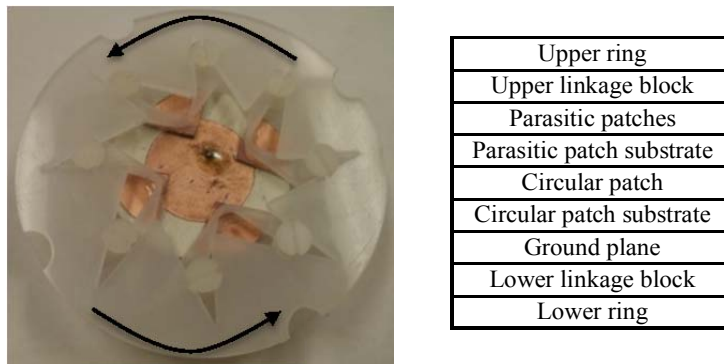


Figure 8.2: Prototype antenna with Hoberman linkage and the two rings (left); table showing the layer stack-up (right).

The proposed mechanism can also be employed in the design of a reconfigurable microwave phased antenna array system with a constant gain and pattern over a broad frequency range, characteristics which are useful in facilitating wireless sensor node interrogation and identification. Different approaches have been proposed to develop broadband antenna arrays

[157, 158, 159, 160, 161, 162, 163]. In such arrays, it is difficult to realize a fixed beam over frequency due to the necessity to adjust the array element spacing. The optimum spacing is a function of the operating frequency and affects the beamwidth, grating lobes, front-to-back ratio, and peak gain. Therefore, a switchable array that uses narrowband antennas may achieve uniform performance over frequency if both the array element and the element spacing are made tunable. In [164], an attempt to realize a fixed-beam antenna array has been demonstrated using the phase reversal technique in combination with varactor diodes, however, the gain, efficiency, and HPBW were not stable over the entire bandwidth. The approach that is adopted in this work is to make the antenna and the array element spacing reconfigurable by incorporating the Hoberman mechanism, with the benefit of achieving a true frequency scaling of the design and correspondingly uniform performance over frequency.

In the following sections, the design, testing and analysis of different prototypes are presented. Section 8.2 illustrates the primary radiating structure and Section 8.3 describes the antenna with the electromagnetically-coupled parasitic patches. Section 8.4 presents the second geometry with the directly connected parasitic patches and the third geometry with the inserted slots is illustrated in Section 8.5. A preliminary study of the reconfigurable array design is given in Section 8.6.

8.2 Antenna Structure

The primary radiating structure that is used in this work is a microstrip circular patch antenna (Figure 8.3. a). The antenna is fed from the bottom by a coaxial probe which was positioned in order to match the input impedance to 50 Ω . On the backside of the patch substrate a ground plane is placed and its size was optimized to reduce the back-side radiation. The substrate is Rogers/RT Duroid 4350 with a nominal relative dielectric constant (ϵ_r) of 3.66, and a

thickness (h) of 0.635 mm. The ground plane radius (R_g) is 25 mm and the circular patch radius (R_c) is 15 mm. The antenna performance was simulated using HFSS 13. The simulated and measured S_{11} for the antenna are compared in Figure 8.3. b. As seen, the measured and simulated data are well-matched.

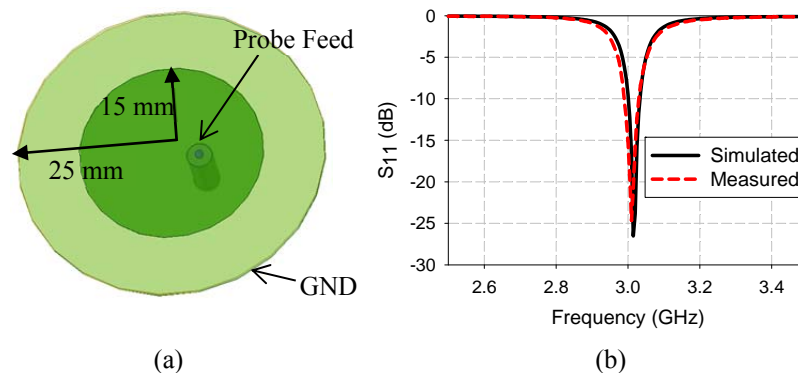


Figure 8.3: a) The circular microstrip antenna geometry and b) measured and simulated S_{11} of the antenna without the parasitic patches.

8.3 Antenna Design Using Electromagnetically-Coupled Parasitic Patches

Frequency tuning of the circular microstrip antenna can be obtained by adding electromagnetically-coupled parasitic patches, and using the planar Hoberman linkage to vary their position relative to the perimeter of the circular antenna. This approach is illustrated in Figure 8.4, where $X1$ denotes the distance from the center of the circular antenna to the vertex of a parasitic patch. The four identical, quarter-circle patches are held approximately 0.635 mm above the circular antenna on a Rogers/RT Duroid 4350 substrate, being connected between the two blocks of the foldable linkage. In this work, the rings and blocks were custom-made of polypropylene material (dielectric constant ~ 2.2) and pins were commercially-available nylon threaded nuts and bolts. The radius of each parasitic patch (R_p) is 15 mm. This symmetrical configuration was selected due to its simplicity and to give more freedom for the mechanical movement without affecting the radiation pattern.

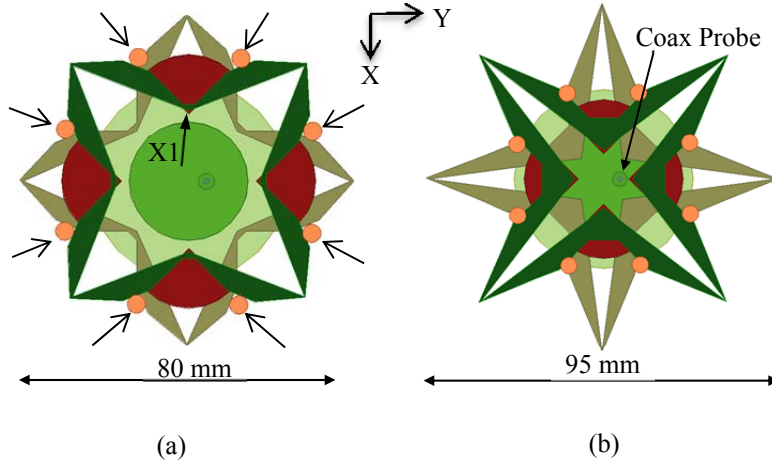


Figure 8.4: View of the RSSS mechanism without the actuation rings: a) unperturbed and b) compressed ($X1=7\text{mm}$) (right).

An equivalent lumped element model for the antenna, developed and simulated using ADS2009u1, is illustrated in Figure 8.5. This model represents the circular antenna and the two parasitic patches located along the Y-axis; these patches are in the direction of the TM_{11} mode resonance because of the probe location, and have the greatest impact on the resonant frequency. The antenna is mathematically modeled using R, L, and C elements. C_{in} represents the coupling capacitance between the parasitic patches and the circular antenna, C_{out} represents the coupling capacitance between the parasitic patches and the ground plane, and L_p represents the inductance of the parasitic patches. Each lumped element value is calculated as a function of X1 using the following equations:

$$C_{in} = \epsilon \times A_{in}/h, \quad (7.1)$$

$$C_{out} = \epsilon \times A_{out}/(2 \times h), \quad (7.2)$$

$$L_p \cong \mu \times 2 \times h \times (R_p - (R_c - X1))/W_p, \quad (7.3)$$

where A_{in} is the overlap area between the parasitic patches and the circular patch calculated by $A_{in} = (R_c - X1)^2 \times 0.25 \times \pi \times 2$ (m), A_{out} is the overlap area with the ground calculated by

$A_{out} = R_p^2 \times 0.25 \times \pi \times 2 - A_{in} (m)$, and W_p is the effective parasitic patch width estimated by $W_p \cong 0.25 \times \pi \times 2 \times (R_p - X1 + 3.8 \times e^{-3})$, (m).

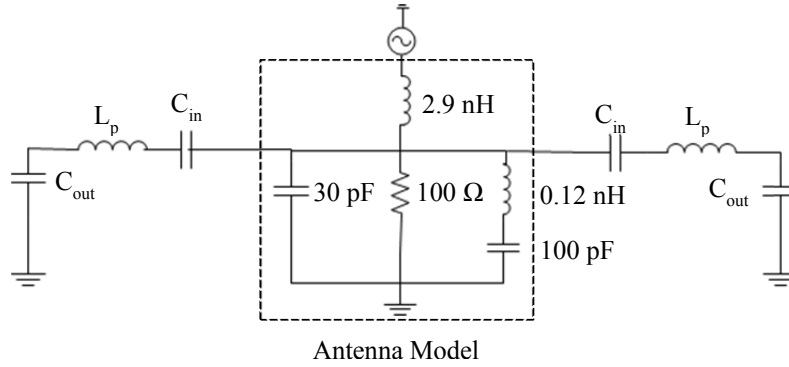


Figure 8.5: Equivalent circuit model for the geometry with EM-coupled parasitic patches.

The change in S_{11} as predicted by the lumped circuit model and the HFSS simulations is compared in Figure 8.6. As seen, the model data match the HFSS results over the entire $X1$ tuning range. As the parasitic patches move inward toward the center, C_{in} increases and C_{out} decreases due to the corresponding changes in A_{in} and A_{out} . L_p decreases as the parasitic patches move inward because their effective length decreases. When there is no overlap between the parasitic patches and the circular patch ($X1 \geq 15$ mm), the parasitic patches do not affect the antenna performance ($C_{in} = 0$). As $X1$ changes from 15 to 7 mm, the resonant frequency varies uniformly from 3.02 to 2.7 GHz (10% tuning) with constant 10 dB return loss bandwidth (~1%). For $X1 = 7$ mm, $C_{in} = 5$ pF, $C_{out} = 6.4$ pF, and $L_p = 0.61$ nH. When $X1$ decreases below 7 mm, C_{in} does not change and C_{out} decreases, therefore, the resonant frequency shifts upward until the parasitic patches completely overlap the circular patch ($C_{out} = 0$) and no further tuning occurs. Simulations show that larger resonance tunability, approximately 20%, can be achieved by using a higher dielectric constant ($\epsilon_r = 10.2$) substrate for the parasitic patches. Also, larger parasitic patches (radius of 25 mm) with a larger Hoberman linkage can provide up to 30% resonance tunability with the same circular patch antenna. The instantaneous bandwidth of the antenna can

be enhanced by considering different types of feeding [135, 136] and by increasing the substrate thickness.

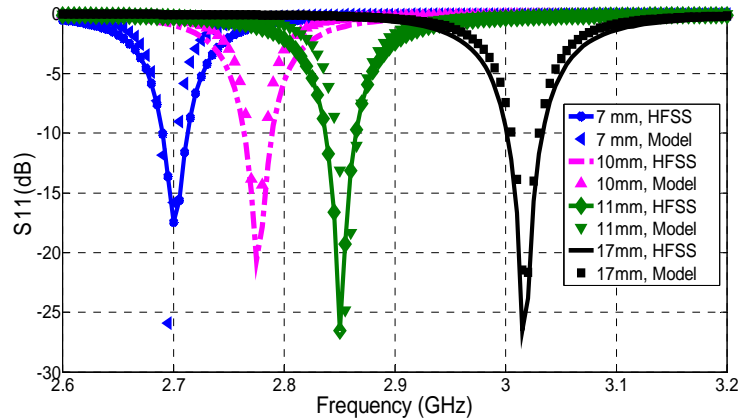


Figure 8.6: The simulated and modeled S_{11} of the geometry with EM-coupled parasitic patches for different X_1 values in mm.

A comparison between the HFSS simulations and measured S_{11} for the reconfigurable antenna is given in Figure 8.7. The agreement is nearly exact for $X_1 = 14$ mm. The deviation of 55 MHz for the case of $X_1 = 8$ mm is due to imperfect control of the gap height between the circular patch and EM-coupled parasitic patches. Ideally, this gap is equal to the thickness of the substrate on which the parasitic patches are printed. The variation in gap height could be reduced by using a more rigid attachment of the quarter-circle patches to the Hoberman linkage.

Figure 8.8 shows the measured co- and -cross-polarized radiation patterns of the antenna for different values of X_1 . The patterns are normalized to the maximum gain over the E-plane pattern for $X_1 = 17$ mm. As seen, the movement of the parasitic patches has minimal effect on the radiation patterns or the gain. The simulated gain is ~ 4.5 dB. The gain can be increased by increasing the ground plane size and the substrate thickness. The measured front-to-back ratio is ~ 17 dB and the measured maximum co-pol to cross-pol gain ratio in the broadside direction remained > 24 dB over the tuning range.

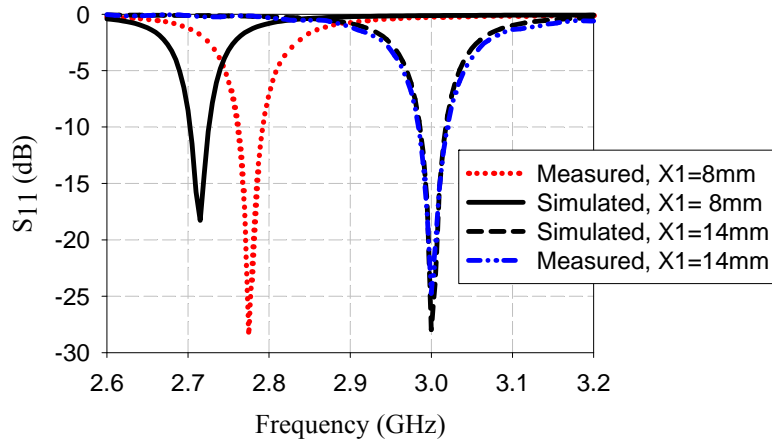


Figure 8.7: The measured and simulated S_{11} of the geometry with EM-coupled parasitic patches for different $X1$ values in mm.

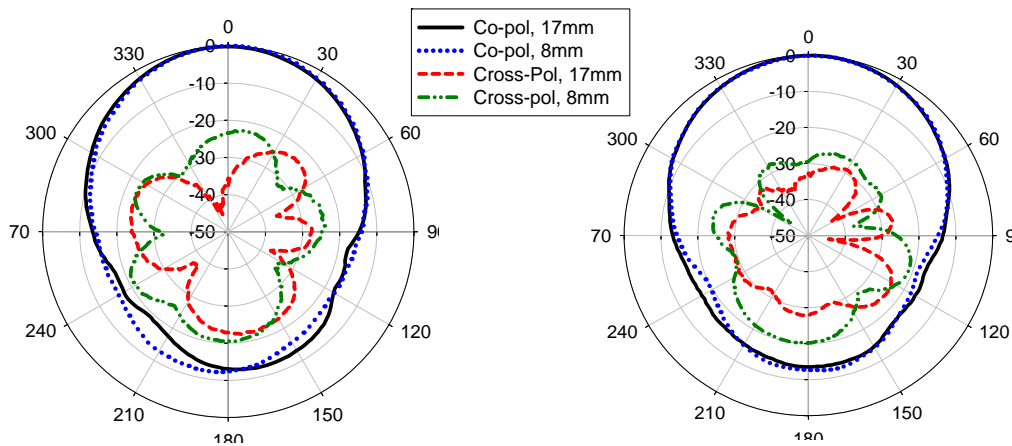


Figure 8.8: The measured co- and cross-pol radiation patterns for the geometry with EM-coupled parasitic patches for $X1=17$ mm at 3.02 GHz, and for $X1=8$ mm at 2.77 GHz; E-plane (left) and H-plane (right).

Table 8.1 shows a comparison between the presented design and a hypothetical design with equivalent tunability that is achieved using an ideal (lossless) tunable L-section matching network (MN). The MN that is used consists of a series-shunt capacitor network that is assumed to be connected at the antenna feed point. Even though the MN losses were ignored, the simulated gain and 10 dB return loss bandwidth decreased due to operation of the antenna away from its natural resonant frequency. For a microstrip antenna, off-resonance operation decreases the gain due to the rapid decrease in the radiation resistance. For the same reason, and because of

the increase in the imaginary part of the input impedance, the return loss bandwidth decreases; in this one example, there is nearly a 50% reduction in bandwidth which may be unacceptably large depending on the application. Alternative tunable matching network configurations, such as π -networks, may yield comparable return loss bandwidths but would not mitigate the gain reduction problem.

Table 8.1: Comparison between the presented approach and results using an l-section matching network (mn)

Resonant Frequency	BW (%) using MN	BW (%) varying X1	Gain using MN (dB)	Gain varying X1
2.85 GHz	0.6	1	3.95	4.65 dB
2.7 GHz	0.36	0.93	2.94	4.55 dB

8.4 Antenna Design Using Directly Connected Parasitic Patches

A second geometry was designed by making a direct contact between the parasitic patches and the circular patch to increase the resonant frequency tunability range (Figure 8.9. a). The electrical contact is made by vertical interconnects (vias that go through the parasitic patch substrates) that are allowed to slide over the circular patch. Relative to the first design, the radius of the parasitic patches is decreased from 15 mm to 10 mm, and the ground plane radius is increased from 25 mm to 35 mm. These changes are made to keep the ground plane size large enough relative to the radiating area.

Figure 8.9 (b) shows the simulated resonant frequency tunability for the second design. As the parasitic patches slide over the circular patch toward its center, the resonant frequency varies uniformly from 2.25 to 3.02 GHz (26% change at the frequency of 3.02 GHz). The resonant frequency moves upward as the parasitic patches move toward the center as this movement is equivalent to reducing the effective diameter of the circular antenna; the parasitic patches have no effect on the resonance when they are completely within the perimeter of the

circular antenna ($X1 \leq 5$ mm). As with the first design, the parasitic patches located along the Y-axis have the greatest impact on the resonant frequency. Based on the simulated resonant frequency, the approximate resonant wavelength ($\lambda_g/2$) of this configuration as a function of $X1$ is found to be: $\lambda_g/2 = 1.4 \cdot R_{\text{eff}} + 12$ mm, within $\pm 4\%$ for $15 \leq R_{\text{eff}} \leq 24$ mm, where $R_{\text{eff}} = R_c + (R_p - (R_c - X1))$.

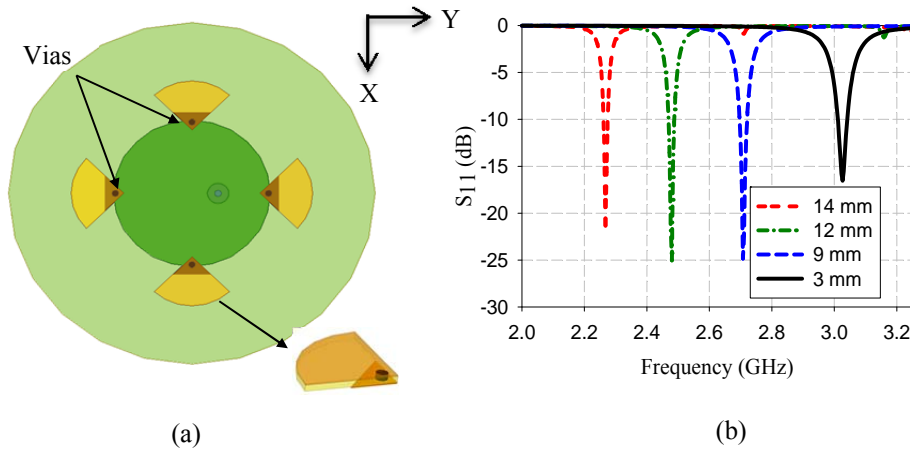


Figure 8.9: a) The RSSS with shorting vias (second geometry) and b) the simulated S_{11} for different $X1$ values in mm.

Figure 8.10 compares the measured and simulated S_{11} for different $X1$ values. The difference in the data for $X1 = 14$ mm is due to imperfect control of the manual movement ($X1$ value). As with the EM-coupled design, greater tunability can be achieved by increasing the size of the parasitic patches, the ground planes, and the Hoberman linkage.

The normalized measured co-and cross-polarized radiation patterns of the second geometry for $X1 = 11$ mm are shown in Figure 8.11. Simulated results show that the peak gain starts to degrade when $X1$ is larger than 12 mm, and the measurements confirm a drop in gain of 3.5 dB for $X1 = 14$ mm. However, as the parasitic patches move away from the center of the circular patch, the ground plane size shrinks relative to the antenna perimeter, and this is the main cause for the gain reduction. Simulated results demonstrate that approximately constant

gain is achieved across the tuning range using a ground plane radius of 50 mm. Over the tuning range the measured co-pol to cross-pol gain ratio in the broadside direction is > 20 dB.

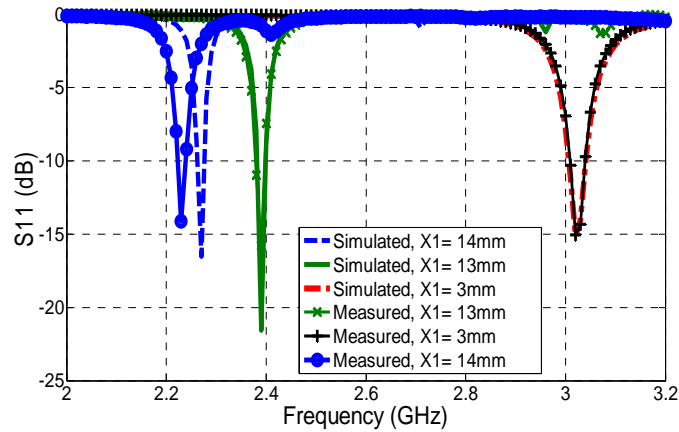


Figure 8.10: The measured and simulated S_{11} for the second geometry for different X_1 values.

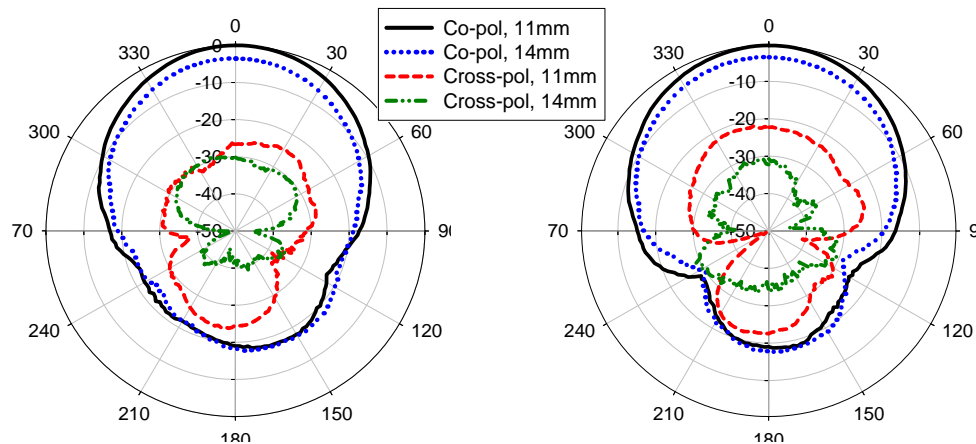


Figure 8.11: The measured co- and cross-pol radiation patterns for the second geometry for $X_1 = 14$ mm at 2.23 GHz and $X_1 = 11$ mm at 2.62 GHz; E-plane (left) and H-plane (right).

8.5 Antenna Design Using Directly Connected Parasitic Patches and Inserted Crossed-Slot

The tuning range of the second geometry presented in Section 7.4 can be significantly improved by inserting slot openings in the radiating circular patch. Inserting slots allows the tuning to continue as the parasitic patches moves further inward toward the center reducing the slot length, instead of having the tuning range ends when the parasitic patches are completely overlapped with the circular patch. Figure 8.12 illustrates the third geometry design for $X_1=17$

mm and the simulated S_{11} . The inserted slot length (L_s) equals 10 mm. R_c , R_p , R_g , and the substrate material are identical to the second geometry while the probe feed location is changed to improve the impedance match. As seen, inserting the crossed-slot lowers the frequency from 3.02 GHz to 2.8 GHz, since inserting the slots extends the surface current path and makes the antenna electrically larger. However, this size miniaturization reduced the gain by 0.6 dB.

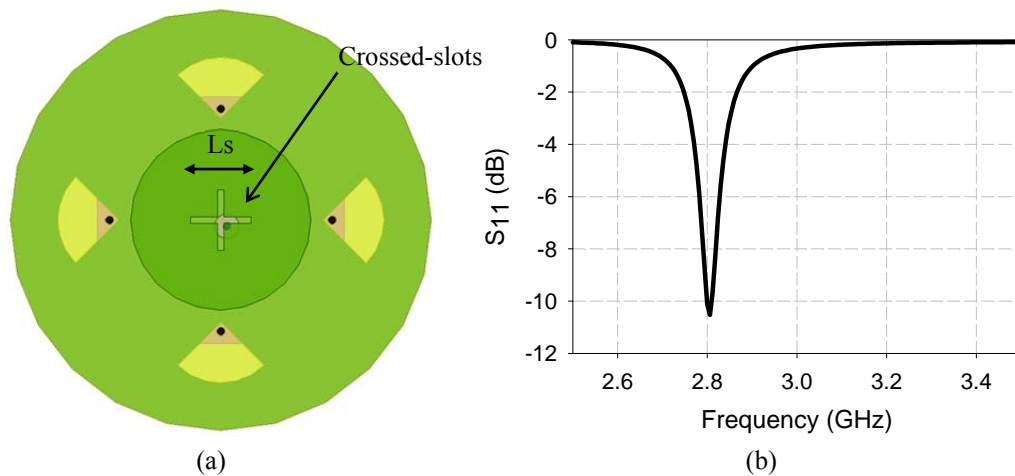


Figure 8.12: a) The RSSS with shorting vias and crossed-slots (third geometry) and b) the simulated S_{11} for $X1=17$ mm.

Figure 8.13 shows the simulated S_{11} for different $X1$ values. As seen, as $X1$ changes from 3 mm to 14 mm the frequency varies uniformly from 2.92 GHz to 1.9 GHz (36.5% change at the frequency of 2.8 GHz). For $X1$ equals 5 mm the parasitic patches are completely overlapped with the circular patch and not covering the slots, thus the frequency is similar to that for $X1$ equals 17 mm. As the parasitic patches moves further inward toward the center ($X1=3$ mm), the frequency moves upward to 2.92 GHz. When parasitic patches continue to move inward ($X1=0$ mm), the frequency increases up to 3 GHz, which is similar to the frequency of the second geometry without the slots, however, the impedance match is degraded (S_{11} is only -2.5 dB). The tuning range can be increased by increasing the slot length, however, the gain will be degraded and the impedance will not be matched to 50Ω over the entire range. The second S_{11} peak at

3.07 GHz shown for $X1=14$ mm is due to the excitation of the TM₂₁ mode which has a conical radiation pattern.

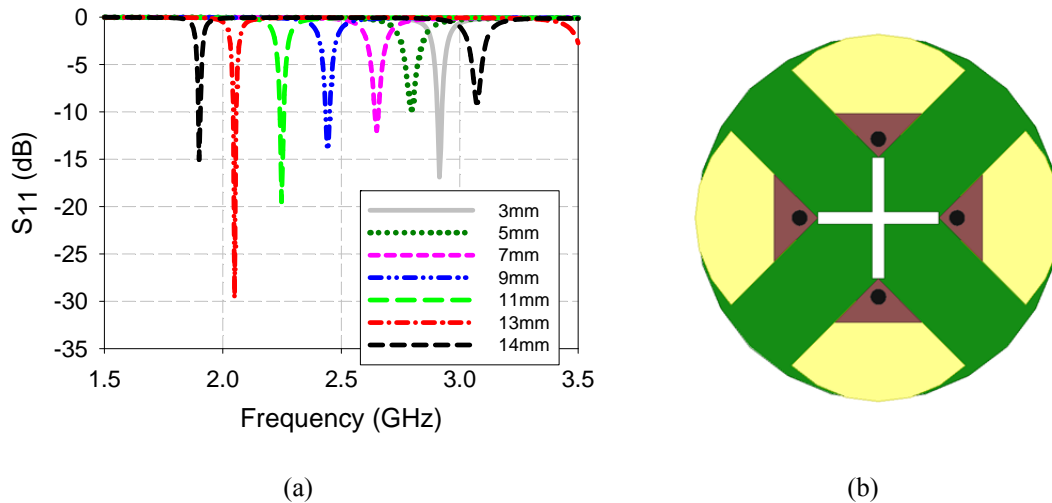


Figure 8.13: a) The simulated S_{11} of the third geometry for different $X1$ values, and b) illustration of the structure for $X1 = 5$ mm.

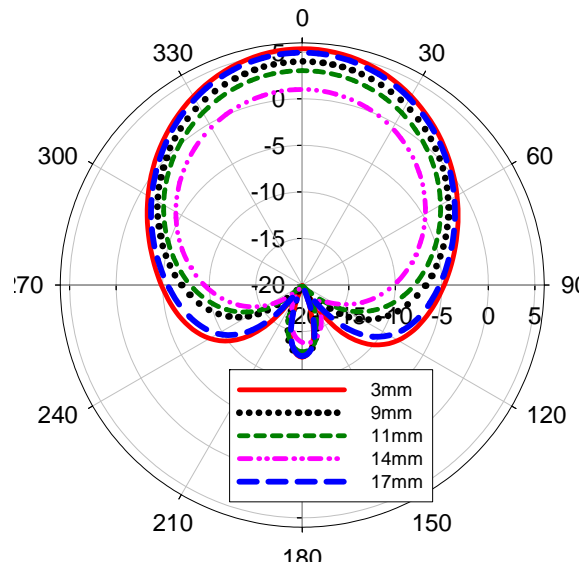


Figure 8.14: The simulated E-plane radiation patterns of the third geometry for different $X1$ values.

Figure 8.14 illustrates the simulated E-plane radiation pattern for different $X1$ values. Unlike the gain performance of the previous geometries over the tuning range, here the gain varies from 1 dBi for $X1 = 14$ mm to 5 dBi for $X1 = 3$ mm. The significant reduction in the gain

for $X_1 = 14$ mm is due to the relatively small ground plane size and the excitation of the TM₂₁ mode. As the parasitic patches extend beyond the circular patch, the TM₂₁ mode radiation gets stronger.

8.6 Broad-Band, Fixed-Beam Antenna Array

Using the Hoberman mechanism, a reconfigurable phased array system with a fixed beam over a wide tuning range can be developed. An illustration of a 2×2 array design is given in Figure 8.15; here, the antenna is similar to the design presented in Section 7.3. This configuration was selected due to its simplicity and to give more freedom for the mechanical movement without affecting the array radiation pattern. The antennas are fed from the bottom by a coaxial probe feed. To increase the coupling capacitance and the tuning range, the parasitic patches are held on a higher dielectric constant material (Rogers RT/Duroid 6010 with a nominal relative dielectric constant (ϵ_r) of 10.2). By attaching the parasitic patches to the upper block of the Hoberman linkage surrounding each individual antenna, they can be moved over the circular antenna to vary its operating frequency, and then the outer (large) linkage can compress and expand sequentially to change the element spacing. As the parasitic patches move inward toward the circular patch center, the resonant frequency decreases. This decrease in the resonant frequency requires the outer linkage to expand to keep the electrical distance between the elements fixed, maintaining the same pattern. The inward (outward) movement of the parasitic patches and the outward (inward) movement of the antenna-patch assemblies can be accomplished simultaneously using a single actuator, by exploiting the opposing changes in R and X_r that result from compressing (expanding) the outer linkage.

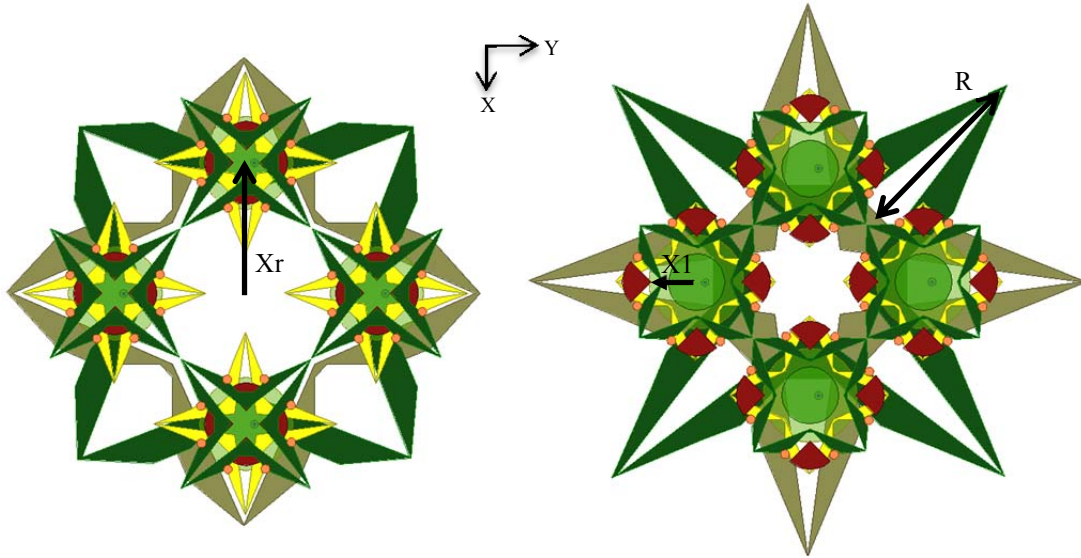


Figure 8.15: A 2×2 array illustration: (left) uncompressed array ($X_1 = 17\text{mm}$, $X_r = 50\text{ mm}$), (right) compressed array ($X_1 = 8.5\text{ mm}$, $X_r = 70\text{ mm}$).

A preliminary study of the illustrated array example has been performed. The elements are all fed in phase and the distance between the array elements is chosen to be $\sim \lambda/2$ over the tuning range. Figure 8.16 (left) shows the simulated S_{11} of the antenna when the antenna element linkages are fully compressed and the outer linkage is expanded ($X_1 = 8.5\text{ mm}$, $X_r = 70\text{ mm}$) and when the array element linkages are expanded and the outer linkage is compressed ($X_1 = 17\text{ mm}$, $X_r = 50\text{ mm}$). As seen, the antenna array demonstrates 20% tuning of the frequency, improvement by a factor of 2 relative to the antenna structure presented in Section 7.3. Figure 8.16 (right) illustrates the simulated E-plane radiation patterns for the 2.4 GHz and 3 GHz states. The H-plane patterns are very similar to the E-plane patterns and therefore are not shown here. Keeping the array element spacing to be with a constant electrical length over the tuning range resulted in maintaining the peak gain and the HPBW to be constant, however, the front-to-back ratio (FBR) varies by 4.5 dB. The FBR degradation can be reduced by backing the array with a larger ground plane. If the spacing between the array elements is held constant, peak gain and

HPBW degradations of 1.5 dB and 12 degrees are expected, Figure 8.17. For wider frequency tuning range, the array spacing impact would be higher.

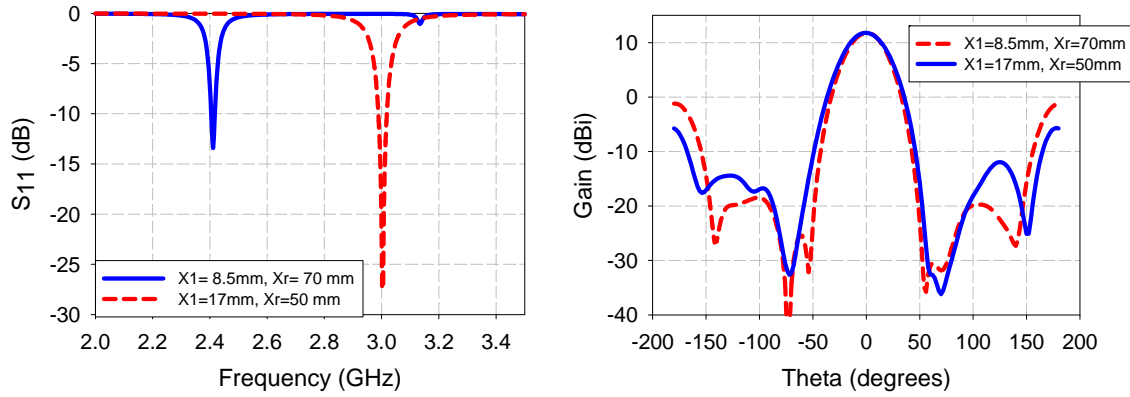


Figure 8.16: The simulated S_{11} (left) and simulated E-plane radiation pattern (right) of the array for two states.

The same design methodology can be used to develop a wide-band circularly-polarized (CP) radiation pattern. The CP radiation property can be obtained by sequentially rotating the antennas in a $0^\circ, 90^\circ, 0^\circ, 90^\circ$ or $0^\circ, 90^\circ, 180^\circ, 270^\circ$ fashion [165, 166]. This approach may be preferred due to the reduction in the feed complexity and the coupling between the neighboring elements. The required phase delay can be obtained using a non-dispersive phase shifter as the one we proposed in [167], which exhibits return loss ≥ 10 dB, insertion loss ≤ 0.5 dB, phase variation of ± 1.5 degrees over a 50% bandwidth, as will be presented in Chapter 11.

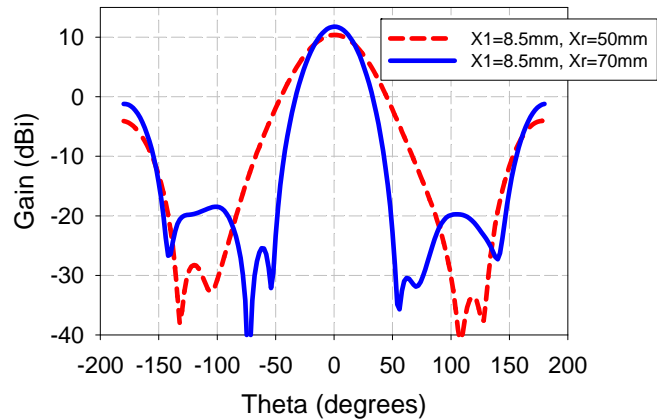


Figure 8.17: The simulated E-plane radiation pattern of the array if the element spacing is not changed.

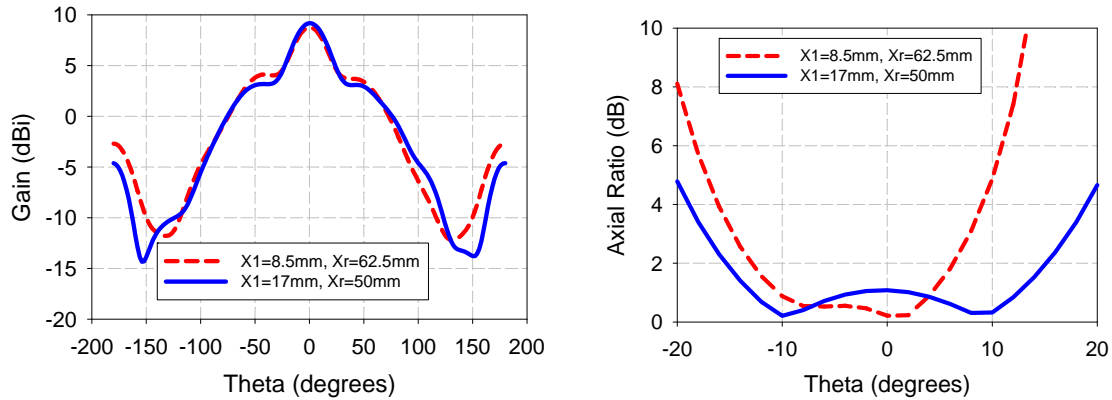


Figure 8.18: The simulated E-plane radiation pattern (left) and the simulated axial ratio (right) of the CP array for two states.

Figure 8.18 illustrates the radiation performance of the array when the array elements are fed in $0^\circ, 90^\circ, 180^\circ, 270^\circ$ phase arrangement. As seen, the corresponding adjustment of the element spacing maintained the CP and gain performance over the tuning range. With this feeding arrangement the array element spacing has more impact on the gain compared to the linearly polarized array. As seen in Figure 8.19, if the spacing is fixed, the gain will be degraded by 2.25 dB. Simulations have shown that the axial ratio performance is only slightly affected with the array spacing is tuned.

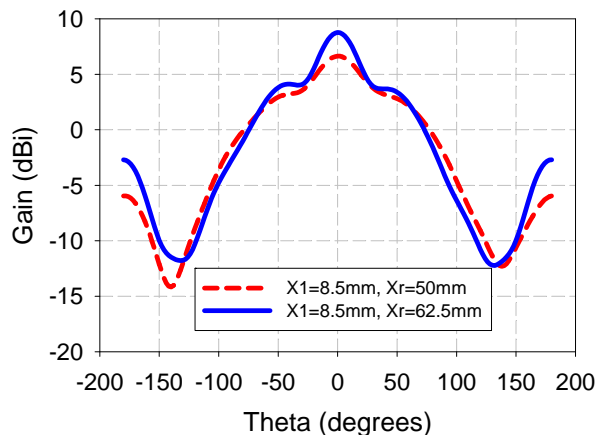


Figure 8.19: The simulated E-plane radiation pattern of the CP array if the element spacing is not changed.

8.7 Conclusion

A new approach for realizing reconfigurable antennas that can be good candidates for the harmonic radar interrogator antenna has been developed. Using a planar Hoberman linkage, resonant frequency-tunable antennas can be designed. Three implementations of the new approach were demonstrated. The first two structures demonstrate good frequency tunability and constant gain and return loss bandwidth. In contrast to an approach using tunable LC matching networks, these techniques perform better in terms of maintaining the antenna instantaneous bandwidth and gain. The tuning range can be further improved by inserting opening slots to the radiating patch, however, this approach does not maintain constant gain and impedance match over the entire range.

The proposed mechanism has also been employed in the design of reconfigurable antenna array to achieve a constant gain and pattern over a broad frequency range. The purpose of this design is to facilitate interrogation and identification of the wireless sensor nodes presented earlier in this dissertation. This type of array also finds use with multifunction radar and measurement systems. The Hoberman linkage is incorporated to make the antenna and the array element spacing reconfigurable. With this approach a true frequency scaling of the design and correspondingly uniform performance over frequency are achieved. Using similar foldable mechanisms, various reconfigurable antennas, antenna arrays, and filters can be developed. Digital additive manufacturing is one technique that can be used to produce linkages compatible with small antenna design.

CHAPTER 9 : MECHANICALLY-RECONFIGURABLE, DUAL-BAND, CPW-FED SLOT ANTENNA

9.1 Introduction

In this chapter, reconfigurable, dual-band, slot dipole antennas are developed for the harmonic radar interrogator design. Compared to the use of a single broadband antenna, reconfigurable dual-band antennas offer advantages of; 1) compact size, 2) nearly persistent radiation pattern, 3) minimal gain variation, and 4) frequency selectivity that is useful for reducing interference and jamming effects. To reduce the antenna cost and weight, the 3-D printing technology is used for the fabrication.

Coplanar waveguide (CPW) fed slot antennas are widely used due to their uni-planar structure, low profile, light weight, wide bandwidth, and ease of fabrication and integration. These antennas have bi-directional patterns that may not be desired for some applications such as high power radar. Several approaches, however, can be employed to realize unidirectional radiation including backing the antenna with a cavity [168], an artificial magnetic conducting reflector [169], or a ground plane. Approaches to allow the use of closely spaced ground planes have also been developed [170, 171, 172].

Slot antennas are one of the most prevalent candidates for multi-frequency applications such as mobile telecommunication systems, GSM, GPS, WLAN, and harmonic radars. The multi-band operation can be realized using several techniques [173, 174]. One of these techniques is to exploit the slot dipole antenna first higher order mode. While this mode has a

different radiation pattern than the fundamental mode (null in the broadside direction), different methods can be introduced to achieve similar desirable patterns at both of the modes. In [175], the pattern of the first harmonic mode has been modified to be broadside by adding coupling slots. Another method to realize similar patterns is by adding slots with different path lengths [176, 177, 178].

Tuning of printed slot dipole antenna has also been of interest. In the literature, tunable slot antennas are realized by incorporating varactor and PIN diodes [179, 180], reactive FET components [181], and shunt switches [182]. In all of these approaches, the tuning range is limited and the radiation properties were not preserved over the entire range, since the most effective approach to tune a slot antenna is varying the slot length. In addition to the limited tunability, to the best of the author's knowledge no approaches have been proposed for tuning the frequency band ratio of multi-band slot antennas, i.e. the ratio between the frequency of the second band and the first band of a dual-band antenna. Having the ability to tune the frequency band ratio allows the antenna to operate at different bands and increases the functionality.

In this work, a new method for the design of tunable dual-band slot antennas is proposed, Figure 9.1. The dual-band performance is achieved by inserting two slot pairs with different lengths, similar to the design presented in [178]. The reconfiguration is accomplished using a rack and pinion mechanism. The linkage comprises dual racks and pinion which convert rotational motion into linear motion and is actuated by a miniature stepper motor to slide the racks over the antenna. The calculated required power to fully compress each of the presented linkages 1 cm (linear distance) in one second is ~ 0.17 W. The sliding motion of the racks is guided by two supports mounted onto the substrate. These supports allow the racks to slide horizontally with minimal resistance yet inhibit rotation, torsion, as well as vertical translation.

The nature of the dual rack and pinion mechanism allows for the horizontal translation of two racks in opposite directions. By attaching parasitic patches to the linkage, they can slide uniformly over the antenna varying the slot length, thus the frequency of operation of each band.

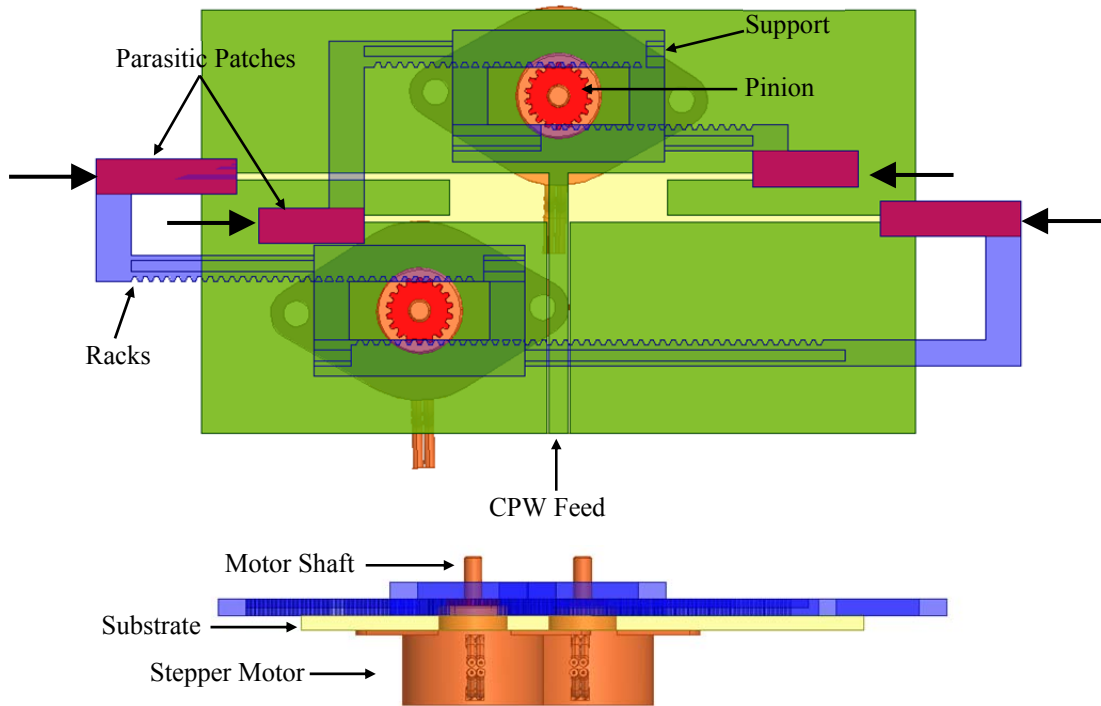


Figure 9.1: Illustration of the reconfigurable dual-band antenna with arbitrary frequency ratio; top view (top) and side view (bottom).

Two dual-band frequency tunable antennas are presented herein. The first design uses two separate motors and has an arbitrary frequency bands ratio, while in the second design one motor is used and a frequency ratio of two is maintained over the tuning range. The tuning of the frequency bands ratio of the first design ranges between 1 and 2.6. The second design has a tuning range from 2-3 GHz for the lower band and 4-6 GHz for the upper band, or 40% tunability for each band. Minimal impact on the gain and radiation patterns is observed for both of the designs. Over the tuning range the polarization remains linear without degradation in the co-pol to cross-pol ratio.

In the following sections, the design, testing and analysis of both of the dual-band antennas are presented. Section 9.2 illustrates the primary antenna structure and Section 9.3 describes the antenna with the arbitrary frequency ratio. Section 9.4 presents the second design with the frequency ratio of two. Testing of the impact of backing the antenna with a cavity is studied in Section 9.5 and preliminary analysis of integrating the antenna into a three-element array arrangement is given in Section 9.6.

9.2 Antenna Structure

Figure 9.2 illustrates the CPW-fed dual-band slot dipole antenna. The dual-band operation is accomplished by reducing the primary slot antenna length (L) and placing additional thin slot pairs in a symmetrical manner around the primary slot axis. The lower band frequency is determined by the length of the longer thin slot (L_L) and the length of the primary slot ($2 \times (L_L + L) \approx \lambda/2$), and the upper band frequency is mainly determined by the length of the upper slot ($2 \times (L_U + L) \approx \lambda/2$). The width W and W_s affects the impedance matching. The size of the conductive patch and the length of the feed line have minimal impact on the antenna performance. The antenna is fabricated with 3-D printing technology by printing silver ink on a 100 mils ABS substrate. The weight of the antenna is measured to be 16 g. The antenna dimensions are provided in Table 9.1.

Table 9.1: The dual-band slot antenna dimensions in mm

W	7	G	0.3
W_s	1.0	L_f	30
L_U	12.1	L_L	30.2
L	14	W_f	2.8

Figure 9.3 shows the measured and simulated S_{11} response. As seen, the measured and simulated S_{11} are matched well. The antenna is designed to have the lower band occur at 2 GHz and the upper band to occur at 4 GHz. The 10 dB RL BW of the lower and upper bands is 17% and 8.25%, respectively. Figure 9.4 illustrates the measured E-and H-plane radiation patterns at both of the frequency bands. The antenna exhibits broadside bi-directional radiation pattern with a maximum simulated gain of 4.5 dBi and 7.2 dBi at the lower and the upper bands, respectively. The gain is lower at the lower band due to the smaller electrical size. The antenna is linearly polarized with a measured co-to-cross pol ratio greater than 25 dB at both of the bands.

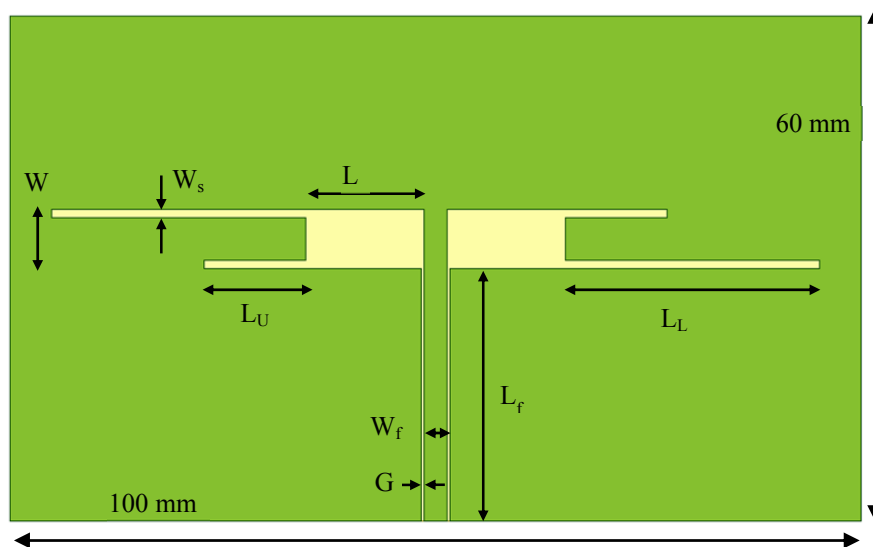


Figure 9.2: Configuration of the dual-band antenna structure.

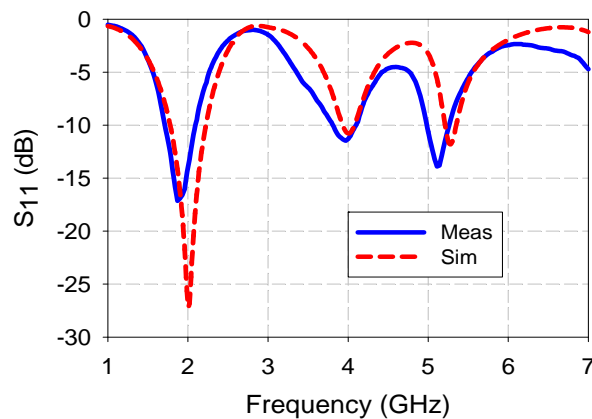


Figure 9.3: The measured and simulated S_{11} of the dual-band slot antenna.

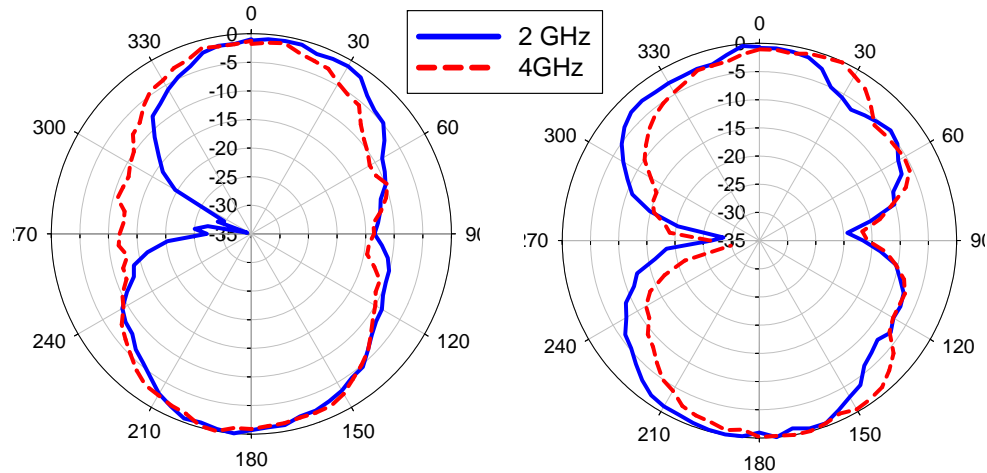


Figure 9.4: Dual-band slot antenna measured radiation patterns; H-plane (left) and E-plane (right).

9.3 Reconfigurable Antenna with Arbitrary Frequency Bands Ratio

Figure 9.5 illustrates the first antenna geometry. Parasitic patches are incorporated to vary the slot pairs length independently. X_1 represents the inward compression of the longer slot pair length and X_u represents the decrease in the shorter slot pair. Figure 9.6 (left) shows the simulated S_{11} for $X_u = 0$ mm and different X_1 values. As seen, varying X_1 changes the lower band frequency without affecting the upper band. As X_1 changes from 0 to 18 mm the lower band frequency increases up to 4 GHz, which occurs when L_L and L_U are equal. Figure 9.6 (right) shows S_{11} performance for $X_1 = 0$ mm and different X_u values. As X_u changes from 0 to 10 mm, the lower band frequency does not change and the upper band frequency changes from 4 GHz to 5.25 GHz. The upper frequency can increase further, if X_1 increases simultaneously. By varying X_1 and X_u independently the frequency bands ratio can vary between 1 and 2.6. Figure 9.7 Figure 9.8 illustrate the measured and simulated S_{11} for different X_1 and X_u values. As seen, the measured and simulated data are well matched.

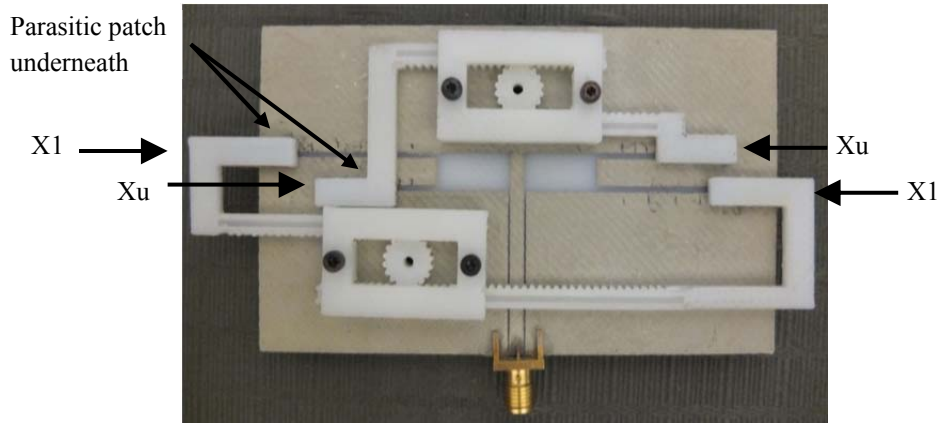


Figure 9.5: The configuration of the dual-band slot antenna with arbitrary frequency ratio.

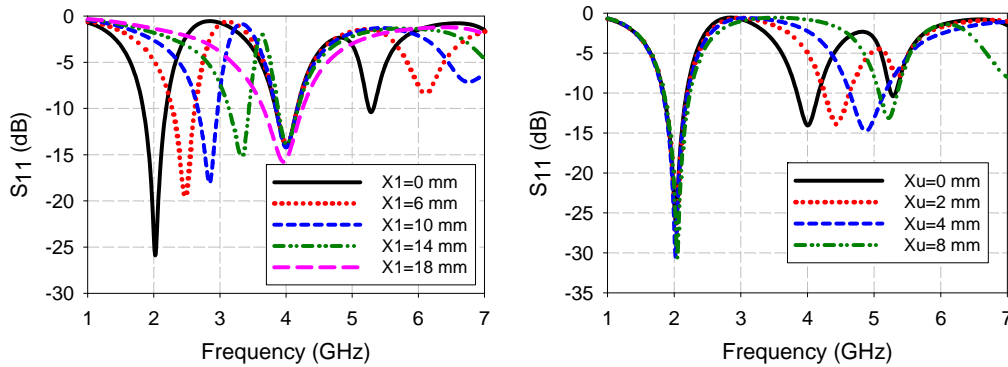


Figure 9.6: The simulated S_{11} of the dual-band antenna with arbitrary frequency ratio for different X_1 and $X_u = 0$ mm (left) and different X_u and $X_1 = 0$ mm (right).

Figure 9.9 (left) illustrates the measured E- and H-plane radiation patterns for $X_1 = 12$ mm and $X_u = 0$ mm at 3 GHz. As seen, the patterns are similar to that shown in Figure 9.4. As X_1 varies from 0 to 18 mm, the gain varies between 4.5 dBi and 6 dBi.

Figure 9.9 (right) shows the measured patterns for $X_1 = 0$ mm and $X_u = 5$ mm at 5 GHz. As seen, pattern distortion starts to occur at the upper frequency limit, however, the peak gain changes by less than 0.6 dB over the tuning range. The axial ratio also remains greater than 22 dB as X_1 and X_u varies.

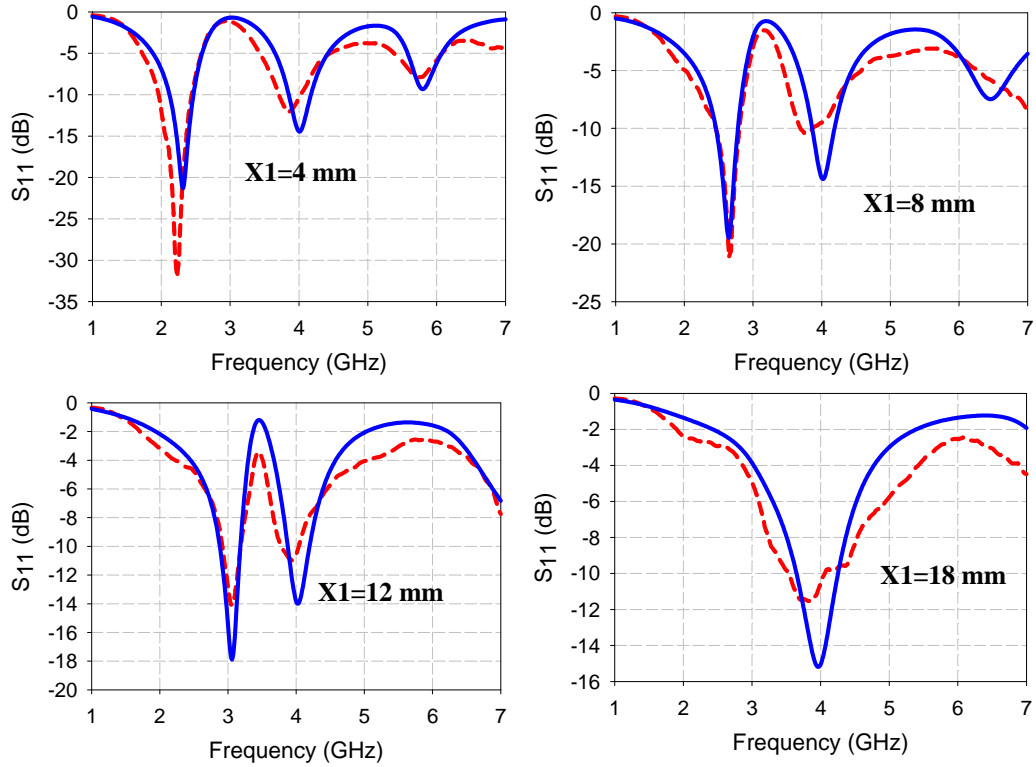


Figure 9.7: The measured (dashed) and simulated (solid) S_{11} for $X_u=0$ mm and different X_1 values.

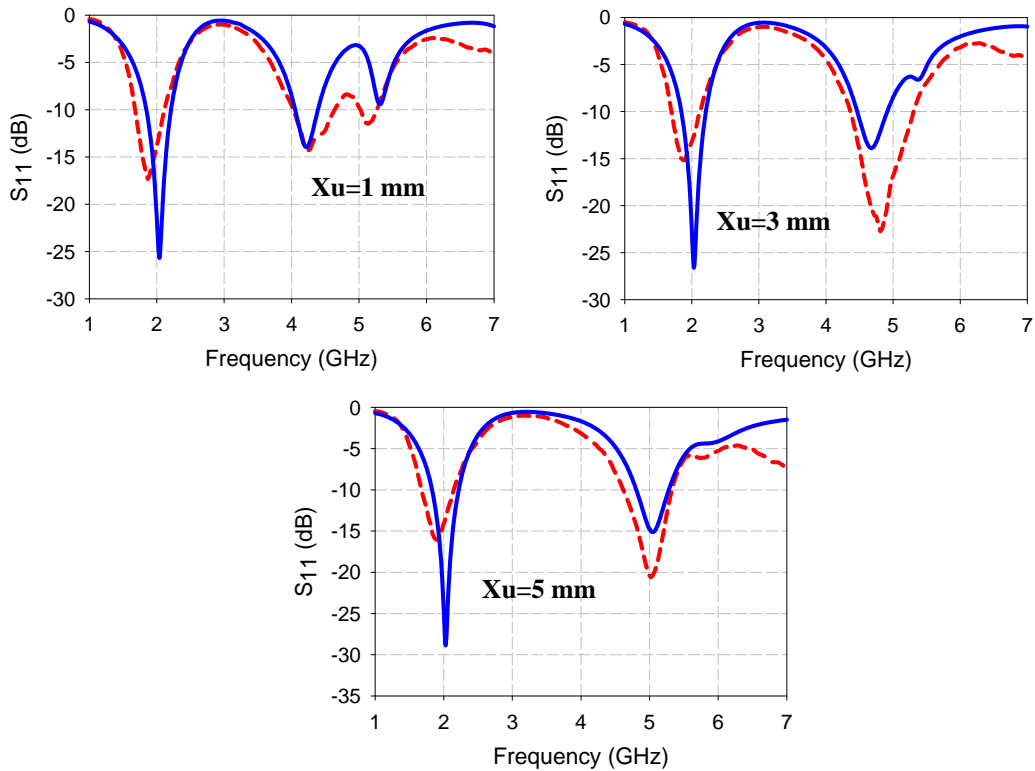


Figure 9.8: The measured (dashed) and simulated (solid) S_{11} for $X_1=0$ mm and different X_u values.

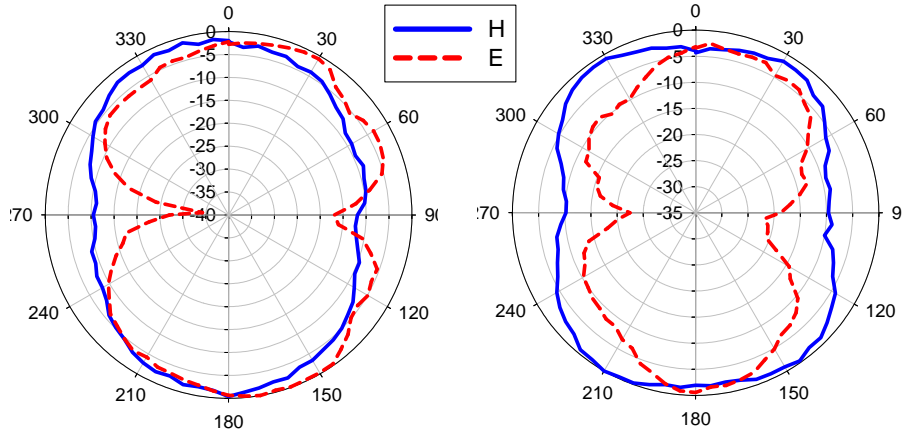


Figure 9.9: Measured E-and H-plane for $X_1 = 12$ mm and $X_u = 0$ mm at 3 GHz (left) and for $X_1 = 0$ mm and $X_u = 5$ mm at 5 GHz.

9.4 Reconfigurable Antenna with a Frequency Ratio of Two

For the harmonic interrogator design, the frequency bands ratio needs to remain fixed with a value of two over the tuning range. This can be accomplished using one actuator and one motor to have the parasitic patches move together. Figure 9.10 illustrates the second design geometry. The primary slot is meandered and L_L and L_u is optimized to be 27.5 and 10.25 mm, respectively, to maintain a frequency ratio of 2 and good impedance match at both of the bands as X_1 varies. Figure 9.11 shows the simulated S_{11} for different X_1 values. As seen, a frequency ratio of 2 is maintained over the tuning range. As X_1 changes between 0 and 10 mm, the lower band frequency changes uniformly between 2 and 3 GHz and the upper band frequency changes between 4 and 6 GHz. While the S_{11} peak of the second band does not occur exactly at twice the frequency of the first band over the entire range, it falls within the 10 dB RL BW of the second band.

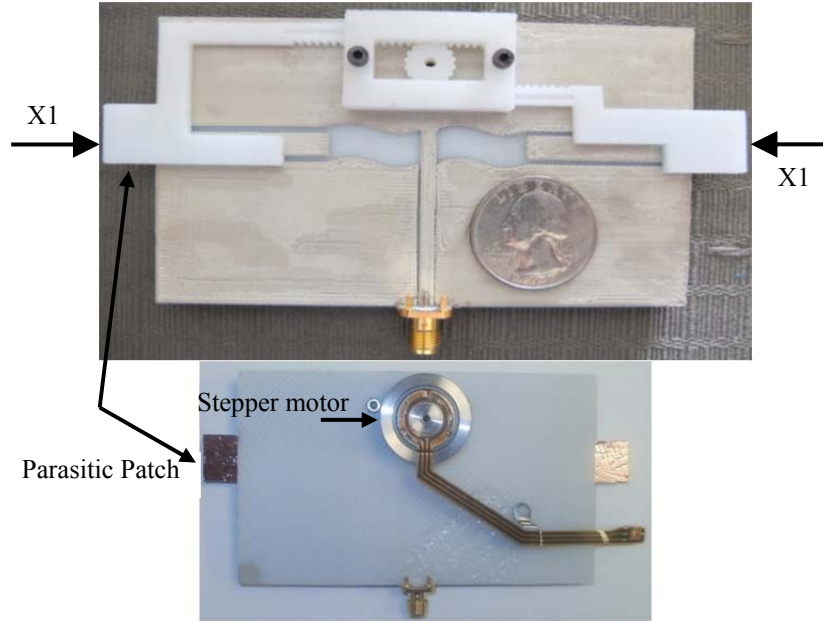


Figure 9.10: The configuration of the dual-band slot antenna with frequency ratio of 2 and one motor. Top view (top) and backside view (bottom).

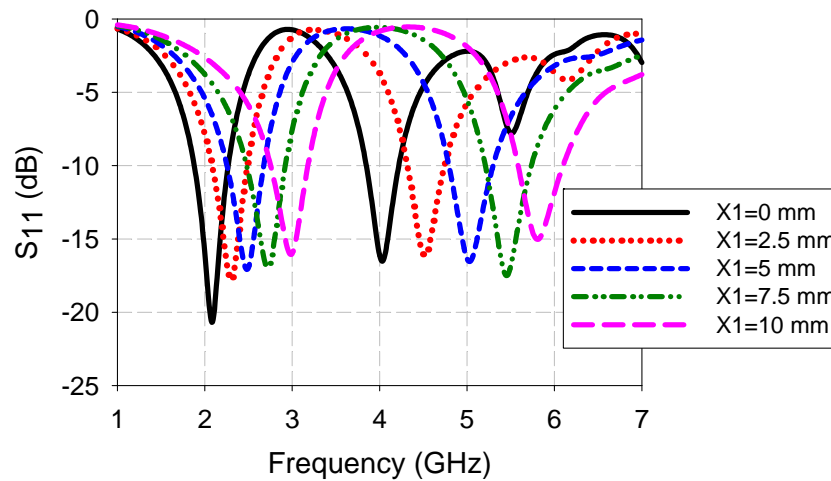


Figure 9.11: The simulated S_{11} of the dual-band antenna with a frequency ratio of 2 for different X_1 values.

Figure 9.12 illustrates the simulated radiation patterns at the upper frequency limit of the lower and upper bands. Compared to Figure 9.4, the patterns at the range upper limit of the lower band are similar, while there is pattern distortion at the upper limit of the upper band. As X_1 changes from 0 to 10 mm, the peak gain varies between 4.5 dBi and 6 dBi over the lower band range, and varies between 6.2 dBi and 5.4 dBi at the upper band range.

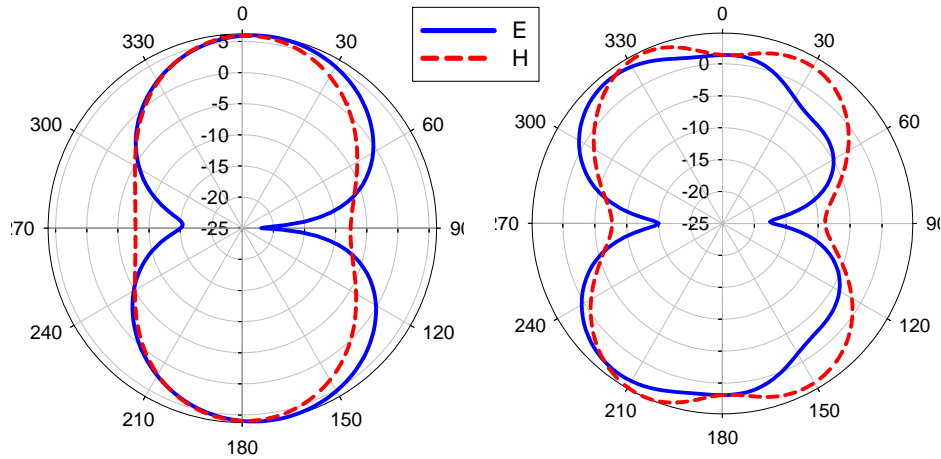


Figure 9.12: Simulated E- and H-plane radiation patterns of the dual-band slot antenna with a frequency ratio of 2 for $X_1 = 10$ mm at 3 GHz (left) and 6 GHz (right).

9.5 Dual-Band Slot Antenna Backed with a Cavity

For radar applications, the bi-directional radiation pattern of the proposed antenna is not desired. As mentioned in Section 9.1, different approaches can be employed to accomplish a unidirectional pattern. In this work backing the antenna with a shallow cavity is studied. Figure 9.13 shows the cavity-backed dual-band slot antenna. In order to have the lower band at 2 GHz and the upper band at 4 GHz, L_L , L_u , and L are optimized to be 32.5 mm, 11 mm, and 20 mm, respectively. The antenna width is increased to 120 mm and the length is reduced to 35 mm by reducing L_f to 20 mm. To maintain good gain and realize a directive pattern, the cavity depth is set to 600 mils ($\sim\lambda/10$ at 2 GHz). The cavity increased the antenna weight to 61.5 g.

Figure 9.14 illustrates the simulated and measured S_{11} of the cavity-backed antenna. As seen, the lower band occurs at 2 GHz and the upper band occurs at 4 GHz. The 10 dB RL BW at the lower and upper bands is 6% and 3%, respectively. Compared to the design without the cavity, the BWs at the lower and upper bands are reduced by a factor of ~ 2.8 . The dips shown in S_{11} can be attributed to the undesired cavity modes.

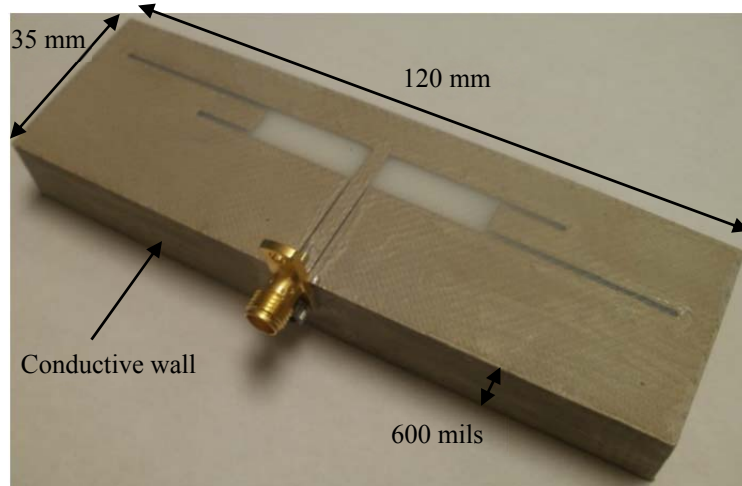


Figure 9.13: A photograph of the cavity-backed dual-band slot antenna.

Figure 9.15 shows the measured radiation patterns at the lower and upper frequency bands. The peak broadside gains at the lower and upper bands are 5.8 dBi and 7.2 dBi, respectively. As seen, unidirectional pattern is realized by backing the antenna with a cavity, however, the back side radiation is high. The measured front-to-back ratios (FBR) at 2 GHz and 4 GHz are ~5 dB and ~10 dB, respectively. The back side radiation can be reduced by increasing the cavity size; e.g., simulations show that using a cavity size of $130 \times 55 \times 20 \text{ mm}^3$ increases the FBR by 6 dB.

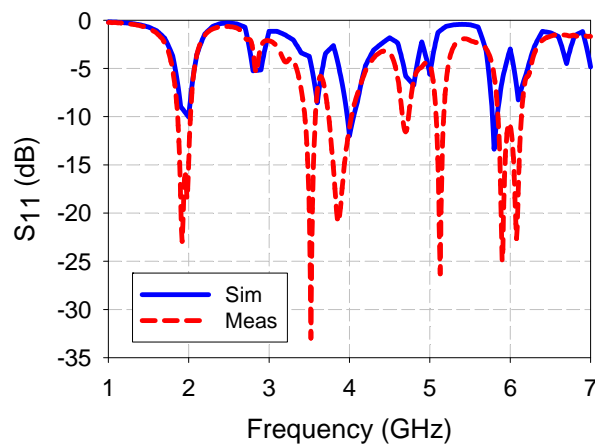


Figure 9.14: Simulated and measured S_{11} of the dual-band cavity-backed slot antenna.

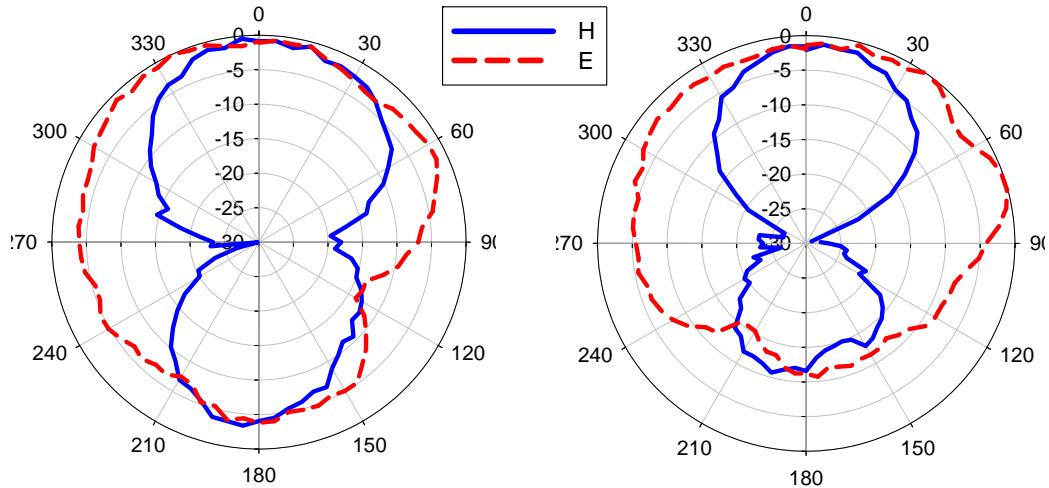


Figure 9.15: Measured E- and H-plane radiation patterns of the dual-band cavity-backed slot antenna at 2 GHz (left) and 4 GHz (right).

Incorporating the linkage to tune the frequency of the proposed cavity-backed antenna was also studied. The study revealed that the tuning range is reduced and the impedance match is not maintained over the entire range. In order to maintain the tuning range, the cavity size needs to be enlarged.

9.6 Dual-Band Array Design

In this section, the suitability of the proposed antenna for array arrangement is studied. The cavity-backed antenna presented in Section 9.5 has been integrated into a three element array configuration, as shown in Figure 9.16. All the elements are fed in phase and the distance between the elements is $\sim \lambda/3$ at 2 GHz. The array size is $0.8 \lambda \times 0.93 \lambda$ at f_0 of 2 GHz. The feeding network design and losses are not considered in this study.

The simulated radiation patterns at the lower and upper frequency bands are illustrated in Figure 9.17. The peak realized gain at the lower and upper bands are 10 dBi and 12.5 dBi, respectively. The FBR is ~ 10 dB at both of the frequency bands. The HPBW over the E-plane pattern is 24° at the upper band and 48° at the lower band. In comparison to the previously

studied arrays, this array has high gain and narrow HPBW in relative to the occupied area. This reveals that the cavity backed slot antenna can be considered a suitable element for antenna array arrangements. The proposed rack and pinion mechanism can also be incorporated here to accomplish a frequency tunable dual-band array with persistent pattern.

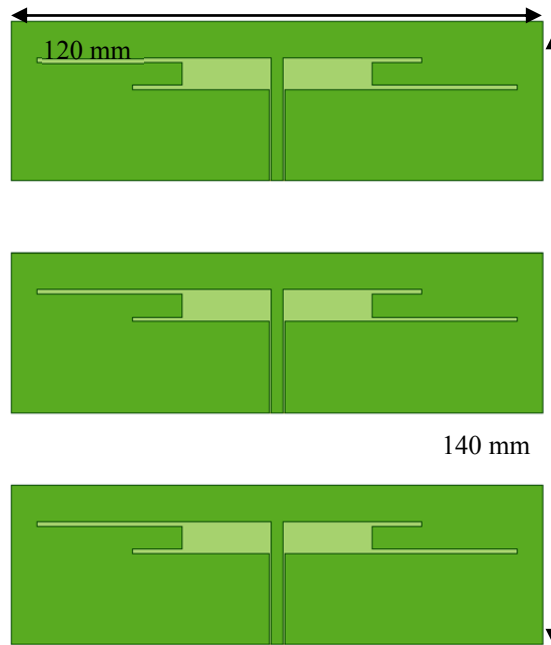


Figure 9.16: Illustration of the dual-band cavity-backed slot antenna array configuration.

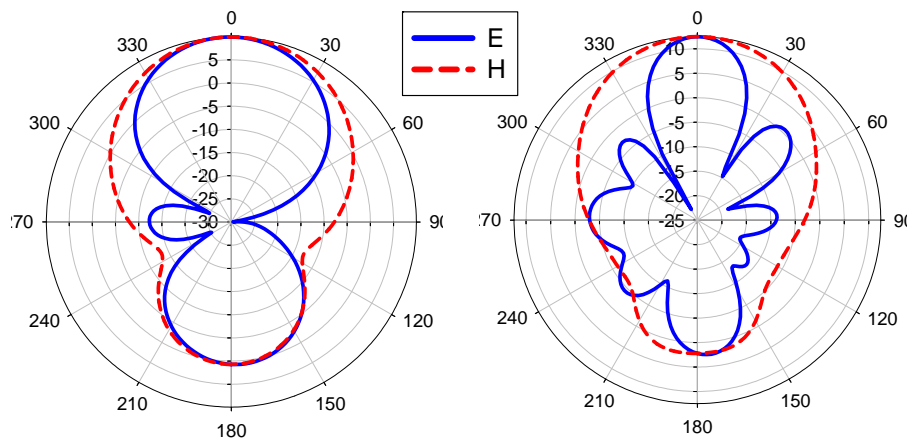


Figure 9.17: Simulated E- and H-plane radiation patterns of the dual-band cavity-backed slot antenna array at 2 GHz (left) and 4 GHz (right).

9.7 Conclusion

A new approach for realizing reconfigurable dual-band slot antennas that can be good candidates for the harmonic radar interrogator has been developed. Using the rack and pinion mechanism different reconfigurable planar antennas can be developed. In this work, two frequency-tunable dual-band antennas were implemented. The first geometry is designed to have a tunable frequency bands ratio and the second geometry is designed to maintain a frequency ratio of 2 over the tuning range. Both of the designs demonstrate good frequency tunability and persistent gain and radiation patterns.

A study of backing the proposed antenna with a cavity to realize unidirectional radiation performance was conducted. Backing the antenna with a cavity increased the FBR from ~ 0 dB to 5 dB at the lower band and to 8 dB at the upper band, making the proposed antenna more desirable for radar applications. The cavity has also increased the peak gain. The drawbacks of the cavity backing are reducing the 10 dB RL by a factor of 2.8 at both of the bands, degrading the tuning range when incorporating the rack and pinion mechanism, and increasing the overall weight.

A preliminary analysis of integrating the cavity-backed dual-band slot antenna into an array configuration has been performed. A three element array has been designed with all the elements are fed in phase. With the array size of $0.8 \lambda \times 0.93 \lambda$, the peak realized gain at the lower and upper bands are 10 dBi and 12.5 dBi, respectively. The FBR is ~ 10 dB at both of the frequency bands. The proposed rack and pinion mechanism can also be incorporated in the array design to realize a frequency tunable dual-band array with persistent pattern.

CHAPTER 10 : A NOVEL MULTI-OCTAVE VIVALDI ANTENNA DESIGN

10.1 Introduction

In this chapter, a broadband interrogator antenna covering multiple octaves is presented. A multi-octave antenna provides the capability to interrogate a large number of harmonic tags that are largely spaced in different frequency bands without the need to change the antenna. Compared to the conventional installation of multiple antennas and reconfigurable antennas on the system, a multi-octave antenna has more potential for high speed, less complexity, less power consumption, and compact size. The multi-octave antenna used in this work is the tapered slot Vivaldi [183], which has interesting characteristics compared to other broadband antennas of being planar, easy to fabricate using printed circuit technology, and more convenient to feed and integrate with the system.

Numerous types of Vivaldi antennas have been developed. Herein, an antipodal Vivaldi design with a dual elliptical tapered slot line is used [184]. The dual elliptical antipodal is a modified version of the antipodal Vivaldi radiator, where the inner and outer edges of the slot line are elliptically tapered. Compared to the typical Vivaldi antenna, the antipodal structure provides the advantages of the wider bandwidth and lower cross polarization [185,186,187] due to the avoidance of the transition from microstrip to slot line and asymmetric feed structures.

One of the issues with tapered slot antennas is the stability of the radiation patterns and directivity over frequency. The Vivaldi antenna operates as a resonant type antenna at low frequencies, but as a traveling wave radiator at high frequencies. The waves travel along the

inner edges of the flared aperture and couple to each other to produce radiation [183]. For maximum radiation in the endfire direction, the phases of the waves on both arms have to be 180 degrees apart. If this condition is ensured, the antenna will have unlimited bandwidth. While the tapered feed line transition from the microstrip line to the radiating part of the antipodal structure provides wideband performance, there are different factors that cause the antenna bandwidth and radiation performance to degrade as the frequency increases. One of these factors is the radiation produced from the currents traveling along the flare termination sections, which leads to some gain reduction and major pattern distortion (as will be illustrated in Section 10.3). This unwanted radiation can be mitigated by corrugating the termination sections as reported in [188] and avoiding the sharp edges which cause wave diffraction [186]. Another reason for the performance degradation at high frequencies is the excitation of undesired modes due to the increase of the electrical thickness of the substrate. These modes alter the phases of the waves traveling along the flare section and cause higher cross polarization levels. The increase of the electrical distance between the aperture flare edges can also be considered one of the major reasons for the radiation performance degradation. The large electrical distance between the antenna arms at high frequency weakens the electric field coupling. In addition, it causes field coupling between different sections on the same arm which leads to side lobes and a null in the end fire direction. For this reason the flare needs to be narrow to maximize the gain at high frequencies. However, a narrow aperture has a higher cutoff frequency, therefore, a compromise is needed between the size, bandwidth, and gain.

In recent literature, several researchers have proposed different techniques to enhance the radiation performance of the tapered slot Vivaldi antenna at high frequencies. These techniques include the use of lenses [188], high permittivity material [189], and zero index material [190,

191] in the aperture flare sections to guide the energy in the endfire direction. Nevertheless, all these techniques improve the performance over a very limited frequency range and increase the design and fabrication complexity and cost. In [185] a novel method for improving the performance of Vivaldi antenna based on the addition of small parasitic patches has been investigated. The addition of the parasitic patches demonstrated improvement in the VSWR bandwidth, however, the gain performance was not improved.

In this work, we propose a new method for improving the Vivaldi antenna bandwidth and directivity over a wide frequency range based on the introduction of a parasitic elliptical patch in the flare aperture (Figure 10.1). The parasitic patch allows the gain to be improved at high frequency without compromising the low frequency performance. Instead of having the radiation at high frequencies only produced from the fields coupling between the arms which would be widely spaced, the parasitic ellipse inclusion induces the fields to couple to both of the ellipse sides and produce stronger radiation in the endfire direction. The inclusion of the elliptical patch also allows a larger portion of the antenna arms to participate in the radiation instead of having only small portion of the arms at the flare throat being responsible for the radiation at high frequencies. The inclusion of the parasitic ellipse enables gain and bandwidth improvement compared to what has been reported for Vivaldi antennas with a compact size. In addition, this approach mitigates the need for extremely thin substrates. Simulation and experimental results reveal that this performance improvement approach performs better than doubling the size of the antenna. The proposed antenna structure including the feeding line and transition measures $140 \times 66 \times 1.5 \text{ mm}^3$ and has a simulated peak gain $> 0 \text{ dBi}$ over the 2-32 GHz frequency range and $> 10 \text{ dBi}$ over the 6-21 GHz range.

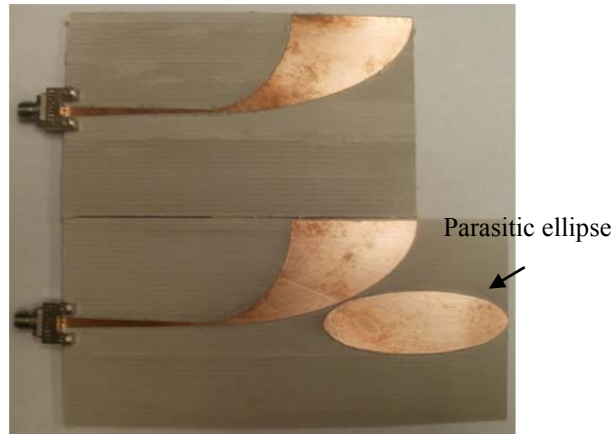


Figure 10.1: Photograph of the proposed Vivaldi antenna with/without the parasitic ellipse (top view).

This chapter investigates the impact of the inclusion of the parasitic elliptical patch on the Vivaldi antenna structure and presents a multi-octave Vivaldi antenna with improved radiation characteristics. Section 10.2 discusses the radiation mechanism of a typical Vivaldi antenna and the primary gain bandwidth limitations and Section 10.3 illustrates the proposed antenna geometry and the function of the parasitic elliptical patch. Different simulated and experimental results demonstrating the proposed antenna performance and the impact of the parasitic patch inclusion on the radiation characteristics are presented in Section 10.4.

10.2 Vivaldi Antenna Radiation Mechanism and Bandwidth Limitations

Figure 10.2 illustrates a dual elliptical tapered Vivaldi antenna. It is comprised of three sections; tapered slot radiator, feed line, and feed transition. The antenna is printed on two sides of a dielectric substrate. The arms are flared in opposite directions and symmetrically rotated around the antenna aperture axial axis.

As mentioned in the introduction, the Vivaldi antenna operates as a resonant type antenna at low frequencies (similar to a $\lambda/2$ dipole antenna), and mainly as a non-resonant, traveling wave radiator at high frequencies. The low frequency end is determined by the width of the antenna

(separation between the arms), which needs to be $\sim \lambda/2$ at the low frequency band of interest. At higher frequencies, the radiation is mainly produced from the waves traveling along the flare edges, as seen in Figure 10.2. As the aperture flare separation increases, the wave energy bound to the conductors becomes weaker and more coupled to radiation in the endfire direction. In order for the radiated fields to be directed in the end fire direction, the phase difference between the waves traveling on both sides needs to be ~ 180 degrees. This condition motivated the development of the antipodal structure, which provides wide band feed transition. At higher frequencies, most of the radiation is originated from the inner sections of the beginning of the flare and the termination sections have minimal impact on the end fire radiation. If these sections were large, side lobes might be created. To mitigate this unwanted radiation, the termination section length needs to be reduced and corrugated. The corrugation function is to alter the phases of the currents flowing along the termination sections in a manner that reverses the direction of the radiated fields to contribute to the endfire radiation [192].

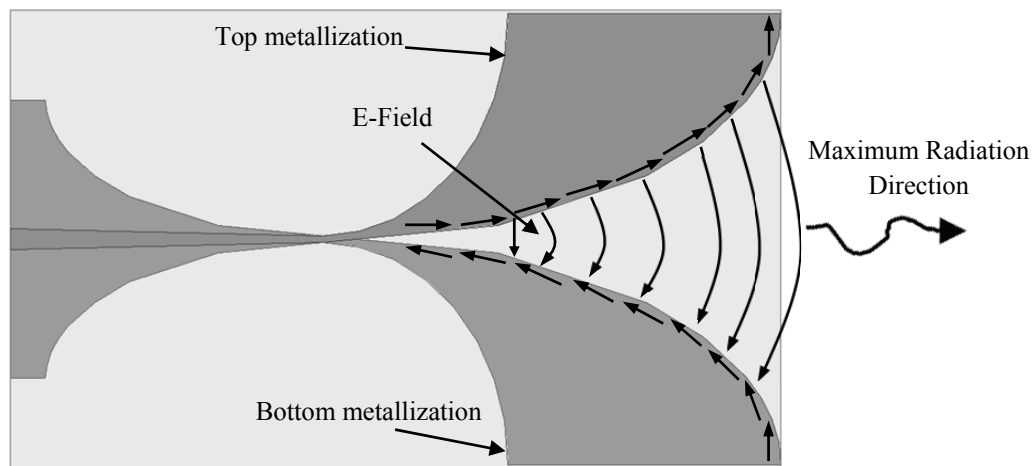


Figure 10.2: Illustration of the radiation mechanism of Vivaldi antennas.

The Vivaldi antenna has theoretically unlimited frequency bandwidth, however, as the frequency increases, different issues start to occur and degrade the radiation properties. One of these issues is the sensitivity to the electrical thickness of the dielectric substrate. As the

electrical thickness increases, undesired modes get excited. With these modes, the electric field between the feeding line and the bottom tapered ground is fringed and skewed. The intense existence of this electric field distribution in the flare throat, which contributes more to the radiation at higher frequencies, deteriorate the radiation characteristics and increase the cross polarization level. To mitigate this degradation it is preferred to use low dielectric constant material with small thickness. According to [193 ,194], the effective substrate thickness is preferred to be less than $0.03 \lambda_0$, where λ_0 is the free space wavelength at the middle of the desired frequency range. Other approaches are to shift the position of the feed line from the center of the tapered ground [187], the addition of a third metallization layer to form the balanced antipodal structure [184], and the use of the substrate integrated waveguide (SIW) technology [195].

The major reason for the performance degradation at high frequency, however, is the increase in the electrical distance between the flare sections. Due to the large electrical distance between the arms, the field coupling between the arms become very weak and the phase of the traveling wave on each arm gets reversed and wrapped, see Figure 10.3. Therefore, most of the endfire radiation is produced from the area near the flare throat. Due to the phase reversal, the radiated fields produced from the end of the flare sections cancel part of the radiation coming from the inner sections. In addition, coupling between different sections on the same arm occurs, which causes a null in the end fire direction and side lobes. The most effective approach to improve the endfire radiation at high frequency is to reduce the size of the flare opening and the flare rate. Reducing the flare opening, however, will increase the lower operating frequency. Hence, there is a tradeoff between the gain and bandwidth.

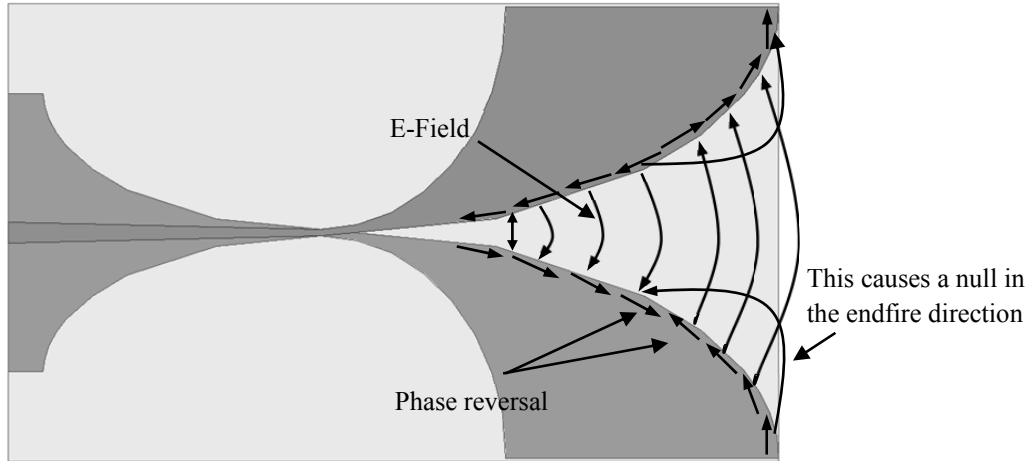


Figure 10.3: Illustration of the E-field distribution at high frequencies.

10.3 Proposed Vivaldi Antenna Structure

Figure 10.4 illustrates the geometry of the proposed antenna structure. The antenna structure without the inclusion of the parasitic ellipse is similar to the design presented in [187]. The substrate is Rogers/RT Duroid 6002 with a nominal relative dielectric constant (ϵ_r) of 2.94, and a thickness of 60 mils. Each arm is formed by a quarter ellipse with a major radius (a_1) of 66 mm and minor radius (a_2) of 33 mm. The outer taper profile is formed by a quarter ellipse with a major radius (b_1) of 32 mm and minor radius (b_2) of 26 mm. The ground taper follows also the outline of a quarter ellipse with a major radius (c_1) of 40 mm and minor radius (c_2) of 20 mm. The feeding consists of a microstrip line which has a width of 3 mm at the input side and transforms linearly into a parallel plate-line with a width of 1 mm at the radiator side. The elliptical parasitic patch major radius (d_1) is 30 mm and minor radius (d_2) is 10 mm and is located at a distance (d_e) of 35 mm from the flare throat center.

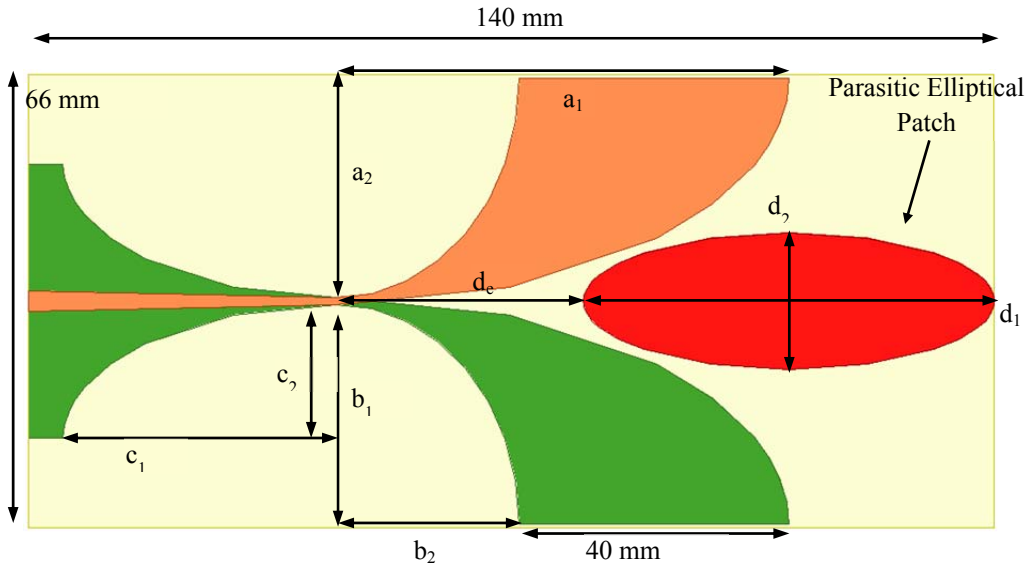


Figure 10.4: Illustration of the geometry of the proposed antipodal Vivaldi antenna.

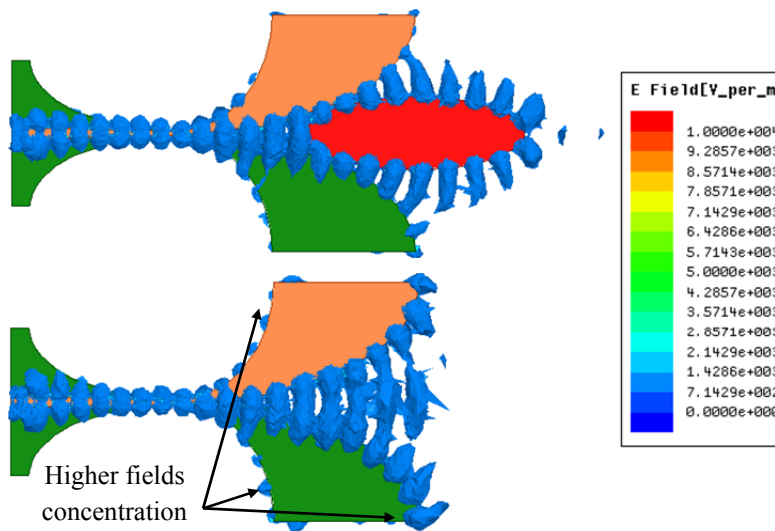


Figure 10.5: The electric field distribution of the proposed Vivaldi antenna with and without the parasitic ellipse at 17 GHz.

As discussed in Section 10.2, at high frequencies the electrical distance between the arms becomes very large which weakens the coupling between the arms and causes an increase in the coupling between different sections on the same arm which results in creating pattern distortion, gain degradation, and null in the endfire direction. Here, we propose a new approach to expand the Vivaldi antenna bandwidth and improve the endfire gain and directivity at high frequencies

based on the inclusion of a parasitic elliptical patch in the slot aperture. Instead of having the radiation only produced from the coupling between the arms, adding the parasitic ellipse induces the waves to couple also from the arms to both sides of the ellipse. Basically the parasitic ellipse divides the tapered slot aperture into two smaller tapered apertures. The elliptical shape is more effective than other shapes because it allows the phase variation condition between the traveling waves on the arm and the ellipse to be closer to the ideal phase difference if the slot aperture was narrow. Figure 10.5 shows the electric field distribution at 17 GHz around the antenna with and without the parasitic ellipse. The figure illustrates the radiation mechanism of the proposed antenna and the impact of including the parasitic ellipse. As seen, with the inclusion of the elliptical patch, the electric field is more concentrated on the flare edges and the radiation is more focused on the end fire direction.

The parameters of the elliptical patch are d_1 , d_2 , and d_e . These parameters affect the endfire gain performance. For optimum performance improvement, the size of the parasitic patch needs to be wide and long enough to improve the wave coupling between the arms and the ellipse. The size of the ellipse also affects the tapering rate which needs to be close enough to the arms tapering. The distance to the antenna has minimal impact on the gain. The ellipse position needs to be optimized to be close enough to the flare throat to improve the coupling, however, not too close to the limit that the field distribution at the flare throat is disturbed.

10.4 The Performance of the Proposed Vivaldi Antenna

The measured and simulated S_{11} of the proposed Vivaldi antenna with and without the parasitic ellipse are given in Figure 10.6. Due to the frequency range limit of the used SMA connector, S_{11} was measured up to 27 GHz. As seen, adding the parasitic ellipse affects S_{11} , however, the 10 dB RL BW is the same. Despite the minimal impact on S_{11} , adding the parasitic

patch improves significantly the gain, as can be seen in Figure 10.7. The deviation between the measured and expected gain improvement is attributed to misalignment errors between the antenna under test and the reference antenna. Compared to the antenna without the parasitic patch, the gain is improved slightly over the lower part of the frequency range and improved significantly for frequencies above 12.5 GHz. The parasitic ellipse patch enables the gain to be greater than 10 dBi over the 6-21 GHz and to stay above 12 dBi from 15-20 GHz. This gain is considered high compared to the antenna occupied area and the substrate thickness.

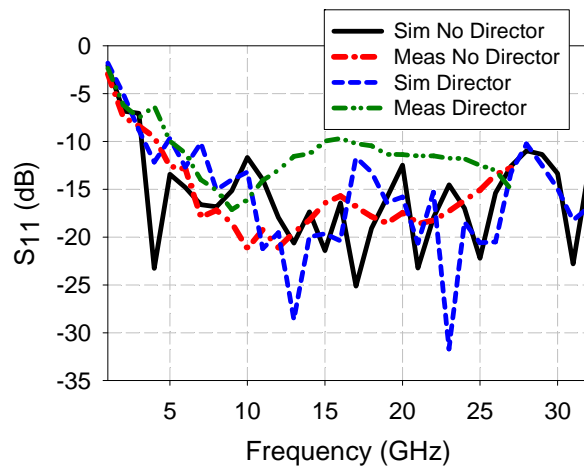


Figure 10.6: Comparison of the measured and simulated S_{11} of the proposed Vivaldi antenna with and without the director.

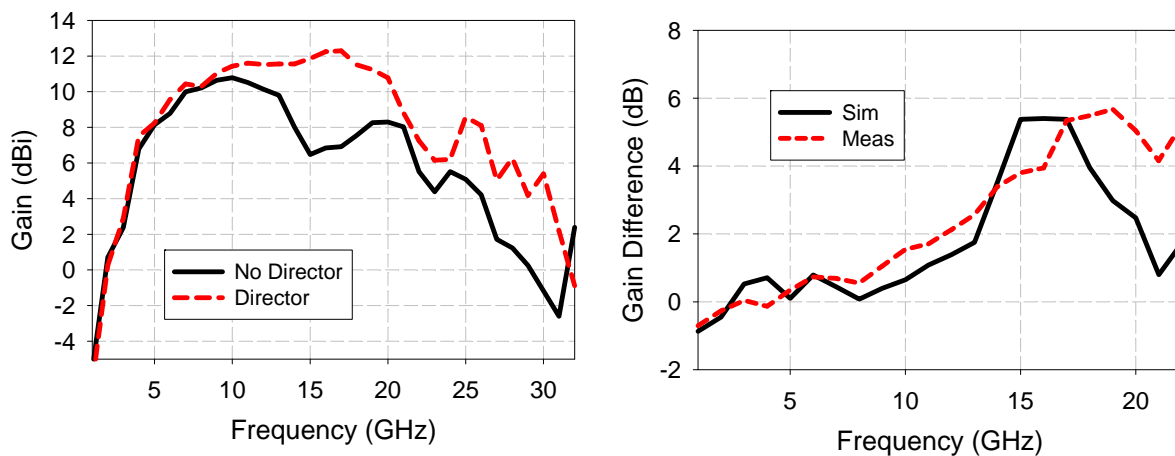


Figure 10.7: Comparison of the simulated realized gain in the endfire direction of the proposed Vivaldi antenna with and without the director (left) and comparison of the measured and simulated gain difference between the two antennas (right).

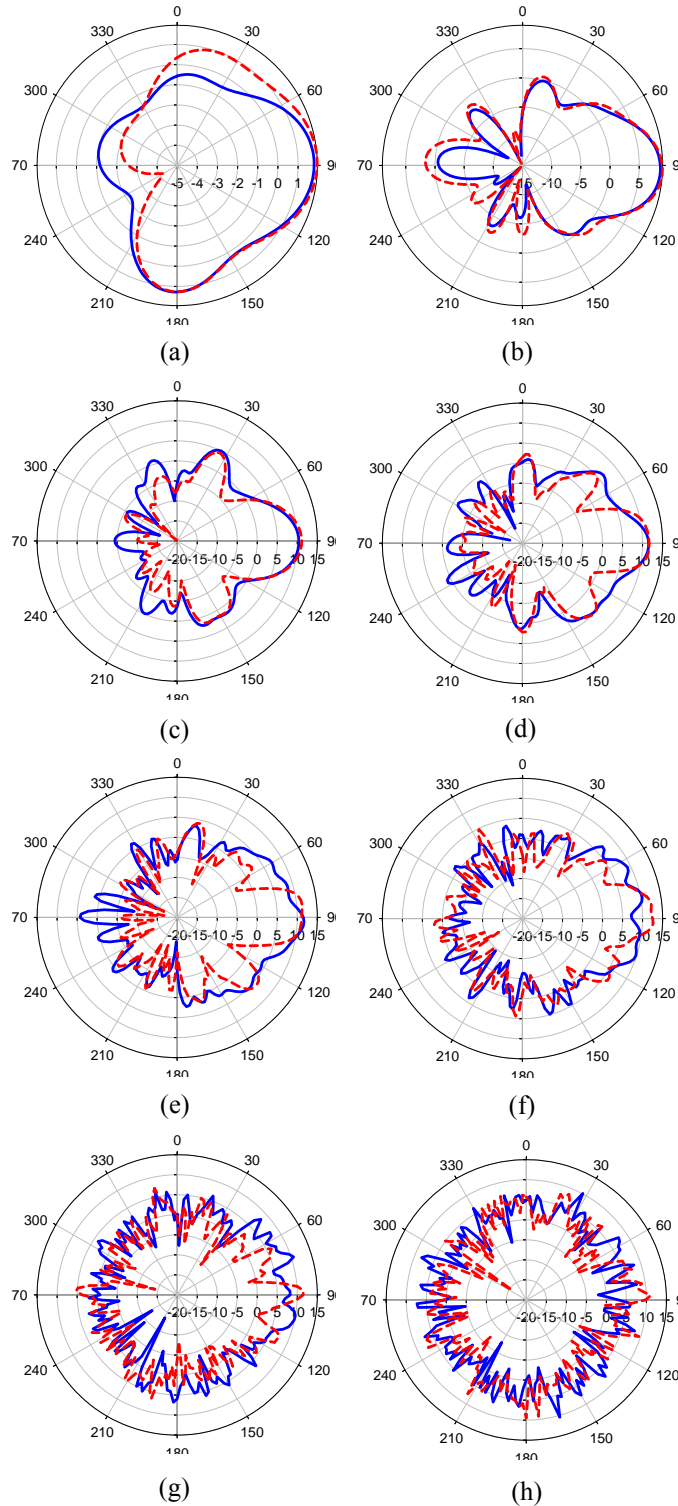


Figure 10.8: Comparison of the simulated E-plane radiation patterns with and without the parasitic ellipse at a) 2 GHz, b) 5 GHz, c) 7 GHz, d) 10 GHz, e) 12 GHz, f) 15 GHz, g) 20 GHz, and h) 25 GHz. Solid line without the director and dashed line with the director.

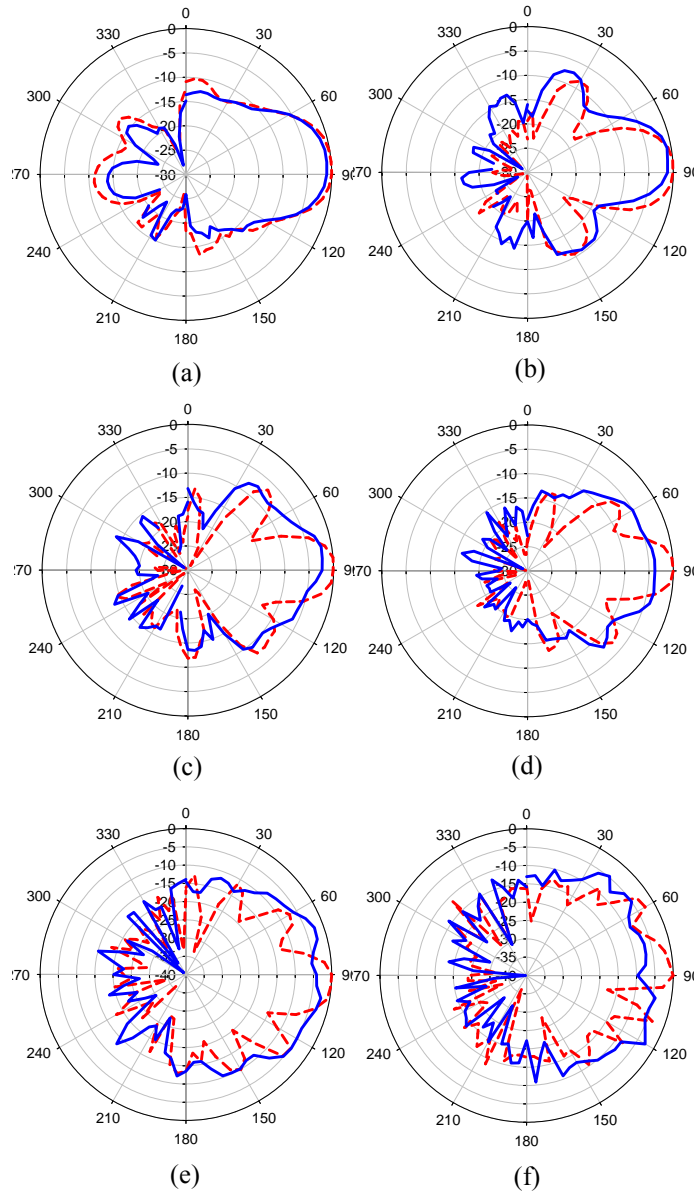


Figure 10.9: Comparison of the measured E-plane radiation patterns with and without the parasitic ellipse at a) 5 GHz, b) 7 GHz, c) 10 GHz, d) 12 GHz, e) 15 GHz, and f) 20 GHz. Solid line without the director and dashed line with the director.

The simulated and measured E-plane (the plane contains the antenna) radiation patterns with and without the parasitic elliptical patch of the proposed antenna at different frequencies are shown in Figure 10.8 and Figure 10.9. The antenna has an endfire radiation pattern directed in the axial direction of the slot aperture. At low frequencies, there is no remarkable difference between the radiation patterns, although the director slightly improves the gain (< 1 dB). For

frequencies from 5 to 12 GHz, the gain is also slightly improved by inserting the parasitic ellipse, while the directivity and HPBW are significantly enhanced. For frequencies above 13 GHz the directivity and gain are improved considerably. From an overall comparison view, the FBR is also improved with the addition of the parasitic ellipse over the 2-20 GHz range.

Figure 10.10 compares the performance of the proposed antenna with the antenna without the director inserted for different sizes. Increasing the width of the antenna from 66 mm to 132 mm and increasing the length of the arms from 40 mm to 75 mm provides gain improvement only at low frequencies. In addition, it is noticeable that increasing the size causes higher gain variation over frequency and causes the gain to drop at lower frequencies.

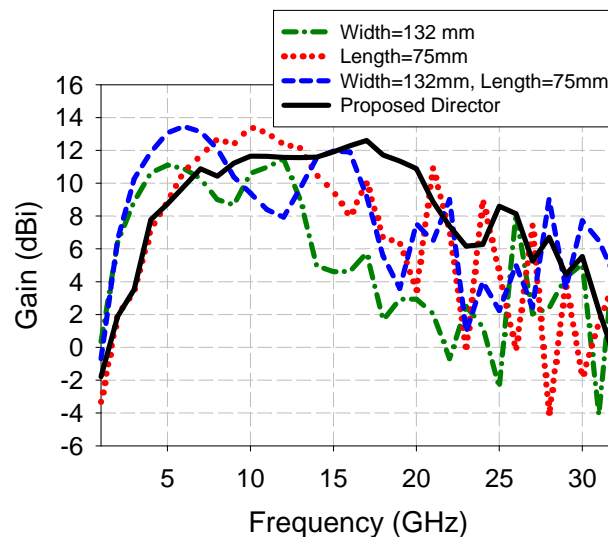


Figure 10.10: Gain comparison of the proposed antenna and typical antipodal Vivaldi without the director and with different sizes.

In order to expand the Vivaldi antenna gain bandwidth to higher frequencies, the substrate thickness needs to be reduced. Figure 10.11 shows the simulated gain of the proposed antenna with and without the director and for different substrate thicknesses. As seen, reducing the substrate thickness by 50% improves the gain at high frequencies, however, not to be better than the addition of the parasitic elliptical patch.

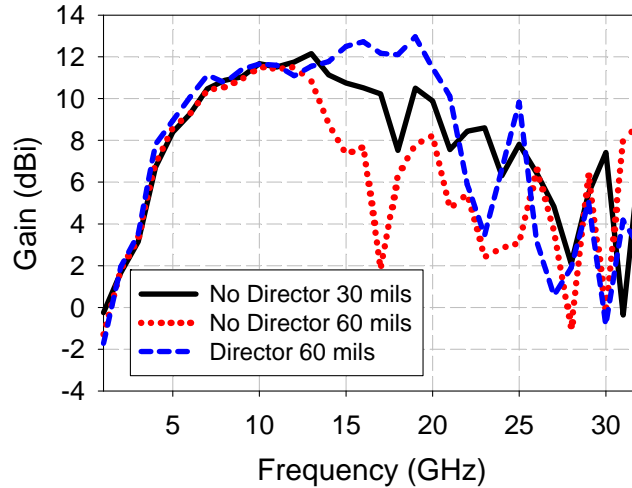


Figure 10.11: The simulated gain of the proposed antenna with/without the director for different substrate thicknesses.

10.5 Conclusion

A multi-octave Vivaldi antenna has been developed to provide the capability to interrogate various harmonic tags. A new approach for improving the gain and bandwidth of the proposed antenna has been investigated. Inserting a parasitic elliptical patch in the slot aperture is found to be an effective approach to provide remarkable gain and directivity improvement. It allows the gain bandwidth to be expanded and reduces the gain variation, compared to what has been reported for antipodal Vivaldi antenna with similar size. This technique was found to be more effective than doubling the size of the antenna. The effectiveness of the proposed approach has been verified experimentally. The proposed antenna performance can be further enhanced by reducing the substrate thickness.

CHAPTER 11 : NON-DISPERSIVE PHASE SHIFTERS

Note to Reader

Portions of this chapter have been previously published in [196], and have been reproduced with permission from IEEE. Permission is included in Appendix A.

11.1 Introduction

Steering the interrogator radiation beam for tracking and locating harmonic sensors is of concern. Beam steering can be accomplished using mechanical and non-mechanical methods. Methods for mechanical beam-steering include rotating the antenna using a gimbal [197], moving parasitic elements or parasitic antenna around the radiator (as discussed in Section 2.5), and the use of mechanical tunable reflectors [104]. Mechanical steering offers better functionality, lower RF power loss, and lower cost, while non-mechanical beam steering is advantageous in terms of size, weight, speed, reliability, and DC power consumption.

This chapter presents a topology to the design of a miniature, wideband, well-matched, non-dispersive phase shifter with low insertion loss on the basis of composite right/left handed (CRLH) transmission line (TL) unit cells [196]. This topology can be employed in the design of a switchable 4-bit phase shifter to provide wideband electronic beam steering. To demonstrate the proposed approach, a lumped element 45° design was prototyped. The lumped element design operates at a center frequency of 2.4 GHz with 50% bandwidth. Experimental results of

the lumped element design demonstrate return loss ≥ 10 dB, insertion loss ≤ 0.5 dB, with a phase shift of 45 ± 1.5 degrees over the entire bandwidth.

In what follows, an overview of broadband phase shifter design is provided in Section 11.2 and a brief description of the operation principle and performance of the proposed CRLH unit cell phase shifter design is presented in Section 11.3. In Section 11.4 the lumped element design and experimental results are demonstrated and an approach for the design of switchable 4-bit phase shifter is discussed in Section 11.5.

11.2 Overview

The phase shifter is one of the key components in the design of phased array antenna system. One of their functions is to adjust the phases of the array element to generate multiple beams. Common approaches to design switchable phase shifters include the switched-line and loaded-line. The switched line approach is more common and uses two paths with different electrical lengths to provide the desired phase delay. The lines can be realized with distributed elements or lumped components loaded with tuning elements such as pin diodes, field effect transistors (FETs), or MEMS devices. To provide different tunable states with precise phase shift angle, different lines with different phase shift are usually cascaded. Each switched line stage is called a bit.

The parameters of concern of such phase shifters are the insertion loss, impedance match, power consumption, speed, and power handling. For the design of wideband phased array, the phase variation and amplitude balance over the bandwidth are also of high concern. There are different techniques to realize broadband 90° and 180° phase shifters such as; the use of coupled lines, microstrip-to-slot line transitions [198, 199], and patterned ground planes [200]. Realizing other than the 90° or 180° phase shift, however, is very challenging. In literature, several

researchers have proposed techniques to develop broadband non-dispersive phase shifters. In [201] the authors combined a conventional delay line with unequal width, equal length lines to achieve a 49% bandwidth. Due to the presence of conventional delay lines, the structure length was considerably large. In [202] a phase shifter topology that combines open and short ended stubs was proposed. This topology led to degradation in the phase variation and impedance matching performances.

In recent literature, different researchers have proposed the use of CRLH TL unit cells to broaden the bandwidth [203, 204, 205]. This technique has the ability to provide an arbitrary phase response. In [203] this technique has been employed in the design of broadband quadrature power splitter. It has been experimentally demonstrated that this technique provides 104% bandwidth with an amplitude imbalance of less than 0.9 dB and a phase error of less than $\pm 5^\circ$. In these studies, the CRLH transmission lines were realized using distributed elements loaded with left-handed section on one path, therefore, the size was large.

More recently, references [206, 207, 208] have proposed to use CRLH unit cells in both of the signal paths integrated with MEMS switches to realize broadband phase shifters. This topology has the potential for reduced size, however, the bandwidth is limited. In addition, all these studies have been limited to varying only one or two lumped component values, thereby resulting in a more limited bandwidth performance. To alleviate the above issues, all the capacitive and inductive loads can be varied. The bandwidth that can be achieved with this approach is $\sim 50\%$.

11.3 CRLH TL Unit Cell Based Phase Shifter

The CRLH unit cell presents a unique design opportunity for phase shifter applications. Utilizing two-circuit states in the phase shifter topology and switching from state #1 to state #2

by simultaneously varying all values of the series and shunt circuit components, a broadband constant phase difference between the states can be realized while maintaining good return loss. To demonstrate the concept, Figure 11.1 shows the lumped element circuit model of the CRLH unit cell and the dispersion diagram of a two-state phase shifter. The phase constant β of the CRLH transmission line is given by [209]:

$$\beta = \omega\sqrt{L_R C_R} - 1/\omega\sqrt{L_L C_L}, \quad (11.1)$$

where L_R is right-handed series inductance, C_R is the right-handed shunt capacitance, C_L is the left-handed series capacitance, and L_L is the left-handed shunt inductance per unit length. Due to the antiparallel phase and group velocity introduced by the left-handed loads, the circuit parameters of the two states can be optimized to maintain nearly identical dispersion diagram slopes over a broad frequency band, (Figure 11.1, right). As a result, the phase difference between the two states can be made almost constant, essentially leading to a non-dispersive circuit component. The phase shift between the two states is given by:

$$\Delta\Phi = |\beta_2 - \beta_1| \times L, \quad (11.2)$$

where β_2 and β_1 are the phase constants of state #2 and state #1, respectively, and L is the effective length of the CRLH TL unit cell. In contrast, the slow-wave based phase shifter structures would fail to provide such broadband performance due to the swift variation in the β - ω slope.

To provide equal return loss performance the right- and left-handed loads can be designed to give the same characteristic impedance. In such a balanced CRLH configuration ($L < \lambda_g/4$) [209], the characteristic impedance is simply given by the ratio $(L_R/C_R)^{1/2} = (L_L/C_L)^{1/2}$ at $\beta=0$ and can be matched to a conventional transmission line over a broad range of frequencies.

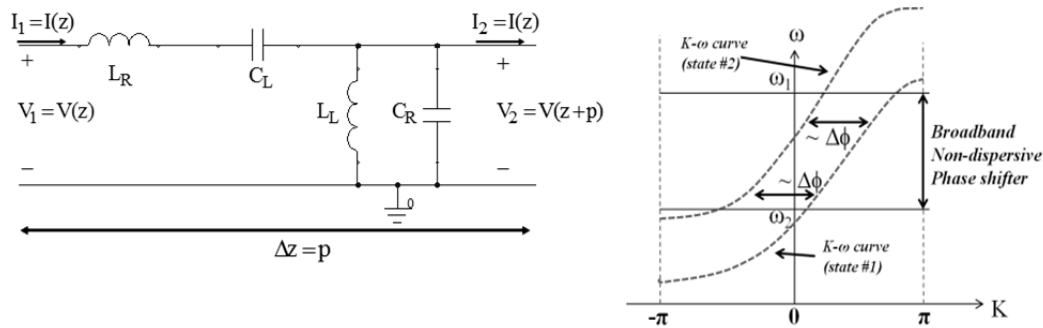


Figure 11.1: Lumped element circuit model of a CRLH unit cell (Left) and representative K - ω diagrams of a balanced CRLH unit cell being switched from state #1 to state #2 (right).

11.4 Lumped Element 45° Phase Shifter Design

The baseline approach that is adopted for the prototype design is to use primarily a lumped element implementation, with minimal distributed elements. Figure 11.2 illustrates the design model of the proposed CRLH based unit cell phase shifter optimized to operate from 1.8 to 3 GHz with minimal phase variation and good impedance match. In the optimized 45° unit cell, the left-handed elements in the high-value state circuit are approximately 1.7 times the value of the corresponding elements in the low-value state and $(L_R/C_R)^{1/2} = (L_L/C_L)^{1/2} \approx 50$ in each state. These ratios were forced to maintain a good impedance match in both states. The used substrate is *Rogers/RT Duroid 5880* with a thickness of 20 mils and ϵ_r of 2.2, and the capacitors and inductors are *Johanson 0201* ($C_{L1}=1.2$ pF, $L_{R1}=1$ nH, $L_{L1}=3.3$ nH, $C_{R1}=0.2$ pF, $C_{L2}=2$ pF, $L_{R1}=1$ nH, $L_{L2}=5.6$ nH, $C_{R2}=0.2$ pF). The circuit has been designed using the simulation tool *ADS 2009u1*.

The simulated and measured return loss, insertion loss, and phase difference between the two states are compared in Figure 11.3. As noted above, the two states were tested separately. As shown, good agreement is found between the expected and measured results. The measured return loss data shows imperfect symmetry between the input and the output ports which could

be attributed to the lumped element values tolerances. The deviation in the insertion loss and phase difference is due to the coaxial connectors and measurement cable effects.

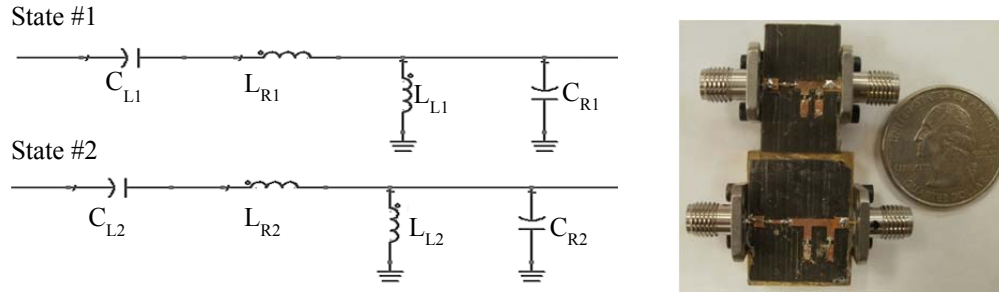


Figure 11.2: Equivalent circuit representations of the 45 degree two-state phase shifter (left) and the fabricated circuits for each state (right).

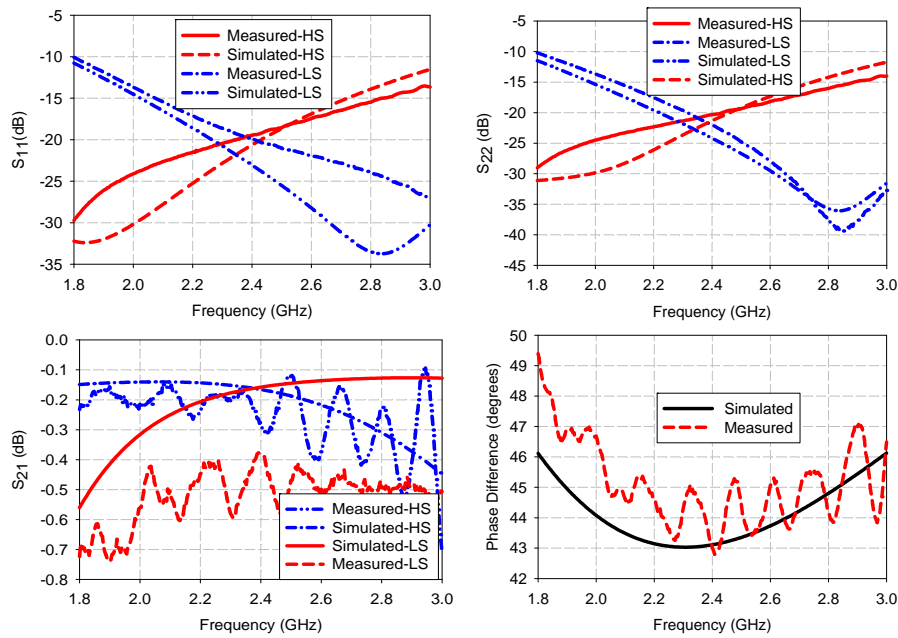


Figure 11.3: The simulated and measured S_{11} (top-left), S_{22} (top-right), S_{21} bottom-left), and phase difference between the two-circuit states (bottom-right).

11.5 4-Bit Phase Shifter Design

Based on the proposed topology, a switchable 4-bit phase shifter (22.5° , 45° , 90° , 180°) can be designed. The approach that can be adopted is utilizing two complete separate circuits and use two single-pole double-throw (SPDT) capacitive RF MEMS switches at each end to switch between state #1 and state #2. All the values of the series and shunt circuit components in the

two states can be varied. This design technique is capable of providing 2^4 different phase shift states. Based on the 45° phase shifter prototype, the expected size of the 4-bit shifter is $\sim 6 \times 7$ cm.

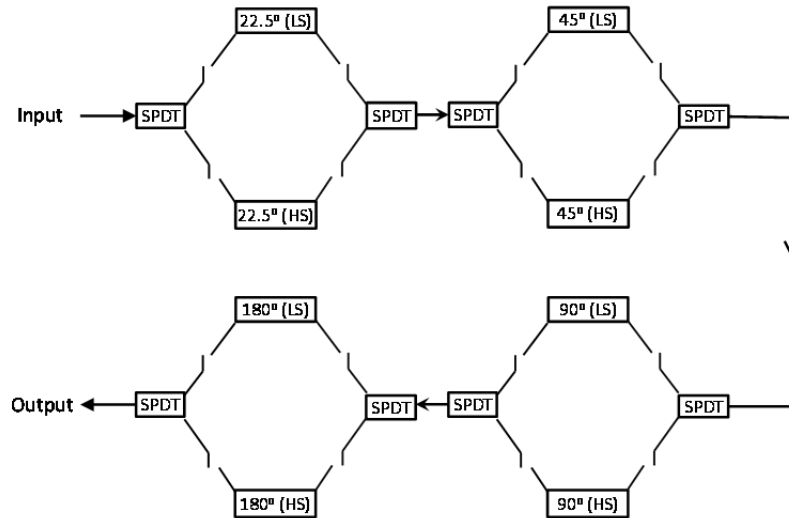


Figure 11.4: Illustration of a 4-bit CRLH transmission line phase shifter.

11.6 Conclusion

A novel metamaterial-based phase shifter topology has been proposed. The preliminary study revealed that the proposed approach has the potential to provide a combination of miniature size, impedance match, broad-bandwidth, and low insertion loss while achieving constant phase versus frequency. Using the same approach, a 4-bit (22.5° , 45° , 90° and 180°) phase shifter can be realized by cascading multiple series LC and shunt LC sections. More investigation on MEMs switches and fabrication approaches is needed to determine the best implementation. The 4-bit phase shifter has the potential to provide wide band beam steering with precise angle.

CHAPTER 12 : SUMMARY AND RECOMMENDATIONS FOR FUTURE WORK

12.1 Summary

This research has demonstrated the potential of the harmonic radar technique for advancing the existing passive wireless sensing technologies. Given the required zero DC power and low RF power operation, the developed sensor nodes address issues of the conversion efficiency, communication range, and occupied volume. Major challenges associated with long-range passive embedded sensing including the remote channel calibration and node identification are also addressed. In addition, effective modulation of the return signal and the suitability of the developed nodes for embedding environment have been experimentally demonstrated. A comparison with others from literature shows that the presented designs outperform previously published designs on the combined basis of conversion efficiency, communication range, and total node volume.

Different options for the harmonic interrogator antenna design have been presented. Depending on the application, each option offers a set of advantages and disadvantages. The first option is based on the use of a dual-channel antenna array. The major advantages of this approach are; 1) the high isolation between the receiving and transmitting channels, and 2) the reduced number of components and complexity of the interrogator unit. The second option is based on the use of mechanically reconfigurable antennas. The major advantages of this option are 1) the potential for reduced size, 2) nearly persistent radiation characteristics over a broad frequency range, and 3) frequency selectivity that is useful for reducing interference and

jamming effects. The third option is based on the use of a single channel multi-octave antenna. The major advantage of this approach is the capability to interrogate a large number of harmonic tags that are largely spaced in different frequency bands without the need to change the antenna.

The advantages of the use of digital additive manufacturing and 3-D printing technologies in the design of electrically-small 3-D antennas and compact 3-D sensor nodes have been demonstrated. The use of these advanced manufacturing technologies enabled the realization of low-cost, light-weight, efficient 3-D RF devices with improved manufacturing reliability and repeatability. These manufacturing technologies also provide an alternative method for miniaturizing planar antennas.

A topology to the design of switchable 4-bit non-dispersive phase shifter has been proposed. This phase shifter can be integrated in the interrogator unit to provide the capability to steer the radiation beam over a wide frequency range. A lumped element 45° phase shifter design demonstrated that this topology has the potential for reduced size and provide low insertion loss and low phase and amplitude imbalance over $> 50\%$ bandwidth.

12.2 Recommendations for Future Work

The proposed sensor nodes have been characterized inside an anechoic chamber, tested outdoor, and embedded inside a 30 cm sand box, however, subsequent field testing in real-world application is still required to verify the suitability of the harmonic radar approach for embedded passive wireless monitoring. Depending on the embedding environment, the embedding may cause severe multipath issues and significant frequency shift and pattern distortion. If the embedding environment has metal objects or high moisture level, significant conversion efficiency decrease could be caused. The packaging process is a necessary activity to pursue to protect the nodes from real world operating conditions.

The modulation capability of the proposed sensor nodes has been demonstrated through the integration of commercial vibration sensors. For structural health monitoring, there are different indicators of more concern such as pH value, humidity and moisture level, and temperature. To measure these parameters, sensor designs that fit the proposed sensor nodes need to be developed. The design of these sensors within a small volume and with no external power source is very challenging.

The overall performance of the wireless system relies heavily on the interrogator design. In this work, we have used off-the-shelf components to test the nodes and we have developed different antenna candidates. However, a complete integrated handheld interrogator radar unit has not been designed. The interrogator is required to have the capability to transmit a narrowband continuous wave (CW) signal and be able to process twice the frequency. The interrogator also needs to have the capability to extract the environment characteristics from the frequency response. In addition, an automated nodes localization capability is highly desirable. For this purpose, mechanical and electronic tuning can be incorporated. An important consideration of the interrogator unit is the isolation between the interrogation signal and the sensor return signal. This issue is one of the major communication range limitations and may limit the antenna choice. In order to improve the detection and the sensitivity, very narrow band filtering is required. These issues in combination may also introduce limitations to the design of a handheld interrogator.

REFERENCES

- [1] J. Caicedo, J. Marulanda, P. Thomson, and S. Dyke, "Monitoring of bridges to detect changes in structural health," *Proceedings of the 2001 American Control Conf.*, Arlington, Virginia, Jun. 2001.
- [2] J. Bernhard, K. Hietpas, E. George, D. Kuchima, and H. Reis, "An interdisciplinary effort to develop a wireless embedded sensor system to monitor and assess corrosion in the tendons of prestressed concrete girders," *IEEE Topical Conf. Wireless Comm Tech*, pp. 241-243, Oct. 2003.
- [3] Shams, K.M.Z.; Ali, M., "Wireless power transmission to a buried sensor in concrete," *IEEE Sens. J.*, vol. 7, no. 12, pp.1573-1577, Dec. 2007.
- [4] S. Yuan, X. Lai, X. Zhao, X. Xu, and L. Zhang, "Distributed structural health monitoring system based on smart wireless sensor and multiagent technology," *J. Smart Mater. Struct.*, vol. 15, pp. 1–8, 2006.
- [5] J. P. Lynch, "Overview of wireless sensors for real-time health monitoring of civil structures," in *Proc. 4th Int. Workshop Struct. Control Monitoring*, New York, Jun. 10–11, 2004.
- [6] J. Ong, Z. You, J. Mills-Beale, E. Tan, B. Pereles, and K. Ong, "A wireless, passive embedded sensor for real-time monitoring of water content in civil engineering materials," *IEEE Sensors J.*, vol. 8, no. 12, pp. 2053-2058, Dec. 2008.
- [7] A. Deivasigamani, A. Daliri, C. Wang, and S John, "A review of passive wireless sensors for structural health monitoring" *Modern applied Science*, vol. 7, no. 2, 2013.
- [8] J. Ong, Z. You, J. Beale, E. Tan, B. Pereles, and K. Ong, "A wireless, passive embedded sensor for real-time monitoring of water content in civil engineering materials," *IEEE Sensors J.*, vol. 8, no. 12, pp. 2053-2058, Dec. 2008.
- [9] A. Bereketli and O. Akan, "Communication coverage in wireless passive sensor networks," *IEEE Commun. Lett.*, vol. 13, no. 2, pp. 133-135, Feb. 2009.
- [10] X. Zhang and F.-Y. Wang, "Key technologies of passive wireless sensor networks based on surface acoustic wave resonators," *IEEE Int. Conf. Networking, Sensing and Contr.*, pp. 1253-1258, Apr. 2008.

- [11] S. Sudevalayam and P. Kulkarni, "Energy harvesting sensor nodes: survey and implications," *IEEE Commun. Surv. Tut.*, vol. 13, no. 3, pp. 443-461, Third Quarter 2011.
- [12] J. Wardlaw, I. Karaman, and A. Karsilayan, "Low-power circuits and energy harvesting for structural health monitoring of bridges," *IEEE Sensors Journal*, , vol. 13, no. 2, pp.709-722, Feb. 2013.
- [13] E. Sazonov, H. Li, D. Curry, and P. Pillay, "Self-powered sensors for monitoring of highway bridges," *IEEE Sensors J.*, vol. 9, no. 11, pp. 1422–1429, Nov. 2009.
- [14] J. Chin, J. Rautenberg, C. Ma, S. Pujol, and D. Yau, "An experimental low-cost, low-data-rate rapid structural assessment network," *IEEE Sensors J.*, vol. 10, no. 7, pp. 1361–1369, Jul. 2010.
- [15] R. Bhuiyan, R. Dougal, and M. Ali, "A miniature energy harvesting device for wireless sensors in electric power system," *IEEE Sensors J.*, vol. 10, no. 7, pp. 1249–1258, Jul. 2010.
- [16] S. Spiekermann and S. Evdokimov, "Critical RFID privacy-enhancing technologies," *IEEE Security Privacy*, vol. 7, no. 2, pp. 56-62, Mar. 2009.
- [17] B. Nath, F. Reynolds, and R. Want, "RFID technology and applications," *IEEE Pervasive Computing*, vol. 5, no. 1, pp. 22- 24, Jan. 2006.
- [18] J. Hines, "Review of recent passive wireless SAW sensor and sensor-tag activity," *IEEE Fly by Wirel. Workshop, 2011 4th Annual Caneus*, pp. 1-2, Jun. 2011.
- [19] V. Plessky and L. Reindl, "Review on SAW RFID tags," *IEEE Trans. Ultrason. Ferroelect. Freq. Contr.*, vol. 57, no. 3, pp. 654-668, Mar. 2010.
- [20] C. Hartmann, L. Claiborne, "Fundamental limitations on reading range of passive IC-based RFID and SAW-based RFID," *IEEE Int. Conf. RFID*, pp. 41-48, Mar. 2007.
- [21] Z. Tsai et al., "A high-range-accuracy and high-sensitivity harmonic radar using pulse pseudorandom code for bee searching," *IEEE Trans. Microw. Theory Techn.*, vol. 61, no. 1, pp. 666-675, Jan. 2013.
- [22] M. Bouthinon, J. Gavan, and F. Zadworny, "Passive microwave transposer, frequency doubler for detecting the avalanche victims," *IEEE Eur. Microw. Conf.*, pp. 579-583, 8-12 Sep. 1980.
- [23] D. Psychoudakis, W. Moulder, C. Chen, H. Zhu, and J. Volakis, "A portable low-power harmonic radar system and conformal tag for insect tracking," *IEEE Antennas Wirel. Propag. Lett.*, vol. 7, pp. 444-447, 2008.

- [24] B. Colpitts and G. Boiteau “Harmonic radar transceiver design: Miniature tags for insect tracking,” *IEEE Trans. Antennas Propag.*, vol. 52, no. 11, pp. 2825–2832, Nov. 2004.
- [25] T. Weller, J. Wang, I. Nassar, J. Dewdney, R. Davidova, J. Frolik, and V. Sakamuri, "A Wireless interrogator - passive sensor approach for deeply embedded sensing applications," *IEEE Antennas Propag. Soc. Int. Symp.*, pp. 1445-1448, Jul. 2011.
- [26] S. Ramadan, L. Gaillet, C. Tessier, and H. Idrissi, “Detection of stress corrosion cracking of high-strength steel used in prestressed concrete structures by acoustic emission technique,” *Appl. Surf. Sci.*, 254, pp. 2255–2261, 2008.
- [27] A. Raghavan, “Guided-wave structural health monitoring,” Ann Arbor, MI: University of Michigan, 2007
- [28] G.J. Tsamasphyros, E.A. Koulalis, G.N. Kanderakis, N.K. Furnarakis, and V.Z. Astreinidis, “Structural health monitoring of a steel railway bridge using optical fibre Bragg grating sensors and numerical simulation,” *Proceedings of the 3rd European Workshop on Structural Health Monitoring*, 2006.
- [29] S. Aoki, Y. Fujino, and M. Abe, “Intelligent bridge maintenance system using MEMS and network technology,” *Proceedings of the SPIE in Smart Systems and NDE for Civil Infrastructures*, San Diego, CA, vol. 5057, pp. 37–42, Mar. 2003.
- [30] M. Basheer, V. Rao, and M. Derriso, “Self-organizing wireless sensor networks for structural health monitoring,” in *Proceedings of the 4th International Workshop on Structural Health Monitoring*, Stanford, CA, pp. 1193–1206, Sep. 2003.
- [31] R. Bennett, B. Hayes-Gill, J. Crowe, R. Armitage, D. Rodgers, and A. Hendroff, “Wireless monitoring of highways,” *Proceedings of the SPIE in Smart Systems for Bridges, Structures, and Highways*, Newport Beach, CA, vol. 3671, pp. 173–182, Mar. 1999.
- [32] J. Binns, “Bridge sensor system delivers results quickly,” *Civil Engineering*, Vol. 74, No. 9, pp. 30–31, 2004.
- [33] B. Carkhuff, and R. Cain, “Corrosion sensors for concrete bridges,” *IEEE Instrumentation and Measurement Magazine*, Vol. 6, No. 2, pp. 19–24, 2003.
- [34] J. Lynch, and K. J. Koh, “A summary review of wireless sensors and sensor networks for structural health monitoring,” *Shock and Vibration Digest*, 38(2): pp. 91–128, 2006.
- [35] J. Butler, A. Viglio, F. Vendi, and S. Walsh, “Wireless passive resonant-circuit, inductively coupled, inductive strain sensor,” *Sensors and Actuators A: Physical*, vol. 102, issue 1-2, pp. 61-66, 2002.
- [36] J. Chuang, D. Thomson, and G. Bridges, “Embeddable wireless strain sensor based on resonant RF cavities,” *Review of Scientific Instruments*, vol. 76, issue 9, 2005.

- [37] F. Umbrecht, M. Wendlandt, D. Juncker, C. Hierold, and J. Neuenschwander, "A wireless implantable passive strain sensor system," *IEEE Sensors*, pp.4, Oct.-Nov. 2005.
- [38] R. Matsuzaki, and A. Todoroki, "Wireless detection of internal delamination cracks in CFRP laminates using oscillating frequency changes," *Composites Science and Technology*, vol. 66, issue 3-4 pp. 407-416, Mar. 2006.
- [39] A. Sample, D. Yeager, P. Powledge, A. Mamishev, and J. Smith, "Design of an RFID-based battery-free programmable sensing platform," *IEEE Trans. Inst. Meas.*, vol. 57, no. 11, pp. 2608-2615, Nov. 2008.
- [40] J. Hines, "Review of recent passive wireless SAW sensor and sensor-tag activity," *IEEE Fly by Wirel. Workshop, 2011 4th Annual Canesus*, pp. 1-2, Jun. 2011.
- [41] V. Plessky and L. Reindl, "Review on SAW RFID tags," *IEEE Trans. Ultrason. Ferroelect. Freq. Contr.*, vol. 57, no. 3, pp. 654-668, Mar. 2010.
- [42] G. Scholl, C. Korden, E. Riha, C. Ruppel, U. Wolff, G. Riha, L. Reindl, and R. Weigel, "SAW-based radio sensor systems for short-range applications," *IEEE Microwave Magazine*, vol. 4, no. 4, pp. 68-76, Dec. 2003.
- [43] R. Want, "Enabling ubiquitous sensing with RFID," *Computer*, vol. 37, no. 4, pp. 84-86, Apr. 2004.
- [44] D. Davies and R. Klensch, "Two-frequency secondary radar incorporating passive transponders," *Electron. Lett.*, vol. 9, no. 25, pp. 592-593, Dec. 1973.
- [45] V. Viikari, H. Seppa, and D.-W. Kim, "Intermodulation read-out principle for passive wireless sensors," *IEEE Trans. Microw. Theory Techn.*, vol. 59, no. 4, pp. 1025-1031, Apr. 2011.
- [46] V. Viikari and H. Seppa, "RFID MEMS sensor concept based on intermodulation distortion," *IEEE Sens. Jour.*, vol. 9, no. 12, pp. 1918-1923, Dec. 2009.
- [47] K. Yamamoto, "A 1.8-V operation 5-GHz-band CMOS frequency doubler using current-reuse circuit design technique," *IEEE Journal of Solid-State Circuits*, vol. 40, no. 6, pp. 1288-1295, Jun. 2005.
- [48] H. Chang, G. Chen, and Y. Hsin, "A broadband high efficiency high output power frequency doubler," *IEEE Microwave and Wireless Components Letters*, vol. 20, no. 4, pp. 226,228, Apr. 2010.
- [49] F. Yu, K. Lyon, and E. Kan, "A novel passive RFID transponder using harmonic generation of nonlinear transmission lines," *IEEE Transactions on Microwave Theory and Techniques*, vol. 58, no. 12, pp. 4121-4127, Dec. 2010.

- [50] S. Simion, G. Bartolucci, and R. Marcelli, "Second harmonic generation on Non-Linear Composite Right-/Left-Handed Transmission Line," *International Semiconductor Conference*, vol. 1, pp.345-348, Oct. 2009.
- [51] C. W. Pobanz and T. Itoh, "A microwave noncontact identification transponder using subharmonic interrogation," *IEEE Trans. Microw. Theory Tech.*, vol. 43, no. 7, pp. 1673–1679, Jul. 1995.
- [52] H. Aumann, E. Kus, B. Cline, and N. Emanetoglu, "A low-cost harmonic radar for tracking very small tagged amphibians," *IEEE Int. Inst. Mea. Tech. Conf.*, pp. 234-237, May 2013.
- [53] J. Kiriazi, J. Nakakura, V. Lubecke, and K. Hall, "Low profile harmonic radar transponder for tracking small endangered species," *IEEE Annual International Conference of the Engineering in Medicine and Biology Society*, pp. 2338-2341, Aug. 2007.
- [54] J. R. Riley and A. D. Smith, "Design considerations for an harmonic radar to investigate the flight of insects at low altitude," *Comput. Electron. Agriculture*, vol. 35, pp. 151–169, 2002.
- [55] N. Tahir and D. G. Brooker, "Recent developments and recommendations for improving harmonic radar tracking systems," *Proc. 5th Eur. Conf. Antennas Propag.*, pp. 1531–1535, Apr. 2011.
- [56] R. Brazee, E. Miller, M. Reding, M. Klein, B. Nudd, and H. Zhu, "A transponder for harmonic radar tracking of black vine weevil in behavioral research," *ASAE Trans.*, pp. 831-838, 2005.
- [57] S. Presas, T. Weller, S. Silverman, and M. Rakijas, "High efficiency diode doubler with conjugate- matched antennas," *IEEE European Microw. Conf.*, pp. 250-253, Oct. 2007.
- [58] S. Aguilar, and T. Weller, "Tunable harmonic re-radiator for sensing applications," *IEEE MTT-S Int. Microw. Symp. Dig.*, pp. 1565-1568, Jun. 2009.
- [59] D. Ahbe, S. Beer, T. Zwick, Y. Wang and M. Tentzeris, "Dual-band antennas for frequency-doubler-based wireless strain sensing," *IEEE Antennas Wireless Propag. Lett.*, vol. 11, pp. 216-219, Feb. 2012.
- [60] G. Vera, Y. Duroc, and S. Tedjini, "Analysis of harmonics in UHF RFID signals," *IEEE Trans. Microwave Theory Techn.*, vol. 61, no. 6, pp. 2481-2490, Jun. 2013.
- [61] I. Nassar, "Small antenna design for 2.4 GHz applications," Master's thesis, University of South Florida, Oct. 2010.
- [62] H.A. Wheeler, "The Radiansphere around a Small Antenna," *Proceedings of the IRE* , vol.47, no.8, pp.1325-1331, Aug. 1959.

- [63] H. A. Wheeler, "Fundamental limitations of small antennas," *Proceedings of the IRE*, vol. 35, no. 12, pp. 1479- 1484, Dec. 1947.
- [64] H. A. Wheeler, "Small antennas," *IEEE Transactions on Antennas and Propagation*, vol. 23, no. 4, pp. 462-469, Jul. 1975.
- [65] L.J. Chu, "Physical limitation of omni-directional antennas," *Journal of Applied Physics*, vol. 19, pp.1163-1175, Dec. 1948.
- [66] R. F. Harrington, "Effect of antenna size on gain, bandwidth and efficiency", *J. Res. Nat. Bur. Stand.*, vol. 64D, No. 1, pp.1-12, Jan./Feb. 1960.
- [67] R.C. Hansen, "Fundamental limitations in antennas," *Proceedings of the IEEE*, vol. 69, no. 2, pp.170-182, Feb. 1981.
- [68] J. S McLean, "A re-examination of the fundamental limits on the radiation Q of electrically small antennas," *IEEE Trans. Antennas Propag.*, vol. 44, no. 5, pp. 672-676, May 1996.
- [69] J. Sten, A. Hujanen, and P. Koivisto, "Quality factor of an electrically small antenna radiating close to a conducting plane," *IEEE Transactions on Antennas and Propagation*, vol. 49, no. 5, pp. 829-837, May 2001.
- [70] D. Sievenpiper, D. Dawson, M. Jacob, T. Kanar, S. Kim, J. Long, and R. Quarfoth, "Experimental validation of performance limits and design guidelines for small antennas," *IEEE Transactions on Antennas and Propagation*, vol. 60, no. 1, pp. 8-19, Jan. 2012.
- [71] A. Thiele, P. Detweiler, and R. Penno, "On the lower bound of the radiation Q for electrically small antennas," *IEEE Transactions on Antennas and Propagation*, vol. 51, no. 6, pp. 1263-1269, Jun. 2003.
- [72] W. Geyi, "A method for the evaluation of small antenna Q," *IEEE Trans. Antennas Propag.*, vol. 51, pp. 2124–2129, 2003.
- [73] A. D. Yaghjian and S. R. Best, "Impedance, bandwidth, and Q of antennas," *IEEE Trans. Antennas Propag.*, vol. 53, pp. 1298–1324, 2005.
- [74] D. Kwon, "On the radiation Q and the gain of crossed electric and magnetic dipole moments," *IEEE Transactions on Antennas and Propagation*, vol. 53, no. 5, pp. 1681-1687, May 2005.
- [75] D. Kwon, "Radiation Q and gain of TM and TE sources in phase-delayed rotated configurations," *IEEE Transactions on Antennas and Propagation*, vol. 56, no. 8, pp. 2783-2786, Aug. 2008.

- [76] D. Pozar, "New results for minimum Q, maximum gain, and polarization properties of electrically small arbitrary antennas," *3rd European Conference on Antennas and Propagation*, pp. 1993-1996, Mar. 2009.
- [77] R. C. Hansen and R. E. Collin, "A new Chu formula for Q," *IEEE Antennas Propag. Mag.*, vol. 51, pp. 38-41, 2009.
- [78] H. L. Thal, "Gain and Q bounds for coupled TM-TE modes," *IEEE Trans. Antennas Propag.*, vol. 57, pp. 1879-1885, 2009.
- [79] G. A. E. Vandebosch, "Reactive energies, impedance, and Q factor of radiating structures," *IEEE Trans. Antennas Propag.*, vol. 58, pp.1112-1127, 2010.
- [80] W. Geyi, P. Jarmuszewski, and Y. Qi, "The Foster reactance theorem for antennas and radiation Q," *IEEE Trans. Antennas Propag.*, vol. 48, pp. 401-408, 2000.
- [81] S. R. Best, "The Foster reactance theorem and quality factor for antennas," *IEEE Antennas Wireless Propag. Lett.*, vol. 3, pp. 306-309, 2004.
- [82] R. Bancroft, "Fundamental Dimension Limits of Antennas Ensuring Proper Antenna Dimensions in Mobile Device Designs", Centurion Wireless Technologies Westminster, Colorado.
- [83] J. Volakis, C. Chin, and K. Fujimoto, "Small Antennas: Miniaturization Techniques & Applications", The McGraw-Hill, PP.1-100, 2010.
- [84] P. Kildal, and S. Best, "Further investigations of fundamental directivity limitations of small antennas with and without ground planes," *IEEE Antennas and Propagation Society International Symposium*, pp. 1-4, Jul. 2008.
- [85] R. Fante, "Maximum possible gain for an arbitrary ideal antenna with specified quality factor," *IEEE Transactions on Antennas and Propagation*, vol. 40, no. 12, pp. 1586-1588, Dec. 1992.
- [86] W. Geyi, "Optimization of the ratio of gain to Q ," *IEEE Transactions on Antennas and Propagation*, vol. 61, no. 4, pp. 1916-1922, Apr. 2013.
- [87] Z. Zahairs, E. Vafiadis, and J. N. Sahalos, "On the design of a dual-band base station wire antenna," *IEEE Antennas Propag. Mag.*, vol. 42, no.6, pp. 144-151, Dec. 2000.
- [88] S. He, and J. Xie, "Analysis and design of a novel dual-band array antenna with a low profile for 2400/5800-MHz WLAN systems," *IEEE Transactions on Antennas and Propagation*, vol. 58, no. 2, pp. 391-396, Feb. 2010.
- [89] M.-I. Lai, T.-Y. Wu, J.-C. Hsieh, C.-H. Wang, and S.-K. Jeng, "Design of reconfigurable antennas based on an L-shaped slot and PIN diodes for compact wireless devices," *IET Microw. Antennas Propag.*, vol. 3, no. 1, pp. 47-54, Feb. 2009.

- [90] N. Haridas et al, "Reconfigurable MEMS antennas," *IEEE NASA/ESA Conference Adaptive Hardware and Systems*, pp. 147-154, Jun. 2008.
- [91] J. Bernhard, E. Kiely, and G. Washington, "A smart mechanically actuated two-layer electromagnetically coupled microstrip antenna with variable frequency, bandwidth, and antenna gain," *IEEE Trans. Antennas Propag.*, vol. 49, no. 4, pp. 597-601, Apr. 2001.
- [92] K. Daheshpour, S. Mazlouman, A. Mahanfar, J. Yun, X. Han, C. Menon, F. Carpi, and R. Vaughan, "Pattern reconfigurable antenna based on moving V-shaped parasitic elements actuated by dielectric elastomer," *Electronics Letters*, vol. 46, no. 13, pp. 886-888, Jun. 2010.
- [93] S. Mazlouman, M. Soleimani, A. Mahanfar, C. Menon, and R. Vaughan, "Pattern reconfigurable square ring patch antenna actuated by hemispherical dielectric elastomer," *Electronics Letters*, vol. 47, no. 3, pp. 164-165, Feb. 2011.
- [94] A. Calmon, G. Pacheco, and M. Terada, "A novel reconfigurable UWB log-periodic antenna," *IEEE Antennas and Propagation Society International Symposium*, pp. 213-216, Jul. 2006.
- [95] M. Khan, G. Hayes, J.-H So, G. Lazzi, and M. Dickey, "A frequency shifting liquid metal antenna with pressure responsiveness," *Applied Physics Letters*, vol. 99, no. 1, pp. 013501-013501, Jul. 2011.
- [96] D. Rodrigo, L. Jofre, and B. Cetiner, "Circular beam-steering reconfigurable antenna with liquid metal parasitics," *IEEE Transactions on Antennas and Propagation*, vol. 60, no. 4, pp. 1796-1802, Apr. 2012.
- [97] S. Cheng, A. Rydberg, K. Hjort, and Z. Wu, "Liquid metal stretchable unbalanced loop antenna," *Appl. Phys. Lett.*, vol. 94, no. 14, p. 144103, 2009.
- [98] J.-H. So, J. Thelen, A. Qusba, G. J. Hayes, G. Lazzi, and M. D. Dickey, "Reversibly deformable and mechanically tunable fluidic antennas," *Adv. Funct. Mater.*, vol. 19, no. 22, pp. 3632-3637, 2009.
- [99] A. Traille, S. Bouaziz, S. Pinon, P. Pons, H. Aubert, A. Boukabache, and M. Tentzeris, "A wireless passive RCS-based temperature sensor using liquid metal and microfluidics technologies," *European Microwave Conference*, pp. 45-48, Oct. 2011.
- [100] A. Mahanfar, C. Menon, and R. G. Vaughan, "Smart antennas using electro-active polymers for deformable parasitic elements," *IET Electron. Lett.*, 2008.
- [101] S. Mazlouman, MA. Mahanfar, C. Menon, and R. Vaughan, "Mechanically reconfigurable antennas using electro-active polymers (EAPs)," *IEEE Int. Sym. Antennas Propag.*, pp.742-745, Jul. 2011.

- [102] Y. Bar-Cohen, "Electroactive polymer (EAP) actuators as artificial muscles – reality, potential and challenges," *SPIE Press*, 2nd Edition, Mar. 2004.
- [103] S. Mazlouman, A. Mahanfar, C. Menon, and R. Vaughan, "Reconfigurable axial-mode helix antennas using shape memory alloys," *IEEE Transactions on Antennas and Propagation*, vol. 59, no. 4, pp. 1070-1077, Apr. 2011.
- [104] D. Sievenpiper, J. Schaffner, R. Loo, G. Tangonan, S. Ontiveros, and R. Harold, "A tunable impedance surface performing as a reconfigurable beam steering reflector," *IEEE Transactions on Antennas and Propagation*, vol. 50, no. 3, pp. 384-390, Mar. 2002.
- [105] P. Joshi, R. Dehoff, C. Duty, W. Peter, R. Ott, L. Love, and C. Blue, "Direct digital additive manufacturing technologies: path towards hybrid integration," *Future of Instrumentation International Workshop*, pp. 1-4, Oct. 2012.
- [106] B. Berman, "3-D printing: The new industrial revolution", *Business Horizons*, vol. 55, pp. 155-162, 2012.
- [107] R.O. Kadara, N. Jenkinson, B. Li, K.H. Church, and C.E. Banks, "Manufacturing electrochemical platforms: Direct-write dispensing versus screen printing " *Electrochem. Commun.*, vol. 10, pp.1517-1519, 2008.
- [108] Y. Ning, Y. Wong, J. Fuh, and H. Loh, "An approach to minimize build errors in direct metal laser sintering," *IEEE Transactions on Automation Science and Engineering*, vol. 3, no. 1, pp. 73-80, Jan. 2006.
- [109] T. Chartier, C. Duterte, N. Delhote, D. Baillargeat, S. Verdeyme, C. Delage, and C. Chaput, "Fabrication of millimeter wave components via Ceramic stereo- and microstereolithography processes," *Journal of the American Ceramic Society*, vol. 91, issue 8, pp. 2469–2474, Aug. 2008.
- [110] M. Vaezi, H. Seitz, and S. Yang, "A review on 3D microadditive manufacturing technologies," *Int. J. Adv. Manuf. Technol.*, vol. 67, issue 5-8, pp. 1721-1754, 2013.
- [111] J. Czyzewski, P. Burzynski, K. Gawel, and J. Meisner, "Rapid prototyping of electrically conductive components using 3D printing technology," *J. Materials Proc.Techn.*, vol. 209, Issue 12-13, pp. 5281-5285, Jul. 2009.
- [112] I. Nassar, T. Weller, and J. Frolik, "A 3-D passive harmonic repeater for compact wireless sensor nodes," *IEEE Transaction on Microwave Theory and Techniques*, vol. 60, no. 10, pp. 3309-3316, Oct. 2012.
- [113] I. Nassar and T. Weller, "Design and characterization of a passive harmonic sensor embedded in sand," *IEEE Wireless and Microwave Technology Conference (WAMICON)*, pp. 1-3, April 2013.

- [114] I. Nassar and T. Weller, "Development of novel 3-D cube antennas for compact wireless sensor nodes," *IEEE Trans. Antennas Propag.*, vol. 60, no. 2, pp. 1059-1065, Feb. 2012.
- [115] M. Faber, J. Chramiec, and M. Adamski, "*Microwave and Millimeter-Wave Diode Frequency Multipliers*," Artech House Norwood, MA, 1995.
- [116] D. Pozar, "Microwave Engineering," Third Edition, *John Wiley & Sons, Inc.*, New Jersey, Ch. 13, pp. 98-106, 2005.
- [117] K. Williams and R. Greeley, "Radar attenuation by sand: laboratory measurements of radar transmission," *IEEE Trans. Geoscience. Remote Sensing*, vol. 39, no. 11, pp. 2521-2526, Nov. 2001.
- [118] I. Nassar, T. Weller, and J. Wang, "A high-efficiency, miniaturized sensor node with machined-substrate antennas for embedded wireless monitoring" *IEEE International Microwave Symposium (IMS 2013)*, to be published.
- [119] Y. Yang and C. Lin, "Vehicle-bridge interaction dynamics and potential applications," *J. Sound Vibrat.*, vol. 284, nos. 1-2, pp. 205-226, 2005.
- [120] S. Kim, S. Pakzad, D. Culler, G. Fenves, S. Glaser, and M. Turon, "Health monitoring of civil infrastructures using wireless sensor networks." *IEEE Int. Conf. Inf. Process. Sensor Net.*, Apr. 2007.
- [121] I. Nassar and T. Weller, "A Compact Dual-Channel Transceiver for Passive Embedded Monitoring," *IEEE Transaction on Microwave Theory and Techniques*, submitted for publication June 2013.
- [122] D. Girbau, A. Ramos, A. Lazaro, S. Rima, and R. Villarino, "Passive wireless temperature sensor based on time-coded UWB chipless RFID tags," *IEEE Trans. Micr. Theory Techn.*, vol. 60, no. 11, pp.3623-3632, Nov. 2012.
- [123] S. Preradovic, I. Balbin, N. Karmakar, and G. Swiegers, "Multiresonator-based chipless RFID system for low-cost item tracking," *IEEE Trans. Micr. Theory Techn.*, vol. 57, no. 5, pp.1411-1419, May 2009.
- [124] I. Nassar and T. Weller, "An electrically-small, 3-D cube antenna fabricated with additive manufacturing" *IEEE Radio and Wireless Symp. (RWS 2013)*, pp. 262-264, Jan. 2013.
- [125] H. Nakano, H. Tagami, A. Yoshizawa, and J. Yamauchi, "Shortening ratios of modified dipole antennas," *IEEE Trans. Antennas Propag.*, vol. 32, no. 4, pp. 385- 386, Apr. 1984.
- [126] I. Nassar, H. Tsang, K. Church, and T. Weller, "A High Efficiency, Electrically-Small, 3-D Machined-Substrate Antenna Fabricated with Fused Deposition Modeling and 3-D Printing," *IEEE Radio and Wireless Symp. (RWS 2013)*, to be published.

- [127] I. Nassar and T. Weller, "An Efficient, Electrically-Small, 3-D Machined-Substrate Antenna," *IEEE Int. Sym. Antennas propag.*, to be published.
- [128] X. Chen, K. Church, and H. Yang, "High speed non-contact printing for solar cell front side metallization," *IEEE Photovoltaic Specialists Conf.* pp. 1343-1347, Jun. 2010.
- [129] S. R. Best, "Low Q electrically small linear and elliptical polarized spherical dipole antennas," *IEEE Trans. Antennas Propag.*, vol. 53, no. 3, pp. 1047-1053, Mar. 2005.
- [130] J. Adams, S. Slimmer, T. Malkowski, E. Duoss, J. Lewis, and J. Bernhard, "Comparison of spherical antennas fabricated via conformal printing: Helix, Meanderline, and Hybrid Designs," *IEEE Antennas Wireless Propag. Lett.*, vol. 10, pp. 1425-1428, 2011.
- [131] C. Kruesi, R. Vyas, and M. Tentzeris, "Design and development of a novel 3-D cubic antenna for wireless sensor networks (WSNs) and RFID applications," *IEEE Trans. Antennas Propag.*, vol. 57, no. 10, pp. 3293–3299, Oct. 2009.
- [132] P. Zade, S. Khade, and N. Choudhary, "Modeling and designing of circular microstrip antenna for wireless communication," *IEEE Int. Conf. on Emerging Trends in Eng. and Tech.*, pp. 1189-1194, Dec. 2009.
- [133] L. RongLin, G. DeJean, M. Maeng, K. Lim, S. Pinel, M. Tentzeris, J. Laskar, "Design of compact stacked-patch antennas in LTCC multilayer packaging modules for wireless applications," *IEEE Transactions on Advanced Packaging*, , vol. 27, no. 4, pp. 581-589, Nov. 2004.
- [134] C. Tsao, Y. Hwang, F. Kilburg, and F. Dietrich, "Aperture-coupled patch antennas with wide-bandwidth and dual-polarization capabilities," *Antennas and Propagation Society International Symposium*, Vol. 3, pp. 936-939, Jun. 1988.
- [135] V. Sarin, M. Nishamol, D. Tony, C. Aanandan, P. Mohanan, and K. Vasudevan, "A broadband L-Strip fed printed microstrip antenna," *IEEE Trans. Antennas Propag.*, vol. 59, no. 1, pp. 281-284, Jan. 2011.
- [136] W. Lo, C. Chan, and K. Luk, "Circularly polarised patch antenna array using proximity-coupled L-strip line feed," *Electronics Letters*, vol. 36, no.14, pp.1174-1175, Jul. 2000.
- [137] T. K. Lo, C. O. Ho, Y. Hwang, E. K. W. Lam, and B. Lee, "Miniature aperture-coupled microstrip antenna of very high permittivity," *Electron. Lett.*, vol. 33, pp. 9–10, Jan. 1997.
- [138] S. Xiao, B-Z. Wang, W. Shao, Y. Zhang, "Bandwidth-enhancing ultralow-profile compact patch antenna," *IEEE Transactions on Antennas and Propagation*, vol. 53, no. 11, pp. 3443-3447, Nov. 2005.

- [139] R. Chair, K. F. Lee, C. L. Mak, K. M. Luk, and A. A. KishK, "Wideband half U-slot patch antennas with shoring pin and shorting wall," in *Proc. IEEE Antennas Propagation Symp. Dig.*, pp. 4132–4135, 2004.
- [140] S. Melais, and T. Weller, "A quasi Yagi antenna backed by a metal reflector," *IEEE Transactions on Antennas and Propagation*, vol. 56, no. 12, pp. 3868-3872, Dec. 2008.
- [141] W. Deal, N. Kaneda, J. Sor, Y. Qian, and T. Itoh, "A new quasi-Yagi antenna for planar active antenna arrays," *IEEE Transactions on Microwave Theory and Techniques*, vol. 48, no. 6, pp. 910-918, Jun. 2000.
- [142] W. Kaswiati, and J. Suryana, "Design and realization of planar bow-tie dipole array antenna with dual-polarization at 2.4 GHz frequency for Wi-Fi access point application," *International Conference on Telecommunication Systems, Services, and Applications (TSSA)*, pp. 218-222, Oct. 2012.
- [143] C-J. Lee, K.M. Leong, and T. Itoh, "A broadband microstrip-to-CPS transition using composite right/left-handed transmission lines with an antenna application," *IEEE International Microwave Symposium Digest*, Jun. 2005.
- [144] G-Y. Chen and J-S. Sun, "A printed dipole antenna with microstrip tapered balun," *Microwave and Optical Technology Lett.*, Vol. 40, Issue 4, pp. 344-346, Jan. 2004.
- [145] M. Bialkowski, and A. Abbosh, "Design of a compact UWB out-of-phase power divider," *IEEE Microwave and Wireless Components Letters*, vol. 17, no. 4, pp. 289-291, Apr. 2007.
- [146] D. Isbell, "Log periodic dipole arrays," *IRE Transactions on Antennas Propagation*, vol. 8, no. 3, pp. 260–267, May 1960.
- [147] J. Yeo and J-I. Lee, "Planar log-periodic bow-tie dipole array antenna with reduced size and enhanced front-back ratio," *Microwave Opt Technol Lett*, vol. 54, no. 6, pp. 1435–1441, Jun. 2012.
- [148] Y. Zhengguang, S. Donglin, and L. Shanwei, "A novel size-reduced strip line log periodic dipole arrays," *IEEE International Symposium on Microwave, Antenna, Propagation and EMC Technologies for Wireless Communications*, vol. 1, pp. 56-59, Aug. 2005.
- [149] H. Jardon-Aguilar, J. Tirado-Mendez, R. Flores-Leal, and R. Linares-Miranda, "Reduced log-periodic dipole antenna using a cylindrical-hat cover," *IET Microwaves Antennas & Propagation*, vol. 5, no. 14, pp. 1697-1702, Nov. 2011.
- [150] D. Anagnostou, J. Papapolymerou, M. Tentzeris, and C. Christodoulou, "A printed log-periodic Koch-dipole array (LPKDA)," *IEEE Antennas and Wireless Propagation Letters*, vol. 7, pp. 456-460, 2008.

- [151] A. Gheethan, and D. Anagnostou, "Reduced size planar Log-Periodic Dipole Arrays (LPDAs) using rectangular meander line elements," *IEEE Antennas and Propagation Society International Symposium*, pp. 1-4, Jul. 2008.
- [152] M. Mangoud, M. Aboul-Dahab, A. Zaki, and S. El-Khamy, "Genetic algorithm design of compressed log periodic dipole array," *IEEE 46th Midwest Symposium on Circuits and Systems*, vol. 3, pp. 1194-1197, Dec. 2003.
- [153] P. C. Buston and G. T. Thompson, "A note on the calculation of the gain of log-periodic dipole antennas," *IEEE Transaction on Antennas and Propagation*, vol. 24, Jan. 1976.
- [154] I. Nassar, T. Weller, and C. Lusk, "Radiating shape-shifting surface based on a planar Hoberman mechanism," *IEEE Transactions on Antennas and Propagation*, vol. 61, no. 5, pp. 2861-2864, May 2013.
- [155] J. Patel and G. Ananthasuresh, "A kinematic theory for radially foldable planar linkages," *Int. Journal of Solids and Structures*, 44, 2007.
- [156] K. Faist and G. Wiens, "Parametric study on the use of Hoberman mechanisms for reconfigurable antenna and solar arrays," *IEEE Aerospace Conference*, pp. 1-8, Mar. 2010.
- [157] B. Munk, D. Janning, R. Marheka, J. McCann, and S. Schneider, "The design of wideband arrays of closely-spaced wire and slot elements," *IEEE Inter. Sym. Antennas Propag. Soc.*, pp. 1-4, Jul. 2010.
- [158] B. Munk et al, "A low-profile broadband phased array antenna," *IEEE Inter. Sym. Antennas Propag. Soc.*, vol. 2, pp. 448- 451, Jun. 2003.
- [159] N. Riley, D. Riley, and J. Jin, "Design and modeling of finite and low-profile, ultra-wideband phased-array antennas," *IEEE Inter. Sym. Phased Array Sys. Tech.*, pp. 484-491, Oct. 2010.
- [160] L. Bian and X. Shi, "Wideband circularly-polarized serial rotated 2×2 circular patch antenna array," *Microw. Opt. Technol. Lett.*, vol. 49, Issue 12, pp. 3122–3124, Sep. 2007.
- [161] M. Jones and J. Rawnick, "A new approach to broadband array design using tightly coupled elements," *IEEE Military Commun. Conf.*, pp. 1-7, Oct. 2007.
- [162] N. Behdad and K. Sarabandi, "A varactor-tuned dual-band slot antenna," *IEEE Trans. Antennas Propag.*, vol. 54, no. 2, pp. 401–408, Feb. 2006.
- [163] J. Aberle, S. Oh, D. Auckland, and S. Rogers, "Reconfigurable antennas for portable wireless devices," *IEEE Antennas Propag. Mag.*, vol. 45, no. 6, pp. 148–154, Dec. 2003.

- [164] N. Yang, C. Caloz, and K. Wu; , "Fixed-beam frequency-tunable phase-reversal coplanar stripline antenna array," *IEEE Trans. Antennas Propag.*, vol. 57, no. 3, pp. 671-681, Mar. 2009.
- [165] J. Huang, "A technique for an array to generate circular polarization with linearly polarized elements," *IEEE Trans. Antennas Propag.*, vol. 34, no. 9, pp. 1113- 1124, Sep. 1986.
- [166] J.-W. Wu and J.-H. Lu, "2×2 Circularly polarized patch antenna arrays with broadband operation," *Microwave Opt Technol. Lett.*, vol. 39, Issue 5, pp. 360-363, Oct. 2003.
- [167] I. Nassar, A. Gheethan, T. Weller, and G. Mumcu "A Miniature, Broadband, Non-Dispersive Phase Shifter Based on CRLH TL Unit Cells" to be presented at *IEEE Inter. Sym. Antennas propag.*, Jul. 2012.
- [168] J. Ouyang, S. Bo, J. Zhang, and Y. Feng, "A low-profile unidirectional cavity-backed log-periodic slot antenna," *Progress In Electromagnetics Research*, Vol. 119, 423-433, 2011.
- [169] J. Joubert, J. Vardaxoglou, W. Whittow, and J. Odendaal, "CPW-fed cavity-backed slot radiator loaded with an AMC reflector," *IEEE Transactions on Antennas and Propagation*, , vol. 60, no. 2, pp. 735-742, Feb. 2012.
- [170] I-C. Lan, S-Y. Chen, and P. Hsu, "Coupled twin slots fed by conductor-backed coplanar waveguide," *IEEE Transactions on Antennas and Propagation*, vol. 56, no. 6, pp. 1784-1786, Jun. 2008.
- [171] I-C. Lan, S-Y Chen, and P. Hsu, "Pattern smoothness and gain enhancement of finite ground slot dipole antenna fed by conductor-backed coplanar waveguide," *IEEE Antennas and Propagation Society International Symposium*, pp. 1-4, Jul. 2008.
- [172] S-S. Zhong, F-W. Yao, and X-L. Liang, "Wideband slot antenna backed by a ground plane," *IEEE Antennas and Propagation Society International Symposium*, pp. 2559-2562, Jul. 2006.
- [173] X-C. Lin, and C-C. Yu, "A dual-band CPW-fed inductive slot-monopole hybrid antenna," *IEEE Transactions on Antennas and Propagation*, vol. 56, no. 1, pp. 282-285, Jan. 2008.
- [174] N. Behdad, and K. Sarabandi, "A wide-band slot antenna design employing a fictitious short circuit concept," *IEEE Transactions on Antennas and Propagation*, vol. 53, no. 1, pp. 475-482, Jan. 2005.
- [175] Y-C. Chen, S-Y. Chen, and P. Hsu, "Modification of radiation patterns of first harmonic mode of slot dipole for dual-frequency Operation," *IEEE Transactions on Antennas and Propagation*, vol. 59, no. 7, pp. 2707-2710, Jul. 2011.

- [176] S.-Y. Chen and P. Hsu, "Broadband radial slot antenna fed by coplanar waveguide for dual-frequency operation," *IEEE Trans. Antennas Propag.*, vol. 53, no. 11, pp. 3448–3452, Nov. 2005.
- [177] S.-Y. Chen, Y.-C. Chen, and P. Hsu, "CPW-fed aperture-coupled slot dipole antenna for tri-band operation," *IEEE Antennas Wireless Propag. Lett.*, vol. 7, pp. 535–537, 2008.
- [178] S.-Y. Chen and P. Hsu, "Dual-band slot dipole antenna fed by a coplanar waveguide," *IEEE International Symposium Antennas and Propagation Society*, pp. 3589-3592, Jul. 2006.
- [179] M. Forman, and Z. Popovic, "A tunable second-resonance cross-slot antenna," *IEEE Antennas and Propagation Society International Symposium*, vol. 1, pp. 18-21, Jul. 1997.
- [180] P.-L. Chi, R. Waterhouse, and T. Itoh, "Compact and tunable slot-loop antenna," *IEEE Transactions on Antennas and Propagation*, vol. 59, no. 4, pp. 1394-1397, Apr. 2011.
- [181] S. Kawasaki, and T. Itoh, "A slot antenna with electronically tunable length," *Antennas and Propagation Society International Symposium*, vol. 1, pp. 130-133, Jun. 1991.
- [182] D. Peroulis, K. Sarabandi, and L. Katehi, "Design of reconfigurable slot antennas," *IEEE Transactions on Antennas and Propagation*, vol. 53, no. 2, pp. 645-654, Feb. 2005.
- [183] P. J. Gibson, "The Vivaldi aerial," in *Proc. 9th Eur. Microw. Conf.*, Brighton, U.K., pp. 101–105, Jun. 1979.
- [184] J. Langley, P. Hall, and P. Newham, "Balanced antipodal Vivaldi antenna for wide bandwidth phased arrays," *IEE Proceedings Microwaves, Antennas and Propagation*, vol. 143, no. 2, pp. 97-102, Apr. 1996.
- [185] M. Agahi, H. Abiri, and F. Mohajeri, "Investigation of a New Idea for Antipodal Vivaldi Antenna Design", *International Journal of Computer and Electrical Engineering*, Vol. 3, No. 2, 2011.
- [186] E. Gazit, "Improved design of the Vivaldi antenna," *IEE Proceedings: Microwaves, Antennas and Propagation*, vol. 135, no. 2, pp. 89–92, 1988.
- [187] X. King, Z. N. Chen, and M. Y. W. Chia, "Parametric study of ultrawideband dual elliptically tapered antipodal slot antenna," *Int. J. Antenna Propag*, Article ID: 267197, 2008.
- [188] G. Teni, N. Zhang, J. Qiu, and P. Zhang "Research on a novel miniaturized antipodal Vivaldi antenna with improved radiation," *IEEE Antennas and Wireless Propagation Letters*, vol. 12, pp. 417-420, 2013.

- [189] J. Bourqui, M. Okoniewski, and E.C. Fear, "Balanced antipodal Vivaldi antenna with dielectric director for near-field microwave imaging," *IEEE Transactions on Antennas and Propagation*, vol. 58, no. 7, pp. 2318-2326, Jul. 2010.
- [190] M. Sun, Z. Chen, and X. Qing, "Gain enhancement of 60-GHz antipodal tapered slot antenna using zero-index metamaterial," *IEEE Transactions on Antennas and Propagation*, vol. 61, no. 4, pp. 1741-1746, Apr. 2013.
- [191] B. Zhou, H. Li, X. Zou, and T.-J. Cui, "Broadband and high-gain planar Vivaldi antennas based on inhomogeneous anisotropic zeroindex metamaterials," *Progress In Electromagnetics Research*, Vol. 120, 235–247, 2011.
- [192] Z. Wang, and H. Zhang, "Improvements in a high gain UWB antenna with corrugated edges," *Progress In Electromagnetics Research*, Vol. 6, 159–166, 2009.
- [193] R. Janaswamy, and D. H. Schaubert, "Analysis of the tapered slot antennas," *IEEE Transactions on Antennas and Propagation*, vol. 35, no. 9, pp. 1058-1065, Sep. 1987.
- [194] F-C. Ren, F-S. Zhang, B. Chen, and Q-C. Zhou, "Compact tapered slot antenna for wideband applications," *IEEE CIE International Conference on Radar*, vol. 2, pp. 1161-1163, Oct. 2011.
- [195] Lin, S., S. Yang, A. E. Fathy, and A. Elsherbini, "Development of a novel UWB vivaldi antenna array using SIW technology," *Progress In Electromagnetics Research*, Vol. 90, 369–384, 2009.
- [196] I. Nassar, A. Gheethan, T. Weller, and G. Mumcu, "A miniature, broadband, non-dispersive phase shifter based on CRLH TL unit cells," *IEEE Antennas and Propagation Society International Symposium*, pp. 1-2, Jul. 2012.
- [197] M. Desnoyer, and K. Guerin, "Stabilizing an S-band antenna for mobile communication from the moon," *IEEE Aerospace conference*, pp. 1-10, Mar. 2009.
- [198] M. Honarvar, F. Jolani, A. Dadgarpour, and B. Virdee, "Compact wideband phase shifter," *Int. J. RF and Microwave Comp. Aid. Eng.*, vol. 23, pp. 47–51, May 2012.
- [199] A. Abbosh, "Ultra-wideband phase shifters," *IEEE Transactions on Microwave Theory and Techniques*, vol. 55, no. 9, pp. 1935-1941, Sep. 2007.
- [200] Z. Zhang, Y.-C. Jiao, S.-F. Cao, X.-M. Wang, and F.-S. Zhang, "Modified broadband schiffman phase shifter using dentate microstrip and patterned ground plane," *Progress Electromagnetics Res. Lett*, vol. 24, pp. 9–16, 2011.
- [201] Y. Cheng, W. Hong, and K. Wu, "Broadband self-compensating phase shifter combining delay Line and equal-length unequal-width phaser," *IEEE Trans. Microw. Theory Tech.*, vol.58, no.1, pp.203-210, Jan. 2010.

- [202] Y. Ko, J. Park, and J. Bu, "Integrated RF MEMS phase shifters with constant phase shift," *IEEE Microw. Theory Tech. Symp.*, pp.1489-1492, Jun. 2003.
- [203] C-H. Tseng and C-L. Chang, "A broadband quadrature power splitter using metamaterial transmission line," *IEEE Microwave and Wireless Components Letters*, vol. 18, no. 1, pp. 25-27, Jan. 2008.
- [204] C-J. Lee, K.M. Leong, and T. Itoh, "A broadband microstrip-to-CPS transition using composite right/left-handed transmission lines with an antenna application," *IEEE MTT-S International Microwave Symposium Digest*, pp. 4, Jun. 2005.
- [205] M. Antoniades and G. Eleftheriades, "A broadband Wilkinson balun using microstrip metamaterial lines," *IEEE Antennas and Wireless Propagation Letters*, vol. 4, pp. 209-212, 2005.
- [206] J. Perruisseau-Carrier, T. Lisee, and A. Skrivervik, "Circuit model and design of silicon-integrated CRLH-TLs analogically controlled by MEMS," *Microw. Opt. Tech. Lett.*, vol. 48, no. 12, pp. 2496-2499, 2006.
- [207] J. Perruisseau-Carrier, K. Topalli, and T. Akin, "Low-loss Ku-band artificial transmission line with MEMS tuning capability," *IEEE Microw. Wireless Compon. Lett.*, vol. 19, no. 6, pp. 377-379, Jun. 2009.
- [208] T. Jang et al, "Switchable composite right/left-handed (S-CRLH) transmission line using MEMS switches," *IEEE Microw. Wireless Compon. Lett.*, vol. 19, no. 12, pp. 804-806, Dec. 2009.
- [209] C. Caloz and T. Itoh, "Electromagnetic Metamaterials: Transmission Line Theory and Microwave Applications" Wiley-IEEE Press, 2005.

APPENDICES

Appendix A: Copyright Permissions

A.1 Permissions for Chapter 3



The screenshot shows the Copyright Clearance Center RightsLink interface. At the top left is the Copyright Clearance Center logo. To its right is the RightsLink logo. Further right are three navigation buttons: Home, Create Account, and Help. Below the logo is a blue box with the IEEE logo and the text: "Requesting permission to reuse content from an IEEE publication". To the right of this box is a list of publication details: Title: A Compact 3-D Harmonic Repeater for Passive Wireless Sensing; Author: Nassar, I.T.; Weller, T.M.; Frolik, J.L.; Publication: Microwave Theory and Techniques, IEEE Transactions on; Publisher: IEEE; Date: Oct. 2012; Copyright © 2012, IEEE. To the right of the details is a login form with fields for User ID and Password, an "Enable Auto Login" checkbox, a "LOGIN" button, and a "Forgot Password/User ID?" link. Below the login form is a message: "If you're a copyright.com user, you can login to RightsLink using your copyright.com credentials. Already a RightsLink user or want to learn more?"

Thesis / Dissertation Reuse

The IEEE does not require individuals working on a thesis to obtain a formal reuse license, however, you may print out this statement to be used as a permission grant:

Requirements to be followed when using any portion (e.g., figure, graph, table, or textual material) of an IEEE copyrighted paper in a thesis:

- 1) In the case of textual material (e.g., using short quotes or referring to the work within these papers) users must give full credit to the original source (author, paper, publication) followed by the IEEE copyright line © 2011 IEEE.
- 2) In the case of illustrations or tabular material, we require that the copyright line © [Year of original publication] IEEE appear prominently with each reprinted figure and/or table.
- 3) If a substantial portion of the original paper is to be used, and if you are not the senior author, also obtain the senior author's approval.

Requirements to be followed when using an entire IEEE copyrighted paper in a thesis:

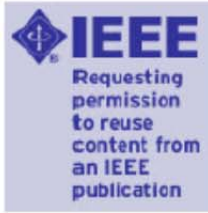
- 1) The following IEEE copyright/ credit notice should be placed prominently in the references: © [year of original publication] IEEE. Reprinted, with permission, from [author names, paper title, IEEE publication title, and month/year of publication]
- 2) Only the accepted version of an IEEE copyrighted paper can be used when posting the paper or your thesis on-line.
- 3) In placing the thesis on the author's university website, please display the following message in a prominent place on the website: In reference to IEEE copyrighted material which is used with permission in this thesis, the IEEE does not endorse any of [university/educational entity's name goes here]'s products or services. Internal or personal use of this material is permitted. If interested in reprinting/republishing IEEE copyrighted material for advertising or promotional purposes or for creating new collective works for resale or redistribution, please go to http://www.ieee.org/publications_standards/publications/rights/rights_link.html to learn how to obtain a License from RightsLink.

If applicable, University Microfilms and/or ProQuest Library, or the Archives of Canada may supply single copies of the dissertation.

BACK

CLOSE WINDOW

Copyright © 2013 [Copyright Clearance Center, Inc.](#) All Rights Reserved. [Privacy statement.](#)



Title: Design and characterization of a passive harmonic sensor embedded in sand

Conference Proceedings: Wireless and Microwave Technology Conference (WAMICON), 2013 IEEE 14th Annual

Author: Nassar, I.T.; Weller, T.M.

Publisher: IEEE

Date: 7-9 April 2013

Copyright © 2013, IEEE

User ID

Password

Enable Auto Login

LOGIN

[Forgot Password/User ID?](#)

If you're a copyright.com user, you can login to RightsLink using your copyright.com credentials. Already a RightsLink user or want to [learn more?](#)

Thesis / Dissertation Reuse

The IEEE does not require individuals working on a thesis to obtain a formal reuse license, however, you may print out this statement to be used as a permission grant:

Requirements to be followed when using any portion (e.g., figure, graph, table, or textual material) of an IEEE copyrighted paper in a thesis:

- 1) In the case of textual material (e.g., using short quotes or referring to the work within these papers) users must give full credit to the original source (author, paper, publication) followed by the IEEE copyright line © 2011 IEEE.
- 2) In the case of illustrations or tabular material, we require that the copyright line © [Year of original publication] IEEE appear prominently with each reprinted figure and/or table.
- 3) If a substantial portion of the original paper is to be used, and if you are not the senior author, also obtain the senior author's approval.

Requirements to be followed when using an entire IEEE copyrighted paper in a thesis:

- 1) The following IEEE copyright/ credit notice should be placed prominently in the references: © [year of original publication] IEEE. Reprinted, with permission, from [author names, paper title, IEEE publication title, and month/year of publication]
- 2) Only the accepted version of an IEEE copyrighted paper can be used when posting the paper or your thesis on-line.
- 3) In placing the thesis on the author's university website, please display the following message in a prominent place on the website: In reference to IEEE copyrighted material which is used with permission in this thesis, the IEEE does not endorse any of [university/educational entity's name goes here]'s products or services. Internal or personal use of this material is permitted. If interested in reprinting/republishing IEEE copyrighted material for advertising or promotional purposes or for creating new collective works for resale or redistribution, please go to http://www.ieee.org/publications_standards/publications/rights/rights_link.html to learn how to obtain a License from RightsLink.

If applicable, University Microfilms and/or ProQuest Library, or the Archives of Canada may supply single copies of the dissertation.

BACK **CLOSE WINDOW**

A.2 Permission for Chapter 6



RightsLink®

Home

Create Account

Help



Title: An electrically-small, 3-D cube antenna fabricated with additive manufacturing
Conference Proceedings: Radio and Wireless Symposium (RWS), 2013 IEEE
Author: Nassar, I.T.; Weller, T.M.
Publisher: IEEE
Date: 20-23 Jan. 2013
Copyright © 2013, IEEE

User ID
Password
 Enable Auto Login
LOGIN
[Forgot Password/User ID?](#)
If you're a copyright.com user, you can login to RightsLink using your copyright.com credentials. Already a RightsLink user or want to [learn more?](#)

Thesis / Dissertation Reuse

The IEEE does not require individuals working on a thesis to obtain a formal reuse license, however, you may print out this statement to be used as a permission grant:

Requirements to be followed when using any portion (e.g., figure, graph, table, or textual material) of an IEEE copyrighted paper in a thesis:

- 1) In the case of textual material (e.g., using short quotes or referring to the work within these papers) users must give full credit to the original source (author, paper, publication) followed by the IEEE copyright line © 2011 IEEE.
- 2) In the case of illustrations or tabular material, we require that the copyright line © [Year of original publication] IEEE appear prominently with each reprinted figure and/or table.
- 3) If a substantial portion of the original paper is to be used, and if you are not the senior author, also obtain the senior author's approval.

Requirements to be followed when using an entire IEEE copyrighted paper in a thesis:

- 1) The following IEEE copyright/ credit notice should be placed prominently in the references: © [year of original publication] IEEE. Reprinted, with permission, from [author names, paper title, IEEE publication title, and month/year of publication]
- 2) Only the accepted version of an IEEE copyrighted paper can be used when posting the paper or your thesis on-line.
- 3) In placing the thesis on the author's university website, please display the following message in a prominent place on the website: In reference to IEEE copyrighted material which is used with permission in this thesis, the IEEE does not endorse any of [university/educational entity's name goes here]'s products or services. Internal or personal use of this material is permitted. If interested in reprinting/republishing IEEE copyrighted material for advertising or promotional purposes or for creating new collective works for resale or redistribution, please go to http://www.ieee.org/publications_standards/publications/rights/rights_link.html to learn how to obtain a License from RightsLink.

If applicable, University Microfilms and/or ProQuest Library, or the Archives of Canada may supply single copies of the dissertation.

BACK

CLOSE WINDOW

Copyright © 2013 [Copyright Clearance Center, Inc.](#) All Rights Reserved. [Privacy statement.](#)

A.3 Permission for Chapter 8



RightsLink®

Home

Create Account

Help



Title: Radiating Shape-Shifting Surface Based on a Planar Hoberman Mechanism
Author: Nassar, I.T.; Weller, T.M.; Lusk, C.P.
Publication: Antennas and Propagation, IEEE Transactions on
Publisher: IEEE
Date: May 2013
Copyright © 2013, IEEE

Enable Auto Login

[Forgot Password/User ID?](#)
If you're a copyright.com user, you can login to RightsLink using your copyright.com credentials. Already a RightsLink user or want to [learn more?](#)

Thesis / Dissertation Reuse

The IEEE does not require individuals working on a thesis to obtain a formal reuse license, however, you may print out this statement to be used as a permission grant:

Requirements to be followed when using any portion (e.g., figure, graph, table, or textual material) of an IEEE copyrighted paper in a thesis:

- 1) In the case of textual material (e.g., using short quotes or referring to the work within these papers) users must give full credit to the original source (author, paper, publication) followed by the IEEE copyright line © 2011 IEEE.
- 2) In the case of illustrations or tabular material, we require that the copyright line © [Year of original publication] IEEE appear prominently with each reprinted figure and/or table.
- 3) If a substantial portion of the original paper is to be used, and if you are not the senior author, also obtain the senior author's approval.

Requirements to be followed when using an entire IEEE copyrighted paper in a thesis:

- 1) The following IEEE copyright/ credit notice should be placed prominently in the references: © [year of original publication] IEEE. Reprinted, with permission, from [author names, paper title, IEEE publication title, and month/year of publication]
- 2) Only the accepted version of an IEEE copyrighted paper can be used when posting the paper or your thesis on-line.
- 3) In placing the thesis on the author's university website, please display the following message in a prominent place on the website: In reference to IEEE copyrighted material which is used with permission in this thesis, the IEEE does not endorse any of [university/educational entity's name goes here]'s products or services. Internal or personal use of this material is permitted. If interested in reprinting/republishing IEEE copyrighted material for advertising or promotional purposes or for creating new collective works for resale or redistribution, please go to http://www.ieee.org/publications_standards/publications/rights/rights_link.html to learn how to obtain a License from RightsLink.

If applicable, University Microfilms and/or ProQuest Library, or the Archives of Canada may supply single copies of the dissertation.

BACK

CLOSE WINDOW

Copyright © 2013 [Copyright Clearance Center, Inc.](#) All Rights Reserved. [Privacy statement.](#)

A.4 Permission for Chapter 11



RightsLink®

Home

Create Account

Help



Title: A miniature, broadband, non-dispersive phase shifter based on CRLH TL unit cells
Conference Proceedings: Antennas and Propagation Society International Symposium (APSURSI), 2012 IEEE
Author: Nassar, I.T.; Gheethan, A.A.; Weller, T.M.; Mumcu, G.
Publisher: IEEE
Date: 8-14 July 2012
Copyright © 2012, IEEE

User ID
Password
<input type="checkbox"/> Enable Auto Login
<input type="button" value="LOGIN"/>
Forgot Password/User ID?
If you're a copyright.com user, you can login to RightsLink using your copyright.com credentials. Already a RightsLink user or want to learn more?

Thesis / Dissertation Reuse

The IEEE does not require individuals working on a thesis to obtain a formal reuse license, however, you may print out this statement to be used as a permission grant:

Requirements to be followed when using any portion (e.g., figure, graph, table, or textual material) of an IEEE copyrighted paper in a thesis:

- 1) In the case of textual material (e.g., using short quotes or referring to the work within these papers) users must give full credit to the original source (author, paper, publication) followed by the IEEE copyright line © 2011 IEEE.
- 2) In the case of illustrations or tabular material, we require that the copyright line © [Year of original publication] IEEE appear prominently with each reprinted figure and/or table.
- 3) If a substantial portion of the original paper is to be used, and if you are not the senior author, also obtain the senior author's approval.

Requirements to be followed when using an entire IEEE copyrighted paper in a thesis:

- 1) The following IEEE copyright/ credit notice should be placed prominently in the references: © [year of original publication] IEEE. Reprinted, with permission, from [author names, paper title, IEEE publication title, and month/year of publication]
- 2) Only the accepted version of an IEEE copyrighted paper can be used when posting the paper or your thesis on-line.
- 3) In placing the thesis on the author's university website, please display the following message in a prominent place on the website: In reference to IEEE copyrighted material which is used with permission in this thesis, the IEEE does not endorse any of [university/educational entity's name goes here]'s products or services. Internal or personal use of this material is permitted. If interested in reprinting/republishing IEEE copyrighted material for advertising or promotional purposes or for creating new collective works for resale or redistribution, please go to http://www.ieee.org/publications_standards/publications/rights/rights_link.html to learn how to obtain a License from RightsLink.

If applicable, University Microfilms and/or ProQuest Library, or the Archives of Canada may supply single copies of the dissertation.

BACK

CLOSE WINDOW

Copyright © 2013 [Copyright Clearance Center, Inc.](#) All Rights Reserved. [Privacy statement.](#)

ABOUT THE AUTHOR

Ibrahim T. Nassar was born on May 16th 1986 in Irbid city, Jordan. He grew up in Hibras village and went to the Yarmouk University Model School. In 2004 he graduated from the high school after passing the general secondary examination with an average of 94.1%. In 2008 he received the B.S. degree from Jordan University of Science & Technology, Irbid, Jordan in electrical engineering. He graduated with a GPA of 81.3% and was ranked upon the top ten among all graduating students. After his graduation, he was one of three students selected to participate in the IRES program (International Research Experience for Students) at the University of Central Florida in summer 2008. In 2009 he moved to the U.S. to continue his education and join the WAMI lab at the University of South Florida as a Graduate Research Assistant. On October 4th 2010, he received the M.S. degree in electrical engineering and on November 4th 2013 he defended his doctoral research dissertation. In summer 2012 he worked as an RF Design Engineer Intern at Texas Instruments Inc., Clearwater, Florida. Up to date, he is the inventor/co-inventor of 6 pending U.S. patents and has 17 published and to be published IEEE transactions journal and conference papers.

Nassar was one of the recipients of the IEEE MTT-S Graduate Fellowship for spring 2013. He also received the best student paper award of the IEEE WAMICON Conference, April 2013 and the IMAPS student award in 2012.